

UNRAVELING THE ROLES OF T CELLS IN PULMONARY IMMUNOLOGY: LESSONS FROM
COVID-19, SIV, AND SINGLE-CELL RNA SEQUENCING

AN ABSTRACT

SUBMITTED ON THE 26th DAY OF OCTOBER 2023

TO THE GRADUATE PROGRAM IN BIOMEDICAL SCIENCES

IN PARTIAL FULFILLMENT OF THE REQUIREMENTS

OF THE SCHOOL OF MEDICINE

OF TULANE UNIVERSITY

FOR THE DEGREE

OF

DOCTOR OF PHILOSOPHY

BY



ALEXANDRA BOOKER MELTON

APPROVED:

Nicholas J. Maness, Ph.D. (Chair)



Amitinder Kaur, M.D.



Robert V. Blair, D.V.M., Ph.D.



Jennifer Manuzak, Ph.D.



Joseph Mudd, Ph.D.



ABSTRACT

T cells play an essential role in the immune response to pathogens, serving as both guardians and regulators of host defenses. This thesis dives into the roles of T cells with a focus on infectious diseases and pulmonary immunology, including the effects of immunosuppression. We first introduce the pigtail macaque (PTM) as a novel model for understanding COVID-19, with an emphasis on T cell-mediated immune responses. We show that pulmonary infiltrates were dominated by T cells, including CD4⁺ T cells that upregulate CD8 and express cytotoxic molecules, as well as virus-targeting T cells that were predominantly CD4⁺. We then investigate the impact of simian immunodeficiency virus (SIV)-induced immunodeficiency on the progression of COVID-19 disease and the persistence and evolution of SARS-CoV-2. We show that while immunodeficiency induced by SIV appeared to modulate the adaptive response to SARS-CoV-2, as evidenced by a failure to generate neutralizing antibodies or virus-specific T cell responses, it did not alter the overall course of disease or viral kinetics in the PTM model, suggesting that SIV alone may not be sufficient in driving the emergence of novel SARS-CoV-2 variants. These studies prompted us to further explore pulmonary T cells, emphasizing a previously overlooked population of cells in the lung's vascular system. Using intravascular staining (ivs), our findings suggest that pulmonary vascular T cells (ivs⁺) are a unique population distinct from mere "blood contaminants." Through flow cytometry and single-cell RNA sequencing, we show that CD8⁺ T cells are enriched within this

group and predominantly exhibit an effector phenotype highlighted by increased Granzyme B (GZMB) expression. These T cells demonstrate a gene expression profile enriched in cell adhesion and extravasation markers, suggesting a unique pulmonary vasculature niche that selects for specific cells. In SIV-infected rhesus macaques (RhM), ivs+ CD8+ T cells showed heightened activity compared to tissue-resident memory CD8+ T cells (T_{RM}). Collectively, this research highlights the role of T cells in infectious disease, particularly within the realm of pulmonary immunology. These findings not only enrich our understanding of T cell biology but also reinforce non-human primates (NHPs) as a valuable animal model in biomedical research, providing crucial insights for the development of novel therapeutics, particularly those that modulate pulmonary T cell responses.

UNRAVELING THE ROLES OF T CELLS IN PULMONARY IMMUNOLOGY: LESSONS FROM
COVID-19, SIV, AND SINGLE-CELL RNA SEQUENCING

A DISSERTATION

SUBMITTED ON THE 26th DAY OF OCTOBER 2023

TO THE GRADUATE PROGRAM IN BIOMEDICAL SCIENCES

IN PARTIAL FULFILLMENT OF THE REQUIREMENTS

OF THE SCHOOL OF MEDICINE

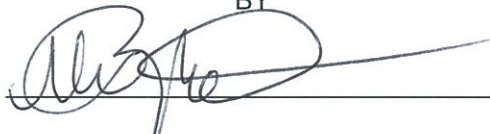
OF TULANE UNIVERSITY

FOR THE DEGREE

OF

DOCTOR OF PHILOSOPHY

BY



ALEXANDRA BOOKER MELTON

APPROVED:

Nicholas J. Maness, Ph.D. (Chair)



Nicholas J. Maness

Amitinder Kaur, M.D.



Amitinder Kaur

Robert V. Blair, D.V.M., Ph.D.



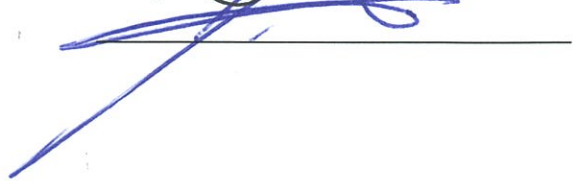
Robert V. Blair

Jennifer Manuzak, Ph.D.



Jennifer Manuzak

Joseph Mudd, Ph.D.



Joseph Mudd

*To my beautiful children, Brittany Alexandra and Hunter Jack,
Being your mom has been the greatest gift. Remember always that dreams and
goals know no boundaries or expiration dates.*

TABLE OF CONTENTS

<i>List of Figures</i>	<i>iv</i>
<i>List of Tables</i>	<i>vii</i>
<i>Introduction and Background</i>	1
<i>Chapter 1</i>	19
<u><i>The Pigtail Macaque (<i>Macaca nemestrina</i>) Model of COVID-19 Reproduces Diverse Clinical Outcomes and Reveals New and Complex Signatures of Disease</i></u>	
Abstract.....	20
Introduction.....	21
Materials and Methods.....	24
Results.....	35
Discussion.....	60
<i>Chapter 2</i>	76
<u><i>The Impact of SIV-Induced Immunodeficiency on Clinical Manifestation, Immune Responses, and Viral Dynamics in SARS-CoV-2 Coinfection</i></u>	
Abstract.....	77
Introduction.....	78
Materials and Methods.....	81
Results.....	89
Discussion.....	96
<i>Chapter 3</i>	105
<u><i>Molecular Transcriptomic Signatures of Pulmonary T Cells in Non-Human Primates: Redefining Lung Vasculature T Cells Beyond Blood Contaminants Through Single-Cell RNA Sequencing</i></u>	
Abstract.....	106
Introduction.....	107
Materials and Methods.....	110
Results.....	116

Discussion.....	141
Conclusion and Future Directions.....	155
List of References.....	162
Acknowledgments.....	199

LIST OF FIGURES

Chapter 1

Figure 1.1 Viral dynamics.....	37
Figure 1.2 Histopathologic findings in SARS-CoV-2 infected pigtail macaques.....	40
Figure 1.3 Inflammatory innate immune response in pigtail macaques challenged with SARS-CoV-2.....	43
Figure 1.4 Pulmonary SARS-CoV-2 infection and macrophage/monocytes in the lung and blood.....	47
Figure 1.5 Monocyte cytokine response in the blood of pigtail macaques challenged with SARS-CoV-2.....	48
Figure 1.6 T cells in the blood.....	50
Figure 1.7 Adaptive T cell responses in the BAL.....	51
Figure 1.8 Changes in T cell cytokine expression in the lung and blood... 	53
Figure 1.9 CD4 and Granzyme B expression in the lungs of SARS-CoV-2 infected macaques at 6- and 21-days post infection.....	56
Figure 1.10 SARS-CoV-2 peptide-specific T cell response in the lung 21 days post- Infection.....	58
Figure 1.11 Humoral immune response in SARS-CoV-2 infected pigtail macaques.....	59
Figure 1.S1 Body temperature and oxygen saturation in SARS-CoV-2 infected pigtail macaques.....	66
Figure 1.S2 Radiographs of pigtail macaques (PTM) challenged with SARS CoV-2.....	67

Figure 1.S3 Gross pathological pulmonary pathology in SARS-CoV-2 infected-pigtail macaques.....	68
Figure 1.S4 Changes in IDO activity post SARS-CoV-2 infection.....	69
Figure 1.S5 SARS-CoV-2 peptide-specific T cell response in the blood 21 days post- infection.....	70
Figure 1.S6 Gating strategies.....	71

Chapter 2

Figure 2.1 Before SARS-CoV-2 exposure, PTM experienced uncontrolled SIV viremia and immunodeficiency due to loss of CD4+ T cells.....	90
Figure 2.2 SARS-CoV-2 viral dynamics.....	92
Figure 2.3 T cell dynamics in blood and BAL following SARS-CoV-2 infection of SIV+ and SIV naïve PTM.....	94
Figure 2.4 SARS-CoV-2 specific T cell responses were undetectable in the lung and blood 21-days-post-infection.....	95
Figure 2.5 Humoral immune response to SARS-CoV-2 infection.....	96
Figure 2.S1 Body temperature, weight, and oxygen saturation in SARS-CoV-2 /SIV coinfecting pigtail macaques.....	101
Figure 2.S2 Radiographs of SIV-infected pigtail macaques (PTM) challenged with SARS-CoV-2.....	102

Chapter 3

Figure 3.1 Intravascular staining (ivs) in Rhesus Macaques (RhM).....	117
Figure 3.2 tSNE analysis of CD3+ T cells isolated from blood and respiratory tissue.....	119
Figure 3.3 CD69 expression on T cells isolated from lung (ivs- and ivs+) and blood.....	120

Figure 3.4 Viral and T cell Dynamics in SIVmac239 infected rhesus macaques (RhM).....	122
Figure 3.5 T cell phenotyping across blood and lung in SIV-infected rhesus macaques (RhM).....	123
Figure 3.6 Pulmonary ivs+ CD8+ T cells have increased cytotoxic capacity.....	124
Figure 3.7 MHC Class-I tetramer staining of SIV-specific CD8+ T cells pre and 4 weeks post-ART cessation.....	126
Figure 3.8 Single-cell sequencing analysis of CD3+ T cells isolated from lung (ivs+ and ivs-), bronchial lymph node (LN), and blood.....	130
Figure 3.9 Single-cell analysis of T cells across tissues.....	132
Figure 3.10 Differential gene expression (DEG) and gene set enrichment analysis (GSEA) of T cells across tissues.....	135
Figure 3.11 Cell-cell communication analysis reveals upregulation of transendothelial migration transcripts in pulmonary ivs+ T cells...	137
Figure 3.12 Transcriptomic expression of genes associated with tissue residency and cytotoxicity in pulmonary ivs+ and peripheral CD8 T cells.....	140
Figure 3.13 Transcriptomic expression of genes associated with vascular cell wall interactions in pulmonary ivs+ and peripheral CD8 T cells.....	141
Figure 3.S1 Granzyme B (GZM-B) expression on CD8 T cell populations isolated from lung (both ivs+ and ivs-).....	146
Figure 3.S2 Functional responses of pulmonary (ivs+ and ivs-) and peripheral CD8 T cells.....	147
Figure 3.S3 Single-cell analysis of T cells across tissues.....	148

LIST OF TABLES

Chapter 1

<i>Table 1.1 PTM cohort used in this study, including sex, age, and weight at the time of SARS-CoV-2 inoculation.....</i>	<i>26</i>
<i>Table 1.S1 Clinical, blood and necropsy observations in pigtail macaques (PTM) challenged with SARS-CoV-2.....</i>	<i>72</i>
<i>Table 1.S2 Monocyte Flow Cytometry Panel.....</i>	<i>73</i>
<i>Table 1.S3 Phenotype Flow Cytometry Panel.....</i>	<i>74</i>
<i>Table 1.S4 T cell Flow Cytometry Panel.....</i>	<i>75</i>
<i>Table 1.S5 T cell SARS-CoV-2 Peptide, PMA/Ionomycin Stimulation.....</i>	<i>75</i>
<i>Table 1.S6 Immunohistochemistry Reagent Panel.....</i>	<i>75</i>

Chapter 2

<i>Table 2.1 Cohort of PTM used in this study.....</i>	<i>81</i>
<i>Table 2.S1 Flow Cytometry Antibodies.....</i>	<i>103</i>
<i>Table 2.S2 XpressBio Simian ELISA Reagents.....</i>	<i>104</i>

Chapter 3

<i>Table 3.S1 Flow Cytometry Antibodies.....</i>	<i>149</i>
<i>Table 3.S2 Top differentially expressed genes (DEG) for each seurat cluster.....</i>	<i>150</i>

Table 3.S3 Differential gene expression between seurat clusters 2

and 1..... 154

Introduction

The study of immune dynamics, particularly in the context of infectious disease, has gained significant attention due to the global crisis caused by the COVID-19 pandemic. Immunity, at its core, is a finely balanced interplay of various cellular players intricately responding to pathogenic invaders. Among these, T cells stand out as faithful defenders due to their ability to recognize specific antigens, proliferate rapidly upon activation, and differentiate into diverse roles, ranging from immediate effectors to long-lived memory cells. Their essential role in adaptive immunity highlights their significance in infectious disease research.

The emergence of SARS-CoV-2 in December 2019, the causative agent of COVID-19, has impacted millions of people worldwide, with over 770 million reported cases and nearly 7 million deaths as of September 2023 [1]. While most cases are mild or asymptomatic, some individuals experience severe complications, including pneumonia, systemic inflammation, and coagulopathy, which can lead to organ failure, shock, and death [2–7]. Research suggests that the intensity of the immune response is linked to the severity and progression of COVID-19, with severe disease typically manifesting 3-4 weeks after initial symptoms [8,9].

In the early stages of the pandemic, establishing animal models that faithfully replicated human disease was paramount for developing effective

vaccines and treatments as well as for understanding the immune response to infection [10]. While non-human primates (NHPs) were found to be naturally susceptible to SARS-CoV-2 infection, these animal models failed to recapitulate the severe disease experienced by some humans [11–15].

As the global health crisis evolved, new variants of concern continued to emerge, further driving the pandemic [16–22]. Persistent and uncontrolled SARS-CoV-2 replication in immunocompromised individuals could be a potential source of these novel viral variants [23–27]. Importantly, immunodeficiency associated with chronic HIV infection may enhance COVID-19 disease or facilitate the persistence and evolution of SARS-CoV-2. However, this relationship has yet to be directly addressed in a controlled setting.

Furthermore, while systemic T cell responses are a pivotal aspect of immunity, the vast majority of these cells reside within peripheral tissues [28]. This emphasizes the importance of local immune response studies in understanding the broader scope of T cell immunity. The complexity of the lung's vascular system, coupled with the potential for cells to reside and function within its network, further underscores the need to delve into tissue-specific immunity [29]. Studies exploring the nuanced differences between tissue-resident T cells, vascular-associated T cells, and circulating blood T cells can provide valuable insights into lung immunology. Such knowledge has direct implications for developing treatment strategies for conditions such as respiratory infections, asthma, COPD, and lung cancer.

This thesis is a journey through the above themes, exploring:

1. The emergence of SARS-CoV-2 and the need for animal models that faithfully recapitulate all aspects of human disease, including severe COVID-19, as well as the intricate immune responses it elicits, particularly those involving T cells. For this, we focused on Pigtail macaques (PTM, *Macaca nemestrina*) as this species demonstrates a rapid and severe disease course when infected with simian immunodeficiency virus (SIV), a simian model of HIV infection. Notably, PTMs manifest severe cardiovascular symptoms similar to those observed in humans with COVID-19. Thus, we hypothesized that PTMs may also experience severe disease if infected with SARS-CoV-2. In this study, we investigated a cohort of SARS-CoV-2-infected PTMs euthanized either six or twenty-one days after respiratory viral challenge using a combination of virologic, immunological, and pathological analyses.
2. The impact of SIV and SARS-CoV-2 coinfection. Here we hypothesized that SIV-induced immunodeficiency and consequent loss of CD4⁺ T cells would facilitate COVID-19 disease progression, viral persistence, and the evolution of novel viral variants. To this end, we conducted a small pilot study in which we exposed two PTMs chronically infected with SIVmac239 to SARS-CoV-2 and monitored them for six weeks for viral replication, viral evolution, and clinical disease. We compared these outcomes with those observed in the SIV-naive PTMs infected with SARS-CoV-2 from our first project and examined the impacts of immunodeficiency on the host's response to SARS-CoV-2, including the impacts on adaptive immune responses.

3. The complexities of pulmonary immunity, focusing on T cell dynamics within the lung vasculature, an often-overlooked aspect of immunity. For this, we utilized intravascular staining (ivs), an innovative technique used to distinguish tissue-resident cells from those within the vasculature. This method is especially valuable for highly vascularized organs such as the lungs. Traditionally, cells that stain positive for the infusion antibody (ivs+) were deemed “blood contaminants.” However, new research is beginning to call this into question [30]. Our study aimed to elucidate the distinct characteristics and functions of ivs+ T cells in the pulmonary vasculature. Utilizing ivs, we analyzed T cells from the lungs and respiratory mucosa of Rhesus Macaques (RhM) via flow cytometry and single-cell RNA sequencing (scRNAseq).

Each chapter dives into the specific details, with methodologies and analyses, to shed light on these topics, providing valuable insights into T cell dynamics.

Background

Danish physician Peter Ludvig Panum initially identified the concept of immunological memory, a cornerstone of adaptive immunity, during his 1846 visit to the Faroe Islands [31]. Panum observed that survivors of the 1781 measles outbreak were unaffected by a subsequent outbreak 64 years later [32]. Whereas younger individuals and those unexposed during the first outbreak fell ill. Today, the science of immunology attributes such lasting immunity to memory T and B cells.

T cell Background

T Cell Activation and Differentiation

With the advent of major histocompatibility complex class I (MHC-I) tetramer technology, a deeper understanding of T cell differentiation during acute infections was made possible [31,33,34]. This differentiation can be categorized into three primary stages:

- **Clonal Expansion:** Following infection, specific T cells recognizing viral or bacterial epitopes become activated and undergo rapid proliferation [34,35]. This expansion phase is influenced by several factors, including the nature of the antigen and the cytokine cues in the local milieu.

- Contraction: Post-neutralization of the pathogen, a vast majority of T cells die by apoptosis, leaving behind a select population of antigen-experienced T cells that mature into memory cells (T_{MEM}) [36,37].
- Memory Formation: The residual cells differentiate into long-lived T_{MEM} cells, which stand guard against potential future encounters, ensuring rapid responses upon repeat exposure [35].

Naïve T cells recognize cognate antigens only when presented by self MHC-I (to CD8+ T cells) or MHC-II (to CD4+ T cells) molecules to the T cell receptor (TCR) [38–40]. Effective T cell activation requires multiple stimuli for differentiation, with cues from the TCR, co-stimulation, particularly involving B7 expressed on antigen-presenting cells (APCs) and CD28 on T cells, and a third signal from cytokines, all tailored to respond to the invading pathogen. Upon activation, T cells undergo differentiation and rapidly proliferate in a largely antigen-independent manner [41–45]. The type of pathogen presented drives the differentiation process, leading to the formation of cytotoxic T lymphocytes (CTLs, CD8+ T cells) or helper T cells (T_h , CD4+ T cells) [39,40,46].

Memory Formation

Post-infection, as the immune response subsides, the population of effector T cells contracts, leaving a small subset to differentiate into T_{MEM} cells (~5-10%) [47,48]. These T_{MEM} cells maintain a rapid and robust antigen-specific recall response throughout the life of the host [33]. Consisting of a diverse group,

T_{MEM} cells are characterized by distinct transcriptional profiles and protein expression, underpinning their various functionalities and localizations [49]. T_{MEM} are typically categorized into three primary subsets: central memory (T_{CM}), effector memory (T_{EM}), and tissue-resident memory T cells (T_{RM}) [50–52]. However, the growing recognition of their heterogeneous nature implies that creating strict, well-defined subsets may not be the most accurate approach.

Journey of Naïve T Cells

Naïve T cells (T_N) continuously migrate from the blood into lymph nodes (LN) and other secondary lymphoid organs (SLO) in search of cognate antigen [53]. Using CD62L and CCR7, T_N cells enter LNs via high endothelial venules (HEVs) [54,55]. If they fail to encounter their cognate antigen, T_N cells re-enter the bloodstream via the thoracic duct lymph (TDL), ready to explore another LN [56]. Encounter with cognate antigen induces proliferation and differentiation of T_N cells into effector T (T_{EFF}) cells. These newly differentiated effector T cells egress from the LNs and migrate toward peripheral tissues, where they carry out their specialized immune functions [57].

Migration Patterns of Memory T Cells

T_{MEM} cells, with their diverse subsets, exhibit distinct patterns of cellular migration. T_{CM} cells maintain expression of CCR7 and CD62L, allowing them to traffic between the bloodstream and secondary lymphoid organs (SLO), similar to T_N , ensuring constant surveillance within these sites [53]. In contrast, T_{EM} cells,

lack the expression of these surface antigens and are thereby excluded from SLO [51,54]. Instead, they predominantly circulate between the bloodstream and non-lymphoid tissues. T_{RM} cells are non-circulating and reside in nearly all tissues. T_{RM} are characterized by their specialized ability to coordinate rapid recall responses as well as maintain homeostasis within the local environment [58–60].

Guidance for T Cell Migration

The migratory path of T cells is regulated by a series of molecular interactions guided by cytokine-induced expression and presentation of chemokines and cell adhesion molecules (CAMs) on endothelial cells [61–67]. Other important players include selectins, a class of glycoproteins, including L-selectins, expressed on immune cells as well as E- and P-selectins, expressed on endothelial cells [68]. Selectins recognize and bind specific carbohydrate ligands, initiating the primary step of lymphocytes rolling on vascular surfaces. Integrins, including LFA-1, MAC-1, and VLA-4, present on the surface of immune cells, are crucial for guiding T cell migration [69]. By recognizing and interacting with specific cell adhesion ligands such as ICAM-1, V-CAM-1, and MadCAM-1 that are differentially expressed on vascular endothelial cells of various tissues, lymphocytes adhere to and navigate specific routes [69].

Translocation Dynamics

Leukocyte translocation into tissues follows a well-organized sequential pattern. Beginning with rolling and tethering, facilitated by selectin-ligand interactions, T cells gently roll along the endothelial layer (step 1) [69,70]. This allows chemokine receptors on the cell surface to come into close contact with endothelial chemokines. Upon this interaction, chemokines induce the expression and clustering of integrins (step 2), leading to a strong adhesion and firm arrest of T cells to the vascular endothelium (step 3) [71,72]. Lymphocytes then undergo actin-driven spreading, polarization, and migration over the endothelium surface mediated by integrin and cell adhesion interactions allowing cells to scout for “hot spots” or sites along the endothelium that are permissive to penetration (step 4) [73–75]. This then sets the stage for diapedesis, wherein leukocytes transverse the endothelial barrier either between cells (paracellular migration) or directly through endothelial cells (transcellular migration) to infiltrate the tissues (step 5) [62,76]. Penetration into the tissues is mediated by integrins and CAMs, along with other adhesion molecules like CD99, PECAM-1, and JAM-1 [77]. Upon entering the tissues, T cells follow a chemokine gradient to the site of inflammation.

T cell Trafficking to the Lung

Though the migration pattern described above is generally observed across most tissues, there are exceptions, particularly in the lungs and liver [78,79]. In these highly vascularized organs, lymphocyte trafficking frequently

occurs in a rolling independent manner, with extravasation at the capillaries. Additionally, lymphocyte subsets have been observed patrolling the endothelium without necessarily entering into the tissues [61,80,81]. The lung's complex vascular system, comprising both bronchial and pulmonary arteries, provides two main routes for leukocyte trafficking: the microvasculature of the tracheobronchial tree and the alveolar capillaries in the lung parenchyma [82]. Another often overlooked vascular system in the lungs, the perivascular bed found surrounding larger pulmonary arteries, may provide a third route for trafficking [29,83]. A murine study of CD8⁺ T_{EFF} trafficking to the lungs showed that T cell retention in the pulmonary vasculature was dependent in part by T cell expression of the integrin LFA-1, a heterodimer of CD11a/*ITGAL* + CD18/*ITGB2* [84].

SARS-CoV-2 Background

Severe Acute Respiratory Syndrome Coronavirus-2 (SARS-CoV-2)

In late 2019, the city of Wuhan, China, became the epicenter of an outbreak caused by a novel coronavirus (CoV). This virus, named SARS-CoV-2, for its genomic similarities to the 2003 [85] severe acute respiratory syndrome coronavirus (SARS-CoV) and several bat sarbecoviruses [86], is responsible for the worldwide COVID-19 pandemic. SARS-CoV-2, a Betacoronavirus (β CoV), is a member of the *Orthocoronavirinae* subfamily within the *Coronaviridae* family and the *Nidovirales* order [87]. Among the seven coronaviruses known to infect humans, MERS-CoV, SARS-CoV, and SARS-CoV-2 are linked to severe disease [88–90]. In contrast, the other four CoVs – Alphacoronaviruses (α CoVs) HCoV-

229E and HCoV-NL63 and β CoVs HCoV-OC43 and HCoV-HKU1 – are widespread and typically cause mild, self-limiting upper respiratory infections. It is estimated that over 90% of adults have been exposed to these milder strains [91].

SARS-CoV-2 is an enveloped, positive-sense, single-stranded RNA virus with an extensive genome of nearly 30,000 nucleotides [92]. SARS-CoV-2 shares a similar genomic structure to other β CoVs with six open reading frames (ORFs) coding for functional proteins and potentially seven ORFs that code for accessory proteins [93]. Although the actual number of accessory ORFs is still being debated. Ordered 5' to 3', ORF1a/ORF1b code for replicase, followed by structural proteins, spike (S), envelope (E), membrane (M), and nucleocapsid (N) located at the 3' end of the viral genome [94].

Similar to SARS-CoV, SARS-CoV-2 utilizes surface angiotensin-converting enzyme 2 (ACE2), found on epithelial cells within the human respiratory and gastrointestinal tract, for cell entry [95]. The receptor binding domain (RBD), located in the S1-C terminal domain of the spike protein, mediates viral fusion with the host cell and serves as a target for neutralizing antibodies [96]. Host proteases, including transmembrane protease serine protease 2 (TMPRSS2), cathepsin L, and furin, activate SARS-CoV-2 by cleaving the S protein, allowing for entry into host cells. Viral replication occurs in host epithelial cells in the upper respiratory tract. If confined here, patients generally experience no or mild symptoms such as cough, sore throat, fever, and malaise [97–99]. If SARS-CoV-2 spreads to the lower airways and lung alveolar epithelial cells, patients can

develop more severe symptoms such as pneumonia. In a subset of individuals, this progression can trigger an intense immune response, leading to cytokine storm syndrome, acute respiratory distress syndrome (ARDS), disseminated intravascular coagulation (DIC), and pulmonary embolism [100].

T cells in COVID-19

Given the pivotal role of cellular immunity in defending multicellular organisms and the historical co-existence of coronaviruses with humans, it is no surprise that numerous studies have demonstrated the importance of T cells in defending against SARS-CoV-2 [101]. During acute infection, the initial viral load and the effectiveness of the innate immune response, primarily driven by type I interferons (IFN- α , IFN- β , IFN- ω), profoundly influence the subsequent adaptive immune response as well as overall clinical outcome [102,103]. While the innate response is vital for managing disease, a coordinated T cell response may be equally important. In the initial week of symptom onset, successful viral clearance and milder disease manifestations are closely correlated with the rapid development of cytotoxic CD8+ T cell responses [104]. Moreover, a positive clinical outcome in acute COVID-19 is often linked to high levels of CD8+ T cell effector molecules. However, overactivation can be detrimental, with extremely high T cell activation corresponding to adverse clinical outcomes. CD4+ T cells are also important in viral control. A type I CD4+ response frequently corresponds with efficient viral clearance, whereas a type 2 phenotype is often observed in severe disease. In contrast to symptomatic cases, which tend towards

inflammatory cytokine responses, virus-specific T cell responses in asymptomatic infections maintain a balance between anti-inflammatory (IL-10) and inflammatory cytokine production [105,106].

Memory T cells in COVID-19

With its broad genetic blueprint, SARS-CoV-2 encompasses over 1,400 potential T cell epitopes. Infection elicits virus-specific central and effector memory CD4⁺ T_{MEM} cells. These cells, representing approximately 0.5% of the CD4⁺ T cell pool, target ~19 viral epitopes [107,108]. Exhibiting a polyfunctional phenotype, they are characterized by heightened IL-2 expression, albeit reduced IFN- γ responses compared to other respiratory infections [107,109].

Development of expanded populations of cytotoxic CD4⁺ and CD8⁺ T cells at four weeks post-infection have been identified, although, cytotoxic CD4⁺ T cells do not appear to be a major factor in the memory recall response [110]. A recent study found that activated cytotoxic CD4⁺ T cells were elevated in the blood of critical patients and suggested that these cytotoxic CD4s may contribute to host cell-mediated tissue damage [111]. Infection also induces the development of CD8⁺ T_{MEM} cells, which target ~17 viral epitopes, and make up around 0.2% of the CD8⁺ T cell repertoire [107,108]. Although there is considerable heterogeneity among individuals, the extensive scope of T cell specificity between CD4⁺ and CD8⁺ T cells is encouraging, implying that viral evolution may not enable SARS-CoV-2 to completely escape T cell recognition [101].

As mentioned above, the vast majority of T cells are housed within tissues acting as sentinels against repeat invaders. Notably, the presence of SARS-CoV-2 T_{RM} in the airways is associated with improved clinical outcomes. Their detection several months post-infection hints at their potential to limit disease severity upon reinfection [105,112].

Vaccination and T cells

The introduction of COVID-19 vaccines has greatly transformed the battle against the pandemic. Primarily designed to deliver spike protein, these vaccines induce robust antibody responses. Although most studies focus on humoral immunity, it is significant to note that vaccination also elicits spike-specific T cell responses [113,114]. COVID-19 vaccines have demonstrated pronounced efficacy in preventing severe disease. However, their overall inability to provide sterilizing immunity is suggestive of the limited capacity of antibodies to block initial infection. This, along with the occurrence of breakthrough infections due to variants of concern (VOCs), which have the ability to evade humoral but cannot easily escape cellular responses, further underscores the potential role of virus-specific T cells in controlling disease progression and preventing extensive tissue damage [101,114].

HIV Background

Human Immunodeficiency Virus (HIV)

Throughout the 1900s, it is believed that HIV transmitted sporadically from non-human primates (NHPs) to humans, but it was not until 1983 that it was officially identified as the causative agent of acquired immunodeficiency syndrome (AIDS) [115–118]. A major cause of morbidity and mortality worldwide, nearly 40 million people are currently living with HIV (PLWH), the majority residing in sub-Saharan Africa [119] (<https://www.who.int/news-room/factsheets/detail/hiv-aids>).

HIV belongs to the *Lentivirus* genus under the *Retroviridae* family and can be divided into two main types: HIV-1 and HIV-2. HIV-1 is the primary driver of AIDS globally, whereas HIV-2 is predominantly found in specific regions of Western and Central Africa. Typical of lentiviruses, HIV infections have a chronic slow progression of disease with a period of latency and low levels of persistent viral replication [120]. Structurally, the HIV genome contains two identical single-stranded positive-sense RNA molecules coated in nucleocapsid proteins [121,122]. This ribonucleoprotein complex is encased in a capsid along with proteins such as protease, integrase, and reverse transcriptase and is surrounded by a lipid bilayer embedded with gp120 and gp41 glycoprotein trimers [122].

HIV Infection

Entry of HIV into target cells is mediated through interactions between viral envelope proteins, gp120 and gp41, and the host cell's CD4 receptor, facilitated by co-receptors CXCR4 and CCR5 [123,124]. Once inside, reverse transcriptase synthesizes a double-stranded DNA copy of the viral RNA genome, which is then transported into the nucleus and, through integrase activity, inserted into the host genome. The integrated provirus remains for the life of the cell, directing the synthesis of essential viral proteins and RNAs necessary for the generation of new viral particles [125].

Transmission of HIV primarily occurs via infected bodily fluids through unprotected sexual contact, unscreened blood transfusions, intravenous drug use, and maternal transmission during childbirth or breastfeeding [126]. During a typical infection, HIV first targets CD4+ T cells within the mucosal tissues before proliferating and spreading through the lymphoid system. Infection progresses from an acute phase, where symptoms appear roughly two to four weeks after exposure, to a chronic phase. Initially, during the acute phase of infection, symptoms resemble that of the flu with fever, fatigue, rash, sore throat, and swollen lymph nodes [127]. Viral levels peak during the acute phase and then stabilize, leading to a prolonged period of asymptomatic infection where viremia levels reach a set-point and become relatively stable, often for years. As the disease progresses and the number of CD4+ T cells declines, patients become vulnerable to opportunistic infections. A typical adult's CD4+ T cell count ranges from 500 to 1,200 cells/ μ L. As CD4+ T cell counts fall below 200 cells/ μ L,

opportunistic infections, such as *Mycobacterium avium* and *Pneumocystis* pneumonia, are common. Advanced stages of AIDS ultimately lead to death of the patient [127].

T cells and HIV/SIV

As indicated above, HIV primarily targets CD4+ T cells, leading to cell loss and a weakening of the immune system leading to long-term chronic inflammation and an eventual progression to AIDS [128,129]. CD4+ T cells are pivotal in adaptive immunity, providing “help” by stimulating other immune cells such as CD8+ T cells, dendritic cells, and monocytes/macrophages, as well as aiding in B cell antibody production. HIV has a profound effect on CD4+ T cells in gut-associated lymphoid tissues (GALT) [130]. Rapid loss of CD4+ T cells in the gut causes a disruption of mucosal barriers, leading to microbial translocation and systemic inflammation. As the CD4+ T cell population is depleted, loss of virus-specific memory CD4+ T cells allows for reactivation of latent viruses, such as Epstein Barr or Cytomegalovirus, further straining the immune system [131].

Though CD8+ T cells play a pivotal role during acute HIV infection by targeting and eliminating virus-infected cells, they are unable to completely clear the virus [132]. Reasons for this include the rapid loss of CD4+ T cell “help”, viral mutations that allow HIV to evade CD8+ T cell responses, the ability for HIV to downregulate MHC-I expression on infected cells, as well as persistent inflammation [132–136]. Despite their reduced efficacy, CD8+ T cells remain crucial in suppressing viral replication during acute and chronic HIV, as

demonstrated in NHP studies involving SIV. These studies show that depletion of CD8+ T cells, either prior to exposure or during chronic SIV/SHIV (SIV/HIV) infection, results in a substantial increase in plasma viral loads [137,138].

In the subsequent chapters, we will explore the diverse roles of T cells in infectious disease, with a spotlight on pulmonary immunology. We will delve into key aspects of SARS-CoV-2 infection, including coinfection with SIV, emphasizing the importance of understanding local immune responses within complex organ systems such as the lung. Through these investigations, we aim to set a foundation for future research and help inform effective strategies against infectious pathogens.

Chapter 1

The Pigtail Macaque (*Macaca nemestrina*) Model of COVID-19 Reproduces Diverse Clinical Outcomes and Reveals New and Complex Signatures of Disease

Alexandra Melton^{1,2}, Lara A Doyle-Meyers^{1,9}, Robert V Blair¹, Cecily Midkiff¹, Hunter J Melton³, Kasi Russell-Lodrigue¹, Pyone P Aye^{1,9}, Faith Schiro¹, Marissa Fahlberg¹, Dawn Szeltner¹, Skye Spencer¹, Brandon J Beddingfield¹, Kelly Goff¹, Nadia Golden¹, Toni Penney¹, Breanna Picou¹, Krystle Hensley¹, Kristin E Chandler¹, Jessica A Plante⁴, Kenneth S Plante⁴, Scott C Weaver⁴, Chad J Roy^{1,8}, James A Hoxie⁵, Hongmei Gao⁶, David C Montefiori⁶, Joseph L Mankowski⁷, Rudolf P Bohm^{1,9}, Jay Rappaport^{1,8}, Nicholas J Maness^{1,8}.

¹Tulane National Primate Research Center, Covington, Louisiana, USA

²Biomedical Science Training Program, Tulane University School of Medicine,

New Orleans, Louisiana, USA, ³Florida State University, Department of

Statistics, Tallahassee, Florida, USA, ⁴World Reference Center for Emerging

Viruses and Arboviruses, Institute for Human Infections and Immunity, University

of Texas Medical Branch, Galveston, Texas, USA, ⁵Perelman School of

Medicine, University of Pennsylvania, Philadelphia, Pennsylvania, USA

⁶Duke University Medical Center, Duke Human Vaccine Institute, Durham, North

Carolina, USA, ⁷Department of Molecular and Comparative Pathobiology, Johns

Hopkins School of Medicine, Baltimore, Maryland, USA, ⁸Department of Microbiology and Immunology, Tulane University School of Medicine, New Orleans, Louisiana, USA, ⁹Department of Medicine, Tulane University School of Medicine, New Orleans, Louisiana, USA

Manuscript published in PLoS Pathog. 2021 Dec 20;17(12):e1010162. doi: 10.1371/journal.ppat.1010162. PMID: 34929014; PMCID: PMC8722729.

Abstract

The novel coronavirus SARS-CoV-2, the causative agent of COVID-19 disease, has killed over five million people worldwide as of December 2021 with infections rising again due to the emergence of highly transmissible variants. Animal models that faithfully recapitulate human disease are critical for assessing SARS-CoV-2 viral and immune dynamics, for understanding mechanisms of disease, and for testing vaccines and therapeutics. Pigtail macaques (PTM, *Macaca nemestrina*) demonstrate a rapid and severe disease course when infected with simian immunodeficiency virus (SIV), including the development of severe cardiovascular symptoms that are pertinent to COVID-19 manifestations in humans. We thus proposed this species may likewise exhibit severe COVID-19 disease upon infection with SARS-CoV-2. Here, we extensively studied a cohort of SARS-CoV-2-infected PTM euthanized either 6- or 21-days after respiratory viral challenge. We show that PTM demonstrate largely mild-to-moderate COVID-19 disease. Pulmonary infiltrates were dominated by T cells, including CD4⁺ T cells that upregulate CD8 and express cytotoxic molecules, as

well as virus-targeting T cells that were predominantly CD4+. We also noted increases in inflammatory and coagulation markers in blood, pulmonary pathologic lesions, and the development of neutralizing antibodies. Together, our data demonstrate that SARS-CoV-2 infection of PTM recapitulates important features of COVID-19 and reveals new immune and viral dynamics and thus may serve as a useful animal model for studying pathogenesis and testing vaccines and therapeutics.

Author Summary

The COVID-19 pandemic has claimed the lives of millions in a span of less than two years. Despite the development of several highly effective vaccines, many millions remain unvaccinated, and several highly transmissible variants have emerged, clearly suggesting the need for new approaches to treat those that become severely ill. The development of new drugs will rely on having animal models that reproduce the most severe disease seen in humans. To date, nonhuman primate models have not exhibited this severe disease. In this study we tested whether pigtail macaques (PTM) might exhibit such severe disease, based on previous work showing this species is prone to more rapid and severe disease when infected with other viruses.

Introduction

In late 2019, a novel coronavirus was found circulating in humans in China. This virus showed substantial genomic similarities with the severe acute

respiratory syndrome coronavirus (SARS-CoV) that caused an outbreak and panic in 2003 [1] in addition to a number of bat sarbecoviruses [2]; hence, it was named SARS-CoV-2 [3]. SARS-CoV-2 is the causative agent of COVID-19 disease and a worldwide pandemic that has killed more than five million persons to date including 790,000 deaths in the United States. Though most infected individuals exhibit no or mild symptoms, a subset experience severe complications, including highly elevated pro-inflammatory cytokines and coagulation biomarkers, acute respiratory distress syndrome (ARDS), and death [4–9]. Most available data suggest that the intensity of the immune response plays a role in determining COVID-19 severity and progression, with severe disease occurring approximately 3-to-4-weeks after initial symptoms [10,11]. Thus, a deep understanding of the immunopathologic mechanisms of disease in those with advanced disease and of viral clearance in asymptomatic infection and those with mild disease is critical for the development of next generation therapies and vaccines.

Animal models that faithfully recapitulate human disease are needed to assess the roles of particular cell subsets in disease etiology [12,13]. Various species of nonhuman primates can be infected by SARS-CoV-2 and exhibit disease ranging from mild to severe [14–18]. The use of timed infections with well characterized viral stocks in animals with relatively high genetic similarity with humans allows the dissection of immune responses with nuance and detail not possible in humans. The most widely used species of NHP for COVID-19 research has been the rhesus macaque (*Macaca mulatta*). This model has

proved valuable for testing vaccines as viral infection dynamics in this species are robust and well-studied and therefore can be compared between treatment groups [19]. However, SARS-CoV-2-induced disease in this species is generally mild and does not recapitulate the more severe disease seen in a subset of humans [16]. Thus, multiple NHP models are needed to capture the spectrum of disease seen in humans. In this study, we infected pigtail macaques (PTM, *Macaca nemestrina*) with SARS-CoV-2 (WA1/2020 isolate) to assess this novel animal model of COVID-19 disease.

PTM are a unique and valuable animal model for other viral diseases. Simian immunodeficiency virus (SIV) infection of rhesus macaques (RhM) is the most widely used nonhuman primate (NHP) model of HIV/AIDS and is used widely for testing vaccines and cure strategies [20]. However, SIV-associated disease in RhM can take up to several years to develop, somewhat limiting their use for studying disease mechanisms. In contrast, infection of PTM with the same viral isolates leads to rapid disease development with enhanced cardiovascular manifestations relative to RhM, which is of particular relevance to COVID-19 disease [21–24]. Thus, we proposed that SARS-CoV-2 infection of PTM may likewise lead to accelerated COVID-19 disease or demonstrate immune features of disease not detected in other animal models. If so, this species will be valuable for assessing COVID-19 disease mechanisms and for testing novel vaccines and therapeutics. We tracked viral and immune dynamics through the course of infection in a cohort of PTM. We found that disease in this model largely mirrored that observed in RhM but with unique immune features,

such as pulmonary infiltration of CD4+ T cells that exhibit antiviral and cytotoxic functions, as is seen in COVID-19 patients [25]. Together, our data characterize, in depth, a novel animal model that may prove useful for assessing moderate COVID-19 disease mechanisms and testing new therapeutics.

Materials and Methods

Ethics Statement

Pigtail macaques used in this study were purpose bred at the University of Washington National Primate Research Center for experiments. Macaques were housed in compliance with the NRC Guide for the Care and Use of Laboratory Animals and the Animal Welfare Act. Animal experiments were approved by the Institutional Animal Care and Use Committee of Tulane University (protocol P0451). The Tulane National Primate Research Center (TNPRC) is fully accredited by AAALAC International, Animal Welfare Assurance No. A3180-01. During the study, animals were singly housed indoors in climate-controlled conditions with a 12/12-light/dark cycle. All the animals on this study were monitored twice daily to ensure their welfare. Any abnormalities, including those of appetite, stool, and behavior, were recorded and reported to a veterinarian. The animals were fed commercially prepared nonhuman primate diet twice daily. Supplemental foods were provided in the form of fruit, vegetables, and foraging items as part of the TNPRC environmental enrichment program. Water was available ad libitum through an automatic watering system. The TNPRC environmental enrichment program is reviewed and approved by the IACUC

semi-annually. Veterinarians in the TNPRC Division of Veterinary Medicine have established procedures to minimize pain and distress using several approaches. Animals were anesthetized with ketamine-HCl (10 mg/kg) or tiletamine/zolazepam (3-8 mg/kg) prior to all procedures. Preemptive and post procedural analgesia (buprenorphine 0.01 mg/kg or buprenorphine sustained-release 0.2 mg/kg SQ) was used for procedures that would likely cause more than momentary pain or distress in humans undergoing the same procedures. The above listed anesthetics and analgesics were used to minimize pain and distress in accordance with the recommendations of the Weatherall Report. The animals were euthanized at the end of the study using methods consistent with recommendations of the American Veterinary Medical Association (AVMA) Panel on euthanasia and per the recommendations of the IACUC. Specifically, the animals were anesthetized with tiletamine/zolazepam (8 mg/kg IM) and given buprenorphine (0.01 mg/kg IM) followed by an overdose of pentobarbital sodium. Death was confirmed using auscultation to confirm the cessation of respiratory and circulatory functions and by the lack of corneal reflexes.

Animal cohort, viral inoculations, and procedures

Four male pigtail macaques (PTM), between the ages of 5 and 6 years old (Table 1, Fig 1A and S1 Table), were exposed to 1×10^6 TCID₅₀ of SARS-CoV-2 USA WA1/2020 (World Reference Center for Emerging Viruses and Arboviruses, Galveston, TX) through both intranasal and intratracheal inoculation. The viral stock was sequenced and determined to have no mutations at greater than 5% of

reads that differed from the original patient isolate. Pre- and post-exposure samples included blood, bronchoalveolar lavage (BAL), and mucosal swabs (nasal, pharyngeal, rectal, and bronchial brush). Physical examination and imaging (radiography S1 Fig) were conducted before viral exposure and weekly after exposure. Animals were monitored for 6 (n=2) or 21 (n=2) days before euthanasia and tissue harvest. At necropsy, samples from each of the major lung lobes (left and right, cranial, middle, and caudal lobes) were collected in TRIzol (Invitrogen, Lithuania) and fresh frozen at -80°C. The remainder of the lung lobes were infused and then immersed in formalin fixative. The rest of the necropsy was performed routinely with collection of tissues from all major organs in DMEM media, fresh frozen, or in formalin fixative.

Animal ID	Sex	Age (y)	Weight (kg)
MA27	Male	6.07	7.55
MA30	Male	5.61	5.80
MA24	Male	5.64	8.40
MA28	Male	5.81	8.60

Table 1.1 PTM cohort used in this study, including sex, age, and weight at the time of SARS-CoV-2 inoculation.

Isolation of Viral RNA

The *Quick-RNA* Viral Kit (Zymo Research, Irvine, CA) was used to isolate viral RNA (vRNA) from mucosal swab and bronchial brush samples collected in 200 μ L DNA/RNA Shield 1X (Zymo Research, Irvine, CA) following the manufacturer's protocol. Briefly, 400 μ L DNA/RNA viral buffer was added to the swab samples. In a modification to the manufacturer's protocol, swabs were

transferred directly to the Zymo spin column for centrifugation. The vRNA was eluted in 50 μ L elution buffer.

Viral RNA Quantification by Quantitative Real-Time PCR

Quantification of viral RNA was performed as described [26] using the CDC N1 primers/probe for quantification of total viral RNA and with primers/probe specific for the nucleocapsid subgenomic RNA to provide an estimate of replicating virus. Specifically, vRNA was quantified using the QuantStudio 6 Real-Time PCR System (Applied Biosystems, Waltham, MA). Five microliters vRNA was added in duplicate to a 0.1 mL 96-well MicroAmp fast optical reaction plate (Applied Biosystems, REF# 4346906). For genomic vRNA quantification, the 2019-nCoV RUO Kit (Integrated DNA Technologies, Coralville, IA) was used, according to the manufacturer's protocol, to target the N1 amplicon of the N gene along with TaqPath 1-Step RT-qPCR Master Mix (Applied Biosystems Waltham, MA). For the subgenomic assay, a forward primer targeting the subgenomic leader sequence and a reverse primer/probe (Integrated DNA Technologies, Waltham, MA) designed to target the N gene, was used along with the TaqPath Master Mix mentioned above. Fifteen microliters of the respective master mix were added to each well and run using the following conditions: 25°C for 2 minutes, 50°C for 15 minutes, 95°C for 2 minutes followed by 40 cycles of 95°C for 3 seconds and 60°C for 30 seconds. In vitro transcribed RNA was quantified and diluted to known copy numbers and used to generate the genomic and subgenomic standard curves. Both genomic

and subgenomic viral copy numbers were calculated by plotting Cq values from unknown samples against the respective standard curve. Positive, negative, and non-template controls were analyzed along with each set of samples.

Isolation of PBMCs

Peripheral blood mononuclear cells (PBMCs) were isolated from whole blood using SepMate-50 Isolation tubes (Stem Cell Technologies, Vancouver, Canada) per the manufacturer's protocol. Cells were counted using a Cellometer Auto 2000 (Nexcelom, Lawrence, MA), resuspended in Bambanker cell freezing medium (GC Lymphotec, Tokyo, Japan) at approximately 1×10^7 cells/mL and cryopreserved at -80°C .

ELISA assays

D-dimer levels in sodium citrate plasma samples were measured via an enzyme-linked immunosorbent assay (ELISA) (Ray Biotech, Peachtree Corners, GA) per the manufacturer's protocol. Samples were diluted 600,000-fold and plated in duplicate. IL-4 levels in plasma samples were measured using a Monkey IL-4 ELISA kit (abcam, Boston, MA) per the manufacturer's protocol. Plasma samples were diluted 1:2 and assayed in duplicate along with two replicates of undiluted sample. In modification to the manufacturer's protocol, the standard/sample incubation time was increased to 2.5 hours. Plates were analyzed using the GloMax Explorer plate reader (Promega, Madison, WI) and GraphPad Prism (GraphPad Software version 9, LaJolla, California). Heatmap

was generated using Microsoft Excel. Data was normalized by dividing raw data values from Day 4, (D-dimer only) 6, 14 and 21 by the baseline value for each animal.

Kynurenine and tryptophan levels in plasma were measured using commercially available enzyme-linked immunosorbent assays (Rocky Mountain Diagnostics, Colorado Springs, CO) per the manufacturer's protocol. The GloMax Explorer plate reader (Promega, Madison, WI) along with GraphPad Prism v9 were used to analyze the plates.

Quantification of Inflammatory Cytokines and Coagulation Biomarkers

BioLegend's bead-based immunosorbent assays were used to measure inflammatory cytokines in serum (LegendPlex NHP Inflammation Panel, BioLegend, San Diego, CA) and coagulation biomarkers in sodium citrate plasma (LegendPlex Human Fibrinolysis Panel). Serum and plasma samples were diluted 4-fold and 10,000-fold, respectively, and assayed in duplicate. Results were read using a MacsQuant 16 Flow Cytometer (Miltenyi Biotec) and LegendPlex's online data analysis tool (Qognit). Heatmap was generated using Microsoft Excel. Data was normalized by dividing raw data values from Day 6, 14 and 21 by the baseline value for each animal.

Flow Cytometry Analysis

Phenotypic and intracellular cytokine analyses of mononuclear cells (MNC) isolated from blood and bronchoalveolar lavage (BAL) were performed

using antibodies against markers listed in S2, S3, and S4 Tables. Briefly, cells were washed and counted with the Cellometer Auto 2000 (Nexcelom Bioscience, Lawrence, MA). Cells were then pelleted and resuspended in Live/Dead stain cocktail (50 μ L PBS + 0.5 μ L live/dead stain per test) (Fixable Aqua Dead Cell Stain Kit, Invitrogen, Lithuania) and incubated in the dark for 20 minutes. Cells were washed in PBS supplemented with 2% FBS, pelleted, resuspended, and incubated in surface-stain cocktail consisting of 50 μ L BD Horizon Brilliant Violet Stain Buffer (BD Bioscience, Franklin Lakes, NJ) plus antibodies (see S2, S3, and S4 Tables) for 20 minutes in the dark. Cells were washed in PBS with 2% FBS, pelleted, then resuspended in 200 μ L BD Cytotfix/Cytoperm solution (BD Biosciences, Franklin Lakes, NJ) and incubated in the dark for 20 minutes. Cells were washed in 1x BD Perm/Wash Buffer (BD Biosciences, Franklin Lakes, NJ), pelleted, and resuspended in intracellular-staining cocktail consisting of 100 μ L 1x BD Perm/Wash Buffer plus antibodies according to S2, S3, and S4 Tables and incubated for 20 minutes in the dark. Finally, cells were washed, pelleted, and resuspended in 200 μ L 1x BD Stabilizing Fixative (BD Biosciences, Franklin Lakes, NJ).

Monocyte Cytokine Expression

To measure monocyte cytokine expression, MNCs from blood and BAL were washed and counted (Cellometer Auto 2000, Nexcelom Bioscience, Lawrence, MA), pelleted, and then resuspended in DMEM (Gibco, Grand Island, NY) with 5% Anti-Anti (Gibco, Grand Island, NY) at 1×10^6 cells/mL. Cells were

stimulated with lipopolysaccharide at 10 ng/mL (Sigma, St Louis, MO) and incubated with 1 μ L/mL Brefeldin-A (BioLegend, San Diego, CA) for 4-6 hours at 37°C, 5% CO₂. Cells were then stained following the procedure described above with antibodies listed in the Monocyte Panel (S2 Table).

T cell Cytokine Expression

MNCs from blood and BAL were counted, washed, pelleted, and resuspended in DMEM with 5% Anti-Anti at 1x10⁶ cells/mL. T cell cytokine expression was measured by stimulating MNCs with cell stimulation cocktail (Biolegend, San Diego, CA) for 4-6 hours at 37°C, 5% CO₂. To measure T cell responses to SARS-CoV-2 antigens, MNCs from blood and BAL were washed, pelleted and resuspended in DMEM with 5% Anti-Anti and 10% FBS at 1x10⁶ cells/mL followed by overnight stimulation at 37°C, 5% CO₂ with either cell stimulation cocktail or with one of the following viral peptide pools obtained through BEI Resources, NIAID, NIH: Peptide Array, SARS Coronavirus Nucleocapsid Protein (NR-52419), Spike Glycoprotein (NR-52402), Membrane Protein (NR-53822), or Envelope Protein (NR-53822) along with Brefeldin-A (S5 Table). Cells were stained as described above using the antibodies listed in the T cell panel (S4 Table).

All samples were acquired on a LSRFortessa Cell Analyzer (BD Biosciences, Franklin Lakes, NJ) using BD FACSDIVA 8.0.1 software. Approximately 1x10⁶ cells were acquired from each sample. Data was analyzed using FlowJo version 10.7.1 for MAC (Becton Dickinson and Company, Ashland,

OR). SARS-CoV-2 antigen specific T cell responses (Figs 10A, 10B, and S5) were generated using the Matlab based tool cyt3 [27]. Data was transformed using arcsin 150. Cytokine expression was measured in FlowJo and, when applicable, applied to cyt3 generated figures. t-distributed stochastic neighbor embedding (tSNE) analysis was performed in FlowJo 10.7.1, nightingale rose plots were generated in R using the ggplot2 [28] package, radial plots were generated in Microsoft Excel.

Histopathology and Immunohistochemistry

Zinc-formalin fixed tissues were processed routinely, embedded in paraffin and cut into 5 μm sections for hematoxylin and eosin (H&E), Masson's Trichrome, or immunohistochemical (IHC) staining.

For H&E staining, tissue samples were collected in Zinc formalin (Anatech, Sparks, NV) and immersion fixed for a minimum of 72 hours before being washed and dehydrated using a Thermo Excelsior AS processor. Upon removal from the processor, tissues were transferred to a Thermo Shandon Histocentre 3 embedding station where they were submersed in warm paraffin and allowed to cool into blocks. From these blocks, 5 μm sections were cut and mounted on charged glass slides, baked overnight at 60°C and passed through Xylene, graded ethanol, and double distilled water to remove paraffin and rehydrate tissue sections. A Leica Autostainer XL was used to complete the deparaffinization, rehydration and routine hematoxylin and eosin stain preparing

the slides for examination by a board-certified veterinary pathologist using HALO software (Indica Labs, Albuquerque, NM).

Trichrome staining was performed as previously described with the exception of an additional 10-minute incubation using Weigert's Iron Hematoxylin Working Solution [29]. Slides were analyzed by a board-certified veterinary pathologist using HALO software for quantification.

For IHC staining, tissue sections were mounted on Superfrost Plus Microscope slides (Fisher Scientific, Carlsbad, CA), incubated for 1 hour at 60°C, and passed through Xylene, graded ethanol, and double distilled water to remove paraffin and rehydrate tissue sections. A microwave was used for heat induced epitope retrieval (HIER). Slides were boiled for 20 minutes in a Tris based solution, pH 9 (Vector Laboratories, Burlingame, CA), supplemented with 0.01% Tween-20. Slides were briefly rinsed in hot, distilled water and transferred to a hot citrate-based solution, pH 6.0 (Vector Laboratories, Burlingame, CA) where they were allowed to cool to room temperature. All slide manipulation from this point forward was done at room temperature with incubations taking place in a black humidifying chamber. Once cool, slides were rinsed in tris buffered saline (TBS) and incubated with Background Punisher (Biocare Medical, Pacheco, CA) for 10 minutes. Slides were then submerged in a solution of TBS supplemented with 0.01% TritonX100 (TBS-TX100) and placed on a rocker platform for two 5-minute washes followed by a TBS rinse before being returned to humidifying chamber to be incubated with serum free protein block (Dako, Santa Clara, CA) for 20 minutes. Mouse anti-Granzyme primary antibody (S6 Table) was then

added to the slides and allowed to bind for 60 minutes. Slides were then washed twice with TBS-TX100 and once with TBS. The labeling of the antibody for visualization was done using the MACH3 AP kit (Biocare Medical, Pacheco, CA). Both the MACH3 probe and polymer were incubated for 20 minutes with TBS-TX100 and TBS washes in between. Slides were incubated with permanent red substrate (Dako, Santa Clara, CA) for 20 minutes and placed in TBS to halt the enzymatic reaction.

All other staining was done consecutively with the following method. Slides were incubated with a blocking buffer comprised of 10% normal goat serum (NGS) and 0.02% fish skin gelatin in phosphate buffered saline (PBS) for 40 minutes. This blocking buffer was also used to dilute both primary and secondary antibodies (S6 Table). Primary antibodies were added to slides for 60 minutes. After washing two times with PBS supplemented with 0.02% fish skin gelatin and 0.01% TritonX100 (PBS-FSG-TX100) and once with PBS-FSG, slides were incubated for 40 minutes with a secondary antibody made in goat, raised against the primary host species, and tagged with an Alexa Fluor fluorochrome (488 or 568). The 3 washes (described above) were repeated before DAPI nuclear stain was added for 10 minutes. Slides were mounted using anti-bleaching mounting media containing Mowiol (Sigma, St Louis, MO) and DABCO (Sigma, St Louis, MO) and allowed to dry overnight before imaging with a Axio Slide Scanner (Zeiss, Hamburg, Germany). HALO software (Indica Labs Albuquerque, NM) was used for quantification and analysis.

Detection of Neutralizing Antibodies in Serum

Pseudovirus neutralization testing of serum samples was performed using a SARS-CoV-2.D614G spike-pseudotyped virus in 293/ACE2 cells, with neutralization assessed via reduction in luciferase activity as described [30,31].

Statistical Analysis

GraphPad Prism (version 9 GraphPad Software, LaJolla California) was used for graphing and statistical analyses. The Kruskal-Wallis test and Dunn's test for multiple comparisons were used to compare changes in cell frequencies as well as surface marker, cytokine and Granzyme B expression. The Mann-Whitney U test for comparison of means was employed to compare viral loads between PTM and RhM at 1-dpi. A multiple linear regression was conducted in R to compare viral titers, both overall and over time, between PTM and RhM, and corresponding plots were created with ggplot2 [28].

Results

Viral dynamics

Four male pigtail macaques (PTM) inoculated with SARS-CoV-2 were followed via blood, mucosal swab and bronchoalveolar lavage (BAL) sampling. Two animals were euthanized at 6 days post infection (dpi) and two at 21 dpi (Fig 1A). Quantitative RT-PCR was used to track viral genomic and subgenomic RNA through the course of the study at multiple sites. We detected both genomic and subgenomic SARS-CoV-2 RNA in all four animals throughout the first

several days of infection (Fig 1B-K). One animal, MA27, euthanized at 6-dpi, showed a spike in genomic and subgenomic viral RNA (sgm vRNA) at necropsy in the pharynx (Fig 1F and 1G), with viral levels also beginning to rise in the nasal cavity (Fig 1B and 1C). MA28, euthanized at 21-dpi, showed detectable levels of vRNA in the nasal and rectal mucosa over the course of the study (Fig 1B and 1D). Next we performed a direct comparison of viral titers between our PTM and a cohort of RhM from a recent study of ours [26]. At 1-dpi, PTM have significantly higher titers of virus in the nasal cavity, significantly lower titers in pharynx and no significant difference in titers in the rectal mucosa (Fig 1L and 1M). Comparison of viral titers over time revealed a significant difference in both nasal and pharyngeal sites between the two species (Fig 1N-1S). Interestingly, we also show a significant difference in the rate at which the genomic viral load decreases in the nasal mucosa. Both species show a decline in viral titers overtime; however, PTM experienced a significantly faster rate of decrease (Fig 1N). The rate of change overtime in pharyngeal sgm vRNA was also found to be significantly different between the two species, with the rise in PTM sgm vRNA driven by MA27 (Fig 1R).

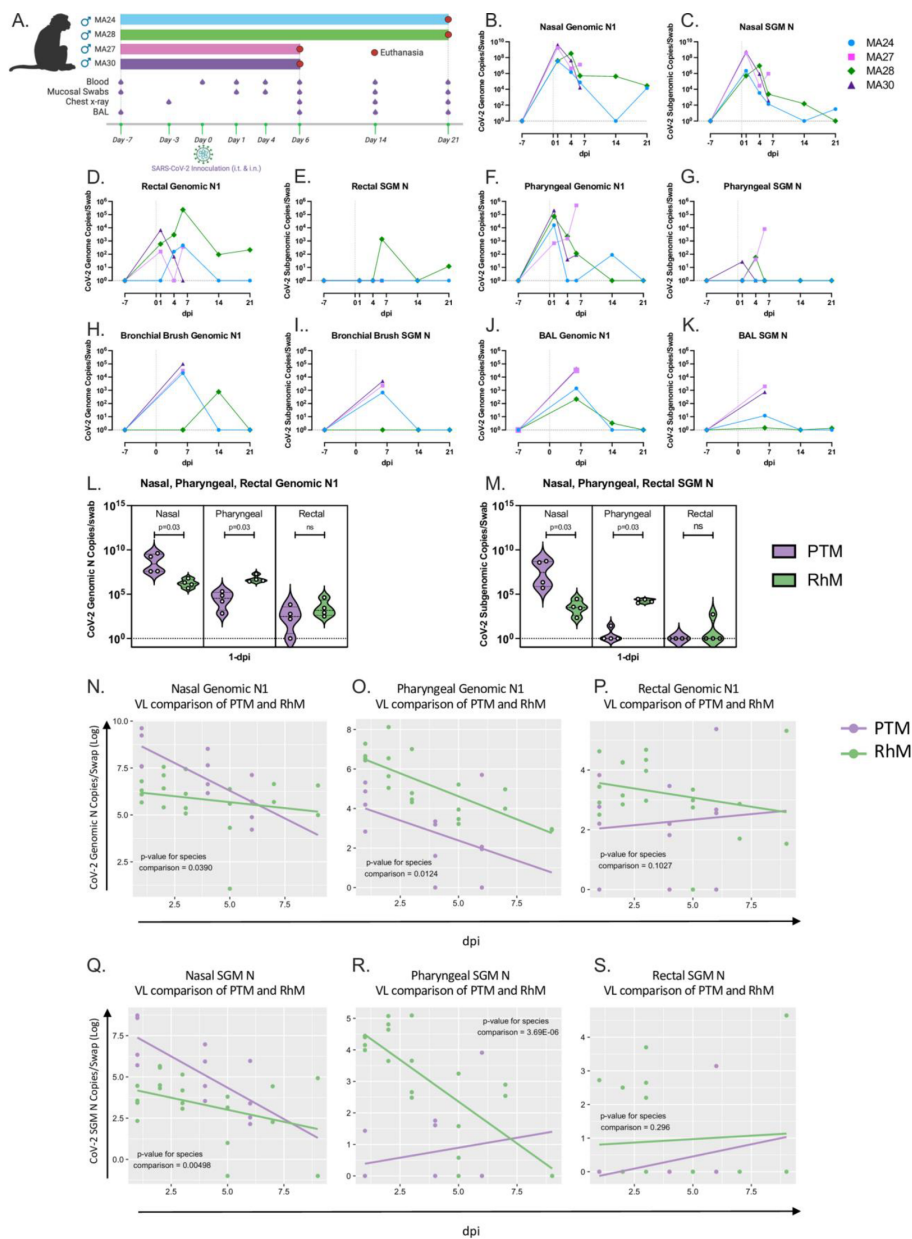


Fig 1.1 Viral dynamics. **A.** Outline of study design. Four male pigtail macaques (PTM) were exposed to 1×10^6 TCID₅₀ of SARS-CoV-2 (isolate WA1/2020) through a combination of intranasal (i.n.) and intratracheal (i.t.) inoculation on Day 0. Figure created with BioRender.com. **B-K.** Quantification of SARS-CoV-2 RNA levels from Pigtail macaque (PTM) mucosal swabs overtime (Quantitative RT PCR). Genomic (**B,D,F,H,J**) Subgenomic (**C,E,G,I,K**). **L-S.** PTM and Rhesus macaque (RhM) viral dynamics (Quantitative RT PCR). Comparison of genomic (**L**) and subgenomic (SGM, **M**) SARS-CoV-2 viral titers from nasal, pharyngeal, and rectal mucosal swabs at 1-day post infection (dpi). **N-S.** Comparison of SARS-CoV-2 RNA levels from nasal (**N** and **Q**), pharyngeal (**O** and **R**), and rectal (**P** and **S**) mucosal swabs overtime. Genomic (**N-P**) SGM (**Q-S**). Figures **B-K**. Baseline: n=4, Day 1: n=4, Day 4: n=4, Day 6: n=4, Day 14: n=2, Day 21: n=2. Figures **L-S**. Day 1: n=8, Day 2: n=4, Day 3: n=4, Day 4: n=4, Day 5: n=4, Day 6: n=4, Day 7: n=2, Day 9: n=2. Mann-Whitney comparison of means (Figures **L** and **M**) or a linear regression t-test (Figures **N-S**) was used to determine significance.

COVID-19 symptoms, pulmonary disease and pathology

The animals in our study were monitored daily for COVID-19 symptoms (S1 Table). Similar to what others have noted in RhM [26], we observed mild COVID-19 symptoms including decreased appetite, soft stool, mild cough and slight increased effort breathing. We found no significant changes in body weight, temperature, or saturation levels of blood oxygen (S1 Fig). Thoracic radiographs were obtained from all animals before infection and weekly thereafter, revealing subtle changes consistent with interstitial pneumonia reflective of mild to moderate COVID-19 (S2 Fig). Postmortem examination at 6-dpi revealed mild-to-moderate SARS-CoV-2-associated pneumonia in one of the two animals, MA27. The pneumonia was characterized by multifocal tan-plum areas of consolidation in the caudal left lung lobe (S3A Fig and S1 Table). At 21-dpi, gross lesions were minimal and only observed in one of two animals, MA28. The lesions noted in this animal were two small, flat tan foci on the dorsolateral aspect of the left caudal lung lobe (S3D Fig and S1 Table). Previous studies in RhM and Cynomolgus macaques (CyM) have demonstrated similar lung pathology with the RM model potentially exhibiting more severe lung lesions than CyM and PTM [16,32]. The PTM in our study revealed a wider range of lung pathology than that seen in other macaque models. Additional studies with an expanded cohort of PTMs may uncover key pathways of lung pathogenesis that occur with varying levels of disease which is representative of the variation seen in humans.

Histopathological findings consistent with SARS-CoV-2 associated pneumonia were observed in both animals at 6-dpi. Both animals had an interstitial pneumonia that was localized to regions of the left caudal lung. Regions of interstitial pneumonia were characterized by alveolar septa that were mild to markedly expanded by a mixture of macrophages, lymphocytes, and neutrophils. Alveolar septa were frequently lined by type II pneumocytes (Fig 2C and 2D), and alveoli contained large numbers of alveolar macrophages with rafts of fibrin in more severely affected areas (Fig 2A-2D).

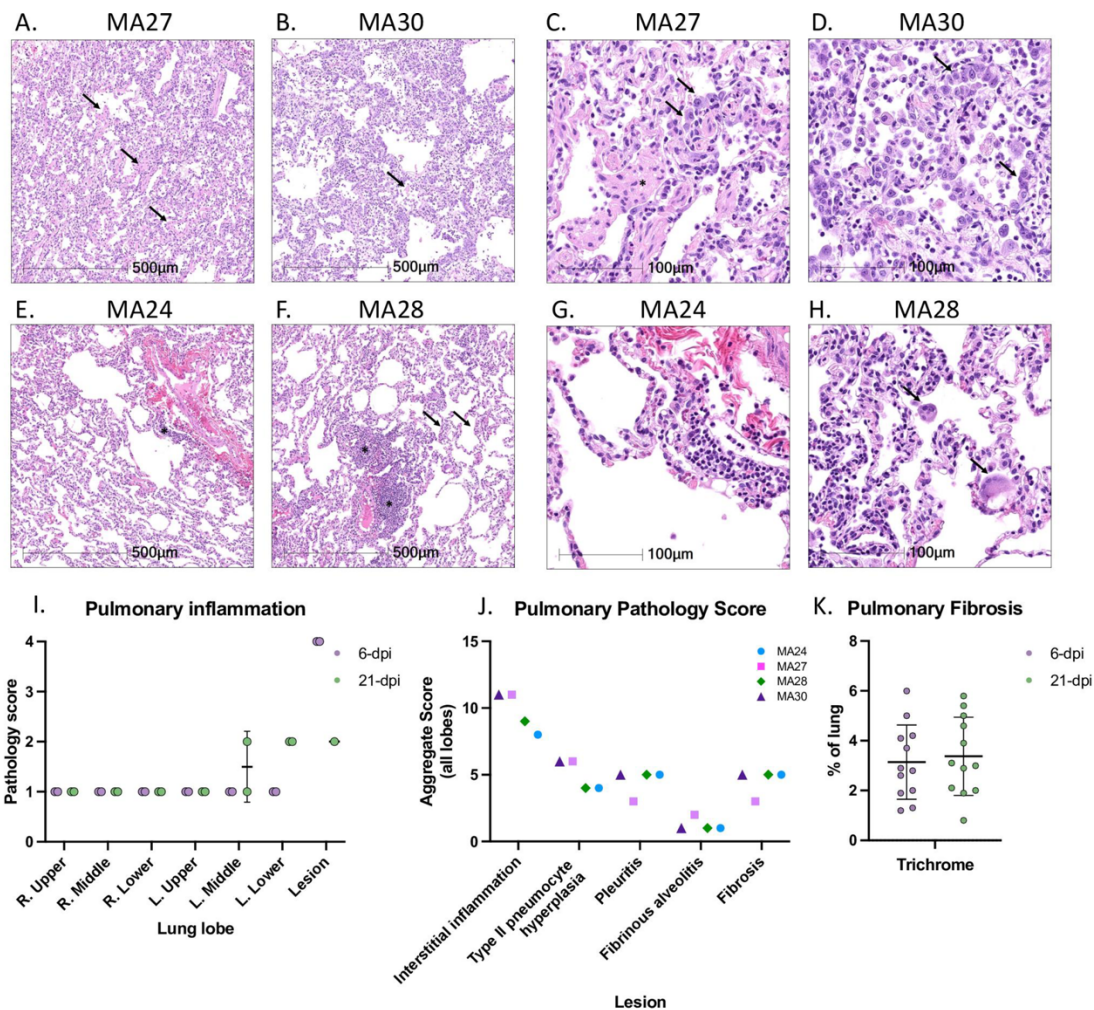


Fig 1.2. Histopathologic findings in SARS-CoV-2 infected pigtail macaques (PTM). Histopathologic findings at 6- (**A-D**) and 21-dpi (**E-H**). **A and B.** At 6-dpi alveolar septa are expanded by inflammatory infiltrate and alveoli contain rafts of fibrin (arrows). **C and D.** The inflammatory infiltrate is composed of a mixture of histiocytes, lymphocytes, and neutrophils, and alveolar septa are frequently lined by type II pneumocytes (arrows). In severely affected areas, alveoli contain fibrin rafts (**C**, asterisks). **E and F.** At 21-dpi, there is residual inflammation composed of perivascular lymphoid aggregates (asterisks), and mild thickening of alveolar septa (arrows). **G and H.** The residual inflammation is composed predominately of lymphocytes, and in MA28, rare multinucleated giant cells (**H**, arrows). A quantitative scoring system was used to assess pulmonary pathology in multiple lung sections (**I** and **J**). Each lung section was manually quantified for the percent of lung affected by interstitial inflammation (**I**). Each section was also quantified for the percent of lung affected by several typical SARS-CoV-2 induced pathologic lesions (**J**). Masson's Trichrome staining was also performed on the lung sections to quantify fibrosis (**K**).

At 21-dpi, minimal-to-mild residual interstitial pulmonary inflammation was observed in both animals. The residual inflammation was composed of perivascular lymphoid aggregates along with mild thickening of alveolar septa (Fig 2E and 2F). The inflammatory infiltrate at this time point was composed

predominately of lymphocytes; however, in one animal, MA28, low numbers of multinucleated giant cells were present in alveoli. (Fig 2H).

A comprehensive histopathological scoring system was designed to quantitatively assess pulmonary inflammation and pathogenic changes in all four animals at necropsy (Fig 2I and 2J). Up to seven lung sections were examined from each animal, one from each major lobe (left and right, upper, middle, and lower lobes) as well as a section of a grossly identified lung lesion (no gross lesion was observed in MA24). Each section of lung was manually quantified for the percentage of lung affected by interstitial inflammation (Fig 2I). Lesions were assigned a score for the interstitial inflammation based on the following scale: 0= 0%, 1= 0-5%, 2= 5-10%, 3= 10-30%, 4= >30% (inclusive of the upper limit). We also quantified each section of lung for the percentage of lung affected by several SARS-CoV-2 induced pathologic lesions including interstitial inflammation, type II pneumocyte hyperplasia, pleuritis, fibrinous alveolitis, and fibrosis (Fig 2J). Lesions were assigned a score based on the percentage of lung affected using the same scale as described above. For the pulmonary pathology score shown in Fig 2J, the scores of all lobes (seven for 6-dpi and six for 21-dpi) were summated to create an aggregate score for each pathologic lesion in each animal. Significant inflammation and pathology were localized to gross lesions and specific regions of the lung (left middle and left lower).

To assess potential SARS-CoV-2 induced lung fibrosis we performed Masson's Trichrome staining of sections from each major lung lobe (left and right, upper, middle, and lower lobes, Fig 2K) at necropsy. No appreciable

fibrosis was indicated at either 6- or 21-dpi. Overall, the SARS-CoV-2 induced pathology observed in our PTM model is consistent with the mild pathology seen in our recent studies of RhM[15,26].

Blood cytokine measures of inflammation

We next measured a panel of cytokines in blood serum after infection. Fluctuations in several inflammatory cytokines, as compared to baseline, were found throughout the study. Interleukin-8 (IL-8), a neutrophil chemoattractant, was the most consistently increased cytokine at 6-dpi whereas IL-6 and IL-12-p40 decreased in all animals at day 6 (Fig 3A). Interestingly, MA27 had a stronger inflammatory cytokine response at 6-dpi compared to the other three animals, as exemplified by increases in several cytokines, including IL-10, IFN- γ , GM-CSF, IL-8, IL-17A, MCP-1 and most notably, TNF- α and IFN- β . As stated previously, this animal had increasing viral loads at 6-dpi suggesting a possible link between the intensity of the inflammatory response and the level of replicating virus. Animal MA28, which exhibited consistently high genomic vRNA levels in both nasal and rectal swabs through 21-dpi, showed a rise IL-10, IL-1 β , IL-12p40 and IP-10 serum levels at necropsy (21-dpi). We also measured levels of IL-4, an anti-inflammatory cytokine, in plasma before and after infection. The IL-4 concentration in our samples was below the level of detection of the assay and is therefore represented in the figure as no change occurring throughout the course of the study.

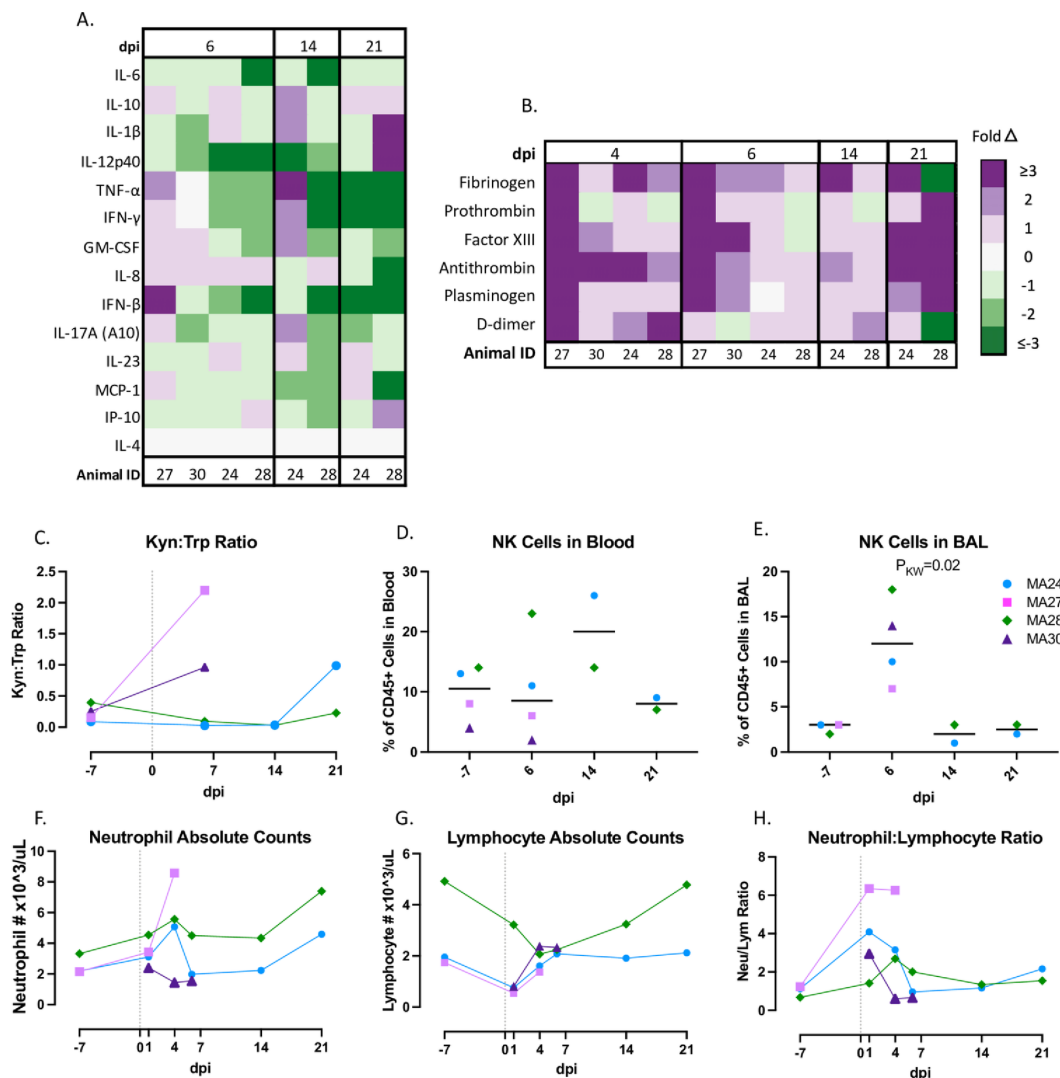


Fig 1.3. Inflammatory innate immune response in pigtail macaques challenged with SARS-CoV-2. **A.** Changes in serum/plasma cytokine levels at 6-, 14- and 21-days post SARS-CoV-2 infection (dpi). Data represent fold changes from baseline. **B.** Changes in coagulation biomarkers in plasma at 4-, 6-, 14- and 21-dpi. Data are fold changes from baseline. **C.** Ratio of Kynurenine (Kyn) to Tryptophan (Trp) as a measure of indoleamine 2,3-dioxygenase (IDO) activity before and after SARS-CoV-2 infection. **D-E.** Frequency of Natural Killer (NK, CD45+ CD3- HLA-DR-/lo CD8+) cells in the blood (**D**) or BAL (**E**) at baseline and 6-, 14- and 21-days post infection (dpi). Bars represent median. **F.** Absolute number of neutrophils pre- and post- SARS-CoV-2 infection. **G.** Absolute number of lymphocytes pre- and post-SARS-CoV-2 infection. **H.** Changes in neutrophil to lymphocyte ratio before and after SARS-CoV-2 infection. Figures **C** and **D**. Baseline: n=4, Day 6: n=4, Day 14: n=2, Day 21: n=2; Figure **E**. Baseline: n=3, Day 6: n=4, Day 14: n=2, Day 21: n=2; Figures **F-H**. Baseline: n=3, Day 1: n=4, Day 4: n=4, Day 6: n=4, Day 14: n=2, Day 21: n=2. Figures **C-H**. Day 0=day of infection. Kruskal-Wallis comparison of overall means (P_{KW}) was used to determine significance. P values ≤ 0.05 reported.

Markers of coagulopathy

Complications related to coagulopathy have been reported in humans with severe COVID-19 disease, with highly elevated levels of D-dimers shown to be a particular correlate of disease severity[33,34]. To examine whether PTM recapitulate this phenotype, we measured multiple biomarkers of coagulation in blood (Fig 3B), including fibrinogen, prothrombin, factor XIII, antithrombin, plasminogen, and D-dimers. We found nearly universal increases in coagulation biomarkers in the first week of infection. Specifically, we noted increased D-dimer levels in all four animals at 4-dpi, with MA27 and MA28 exhibiting a greater than 3-fold increase relative to baseline before resolving to near baseline levels. Interestingly, several biomarkers (prothrombin, factor XIII, antithrombin, and plasminogen) began to rise again at 21-dpi.

Kynurenine tryptophan pathway

Pro-inflammatory cytokines, specifically interferon gamma- γ (IFN- γ), promote the kynurenine (Kyn) pathway (KP) of tryptophan (Trp) catabolism [35]. Recent studies in humans hospitalized with COVID-19 suggest that the Kyn:Trp ratio positively correlates with disease severity [36]. We measured the Kyn:Trp ratio in plasma at baseline, and days 6, 14 and 21 (Figs 3C, S4A and S4B). Again, MA27 showed the greatest increase in the Kyn:Trp ratio at 6-dpi possibly providing another biomarker of the more severe disease course seen in this animal.

NK cells

The initial immune response to SARS-CoV-2 infection involves the intricate interplay between the cells of the innate immune system. Natural killer (NK) cells are cytotoxic lymphocytes that often play a key role in the early defense against viral infections. Studies of hospitalized COVID-19 patients show that decreases in circulating NK cells correlate with disease severity [37,38]. Here, we measured the percentage of NK cells (defined as CD45⁺ CD3⁻ HLA-DR^{-/lo} CD8⁺) in both the blood and bronchoalveolar lavage fluid (BAL) at baseline, and days 6-, 14-, and 21-post infection (Fig 3D and 3E). We did not find significant changes in peripheral NK cells in our study. However, MA28 and MA24 had slight increases in circulating NK cells at day 6 and day 14, respectively. Flow cytometry analysis of BAL indicated an increase in infiltrating NK cells in the lung at 6-dpi in all four animals.

Neutrophil to lymphocyte ratio

A high incidence of neutrophilia coupled with lymphocytopenia has been reported in COVID-19 patients [38,39]. Animals MA24, MA27, and MA28 all experienced neutrophilia and lymphocytopenia during the course of the study. However, these changes were mild, and values largely remained within normal limits. Pre-infection data on these cells were not available for MA30 (S1 Table). The neutrophil to lymphocyte ratio (NLR) has been identified as an important predictor of disease severity in human patients [40]. Thus we measured the NLR at baseline and 6-, 14- and 21-dpi. Interestingly, the highest NLR at 1- and 4-

days post infection was noted in MA27 (Fig 3F-H). These data are consistent with the increasing viral titers noted at 6-dpi, the increased levels of inflammatory cytokines and D-dimers, as well as the elevated K:T ratio observed in MA27. Each potentially correlate with or contribute to the more severe lung pathology noted in this animal at necropsy.

SARS-CoV-2 infection and macrophage pulmonary infiltration

Fluorescent immunohistochemistry of the lung for SARS-CoV-2 nucleoprotein identified small clusters of SARS-CoV-2 infected cells, predominately lining the alveolar septa, in both animals sacrificed at 6-dpi (Fig 4A, 4B and 4E). COVID-19 disease is commonly characterized by pulmonary infiltration of inflammatory immune cells [41]. Innate cells, particularly monocytes/macrophages are considered important mediators of disease progression [42]. At 6-dpi, the alveoli contained large numbers of IBA1+ macrophages (Fig 4A, 4B and 4F). By 21-dpi, macrophage numbers were greatly reduced and no SARS-CoV-2+ cells were detected in either MA24 or MA28 (Fig 4C-F).

Flow cytometry showed increases in CD14+ CD16- classical monocytes in both the blood and BAL at 6-dpi (Fig 4I and 4L) and an increase in CD14+ CD16+ intermediate monocytes (Fig 4M) in BAL at 6-dpi. Heterogeneous fluctuations of circulating intermediate and CD14- CD16+ non-classical monocytes occurred throughout the study (Fig 4J and 4K). MA27 and MA24

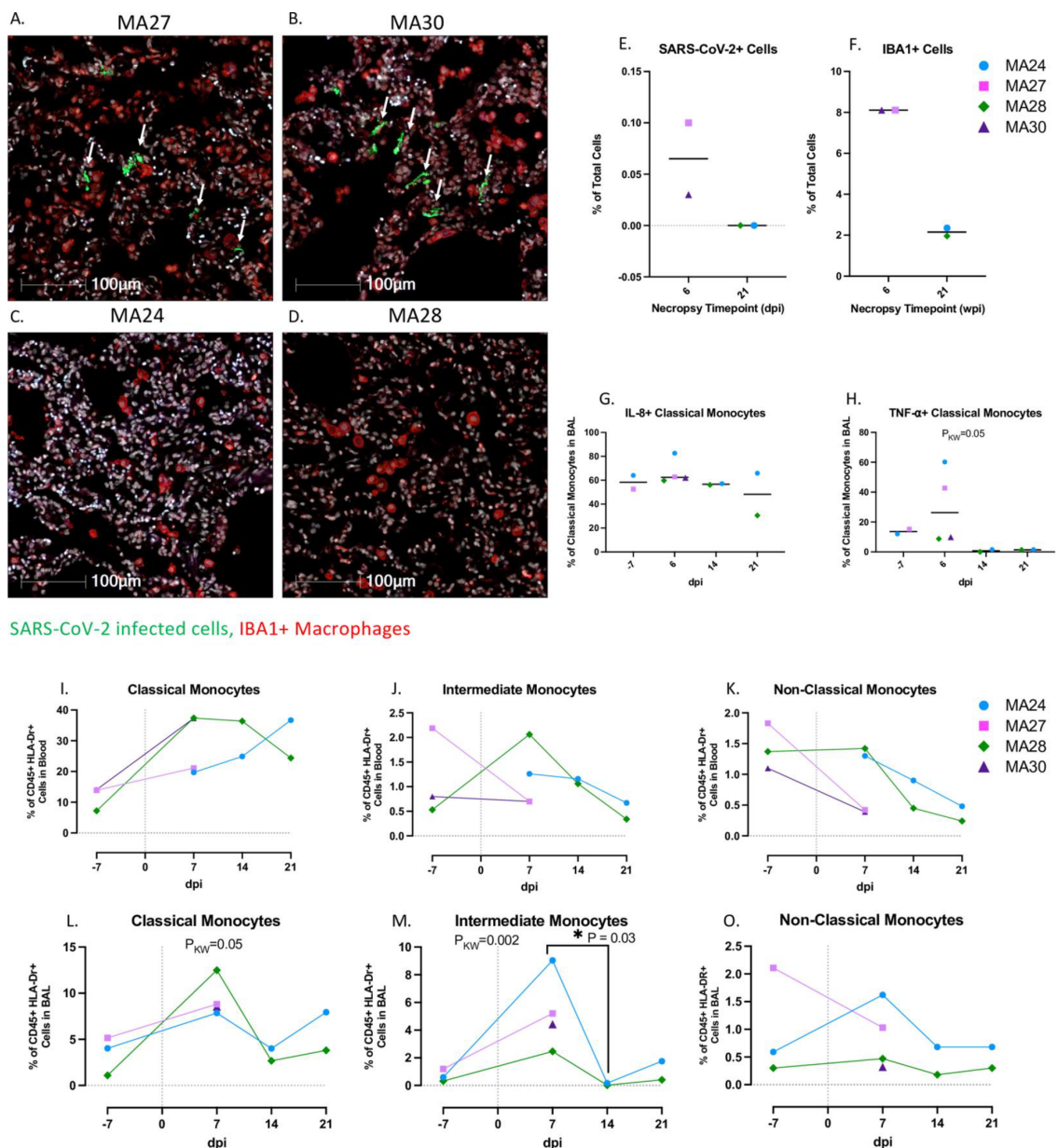


Fig 1.4. Pulmonary SARS-CoV-2 infection and macrophage/monocytes in the lung and blood. **A-D.** SARS-CoV-2 infection and macrophage infiltration in the lungs of pigtail macaques at 6- (**A** and **B**) and 21- days post infection (dpi, **C** and **D**). DAPI=White, Green=SARS-CoV-2, Red=IBA1, Blue=Autofluorescence. **E** and **F.** Percentage of SARS-CoV-2 infected cells (**E**) and IBA1+ macrophages (**F**) in the lung at necropsy. Bars represent median. **G** and **H.** Frequency of IL-8 (**G**) and TNF- α (**H**) expressing classical monocytes (CD45+ HLA-DR+ CD14- CD16+) in BAL. **I-O.** Frequencies of Classical (**I** and **L**) intermediate (CD45+ HLA-DR+ CD14+ CD16+) (**J** and **M**), and non-classical monocytes (CD45+ HLA-DR+ CD14- CD16+) (**K** and **O**) in the blood and BAL before and after SARS-CoV-2 infection. Day 0=day of infection. Figures **I-O.** Baseline (day -7): n=3, Day 6: n=4, Day 14: n=2, Day 21: n=2. Kruskal-Wallis comparison of overall means (P_{KW}) and Dunn's Multiple comparisons (designated by line, P_D) tests used to determine significance. P values ≤ 0.05 reported.

showed increases in inflammatory cytokine, tumor necrosis factor- α (TNF- α)-expressing classical monocytes in the BAL at 6-dpi (Fig 4H). Interleukin-1 β (IL-1 β) and IL-6 are key inflammatory cytokines involved in the pathophysiology of COVID-19 disease in humans [43,44]. Here, we noted increases in IL-1 β expression in peripheral classical monocytes throughout the study (Fig 5A). As previously shown in Fig 3A, serum levels of the inflammatory cytokine IL-6 remained low after SARS-CoV-2 infection. We also found that peripheral monocyte expression of IL-6 remained relatively stable post infection, with only one animal, MA24, showing an increase at days 14 and 21 as compared to day 6 (Fig 5B). Lastly, an upward trend in neutrophil chemoattractant (IL-8+) expressing classical monocytes was observed throughout infection, although this trend was not statistically significant (Fig 5C).

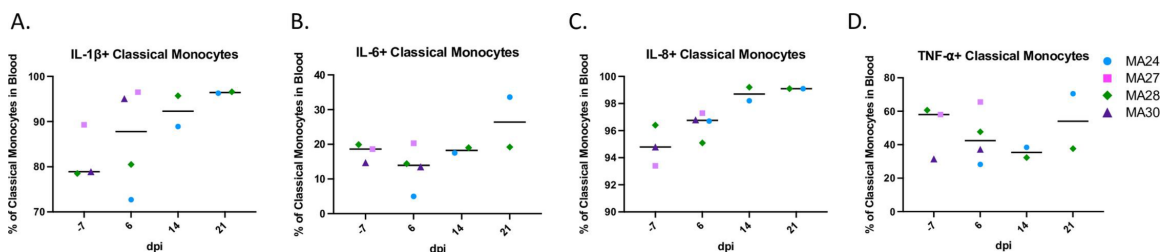


Fig 1.5. Monocyte cytokine response in the blood of pigtail macaques challenged with SARS-CoV-2. A-D. Frequency of IL-1 β (A), IL-6 (B), IL-8 (C) and TNF- α (D) expressing classical monocytes (CD45+ HLA-DR+ CD14- CD16+) in the blood. Bars represent median. Day 0=day of infection. Baseline (-7): n=3, Day 6: n=4, Day 14: n=2, Day 21: n=2.

Peripheral T cell responses

Understanding the role of the adaptive immune response to SARS-CoV-2 infection is a key component to the development of effective vaccines and treatment options for COVID-19. Using flow cytometry, we measured changes to T cell populations in both the blood and BAL at baseline and 6-, 14-, and 21-dpi. CD3⁺ T cell fluctuations in the blood were driven by CD4 T cells which showed levels increasing significantly between days 14- and 21-pi (Fig 6A). As the percentage of CD4 T cells rise and fall over the course of the study, we observed the opposite pattern in the percentage of cytotoxic CD8 T cells (Fig 6B). We found increases in Ki-67⁺ CD4 T cells at 6-dpi (MA27, MA28 and MA30) and 14-dpi (MA24 and MA28) indicating increased CD4 T cell proliferation (Fig 6C and 6D). Increases in expression of the T cell exhaustion marker, PD-1, have been noted in a number of studies involving human COVID-19 patients [45–47]. Here we found a significant increase in PD-1⁺ CD4 T cells at 14-dpi (Fig 6I). Interestingly, we saw a decrease in the percentage of CD4 T cells at this same timepoint.

We then used tSNE analysis to show changes in PD-1 expressing cell populations over the course of the study (Fig 6E-H). At baseline, CD4⁻ CD8⁻ (double negative) T cells made up the greatest proportion of PD-1⁺ CD3⁺ T cells (Fig 6H). Beginning at day 6-pi, CD4 T cells made up the majority of PD-1 expressing cells, with only one animal, MA28, showing increases in PD-1 expressing cytotoxic T cells at 6 and 14-dpi (Fig 6J).

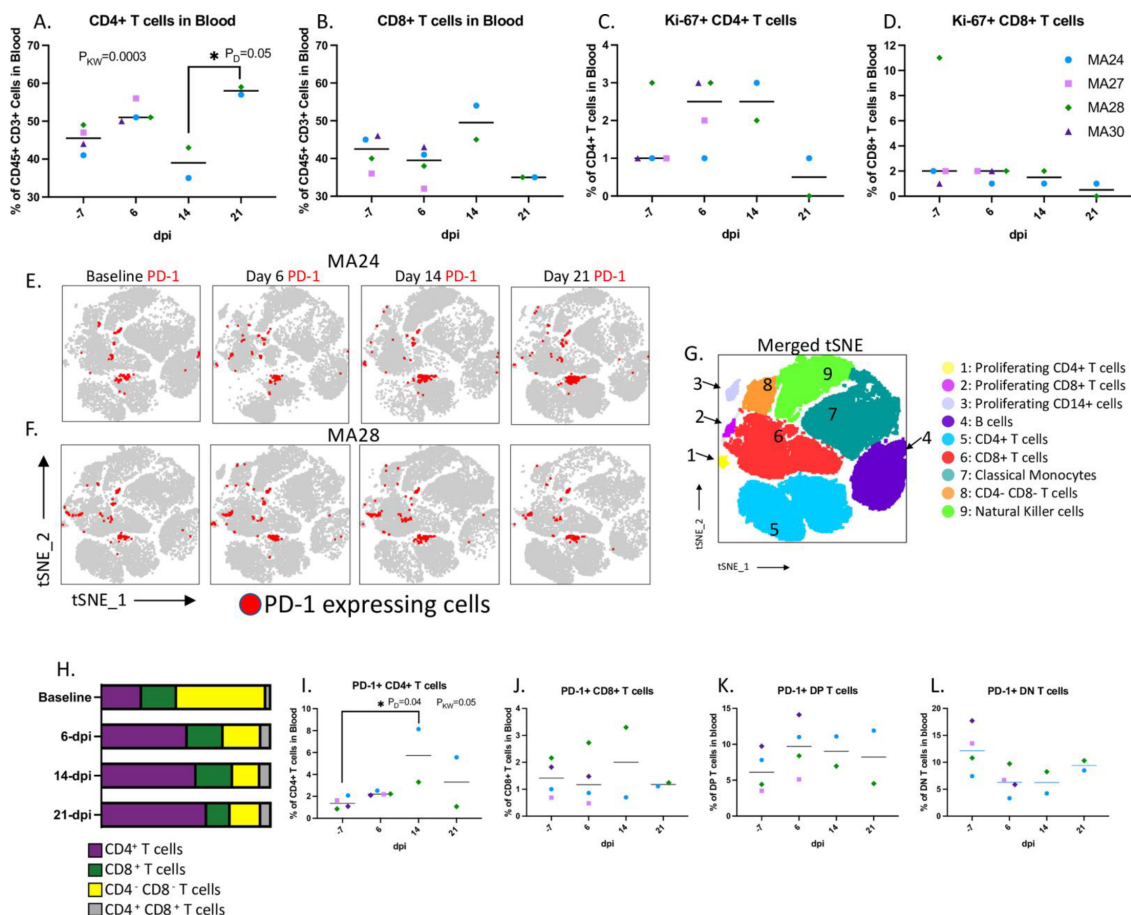


Fig 1.6. T cells in the blood. A-B. CD4+ (A) and CD8+ (B) T cell frequencies in the blood before and 6-, 14-, and 21-days post SARS-CoV-2 infection. C-D. Changes in Ki-67 expressing CD4+ (C) and CD8+ (D) T cells. Bars represent median. E. tSNE plots displaying changes in PD-1 expression (red) in peripheral CD45+ cells overtime. MA24 (E) and MA28 (F) displayed as representative animals. G. Merged tSNE indicating phenotype of the tSNE defined cell populations in E and F. H. Average changes in the percentages of CD4+, CD8+, CD4- CD8- (DN) and CD4+ CD8+ (DP) T cells within the total PD-1+ CD3+ cell population. I-L. Frequency of PD-1+ expressing CD4+ (I), CD8+ (J), DP (K) and DN (L) T cells in the blood. Bars represent median. Kruskal-Wallis comparison of overall means (P_{KW}) and Dunn's Multiple comparisons (designated by line, P_D) tests used to determine significance. P values ≤ 0.05 reported. Baseline (-7): n=4, Day 6: n=4, Day 14: n=2, Day 21: n=2.

Pulmonary T cell responses

We next sought to characterize the dynamics of pulmonary T cell populations over the course of infection by examining the frequency as well as cytokine and surface protein expression before SARS-CoV-2 infection, and at days 6-, 14-, and 21-post viral challenge. Using PMA stimulation, we noted

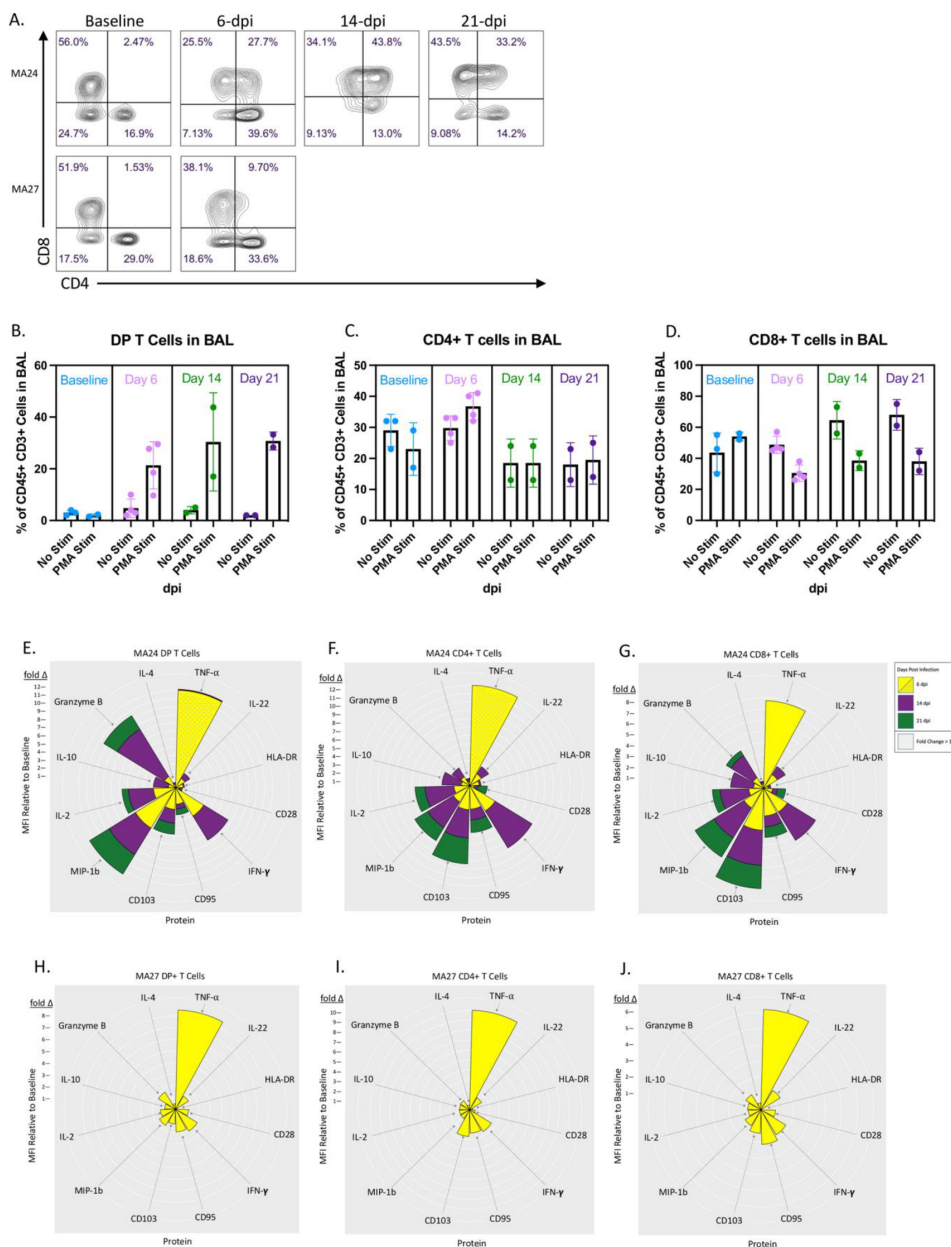


Fig 1.7. Adaptive T cell responses in the BAL. **A.** Representative flow cytometry plots showing changes in CD4 and CD8 expression in PMA/ionomycin stimulated CD3⁺ cells in BAL. Two animals shown (MA24 euthanized at 21-dpi, MA27 euthanized at 6-dpi). **B-D.** Effect of PMA/ionomycin on the frequency of CD4⁺ CD8⁺ (DP, **B**), CD4⁺ (**C**) and CD8⁺ (**D**) T cells in BAL before and 6-, 14-, and 21-days post SARS-CoV-2 infection. Bars represent mean and standard deviation. **E-J.** Nightingale Rose Plots (NRPs) showing fold changes in cytokine and surface protein expression compared to baseline (MFI). Yellow=6-dpi, Purple=14-dpi, Green=21-dpi. Size of petals represents magnitude of increase in expression. Distance from one white ring to the next is a 1-fold change. A decrease in expression is represented by a petal size less than the distance between two rings. Two animals shown (MA24 euthanized at 21-dpi, MA27 euthanized at 6-dpi). At 6-dpi, MA24 DP T cell TNF- α MFI is 24x baseline and CD4⁺ T cell TNF- α MFI is 50x baseline. Graph cutoff is set to a 12-fold change. Figures **B-D.** Baseline: n=3 (No Stimulation (Stim)) and n=2 (Stim), Day 6: n=4 (No Stim) and n=4 (Stim), Day 14: n=2 (No Stim) and n=2 (Stim), Day 21: n=2 (No Stim) and n=2 (Stim).

increased frequencies of CD4⁺/CD8⁺ double positive (DP) T cells after viral challenge which remained elevated throughout the study (Fig 7A and 7B) ((Median DP T cells as a percentage of CD3⁺ T cells: Baseline: 2% (n=2), 6-dpi: 23% (n=4), 14-dpi: 30% (n=2), 21-dpi: 31% (n=2)). We also examined fold changes in surface protein and cytokine expression among the DP, CD4 and CD8 single positive T cell populations as compared to baseline in two of the animals, MA24 and MA27 (Fig 7E-J). Both MA24 (euthanized at 21-dpi) and MA27 (euthanized at 6-dpi) showed large increases among all three T cell subsets in TNF- α expression at 6-dpi. At fourteen days post infection, MA24 showed increased expression of Granzyme B in both the DP and CD8 T cell populations. Interestingly, it was the DP T cell population which showed the greatest fold increase in Granzyme B over baseline indicating the cytotoxic potential of this DP T cell population.

We also compared the activity of each T cell subtype within the same time point of infection (Fig 8A-O). Prior to infection, DP T cells showed higher TNF- α , IL-10, MIP-1 β , and IL-22 expression than traditional CD4 and CD8 T cells, suggesting that these cells may potentially perform a non-specific function in the pulmonary immune response [48]. After viral challenge, we found higher frequencies of Granzyme B expressing DP T cells compared to CD4 T cells and, most notably, CD8 T cells at each timepoint post infection (Fig 8E, 8J and 8O). We found significant increases in CD4 T cells expressing IL-2, IL-10, TNF- α and MIP-1b (Fig 8A-E). At 14-dpi, we noted a significant increase in MIP-1 β

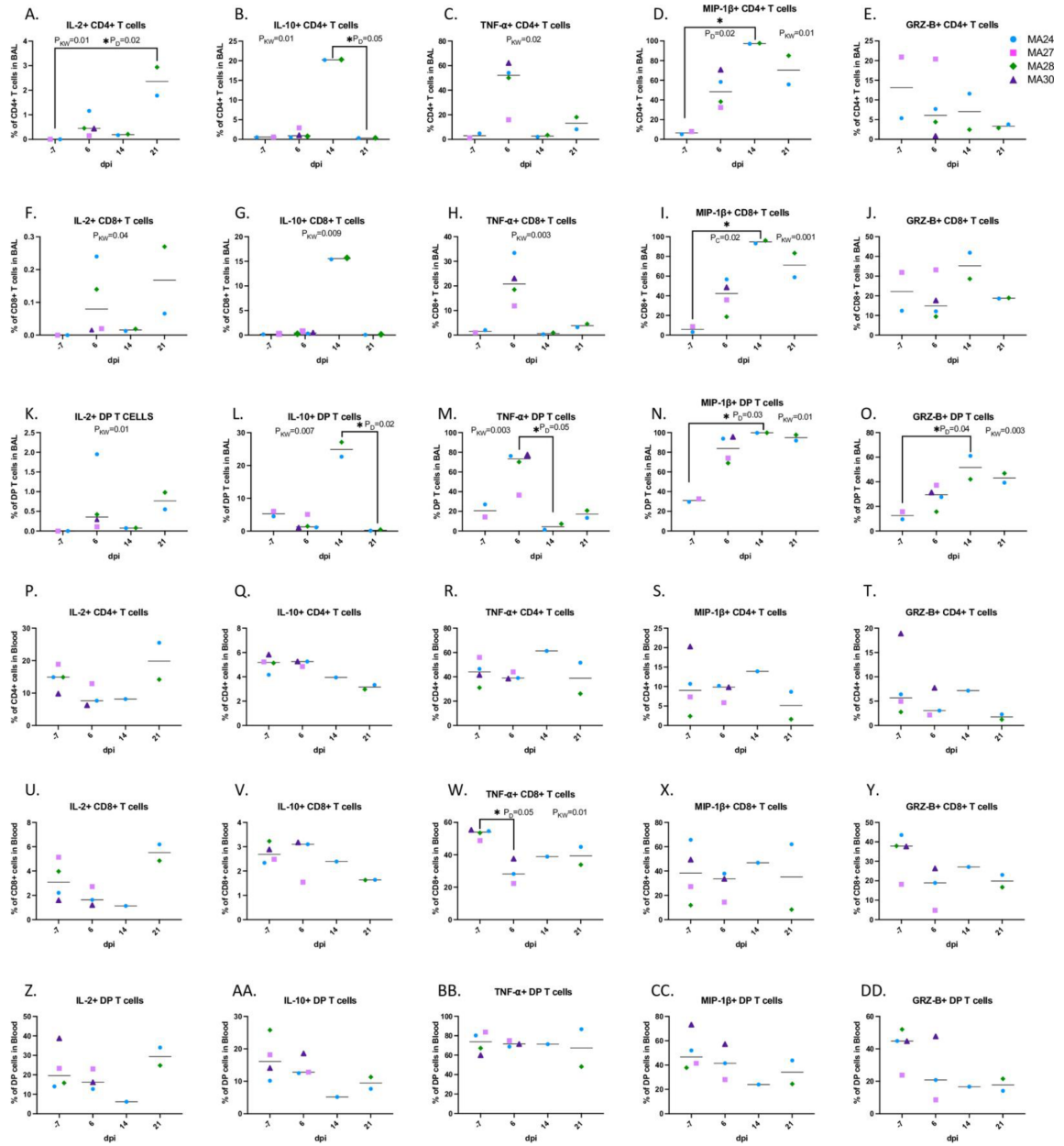


Fig 1.8. Changes in T cell cytokine expression in the lung (A-O) and blood (P-DD). PMA/ionomycin stimulated CD4+ T cells (BAL: A-E, Blood: P-T), CD8+ T cells (BAL: F-J, Blood: U-Y), and CD4+ CD8+ (DP) T cells (BAL: K-O, Blood: Z-DD). Bars represent median. Kruskal-Wallis comparison of overall means (P_{KW}) and Dunn's Multiple Comparisons (designated by line, P_D) tests used to determine significance. P values ≤ 0.05 reported. Figures A-O. Baseline (-7): n=2, Day 6: n=4, Day 14: n=2, Day 21: n=2. Figures P-DD. Baseline (-7): n=4, Day 6: n=3, Day 14: n=1, Day 21: n=2.

expressing CD8 T cells (Fig 8I) along with significant changes in IL-2, IL-10 and TNF- α expression. DP T cells also showed increased activity post viral challenge with significant increases in the frequency of IL-10, TNF- α , MIP-1 β and Granzyme B expressing cells. Taken together, these findings show that the DP T cell population has functions which overlap with both CD4 and CD8 T cells [48]. We speculate that these cells are major histocompatibility complex class II (MHC-II) restricted CD4 T cells which upregulate CD8 upon activation, generating the described DP T cell population which has greater cytotoxic potential than traditional CD4 T cells. Pulmonary infiltrating cytotoxic CD4 T cells potentially aid CD8 T cells in viral clearance and are a unique aspect of COVID-19 disease [25].

Peripheral T cell cytokine responses

We next performed T cell subtype cytokine analysis in the blood using the same panel we used for BAL (Fig 8P-DD). We found that the dynamic changes in T cell activity occurred mainly in the BAL (Fig 8A-O) with very few changes occurring in the periphery (Fig 8P-DD). As COVID-19 is a respiratory disease, these results are not surprising. The only significant change noted in the blood was a decrease in TNF- α expressing CD8⁺ T cells at 6-dpi (Fig 8W). Interestingly, we see an increase in TNF- α expressing CD8⁺ T cells in the lung at this same timepoint.

CD4 T cell and Granzyme B expression in the lungs

Fluorescent Immunohistochemistry (IHC) identified cytotoxic CD4 T cells (CD4+ Granzyme B+) in the lungs of all four PTM at necropsy (Fig 9). We detected large numbers of infiltrating Granzyme B positive cells in the lungs of MA27 and MA30 (euthanized at 6-dpi) along with rare cytotoxic T cells (Fig 9A, 9B, 9F and 9G). At 21-dpi, MA24 (Fig 9C) showed low numbers of Granzyme B+ cells compared to MA28 (Fig 9D) and the other two animals which were euthanized at 6-dpi. Cytotoxic CD4 T cells were detected in the lung of MA28 and, with less frequency, in MA24 (Fig 9G).

We then used flow cytometry to measure cytotoxic CD4 T cells in BAL (CD45+CD3+CD4+Granzyme B+). To mirror the IHC analysis, we did not exclude CD8+ cells from our cytotoxic CD4+ population. Mononuclear cells were incubated with or without PMA stimulation cocktail for 4-6 hours and cytotoxic CD4 T cells were measured as a percentage of CD45+ cells (Fig 9H and 9J) and CD3+ cells (Fig 9I and 9K) in both the stimulated and unstimulated conditions. We noted a considerable increase in cytotoxic CD4 T cells in BAL at 14-dpi.

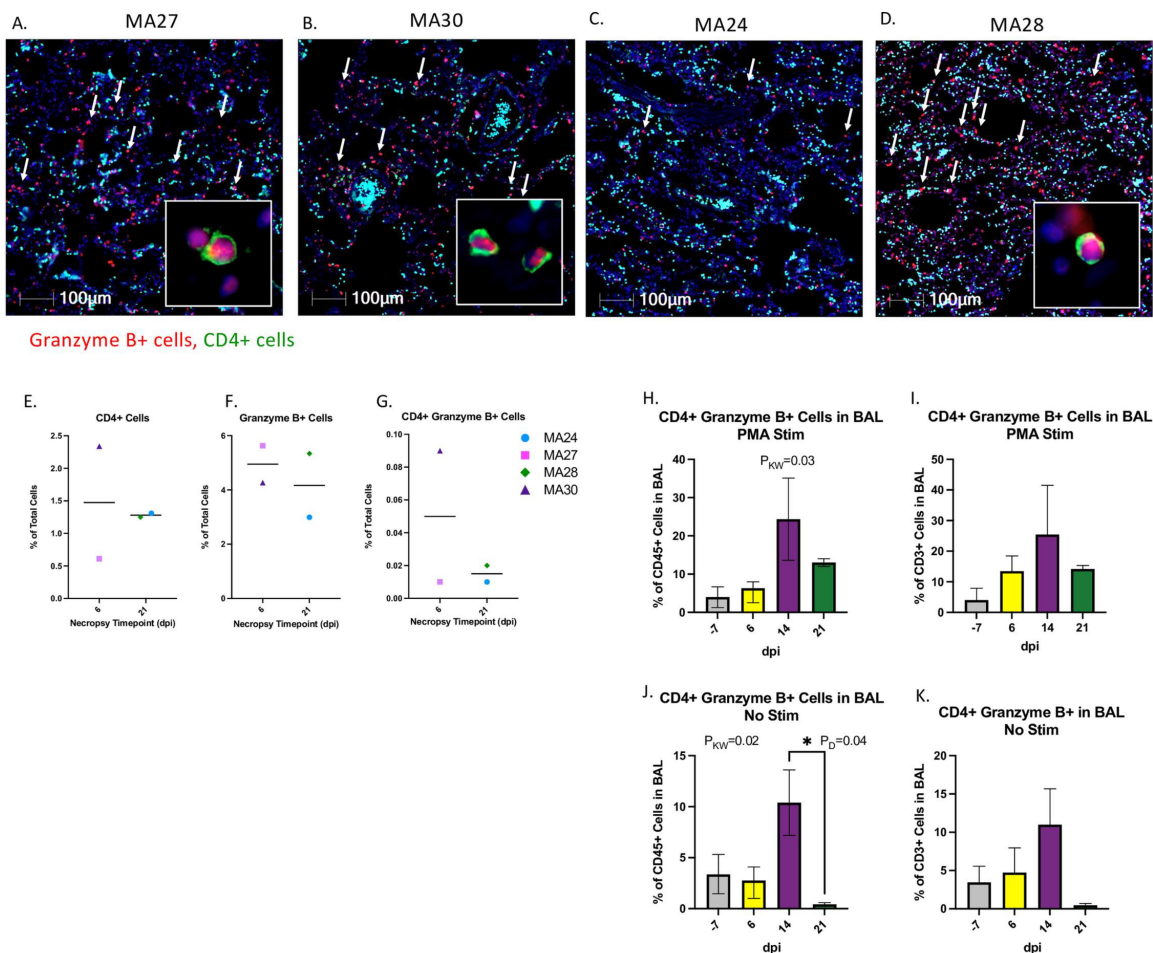


Fig 1.9. CD4 and Granzyme B expression in the lungs of SARS-CoV-2 infected macaques at 6- (A and B) and 21-days post infection (dpi, C and D). At 6-dpi, MA27 (A) and MA30 (B) the lungs are infiltrated by large numbers of Granzyme B positive cells (red, arrows). Insets: Rare CD4+ cells (green) exhibit granzyme expression. At 21-dpi, MA24 (C) exhibits low numbers of Granzyme B positive cells (red, arrows) compared to MA28 (D) and the two, 6-dpi animals (A and B). DAPI=Blue, Green=CD4, Red=Granzyme B. **E-G.** Percentage of CD4+ (E), Granzyme B+ (F) and CD4+ Granzyme B+ (G) cells in the lung at necropsy. Bars represent median. **H-K.** CD4+ Granzyme B+ T cells (CD45+ CD3+ CD4+ Granzyme B+) in BAL at Baseline (-7) and 6-, 14- and 21-dpi as a percentage of CD45+ cells (H and J) and CD3+ cells (I and K). H and I. Mononuclear cells, isolated from BAL, were stimulated with PMA/ionomycin for 4-6 hours. Bars represent median and standard deviation. Kruskal-Wallis comparison of overall means (P_{KW}) and Dunn's Multiple comparisons (designated by line, P_D) tests used to determine significance. P values ≤ 0.05 reported. Figures H-K. Baseline: n=3 (No Stimulation (Stim)) and n=2 (Stim), Day 6: n=4 (No Stim) and n=4 (Stim), Day 14: n=2 (No Stim) and n=2 (Stim), Day 21: n=2 (No Stim) and n=2 (Stim).

SARS-CoV-2 peptide specific T cell response in the lung 21-days post infection

Mononuclear cells, isolated from BAL, were incubated overnight with SARS-CoV-2 peptides and analyzed by flow cytometry. We detected specific CD4 T cell responses against SARS-CoV-2 that localized to the lung 21 days after viral infection. Specifically, we identified CD4 T cell responses to membrane, nucleocapsid and to a lesser degree, spike peptides (Fig 10A). CD8 T cell responses against the virus were also noted, but at lower frequencies (Fig 10B). In FlowJo, we gated on the CD4 T cell population and applied tSNE analysis to identify and characterize virus specific CD4 T cells responding to membrane and nucleocapsid viral peptides (Fig 10C and 10D). tSNE analysis revealed a unique cluster of CD4 T cells that responded to stimulation. In this population of responding cells (Fig 10E and 10F), we noted increased expression of CD8 and HLA-DR, indicating cell activation. Increased expression of inflammatory cytokines and chemokines was also detected in the antiviral CD4 T cells. We noted a decrease in Granzyme B expression suggesting that the antigen specific CD4 T cells have reduced cytotoxic capacity, unlike the DP T cells (cytotoxic CD4) described previously (Figs 7, 8 and 9). As expected, antiviral CD4s have increased CD95 expression reflecting a memory phenotype. Numerous studies of SARS-CoV-2 convalescent humans have described antiviral T cells with a relative predominance of CD4 T cells [49,50]. These antiviral responses are most often noted in the blood. In our study, we were unable to detect antigen-specific T cell responses in the blood 21 days after viral infection (S5 Fig). Taken together, our data provide a valuable addition to the

data from humans and may suggest important roles for antiviral CD4 T cells the pulmonary compartment.

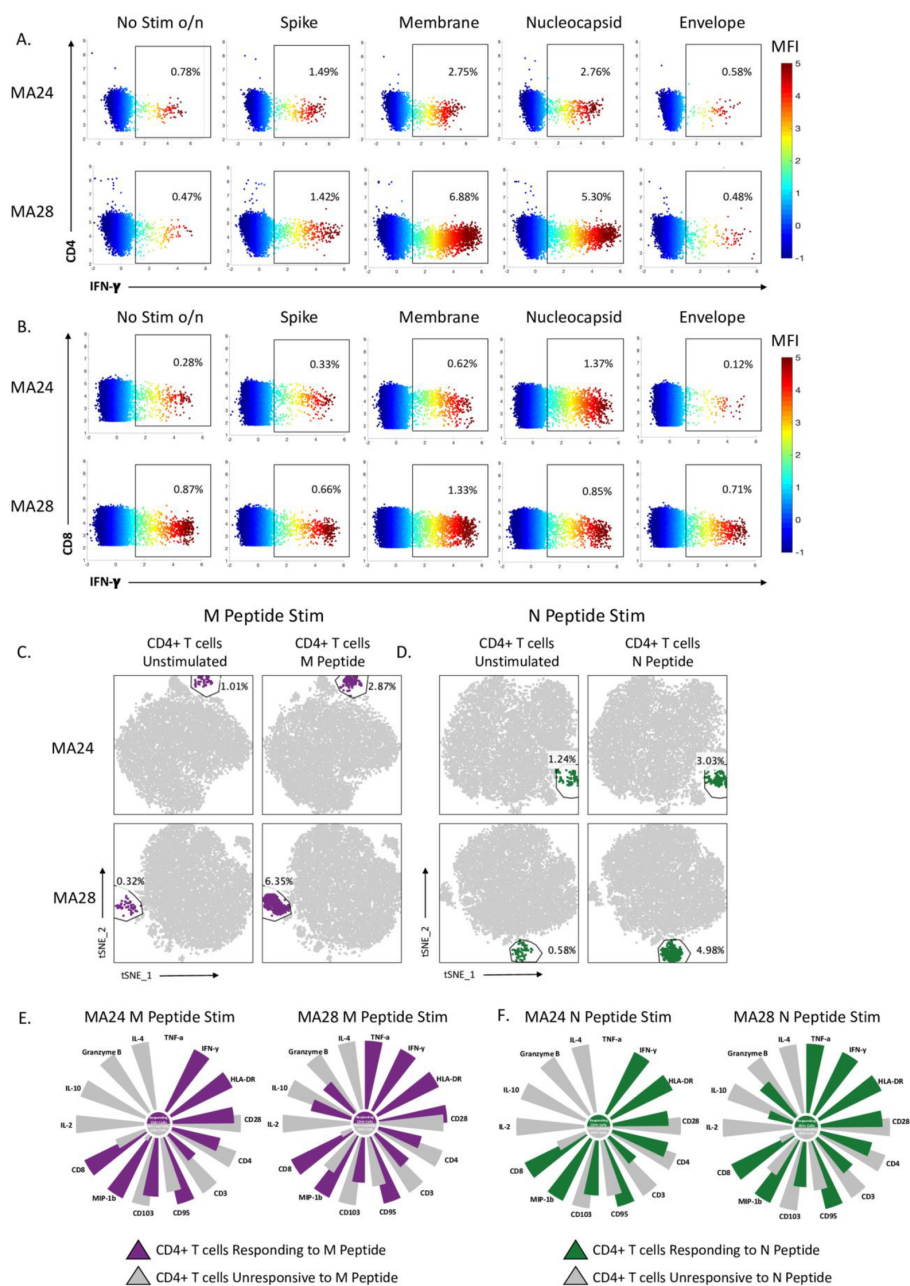


Fig 1.10. SARS-CoV-2 peptide-specific T cell response in the lung 21 days post-infection. Two animals shown (MA24 and MA28 euthanized at 21-dpi) A and B. Flow cytometry dot plots showing CD4+ (A) and CD8+ (B) T cell Interferon- γ (IFN- γ) response to overnight SARS-CoV-2 peptide (spike, membrane, nucleocapsid and envelope) stimulation. No stim o/n=cells incubated overnight without stimulation. Heatmap represents arcsin transformed MFI values. C and D. tSNE plots of CD4+ T cells showing an expansion in cells following overnight peptide stimulation. M=SARS-CoV-2 membrane peptides (C), N=SARS-CoV-2 nucleocapsid peptides (D). E and F. Radial bar plot comparing MFI values of the expanded CD4+ T cell population gated on in Figures C and D to the unchanged CD4+ population within the same tSNE plot. Representative animals MA24 and MA28 (euthanized at 21-dpi). The higher MFI value is set to 100 and the percent difference is calculated between the higher and lower MFI values. Size of the petals represents this analysis.

Humoral immune responses

Using flow cytometry, we measured B cell kinetics in the blood at baseline and days 6-, 14- and 21-post infection (Fig 11A). We did not detect any significant changes in the percentage of peripheral B cells over the course of the study. We next tested serum from infected animals for neutralizing antibodies using a pseudovirus assay. Unsurprisingly, no neutralization was detected at 6-dpi in any sample, including the animals euthanized at that time point. By 14-dpi, neutralizing antibody responses were detectable in both MA24 and MA28 with responses decreasing by 21-dpi (Fig 11B).

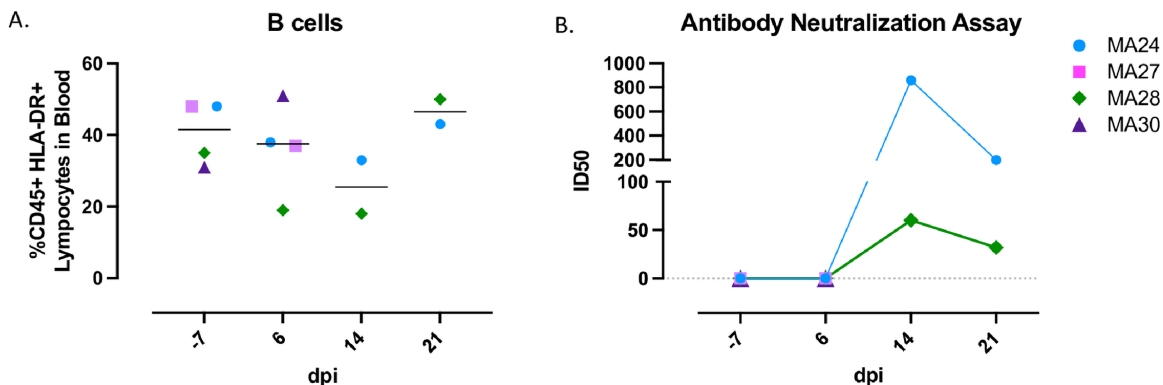


Fig 1.11. Humoral immune response in SARS-CoV-2 infected pigtail macaques. **A.** B cell frequencies in the blood before and 6-, 14-, and 21-days post (dpi) SARS-CoV-2 infection. Bars indicate median. **(B)** Pseudovirus neutralization assay showing serum antibody levels against SARS-CoV-2 using HEK 293T/ACE2 cells. Baseline (-): n=4, Day 6: n=4, Day 14: n=2, Day 21: n=2

Discussion

The novel coronavirus SARS-CoV-2 has caused a global pandemic with little precedent. As of the time of submission, this virus has infected nearly 270 million individuals worldwide and killed over five million, including almost 800,000 in the United States. Illness caused by this virus, termed COVID-19, ranges from asymptomatic [51,52] to flu-like symptoms to severe pneumonia [53,54]. In the most severe cases, patients have experienced acute respiratory distress syndrome (ARDS) and death [55]. It has also become apparent that a number of surprising symptoms can be associated with SARS-CoV-2 infection, including: coagulopathy, thrombosis, kidney failure, and chronic respiratory/neurological issues that seemingly persist well beyond viral clearance [43,56–63]. Although several highly effective vaccines have been created to combat the COVID-19 pandemic [64–66], billions of individuals remain unvaccinated worldwide. Furthermore, the emergence of new viral variants with enhanced transmissibility [67–70] and the ability to infect even the vaccinated [71] (though this population is overwhelmingly protected from severe disease [72–74]) suggest that this virus will persist indefinitely. Barring the development and mass deployment of vaccines capable of inducing sterilizing immunity, an exceedingly difficult task, intense research focus must remain to decipher disease mechanisms so those that do become infected can be treated.

Critical to both understanding and treating the broad spectrum of disease sequelae caused by SARS-CoV-2 is the development of animal models that faithfully recapitulate COVID-19. Animal models allow timed infection and

ethanasia along with extensive sample collection that are not possible during human infections. Rhesus macaques (RhM), cynomolgus macaques (CyM), African green monkeys (AGM), baboons and marmosets have all been used to achieve this goal [14–17,75,76]. To date, none of these models consistently recapitulate severe COVID-19 disease but some data suggest AGM may exhibit more severe disease than the others [14,15]. When infected with simian immunodeficiency virus (SIV), pigtail macaques (PTM) exhibit rapid and severe disease relative to RhM and CyM, including rapid destruction of the CD4 immune compartment, severe gastrointestinal disease, and complications related to coagulopathy [21–23,77–79]. Many of these disease features are also relevant to severe COVID-19 disease [56–61,80–82]. PTM have been successfully used to model other viral infections and in some cases show severe disease. Compared to other macaque models, the PTM pregnancy model of Zika infection is more likely to show congenital disease with implications of fetal brain injury similar to that seen in humans [83]. PTM are also susceptible to influenza infection and show a strong persistent immune response to infection [84]. A recent report demonstrated that a related species of pigtail macaques (*Macaca leonine*) showed an abbreviated period of SARS-CoV-2 viral replication but possibly more severe disease than RhM [85]. Thus, PTM may be a reasonable model for severe disease and used to test novel therapeutics and vaccines to prevent disease. Until recently, the northern PTM (*Macaca leonina*), mentioned above, was considered a subspecies of the southern PTM (*Macaca nemestrina*), the species used in our study. They are now considered two distinct species.

Unfortunately, PTM in general are not as widely used for biomedical research as are other species such as RhM, so we cannot be certain if our data are representative of northern PTM or any other related species.

We infected a small cohort of PTM with SARS-CoV-2 through a combination of intratracheal and intranasal instillation. Animals were tracked for viral replication in multiple sites, for immune dynamics in blood and bronchoalveolar lavage cells, and for innate and other markers of disease in blood and tissues. We identified a range of disease severity, even in our small cohort, with one animal euthanized at six days post infection showing more severe pulmonary lesions than the rest. Interestingly, multiple early indicators that are consistent with a more severe disease course in humans, were also detected in this animal, including: viral titer, an elevated neutrophil to lymphocyte ratio, elevated kynurenine to tryptophan ratio, and elevated serum inflammatory cytokines. Our findings suggest that these factors correlate with and may predict disease severity. Hyperproduction of pro-inflammatory cytokines such as IL-1 β , IL-6, IL-12, IFN- γ and TNF- α have been linked to the pathogenesis of tissue injury observed in SARS-CoV-2 induced pneumonia seen in humans [86,87]. The exact role that these cytokines play in disease pathology is not fully understood therefore expanded cohort sizes of PTM that include both males and females as well as aged animals may reveal answers not only to this question but may also uncover additional clinical manifestations.

Viral dynamics were similar in PTM as we have reported in RhM [14,15]. Viral RNA, including subgenomic RNA, was consistently detected throughout the first several days of infection. We detected persistent viral titers at multiple sites in some of the animals throughout the course of the study. These data confirm PTM as a robust model of viral infection and replication, similar to RhM, and suggest this model may be used to study novel virus host relationships.

COVID-19 disease is commonly characterized by pulmonary infiltration of inflammatory immune cells [41]. Innate cells, particularly monocytes, are considered important mediators of disease progression [42]. Although infiltrating monocytes were identified in our PTM, T cells were a more dominant cellular infiltrate into lungs as detected in bronchoalveolar lavage sampling. Specifically, we identified a unique population of CD4⁺/CD8⁺ double positive T cells (DP T cells) that upregulated inflammatory cytokines such as TNF- α as well as Granzyme B over the course of infection. DP T cells with cytotoxic capacity have been identified in human and animal studies of influenza [88,89], human studies of HIV [90,91], as well as animal studies of tuberculosis [48] and SHIV [92]. Traditionally, these cells would be predicted to be major histocompatibility complex class II (MHC-II) restricted CD4 T cells that upregulate CD8 upon activation. Pulmonary infiltrating CD4 T cells with cytotoxic capacity, as measured by Granzyme B, identified in our PTM and recently in humans with severe COVID-19 [25], are a unique and possibly understudied aspect of the disease.

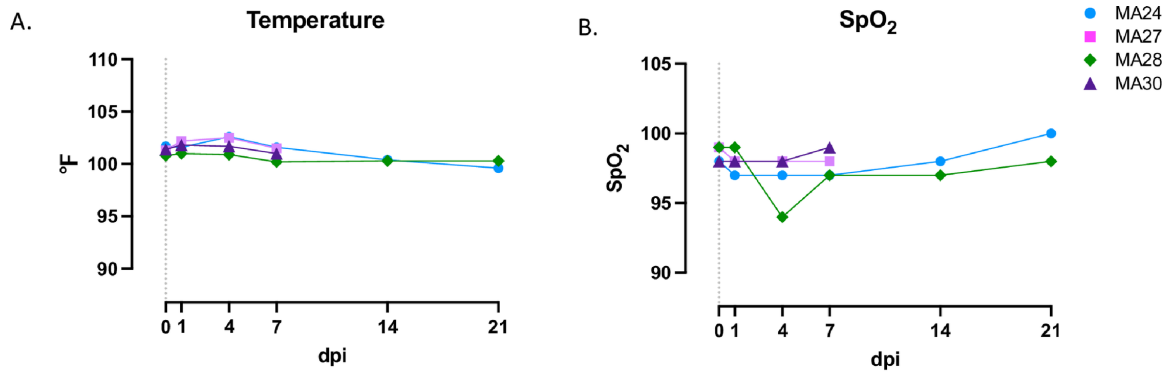
We also identified relatively high magnitude CD4 T cell responses against the virus that localized to the lung 21 days after viral infection. CD8 T cells against the virus were also noted, but at lower frequencies. Many studies have reported antiviral T cells in SARS-CoV-2 convalescent humans, with a relative predominance of CD4 T cells, however these responses are nearly always noted in blood [49,50]. Thus, our data provide a valuable addition to the data from humans and may suggest important roles for antiviral CD4 T cells in pulmonary sites.

RhM have proved invaluable for testing vaccines and therapeutics [19] due to the robust viral replication and mild but consistent disease seen in this species. However, RhM and other NHP species tested to date do not recapitulate the most severe form of the disease. Based on disease severity with other viruses, we proposed that PTM may provide such a model. Here, we found that PTM largely recapitulate the level of disease severity found in RhM. However, we also found that PTM do demonstrate some important aspects of disease, including the pulmonary infiltration of specific immune cells that may be important in COVID-19 disease. Thus, this species may be complementary to the RhM model for vaccine testing but may also prove uniquely useful for testing certain immune modulating therapeutics.

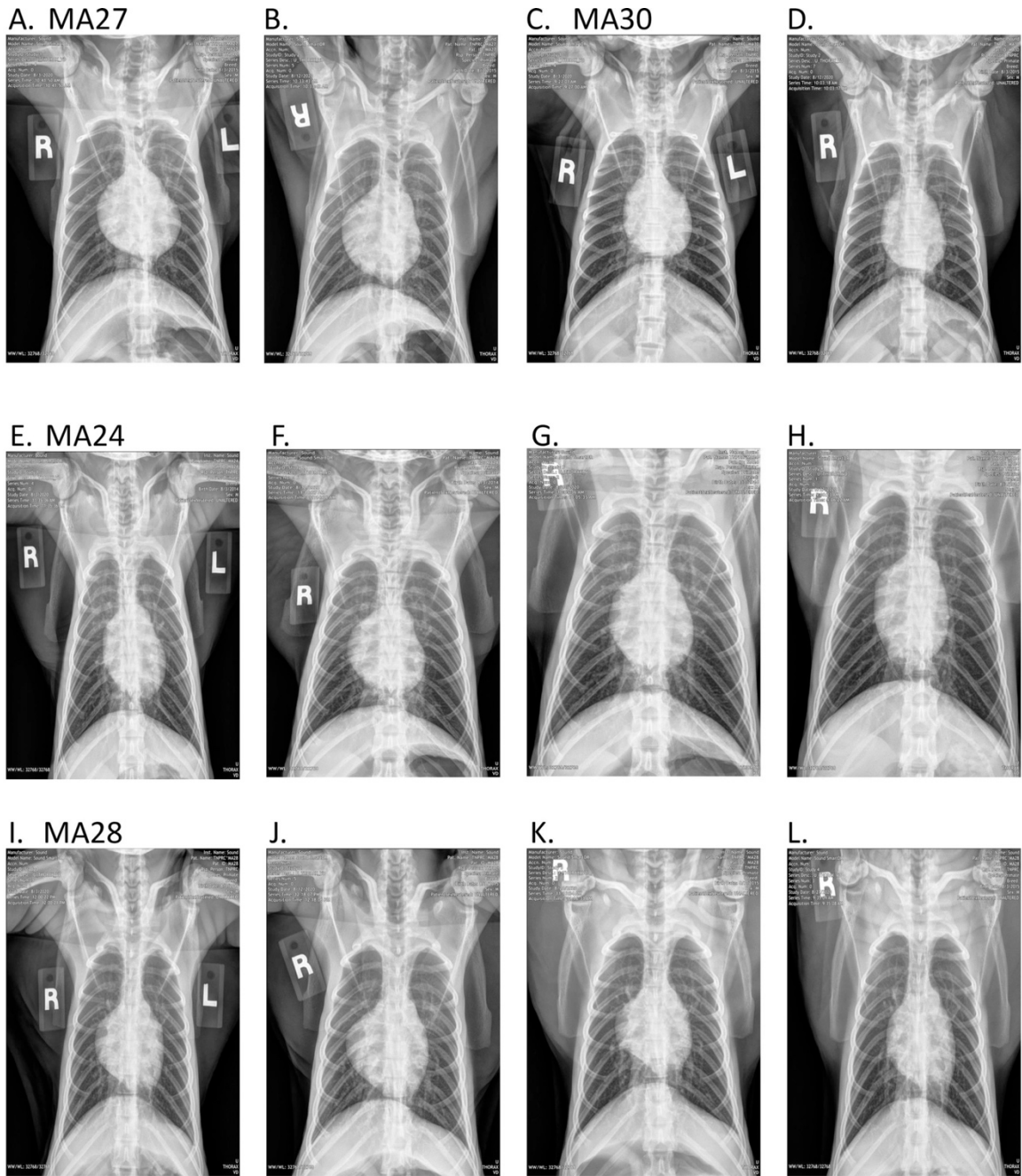
Taken together, our data define a new animal model for COVID-19. PTM show robust viral replication, SARS-CoV-2 associated pneumonia, and complex innate and adaptive immune responses that may shed light on mechanisms of COVID-19 disease. This model may prove valuable for testing novel

immunomodulatory therapeutics and vaccines, including those that modulate pulmonary infiltration of T cells and other inflammatory cells. Finally, our data confirmed COVID-19 associated inflammation was not always resolved 21-dpi, despite no evidence of continued viral replication at that time point. Thus, this model may also be valuable for the study of long-term chronic effects associated with SARS-CoV-2 infection.

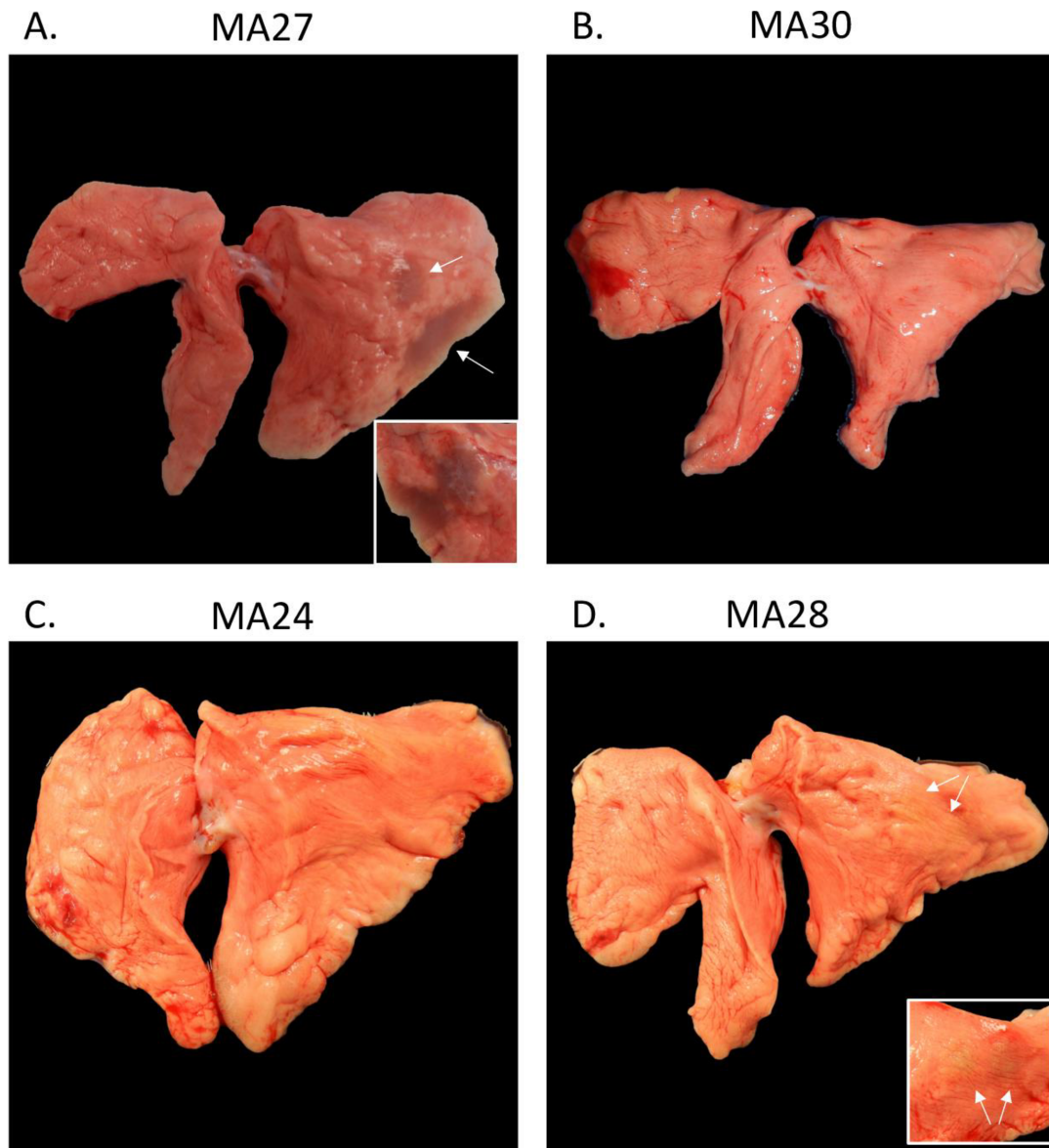
Supplemental Figures



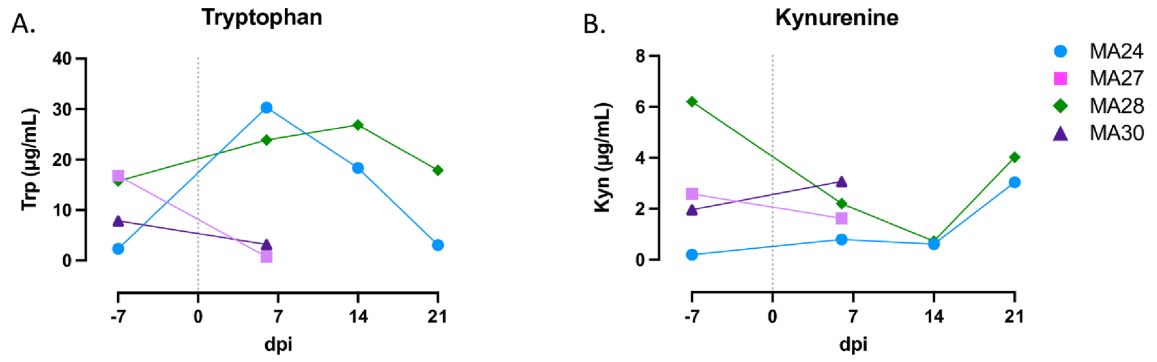
Supplemental Figure 1.1. Body temperature and oxygen saturation in SARS-CoV-2 infected pigtail macaques. **A.** Body temperature measurements before and 1-, 4-, 6-, 14-, and 21-days post (dpi) SARS-CoV-2 infection. **B.** Saturation of peripheral oxygen (SpO₂) levels before and 1-, 4-, 6-, 14-, and 21-dpi. Baseline (Day of infection): n=4, Day 4: n=4, Day 6: n=4, Day 14: n=2, Day 21: n=2



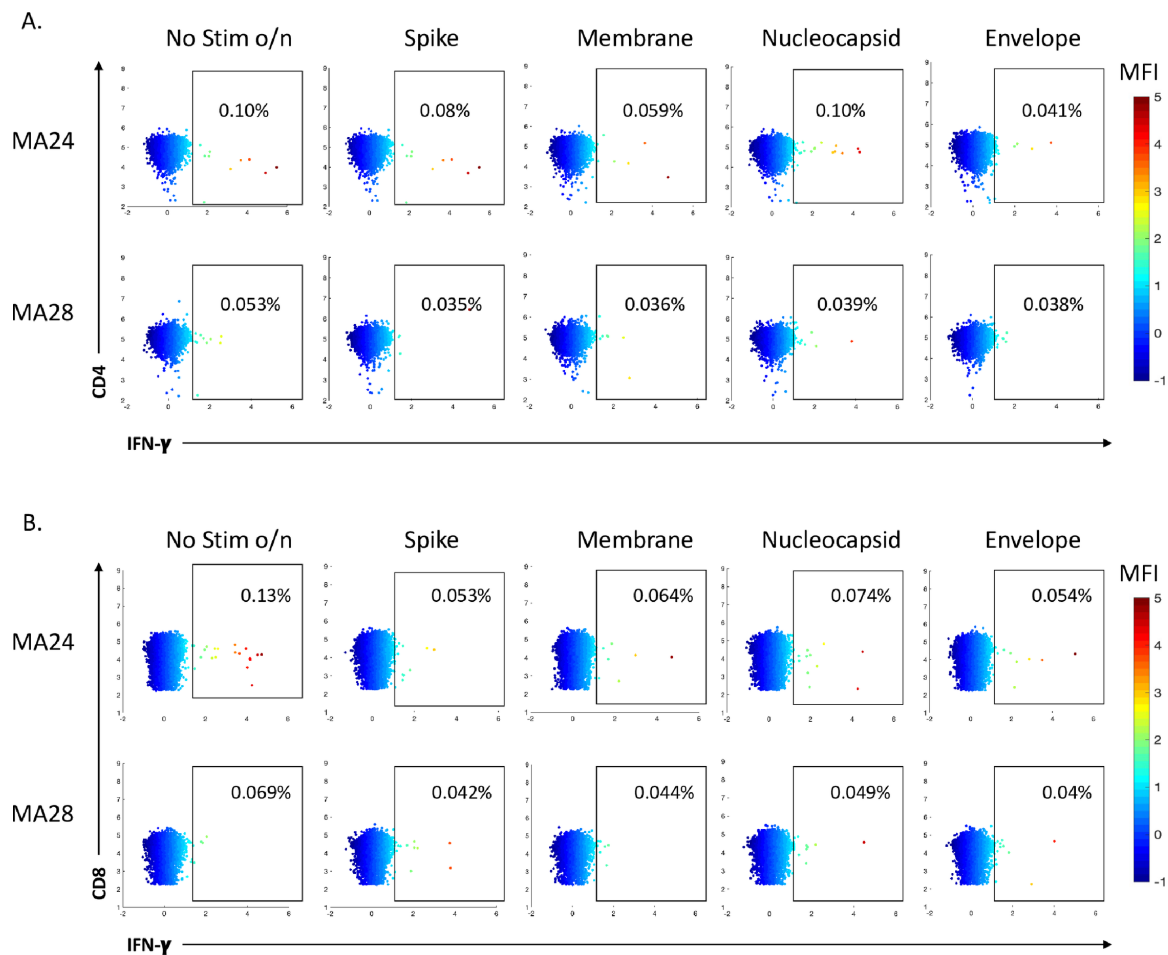
Supplemental Figure 1.2. Radiographs of pigtail macaques (PTM) challenged with SARS-CoV-2. MA27 baseline (A) and 6-days post infection (dpi) (B). MA30 at baseline (C) and 6-dpi (D). MA24 at baseline (E), 6-dpi (F), 14-dpi (G) and 21-dpi (H). MA28 at baseline (I), 6-dpi (J), 14-dpi (K) and 21-dpi (L). Baseline for all four PTM was established 3-days prior to infection.



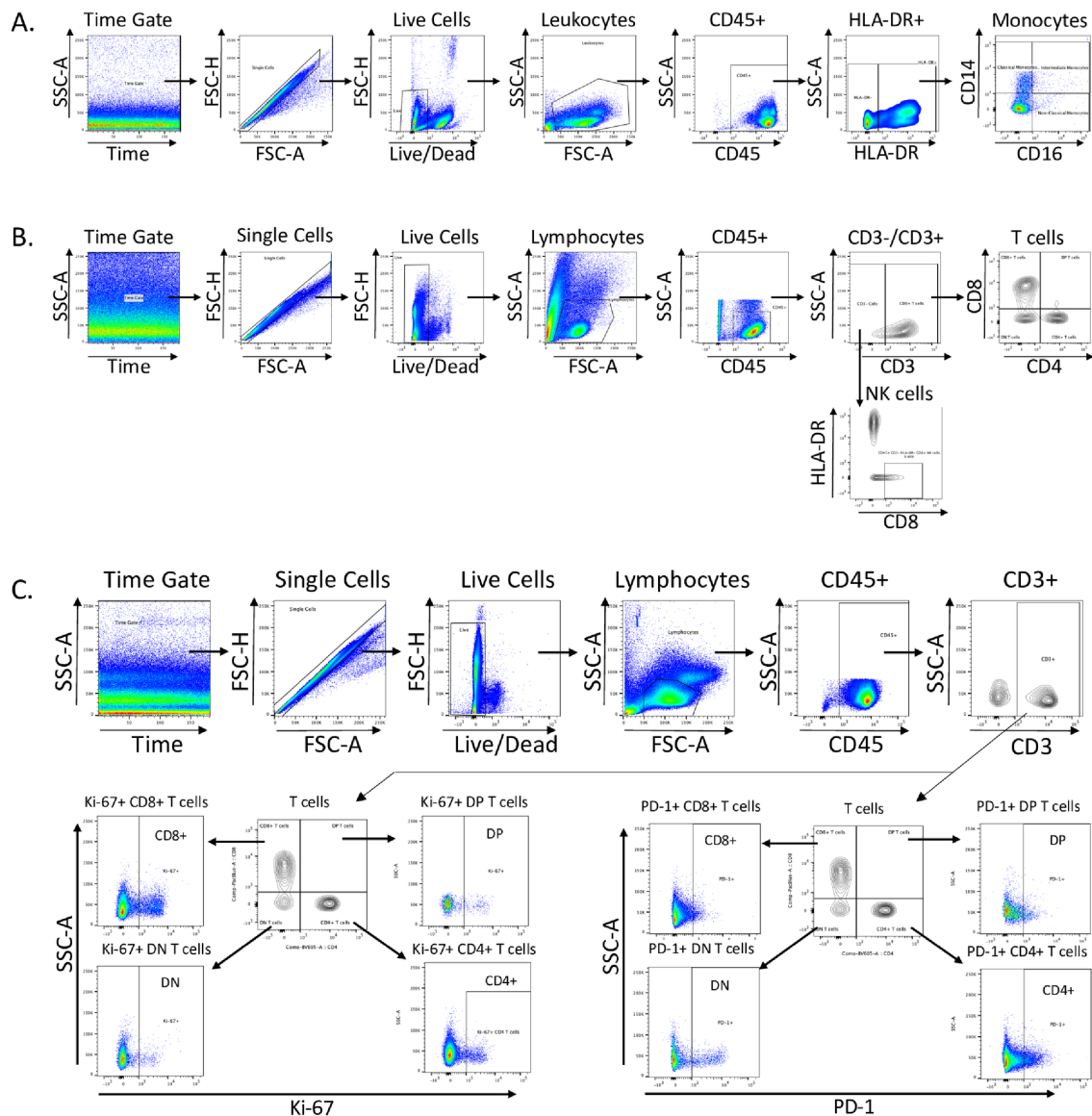
Supplemental Figure 1.3. Gross pathological pulmonary pathology in SARS-CoV-2 infected pigtail macaques (PTM). A-D. Gross pulmonary pathology at 6- (**A** and **B**) and 21-days post infection (dpi, **C** and **D**). **A.** MA27, the left caudal lung lobe has multifocal tan-plum areas of consolidation (arrows). Inset: the consolidation extends to the diaphragmatic and medial surface of the left caudal lung. There is no evidence of gross pathology in MA30 (**B**) or MA24 (**C**). **D.** MA28, the laterodorsal aspect of the left caudal lobe contains two small, flat tan foci (arrows). Inset: closer view of tan foci.



Supplemental Figure 1.4. Changes in IDO activity post SARS-CoV-2 infection. (A) Tryptophan (Trp) and (B) Kynurenine (Kyn) levels in plasma before and after SARS-CoV-2 infection. Day 0=day of infection, Baseline: n=4, Day 7: n=4, Day 14: n=2, Day 21: n=2. Dpi=days post infection.



Supplemental Figure 1.5. SARS-CoV-2 peptide-specific T cell response in the blood 21 days post-infection. Two animals shown (MA24 and MA28 euthanized at 21-dpi). Flow cytometry dot plots showing CD4+ (A) and CD8+ (B) T cell Interferon- γ (IFN- γ) response to overnight SARS-CoV-2 peptide (spike, membrane, nucleocapsid and envelope) stimulation. No stim o/n=cells incubated overnight without stimulation. Heatmap represents arcsin transformed MFI values.



Supplemental Figure 1.6. Gating strategies. **A.** Example gating of Monocytes: Time (SSC-A vs. Time), Single cells (FSC-H vs. FSC-A), Live cells (FSC-H vs live/dead), Leukocytes (SSC-A vs. FSC-A), CD45+ Leukocytes (SSC-A vs. CD45), HLA-DR+ (SSC-A vs. HLA-DR), Monocytes (CD14 vs. CD16): Classical Monocytes: CD14+ CD16-, Intermediate Monocytes: CD14+ CD16+, Non-classical Monocytes: CD14-CD16+. **B.** Example gating of T lymphocytes and Natural killer (NK) cells: Time (SSC-A vs. Time), Single cells (FSC-H vs. FSC-A), Live cells (FSC-H vs. live/dead), Lymphocytes (SSC-A vs. FSC-A), CD45+ Lymphocytes (SSC-A vs. CD45), CD3[±] (SSC-A vs. CD3), CD3⁺ T cells (CD8 vs. CD4) T helper: CD4⁺CD8⁻, Cytotoxic T: CD8⁺CD4⁻, Double Positive (DP): CD4⁺CD8⁺, Double negative (DN): CD4⁻CD8⁻, NK cells: CD3⁺HLA-DR^{low}CD8⁺ (HLA-DR vs. CD8). **C.** Example gating of PD-1⁺ and Ki-67⁺ T cell subsets.

Supplemental Table 1. Clinical, Blood and Necropsy Observations		Blood Cell Counts		Blood Chemistry		Gross Findings		Necropsy Observations		Other Notes		
Macaque ID	Sex	Age (yr)	Clinical Observations	Neutrophils (4)	Lymphocytes (1)	Eosinophils (1)	Basophils (1)	Monocytes (1)	CRP (1)	Gross Findings	Necropsy Observations	Other Notes
MA27	M	5.07	Decreased appetite (5) Soft stool (5) Necropsy 4 dpi	Neutrophilia (4), Monocytosis (4) Lymphocytopenia (1), Eosinopenia (1), Basopenia (1) Neu/Lym ratio 6.35 (1), 4.26 (4)						Mid subacute pneumonia, lymphoid hyperplasia	Lung lesions in caudal left lobe coincide with gross lesions. Lesions are characterized by mild alveolar epithelial hyperplasia and minimal lymphocytic infiltration. Lymphoid hyperplasia noted in the spleen and all lymph nodes. Findings are compatible with lesions in SARS-CoV-2 inoculated rhesus monkey.	Lung: caudal left lobe contains two red star regions 1 and 2 cm on the lateral aspect and a 3x4 cm zone on the medial aspect. Lymph nodes: Enlarged 3x normal
MA30	M	5.67	Mild cough (2,3) Decreased appetite (1, 5, 9) Necropsy 4 dpi	No baseline to compare					2x fold P, in CRP (1)	Minimal focal subacute pneumonia and lymphoid hyperplasia	Lung lesions are scattered in multiple lobes but are most severe in the caudal left lobe. Lesions consist of extensive alveolar-epithelial hyperplasia with lymphocytic infiltration. Lymphoid hyperplasia is noted in the lung, spleen and all lymph nodes. Findings are compatible with lesions in SARS-CoV-2 inoculated rhesus monkey.	Lung: caudal left lobe contains a 1 cm gray/red zone on the anterior medial aspect. Lymph nodes: Enlarged 3x normal
MA24	M	5.67	Mild cough (1), Slight increased effort breathing (20) Decreased appetite (3, 5, 7, 15, 16) Soft stool (4, 5, 8, 9, 16, 17, 20) Necropsy 21 dpi	Neutrophilia (4, 21), Eosinophilia (4, 21), Basophilia (4, 14, 21) Lymphocytopenia (1), Monocytopenia (14) Neu/Lym ratio: 4.09 (1), 3.15 (4)					8 fold P, in CRP (1)	No significant gross abnormalities	Mild multifocal interstitial pneumonia with rare areas of pneumocyte hyperplasia and septal thickening. Findings could be compatible with a resolving viral pneumonia. Lymphoid hyperplasia was observed in the bronchial lymph node and spleen. Proximal large intestine showed chronic inflammation compatible with chronic bacterial colitis.	Lung: No gross lung lesions.
MA28	M	5.81	Slight increased effort breathing (8, 22, 24, 19) Decreased appetite (7, 9, 15, 16) Necropsy 21 dpi	Neutrophilia (21), basophilia (21) Lymphocytopenia (4, 6), Monocytopenia (4, 14), Eosinopenia (4, 6)						Two small areas of consolidation in the left caudal lobe with interstitial and intralobular lymph node enlargement	Mild interstitial pulmonary inflammation with minimal pneumocyte hyperplasia and rare fibrosis. Granulomatous inflammation within the left caudal lung, along with foreign debris, indicates subclinical aspiration pneumonia. The interstitial pneumonia is compatible with SARS-CoV-2 infection, but the character and severity suggest a resolving infectious pneumonia. No evidence of thrombosis or vasculopathy was noted. Upper respiratory system also exhibited chronic inflammation that was a bit more acute than the inflammation observed in the caudal respiratory tract.	Lung: left caudal lung lobe contains 2 round, flat, pale tan foci ~1 cm in size on the lobular surface at the level of the termination of the bronchial tree. Lymph nodes: Mesenteric and Mediastinal 2x normal

Reference

1. Wosley C, Boresech V, Prahar AN, Ajana RN, Deer DJ, Dobos MS, et al. Establishment of an African green monkey model for COVID-19 and protection against re-infection. *Nat Immunol*. 2021;22(11):96-98.

Supplemental Table 1.1. Clinical, blood and necropsy observations in pigtail macaques (PTM) challenged with SARS-CoV-2 (n=4). Values in parenthesis represent days post SARS-CoV-2 infection. Neutrophilia, eosinophilia, basophilia, and monocytosis defined as ≥ 2 -fold increase over baseline¹. Lymphocytopenia, monocytopenia, eosinopenia, basopenia defined as a 35% reduction from baseline¹. CRP: C-reactive protein

Supplemental Table 2. Monocyte Panel						
Fluorochrome	Antigen	Volume (uL)/Test	Clone	Catalog#	Lot#	Company
FITC	IL-6*	5	MQ2-6A3	554696	6168973	BD Pharmingen
PCP-Cy5.5	CD169	5	7-239	346020	B309159	BioLegend
AL647	IL-1B*	5	JK1B-1	508208	B274564	BioLegend
AL700	TNF-a*	5	MAb11	502928	B221571	BioLegend
APC-Cy7	HLA-DR	5	L243	307618	B295253	BioLegend
PacBlue	CD66	2	TET2	130-119-851	1320070484	Miltenyi Biotec
BV510	Live/Dead	0.5	Fixable Aqua Dead Cell Stain Kit	L34957		Invitrogen
BV605	CD45	5	D058-1283	564098	9051992	BD Horizon
BV650	CD11c	5	S-HCL-3	744437	0203626	BD OptiBuild
BV711	CD16	5	3G8	302044	B296475	BioLegend
BV786	CD103	5	Ber-ACT8	350230	B274642	BioLegend
PE-CF594	IL-8*	5	G265-8	563531	0219387	BD Horizon
PE-Cy7	CD68*	5	Y1/82A	565595	0079803	BD Pharmingen
BUV395	CD123	5	7G3	564195	9337379	BD Horizon
BUV496	CD206	5	19.2	741173	0261803	BD OptiBuild
BUV737	CD14	5	M5E2	612764	0140605	BD Horizon

Supplemental Table 1.2. Monocyte Flow Cytometry Panel.

Supplemental Table 3. Phenotype Panel						
Fluorochrome	Antigen	Volume (uL)/Test	Clone	Catalog#	Lot#	Company
FITC	CD21	5	B-Ly4	561372	0149866	BD Pharmingen
PCP-Cy5.5	CD169	5	7-239	346020	B309159	BioLegend
APC	CD11c	5	S-HCL-3	340714	70397	BD Pharmingen
AL700	Ki67*	5	B56	561277	9261927	BD Pharmingen
APC-Cy7	CD20	5	L27	561277	8320624	BD Bioscience
PacBlue	CD8	5	SK1	344718	B280004	BioLegend
BV510	Live/Dead	0.5	Fixable Aqua Dead Cell Stain Kit	L34957		Invitrogen
BV605	CD4	5	OKT4	317438	B297647	BioLegend
BV650	CD3	5	SP34-2	563916	D163859	BD Horizon
BV711	CD16	5	3G8	302044	B296475	BioLegend
BV785	CD27	5	O323	302832	B264783	BioLegend
PE	FasL	5	NOK-1	306407	B269886	BioLegend
PE-CF594	HLA-DR	5	L243	307654	B320176	BioLegend
PE-Cy5	CD95	5	DX2	15-0959-42	2252537	Invitrogen
PE-Cy7	PD-1 (CD279)	5	J105	25-2799-42	228650	Invitrogen
BUV395	CD45	5	D058-1283	564099	0192257	BD Horizon
BUV496	CD28	5	CD28.2	741168	0203628	BD OptiBuild
BUV737	CD14	5	M5E2	612764	0140605	BD Horizon

* Intracellular

1.S3 Table. Phenotype Flow Cytometry Panel.

Supplemental Table 4. T cell Panel						
Fluorochrome	Antigen	Volume (uL)/Test	Clone	Catalog#	Lot#	Company
FITC	MIP-1b*	20	D21-1351	560565	348912	BD Parmingen
PCP-Cy5.5	IL-2*	5	MQ1-17H12	560708	8142599	BD Parmingen
AL647	IFN-g*	5	4S-B3	502516	B228928	BioLegend
AL700	TNF-a*	5	MAB11	557996	8179967	BD Parmingen
APC-Cy7	HLA-DR	5	L243	307618	B295253	BioLegend
PacBlue	CD8	5	SK1	344718	B280004	BioLegend
BV510	Live/Dead	0.5	Fixable Aqua Dead Cell Stain Kit	L34957		Invitrogen
BV605	CD4	5	OKT4	317438	B297647	BioLegend
BV650	CD3	5	SP34-2	563916	D163859	BD Horizon
BV711	CD95	5	DX2	563132	004458	BD Horizon
PE	IL10*	5	JES3-9D7	501404	B273796	BioLegend
PE-CF594	GZB*	5	GB11	562462	0050626	BD Horizon
PE-Cy7	IL-4*	5	MP4-25D2	500824	B293168	BioLegend
BUV395	CD45	5	D058-1283	564099	0101778	BD Horizon
BUV496	CD28	5	CD28.2	741168	0203628	BD OptiBuild

* Intracellular

1.S4 Table. T cell Flow Cytometry Panel.

Supplemental Table 5. T cell SARS-CoV-2 Peptide, PMA/Ionomycin Stimulation				
Stimulant	Volume (uL)/mL	Catalog#	Lot#	Company
Cell Stimulation Cocktail	1	423301	B295704	BioLegend
SARS-CoV-2 Spike Peptide	10	NR-52402		BEI Resources, NIAID, NIH
SARS-CoV-2 Membrane Peptide	5	NR-53822		BEI Resources, NIAID, NIH
SARS-CoV-2 Nucleocapsid Peptide	5	NR-52419		BEI Resources, NIAID, NIH
SARS-CoV-2 Envelope Peptide	5	NR-53822		BEI Resources, NIAID, NIH
Brefeldin-A	1	420601	B211242	BioLegend

1.S5 Table. T cell SARS-CoV-2 Peptide, PMA/Ionomycin Stimulation

Supplemental Table 6. Immunohistochemistry						
Primary Antibody	Species	Company	Catalog#	Dilution	Secondary Antibody	
					Species	Fluorochrome
SARS	Guinea Pig	BEI	NR-10361	1:1000	Goat anti-guinea pig	Alexa Fluor488
IBA1	Rabbit	Wako	019-19741	1:50	Goat anti-Rabbit	Alexa Fluor568
CD3	Mouse IgG1	Agilent	M7254	1:20	Goat anti-MS IgG1	Alexa Fluor568
CD4	Rabbit	Abcam	Ab133616	1:10	Goat anti-Rabbit	Alexa Fluor488
Granzyme	Mouse IgG2a	Agilent	M7235	1:50	Permanent Red (Agilent K0640)	
Dapi		Invitrogen	D1306	1:20,000		

1.S6 Table. Immunohistochemistry Reagent Panel.

Chapter 2

The Impact of SIV-Induced Immunodeficiency on Clinical Manifestation, Immune Response, and Viral Dynamics in SARS-CoV-2 Coinfection

Alexandra Melton^{1,2}, Lori A Rowe¹, Toni Penney¹, Clara Krzykwa¹, Kelly Goff¹, Sarah Scheuermann¹, Hunter J Melton³, Kelsey Williams¹, Nadia Golden¹, Kristyn Moore Green¹, Brandon Smith¹, Kasi Russell-Lodrigue^{1,4}, Jason P Dufour^{1,4}, Lara A Doyle-Meyers^{1,4}, Faith Schiro¹, Pyone P Aye^{1,4}, Jeffery D Lifson⁵, Brandon J Beddingfield^{1,9}, Robert V Blair¹, Rudolf P Bohm^{1,4,6}, Jay K Kolls^{7,8}, Jay Rappaport^{1,9}, James A Hoxie¹⁰, Nicholas J Maness^{1,9*}

¹Tulane National Primate Research Center, Covington, Louisiana

²Biomedical Science Training Program, Tulane University School of Medicine, New Orleans, Louisiana

³Florida State University, Department of Statistics, Tallahassee, Florida

⁴Department of Medicine, Tulane University School of Medicine, New Orleans, Louisiana

⁵AIDS and Cancer Viruses Program, Leidos Biomedical Research, Inc., Frederick National Laboratory, Frederick, Maryland, United States of America

⁶Present address: Oregon National Primate Research Center, Oregon Health and Science University, Beaverton, Oregon

⁷Departments of Medicine and Pediatrics, Center for Translational Research in Infection and Inflammation, Tulane University School of Medicine, New Orleans, LA 70112, USA.

⁸Department of Pulmonary Critical Care and Environmental Medicine, Tulane University School of Medicine, New Orleans, LA 70112, USA.

⁹Department of Microbiology and Immunology, Tulane University School of Medicine, New Orleans, Louisiana

¹⁰Perelman School of Medicine, University of Pennsylvania, Philadelphia, Pennsylvania

*Whom to address correspondence

Abstract

Persistent and uncontrolled SARS-CoV-2 replication in immunocompromised individuals has been observed and may be a contributing source of novel viral variants that continue to drive the pandemic. Importantly, the effects of immunodeficiency associated with chronic HIV infection on COVID-19 disease and viral persistence have not been directly addressed in a controlled setting. Here we conducted a small pilot study wherein two pigtail macaques (PTM) chronically infected with SIVmac239 were exposed to SARS-CoV-2 and monitored for six weeks for clinical disease, viral replication, and viral evolution, and compared to our previously published cohort of SIV-naïve PTM infected with

SARS-CoV-2. At the time of SARS-CoV-2 infection, one PTM had minimal to no detectable CD4+ T cells in gut, blood, or bronchoalveolar lavage (BAL), while the other PTM harbored a small population of CD4+ T cells in all compartments. Clinical signs of severe COVID-19 were not observed in either PTM. Neither SIV-infected PTM mounted detectable anti-SARS-CoV-2 T cell responses in blood or BAL, nor anti-SARS-CoV-2 neutralizing antibodies. Interestingly, despite the diminished cellular and humoral immune responses, SARS-CoV-2 viral kinetics and evolution were indistinguishable from SIV-naïve PTM in all sampled mucosal sites (nasal, oral, and rectal), with clearance of virus by 3-4 weeks post infection. Our findings demonstrate that SIV-induced immunodeficiency significantly impacted immune responses to SARS-CoV-2 but did not alter disease progression, viral kinetics or evolution in the PTM model. Therefore, SIV-induced immunodeficiency alone may not be sufficient to drive the emergence of novel viral variants.

Introduction

The global outbreak of Coronavirus disease 2019 (COVID-19), caused by the highly infectious severe acute respiratory syndrome coronavirus 2 (SARS-CoV-2), has posed a significant and urgent public health challenge. First identified in Wuhan, China, in December 2019, the outbreak quickly spread to other countries across the globe. As of September 2023, the World Health Organization (WHO) has reported over 770 million global cases and nearly 7 million deaths [1]. While the majority of cases are asymptomatic or exhibit only

mild symptoms, some individuals develop severe complications such as pneumonia, systemic inflammation, and coagulopathy, which can lead to organ failure, shock, and death [2–7]. Certain factors, such as a compromised immune system, advanced age, and comorbidities, including cardiovascular disease, diabetes, and obesity, increase the risk of developing severe disease [8,9].

People living with HIV (PLWH) face an increased risk of several of these conditions, including a compromised immune system and a higher prevalence of cardiovascular disease. Additionally, PLWH have increased susceptibility to opportunistic infections such as pneumocystis pneumonia, which is the most common respiratory infection in patients with AIDS [10–12]. PLWH also experience elevated levels of inflammation, which significantly contributes to the development of severe respiratory disease, thromboembolisms, and other adverse outcomes associated with COVID-19 [13–15]. This raises concerns about the impact of HIV on the severity and persistence of SARS-CoV-2 infections. Studies examining whether HIV increases the risk of severe COVID-19 have yielded conflicting results. Initial studies indicated that PLWH had similar or even better outcomes [16–18] compared to those without HIV. However, larger population-based studies suggest that PLWH experience higher hospitalization rates and COVID-19-related deaths compared to the general population [19–23]. More recent research has suggested that unsuppressed viral loads or low CD4+ T cell counts are linked to suboptimal adaptive immune responses to SARS-CoV-2, affecting both T cell and humoral responses [24,25].

In addition to the concern of increased severity, HIV-associated immunodeficiency could potentially facilitate SARS-CoV-2 persistence and evolution, leading to the emergence of new variants of concern. A recent study by Karim et al. highlighted a case of an individual with advanced HIV who exhibited prolonged SARS-CoV-2 shedding with high viral loads and the emergence of multiple viral mutations [26]. While retrospective studies have explored the effects of HIV status on COVID-19 incidence and severity, controlled studies are lacking. To address these gaps, we utilized a nonhuman primate model of HIV/AIDS and conducted a pilot study involving two pigtail macaques (PTM) chronically infected with SIVmac239. We exposed them to SARS-CoV-2 and monitored the animals for six weeks for clinical disease, viral replication, and viral evolution. Additionally, we performed detailed analyses of adaptive immune responses, utilizing flow cytometry and antibody binding and neutralization assays following SARS-CoV-2 infection. We compared our findings with data from our previously published cohort of SIV-naïve, SARS-CoV-2-infected PTMs [27]. Despite the marked decrease in CD4⁺ T cells in the SIV⁺ animals prior to exposure to SARS-CoV-2, we found that disease progression, viral persistence and evolution of SARS-CoV-2 were comparable to the control group. Overall, our findings suggest that SIV-induced immunodeficiency alters the immune response to SARS-CoV-2 infection, leading to impaired cellular and humoral immunity. However, this impairment does not significantly alter the course of infection. These findings contribute to a deeper understanding of the interplay between immunodeficiency and SARS-CoV-2 infection and propose a

valuable model for evaluating vaccine and therapeutic strategies for immunocompromised individuals.

Materials and Methods

Research Animals

Two female pigtail macaques (PTM, Table 1) were inoculated intravenously with SIVmac239 (100 TCID₅₀), followed by intranasal (0.5 mL per nares) and intratracheal (1 mL) administration of SARS-CoV-2 (1.1x10⁶ PFU/mL, USA WA1/2020) approximately one year later. Animals were monitored for six weeks following SARS-CoV-2 inoculation. Blood, bronchoalveolar lavage (BAL), and endoscopic gut biopsies were collected before and after SIVmac239 infection. Sampling pre- and post-SARS-CoV-2 infection included blood, BAL, and mucosal swabs (nasal, pharyngeal, and rectal). Physical examinations were performed throughout the course of the study. At the end of the study, complete postmortem examinations were performed with collection and histopathologic evaluation of 43 different tissues including all major organs and sections from each major lung lobe.

Animal ID	Sex	Age (y)	Weight (kg) at time of SIV inoculation	Weight (kg) at time of SARS-CoV-2 inoculation
NV18	Female	3.82	4.45	4.45
NV19	Female	4.67	5.76	5.85

Table 2.1 Cohort of PTM used in this study.

Ethics Statement

Pigtail macaques used in this study were purpose bred at Johns Hopkins University and moved to Tulane National Primate Research Center (TNPRC) for these experiments. Macaques were housed in compliance with the NRC Guide for the Care and Use of Laboratory Animals and the Animal Welfare Act. Animal experiments were approved by the Institutional Animal Care and Use Committee of Tulane University. The TNPRC is fully accredited by AAALAC International (Association for the Assessment and Accreditation of Laboratory Animal Care), Animal Welfare Assurance No. A3180-01. Animals were socially housed indoors in climate-controlled conditions with a 12/12-light/dark cycle. All the animals on this study were monitored twice daily to ensure their welfare. Any abnormalities, including those of appetite, stool, behavior, were recorded and reported to a veterinarian. The animals were fed commercially prepared monkey chow twice daily. Supplemental foods were provided in the form of fruit, vegetables, and foraging treats as part of the TNPRC environmental enrichment program. Water was available at all times through an automatic watering system. The TNPRC environmental enrichment program is reviewed and approved by the IACUC semi-annually. Veterinarians at the TNPRC Division of Veterinary Medicine have established procedures to minimize pain and distress through several means. Monkeys were anesthetized with ketamine-HCl (10 mg/kg) or tiletamine/zolazepam (3-8 mg/kg) prior to all procedures. Preemptive and post procedural analgesia (buprenorphine 0.03 mg/kg IM or buprenorphine sustained-release 0.02 mg/kg SQ) was required for procedures that would likely cause

more than momentary pain or distress in humans undergoing the same procedures. The animals were euthanized at the end of the study using methods consistent with recommendations of the American Veterinary Medical Association (AVMA) Panel on euthanasia and per the recommendations of the IACUC. Specifically, the animals were anesthetized with tiletamine/zolazepam (8 mg/kg IM) and given buprenorphine (0.01 mg/kg IM) followed by an overdose of pentobarbital sodium. Death was confirmed by absence of respiration, cessation of heartbeat, pupillary dilation, and lack of corneal reflex. The TNPRC policy for early euthanasia/humane endpoint was included in the protocol in case those circumstances arose.

Isolation and Quantification of SIVmac239

Plasma SIVmac239 viral RNA (vRNA) extraction and quantification were performed essentially as previously described [28].

Isolation of SARS-CoV-2 RNA

SARS-CoV-2 vRNA was isolated from BAL supernatant (200 μ L) and mucosal swabs (nasal, pharyngeal, and rectal) using the Zymo Quick-RNA Viral Kit (Zymo Research, USA) as previously described [27,29]. Mucosal swabs, collected in 200 μ L DNA/RNA Shield (Zymo Research, USA), were placed directly into the Zymo spin column for centrifugation to ensure complete elution of the entire volume. The Roche high pure viral RNA kit (Roche, Switzerland) was used to isolate vRNA from plasma (200 μ L) per the manufacturer's protocol. After

isolation, samples were eluted in 50 µL DNase/RNase-free water (BAL and mucosal swabs) or Roche elution buffer (plasma) and stored at -80°C until viral load quantification.

Quantification of SARS-CoV-2 RNA

The quantification of SARS-CoV-2 RNA was performed according to methods previously described [27,29]. Genomic vRNA was quantified using CDC N1 primers/probe to determine the total amount of vRNA present. Additionally, primers/probe specific to nucleocapsid subgenomic (SGM) vRNA were utilized to estimate the quantity of replicating virus.

Isolation of Cells

SepMate-50 Isolation tubes (Stem Cell Technologies, Vancouver, Canada) were used according to the manufacturer's protocol to isolate peripheral blood mononuclear cells (PBMCs) from whole blood. BAL samples were centrifuged at 1800 rpm at room temperature for 5 minutes. BAL supernatant was collected and stored at -80°C. BAL cell pellets were washed with PBS supplemented with 2% FBS. Tissue-specific lymphocytes were isolated from endoscopic duodenal pinches collected during the SIV portion of the study. Finely cut tissue pieces were added to a T-25 tissue culture flask and incubated in 25 mL Hanks Balanced Salt Solution (HBSS, Corning, USA) supplemented with 1mM EDTA (Invitrogen, USA) for 30 minutes at 37°C at 400 rpm. After supernatant removal, samples underwent a second digestion in 25 mL RPMI

(Gibco, USA) supplemented with 5% FBS, Collagenase II (60 units/mL, Sigma-Aldrich, USA), penicillin/streptomycin (100 IU/mL, Gibco, USA), 2 mM glutamine (Gibco, USA), and 25 mM HEPES buffer (Gibco, USA) for 30 minutes at 37°C at 400 rpm. Samples were filtered through a 70- μ m sterile cell strainer, washed, and resuspended in PBS with 2% FBS. Nexcelom's Cellometer Auto 2000 (Nexcelom, USA) was used to count the cells. PBMCs were cryopreserved at approximately 1×10^7 cells/mL in Bambanker cell freezing medium (GC Lymphotec, Japan).

Flow Cytometry

Whole blood, thawed cryopreserved PBMCs, and freshly isolated cells from BAL and gut were washed with PBS supplemented with 2% FBS and stained with fluorescently labeled antibodies against markers listed in the Supplemental Section (S1 Table) as previously described [27]. Briefly, cells were incubated in Live/Dead stain cocktail (50 μ L PBS + 0.5 μ L live/dead stain per test) (Fixable Aqua Dead Cell Stain Kit, Invitrogen, Lithuania) in the dark for 20 minutes at room temperature. Cells were then washed and incubated in surface-stain cocktail containing 50 μ L Brilliant Stain Buffer (BD Bioscience, USA) and antibodies listed in Supplemental Table 1. All samples were run on a BD FACSymphony A5 Cell Analyzer (BD Bioscience, USA), and data were analyzed with FlowJo 10.8.1 for Mac OS X (Tree Star, USA).

T cell Cytokine Response to SARS-CoV-2

Mononuclear cells (MNCs) from blood and BAL were washed, pelleted, and resuspended in DMEM with 1% Anti-Anti and 10% FBS at 1×10^6 cells/mL. Cells were stimulated overnight at 37°C, 5% CO₂ with either cell stimulation cocktail (Biolegend, USA) or one of the following viral peptide pools obtained through BEI Resources, NIAID, NIH: Peptide Array, SARS Coronavirus Nucleocapsid Protein (NR-52419), Spike Glycoprotein (NR-52402), or Membrane Protein (NR-53822), along with co-stimulatory antibodies (CD28 and CD49d at 1 µL/mL) and Brefeldin-A (1 µL/mL, BioLegend, USA). LIVE/DEAD and surface staining was performed as described above. To measure cellular response to viral antigen, cells were washed in PBS containing 2% FBS, fixed and permeabilized with Cytofix/Cytoperm Buffer (BD Biosciences, USA). Cells were incubated in intracellular stain cocktail for 30 minutes at room temperature (S1 Table), washed with 1x BD Perm/Wash Buffer and fixed in 1x BD Stabilizing Fixative (BD Biosciences, Franklin Lakes, NJ).

Overnight stimulation, surface and intracellular staining of BAL cells isolated from SARS-CoV-2 infected animals were performed under BSL-3 safety conditions. Cells were fixed with 2% Paraformaldehyde for 60 minutes before removal from BSL-3. Samples were run on the BD FACSymphony and analyzed via FlowJo as described above.

Meso Scale COVID-19 IgA and IgG Panels

V-PLEX COVID-19 serological assays were used to quantify serum levels of IgA and IgG binding antibodies to SARS-CoV-2 Spike, Spike N-Terminal Domain (S1 NTD), and Spike Receptor Binding Domain (S1 RBD) (Panel 1, Meso Scale Discovery, USA), following the manufacturer's protocol. Briefly, plates were first incubated at room temperature on a shaker in MSD Blocking solution for 30 minutes, followed by 3 washes with 1X MSD Wash buffer. Plasma samples were diluted 100- (IgA kit) or 1000-fold (IgG kit) and plated in duplicate, along with controls and standards used to generate a seven-point calibration curve. Plates were then sealed and incubated at room temperature on a shaker for 2 hours. Following this, the plates were washed three times before addition of 1X detection antibody to each well. After a 1-hour incubation, plates were washed a final 3 times, and MSD GOLD Read Buffer B was added to the plates. Plates were read immediately using a MESO QuickPlex SQ 120MM instrument. The concentration of IgA and IgG antibodies was determined using the standard curve generated by plotting the known concentrations of the standards and their corresponding signals.

SARS-CoV-2 Microneutralization (PRMNT) Assay

A microneutralization assay (PRMNT) adapted from Amanat et al. 2020 [30] was used to assess the presence of neutralizing antibodies in serum of SIV+ and SIV naïve SARS-CoV-2 infected PTMs. Vero/TMPRSS2 cells (JCRB Cell Bank, Japan) were seeded in 96-well tissue culture-treated plates to be

subconfluent at the time of assay. Serum samples were diluted in dilution buffer (DMEM, 2% FBS, and 1% Anti-Anti) to an initial dilution of 1:5, followed by six 3-fold serial dilutions. SARS-CoV-2 (WA1/2020, BEI, USA) was diluted 1:3000 in dilution buffer and added in equal proportions to the diluted sera under Biosafety Level 3 (BSL-3) conditions. Samples were then incubated at room temperature for 1 hour. The culture media was removed from the 96-well Vero cell culture plates, and 100 μ L of the virus/sera mixture was added to each well. Dilution buffer and diluted virus (1:6000) were used as the negative and positive controls, respectively. Plates were then incubated for 48 hours at 37°C and 5% CO₂. After the incubation period, the medium was removed, and 100 μ L of 10% formalin was carefully added to each well. The plates were allowed to fix overnight at 4°C before being removed from the BSL-3 facility.

The staining of the plates was conducted under BSL-2 conditions. After carefully removing the formalin, the cells were washed with 200 μ L PBS, followed by the addition of 150 μ L of permeabilization solution (0.1% Triton/PBS). Plates were then incubated at room temperature for 15 minutes. Following the incubation, the cells were washed with PBS and blocked with 100 μ L of blocking solution (2.5% BSA/PBS) for 1 hour at room temperature. After removing the blocking solution, 50 μ L of the primary antibody (SARS-CoV-2 Nucleocapsid Antibody, Mouse Mab, Sino Biologicals, #40143-MM08) diluted 1:1000 in 1.25% BSA/PBS was added to each well, followed by a 1-hour incubation at room temperature. The plates were then washed twice with PBS, decanted, and gently tapped on a paper towel to ensure complete antibody removal. Next, 100 μ L of

the secondary antibody, Goat anti-Mouse IgG (H+L) Cross-Adsorbed Secondary Antibody (Invitrogen, #A16072) diluted 1:3000 in 1.25% BSA/PBS was added to each well. The plates were incubated for 1 hour at room temperature. Following the incubation period, cells were washed as described above. To initiate color development, 100 μ L of 1-Step Ultra TMB-ELISA developing solution (Thermo Scientific, #34028) was added to each well. The plates were then incubated in the dark at room temperature for 10 minutes. To stop the reaction, 50 μ L of 1N sulfuric acid was added to each well. The optical density was measured and recorded at 450 nm on a Tecan Sunrise Microplate Reader (Tecan, Switzerland). The averages of the positive control wells and negative control wells were calculated separately, and percent inhibition was calculated for each well.

Results

Experimental Design and Viral Dynamics in SIV-infected Pigtail Macaques Prior to SARS-CoV-2 Exposure

Two female pigtail macaques (PTM, NV18 & NV19) were infected intravenously (iv) with SIVmac239 (100 TCID₅₀) and monitored for approximately one year prior to exposure to SARS-CoV-2 (Wa1/2020, 2.2x10⁶ PFU, in/it) (Fig 1A). SIV viral dynamics in plasma followed the typical pattern, with peak viremia occurring approximately two weeks after infection, followed by a set point of around 1x10⁶ for NV18 and 1x10⁵ for NV19 (Fig 1B). The uncontrolled viremia led to a substantial progressive decrease in CD4⁺ T cells in all sampled compartments (plasma, BAL, and gut) (Fig 1C-E). Notably, beginning at

approximately eight weeks post-SIV infection, NV18 exhibited little to no detectable CD4⁺ T cells in BAL and gut, and these levels remained persistently low until the time of SARS-CoV-2 exposure. The other animal, NV19 also experienced a decline in CD4⁺ T cells across all sampled compartments, and although levels began to rebound, they never returned to pre-infection levels.

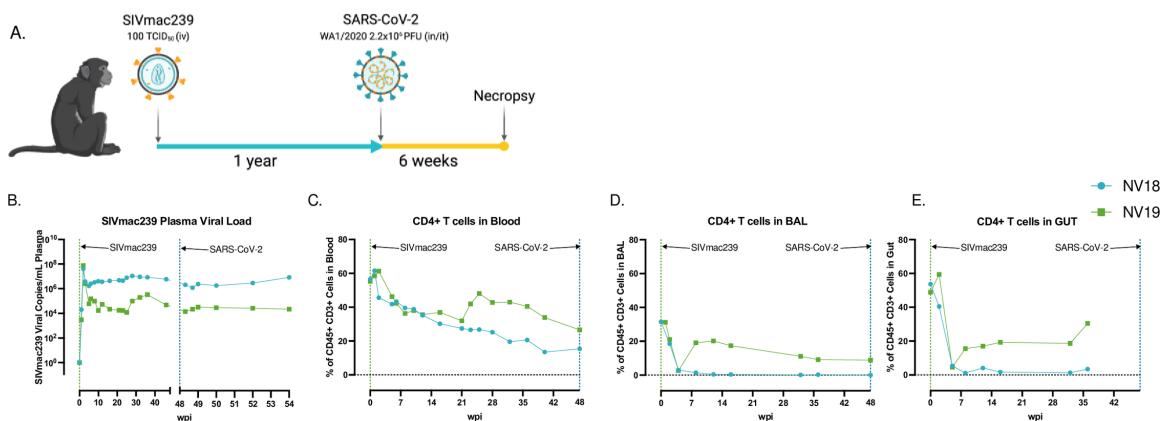


Figure 1. Before SARS-CoV-2 exposure, PTM experienced uncontrolled SIV viremia and immunodeficiency due to loss of CD4⁺ T cells. A. Overall study design. Two female pigtail macaques (PTM, NV18 & NV19) were inoculated with SIVmac239 (100 TCID₅₀, iv), followed by SARS-CoV-2 (Wa1/2020, 2x10⁶, in/it) challenge approximately one year later. **B.** Quantification of SIVmac239 RNA levels in plasma overtime (Quantitative RT PCR). **C-E.** CD4⁺ T cell kinetics following SIVmac239 infection in blood (**C**), bronchoalveolar lavage (BAL) (**D**), and gut (**E**).

Impact of SIV-Induced Immunodeficiency on SARS-CoV-2 Replication and Evolution

We then sought to investigate how SIV-induced immunodeficiency affects SARS-CoV-2 viral replication and evolution in our PTM model. We hypothesized that the observed immunodeficiency in the SIV-infected PTMs would enhance SARS-CoV-2 viral persistence, thereby increasing the risk of viral evolution. Using qRT-PCR, we tracked viral genomic (Fig 2A-E) and subgenomic (SGM, Fig 2F-J) RNA in mucosal swabs (nasal, pharyngeal, and rectal), BAL

supernatant (sup), and plasma for six weeks. We compared viral dynamics in our coinfecting animals with our previously published cohort of SIV-naïve PTMs [27]. Viral dynamics in BAL showed robust viral replication during acute infection in both the SIV+ and the controls with viral levels becoming undetectable in all animals by 21 days post infection (dpi). The coinfecting animals cleared vRNA in the rectal mucosa by 14-dpi, the pharynx by 21-dpi, and the nasal mucosa by 28-dpi. The SIV-naïve animals had low levels of detectable virus in the nasal and rectal mucosa at their study end point of 21-dpi, with no detectable virus in the pharynx or plasma. Furthermore, we were unable to detect genomic or SGM vRNA in plasma in either of the coinfecting animals. Surprisingly, both SIV+ animals cleared SARS-CoV-2, similar to the controls, and the absence of prolonged viral persistence consequently precluded any significant viral evolution, with H655Y being the only spike mutation detected in multiple samples from both coinfecting animals at more than 25% of sequence read, including NV18 nasal and pharyngeal from day 2 and pharyngeal from day 5 and NV19 rectal sample from day 2. However, this mutation was also present at a low frequency in the inoculum, precluding any analysis of intrahost selection.

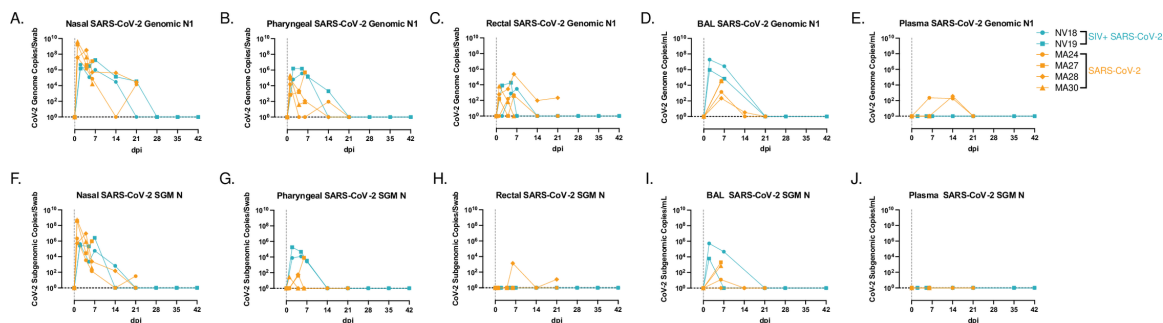


Figure 2. SARS-CoV-2 viral dynamics. NV18 and NV19 were inoculated with SARS-CoV-2 (1×10^6 TCID₅₀) 48 weeks post SIVmac239 infection through a combination of intranasal (in) and intratracheal (it) exposure, indicated as Day 0. **A-J.** Comparison of genomic (**A-E**) and subgenomic (SGM, **F-J**) SARS-CoV-2 mRNA levels in mucosal swabs (**A-C**, **F-H**), BAL supernatant (**D**, **I**) and plasma (**E**, **J**) in coinfecting animals (blue) and a previously published cohort of SIV naïve PTM (orange).

Clinical Manifestations and Postmortem Observations in Coinfecting PTM

Animals coinfecting with SIVmac239 and SARS-CoV-2 were closely monitored for six weeks following SARS-CoV-2 inoculation. In line with clinical findings in our previous pigtail study, the coinfecting animals exhibited only mild COVID-19 symptoms. This outcome was unexpected given that previous studies have indicated PLWH face a higher risk of severe disease attributed to factors such as low CD4⁺ T cell counts and uncontrolled viremia, both of which were observed in our SIV⁺ animals [19–23]. Similar to the controls, no significant changes in body weight, temperature, or blood oxygen saturation levels were observed in the coinfecting animals (S1 Fig). Furthermore, thoracic radiographs of the coinfecting animals closely resembled those of the control group, revealing only subtle changes consistent with mild to moderate manifestations of COVID-19 (S2 Fig). Upon postmortem examination, both animals demonstrated histopathologic changes consistent with chronic SIV infection. Neither animal had lesions that were attributed to SARS-CoV-2 infection indicating that lesions had resolved. The resolution of SARS-CoV-2-associated lesions is expected given

the six-week post-infection time point, viral clearance in these animals, and what has previously been reported in the NHP model. One animal, NV18, had an opportunistic *Pneumocystis* infection and SIV syncytial giant cells compatible with simian AIDS (SAIDS).

T cell Dynamics in Blood and BAL Following SARS-CoV-2 Infection

T lymphopenia, specifically of CD4⁺ T cells, is a common feature observed in human COVID-19 patients. This, compounded with low CD4⁺ T cell counts due to advanced HIV/SIV infection, may delay the clearance of SARS-CoV-2, increase the risk of viral evolution, and promote disease progression [31,32]. In our study, both coinfecting animals displayed signs of immunodeficiency with a substantial loss of CD4⁺ T cells in blood, lung, and gut prior to SARS-CoV-2 exposure (Fig 1C-E). Acutely following SARS-CoV-2 infection, both animals experienced a further decline in peripheral CD4⁺ T cells. In NV19, this decline was transient and reached a nadir at 2-dpi. However, in the more immunocompromised animal, NV18, the loss persisted, and CD4⁺ T cells remained undetectable in both blood and BAL for the remainder of the study (Figs 3A, 3C, 3E, and 3G). Both animals showed a reduction in the overall CD3⁺ T cell population in BAL at 2-dpi, with levels returning to baseline in NV19 at 7-dpi (Fig 3F). T cell dynamics in the SIV-naïve animals exhibited patterns similar to those of NV19, though with slightly delayed kinetics (Figs 3B-D and 3F-H). Despite the loss of CD4⁺ T cells, both coinfecting animals successfully cleared

SARS-CoV-2, suggesting the involvement of innate immune mechanisms in controlling the infection.

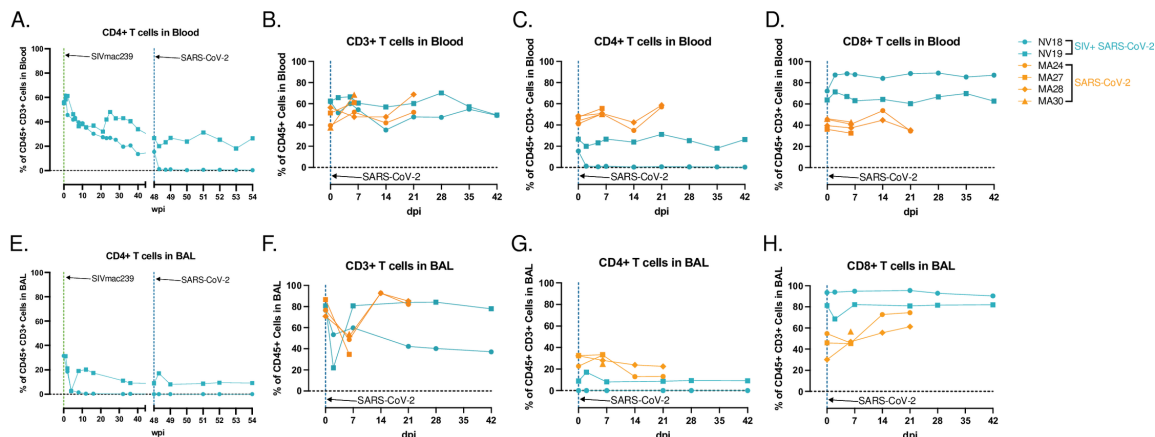


Figure 3. T cell dynamics in blood and BAL following SARS-CoV-2 infection of SIV+ and SIV naïve PTM. CD4+ T cell kinetics in blood (A) and BAL (G), following SIVmac239 and SARS-CoV-2 infection. H-L. Peripheral and pulmonary T cell dynamics in SIV+ SARS-CoV-2 coinfecting PTM (blue). Historical data from four SIV naïve SARS-CoV-2 infected PTM in orange. Comparison of overall CD3+ T cell populations (B&F) as well as T cell subsets; CD4+ (C&G), CD8+ (D&H).

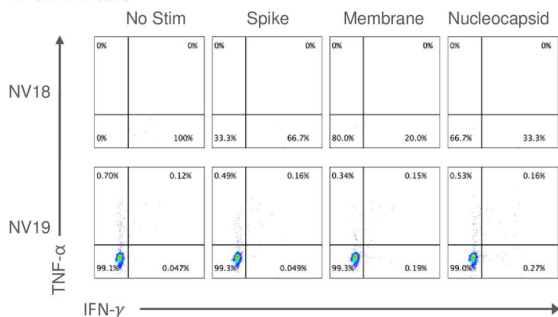
Diminished Cellular Immune Response to SARS-CoV-2 in Coinfected Animals with Severe T Cell Lymphopenia

To evaluate the cellular immune response to SARS-CoV-2 infection, we stimulated mononuclear cells isolated from BAL with peptides derived from SARS-CoV-2 Spike, Membrane, or Nucleocapsid proteins and assessed cytokine responses using flow cytometry. In our previous PTM study, we showed that at 21-dpi, the SIV-naïve animals developed pulmonary but not peripheral CD4+ and CD8+ SARS-CoV-2-specific T cell responses, that were predominately CD4 driven. However, in our current study, neither coinfecting animal had detectable virus-specific cellular immune responses to peptide stimulation (Figs 4A and 4B). Consistent with our previous findings, we were unable to detect virus-specific T-

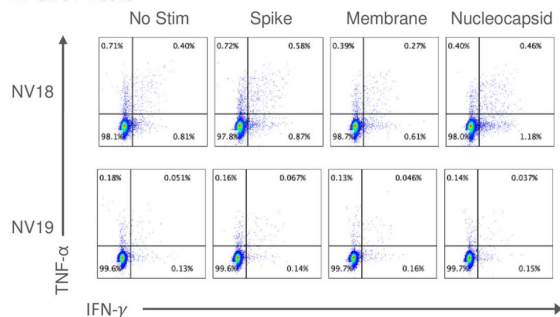
cell responses in the blood at 21-dpi (Figs 4C and 4D). Our findings show that severe CD4+ T-cell lymphopenia, resulting from advanced SIV infection, significantly impairs the cellular immune response to SARS-CoV-2 in the lungs.

BAL

A. CD4+ T cells



B. CD8+ T cells



Blood

C. CD4+ T cells



D. CD8+ T cells

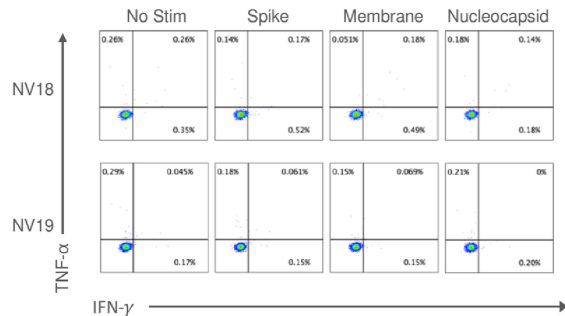


Figure 4. SARS-CoV-2 specific T cell responses were undetectable in the lung and blood 21-days-post-infection. Two female pigtail macaques (PTM, NV18 & NV19) co-infected with SIVmac239 and SARS-CoV-2 shown. **A-D.** Flow cytometry dot plots demonstrating the CD4+ (**A, C**) and CD8+ (**B, D**) IFN- γ and TNF- α response to overnight SARS-CoV-2 peptide (spike, membrane, and nucleocapsid) stimulation. No Stim = cells incubated overnight without peptide stimulation.

Impaired Humoral Immune Response to SARS-CoV-2 Infection

We then aimed to assess neutralization capacity of serum antibodies using a microneutralization assay (PRMNT) [30]. By 14-dpi, the SIV-naïve animals demonstrated detectable neutralizing antibodies against SARS-CoV-2, whereas the coinfecting animals failed to generate a neutralizing antibody response (Fig 5A). Additionally, using the V-PLEX COVID-19 serological assay

kit from Meso Scale Discovery, we measured IgA and IgG binding antibody levels in serum. By 21-dpi, we detected IgA (Fig 5B) and IgG (Fig 5C) binding antibodies targeting various domains of the Spike protein, including the receptor binding domain (RBD), Spike S1 and S2 domains, and the Spike N-terminal domain (NTD) in the SIV-naïve PTMs. However, we were unable to detect IgA or IgG binding antibodies in the serum of the coinfecting animals. Our data demonstrate that the coinfecting animals failed to generate virus-specific T cell and humoral immune responses highlighting the impact of pre-existing immunodeficiency on the development of adaptive immunity during coinfection.

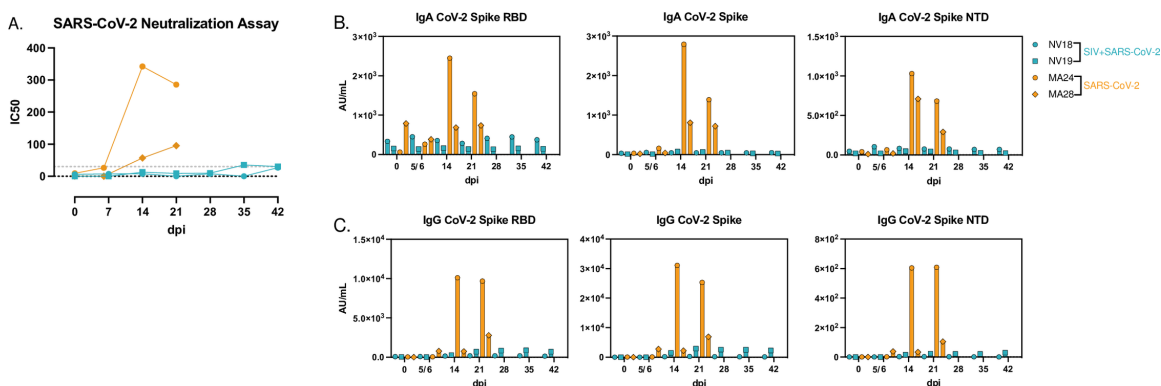


Figure 5. Humoral immune response to SARS-CoV-2 infection. **A.** SARS-CoV-2 neutralization assay depicting serum antibody levels against SARS-CoV-2 using Vero TMPRSS2 cells. **B&C.** MesoScale analysis of IgA (**B**) and IgG (**C**) binding antibodies to SARS-CoV-2 Spike receptor binding domain (RBD), Spike glycoprotein 1 and 2 (S1&S2), and Spike N-Terminal Domain (NTD).

Discussion

Since its emergence in December 2019 in Wuhan, China, the novel coronavirus SARS-CoV-2 has had a profound global impact [1]. COVID-19, caused by SARS-CoV-2, encompasses a spectrum of disease manifestations,

ranging from asymptomatic [33,34] to mild flu-like symptoms to pneumonia [35,36]. While the majority of infected individuals exhibit mild to moderate symptoms, a select group can experience severe complications marked by significantly elevated levels of coagulation biomarkers and proinflammatory cytokines, which can lead to acute respiratory distress syndrome (ARDS), and in some cases, death [37]. Risk factors such as a compromised immune system, advanced age, and comorbidities such as cardiovascular disease, diabetes, and obesity increase the likelihood of severe disease.

The presence of HIV infection poses additional risks for individuals, including a compromised immune system and a higher prevalence of cardiovascular disease, raising concerns about the impact of HIV on the severity and persistence of SARS-CoV-2 infections [13–15]. While initial research indicated similar or improved outcomes for people living with HIV (PLWH) compared to the general population [16–18], larger population-based studies reported higher rates of hospitalization and COVID-19-related deaths among PLWH [19–23]. Recent studies suggest that unsuppressed viral loads or low CD4+ T cell counts are associated with suboptimal cellular and humoral immune responses to SARS-CoV-2 [24,25].

Immunodeficiency associated with HIV not only raises concerns about increased severity but also the potential facilitation of SARS-CoV-2 persistence and evolution, leading to the emergence of novel viral variants. Karim et al, (2021) highlighted this concern in a recent study in which an individual with advanced HIV showed prolonged shedding of SARS-CoV-2, high viral loads, and

the development of multiple viral mutations [26]. Although retrospective studies have explored the impact of HIV status on COVID-19 incidence and severity, controlled studies in this area are lacking.

To address these gaps, we conducted a small pilot study involving two pigtail macaques (PTMs) infected with SIVmac239, a strain that is highly pathogenic in PTM and models progressive HIV infection, and subsequently exposed them to SARS-CoV-2 after approximately one year. Notably, PTMs infected with SIV exhibit comparatively rapid progression to AIDS and demonstrate cardiovascular abnormalities similar to those observed in humans with advanced HIV, making them an ideal model for evaluating the effects of chronic SIV infection on SARS-CoV-2 dynamics [38–41]. Our study aimed to investigate the impact of SIV-induced immunodeficiency on the clinical manifestation of COVID-19, along with its impacts on viral replication and evolution in a controlled setting. We compared the clinical, virological, and immunological outcomes of the coinfecting animals with our previously published cohort of SIV-naïve PTMs infected with SARS-CoV-2 [27].

One of the key findings of our study is that SIV-induced immunodeficiency did not lead to enhanced COVID-19 disease in the coinfecting animals. Despite the presence of significant immunodeficiency, as evidenced by the severe reduction in CD4⁺ T cells, the coinfecting animals exhibited only mild COVID-19 symptoms, similar to the control group. This finding contrasts with previous studies that have reported a higher risk of severe disease and mortality in PLWH [19–23], suggesting that aspects beyond immunodeficiency, such as

comorbidities or host-related factors, may contribute to the elevated risk of severe COVID-19 observed in PLWH.

Our analysis of SARS-CoV-2 viral dynamics in the coinfecting animals revealed that SIV-induced immunodeficiency did not significantly impact viral replication or evolution, with viral dynamics indistinguishable from the controls. Despite higher levels of vRNA in BAL of the more immunocompromised animal (NV18), vRNA levels became undetectable in both of the coinfecting animals by three- or four-weeks post-infection in all sampled mucosal sites indicating that underlying SIV infection alone is insufficient to drive uncontrolled SARS-CoV-2 replication.

However, we did observe a notable difference in the adaptive immune response to SARS-CoV-2 infection between the SIV+ and SIV-naïve PTMs. By 21-dpi, the control animals exhibited detectable SARS-CoV-2-specific neutralizing antibodies, IgA and IgG binding antibodies, and virus-specific T cell responses. In contrast, both coinfecting animals failed to generate virus-specific humoral or cellular immune responses against SARS-CoV-2. This finding is consistent with studies linking uncontrolled HIV infection to suboptimal T cell and antibody responses to SARS-CoV-2 [24,25]. These results underscore the impact of pre-existing immunodeficiency on the development of adaptive immunity during coinfection. The observed inability to mount effective virus-specific cellular and humoral immune responses sheds light on the potential challenges faced by individuals with advanced HIV infection when encountering SARS-CoV-2 and raises concerns about the potential impacts of reinfection.

Conclusion

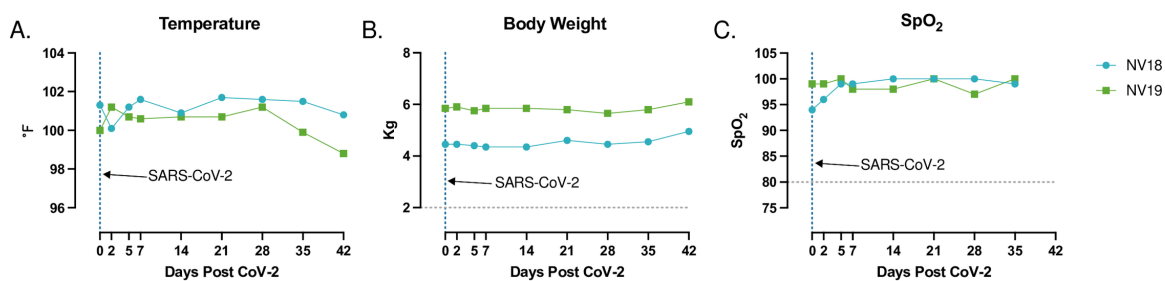
Overall, our study provides valuable insights into the interplay between SIV-induced immunodeficiency and SARS-CoV-2 infection. Despite the notable immunodeficiency observed in the coinfecting animals, we found no evidence of enhanced COVID-19 disease nor significant impacts on viral replication or evolution. However, the impaired T-cell response and lack of neutralizing antibodies in the coinfecting animals highlight the impact of underlying SIV-induced immunodeficiency on the immune response to SARS-CoV-2. These findings contribute to our understanding of COVID-19 pathogenesis in immunocompromised individuals and may help guide the development of strategies to manage COVID-19 in vulnerable populations.

Limitations

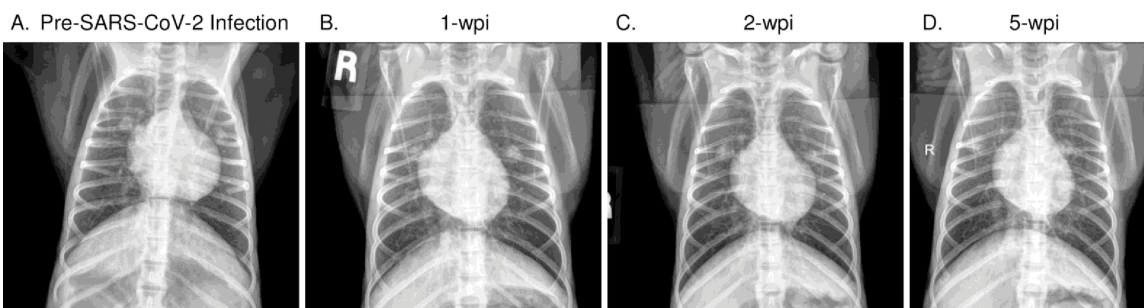
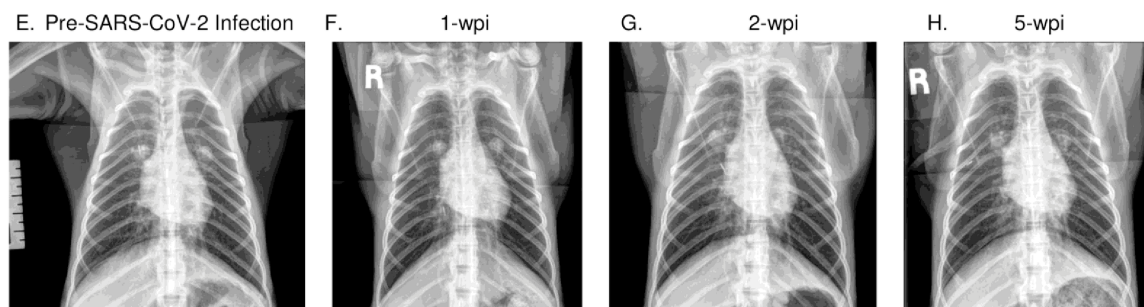
As this was a preliminary study involving only two female animals, it will be necessary to conduct follow-up studies with larger cohorts in order to validate our findings. It's important to note that the control animals used in this study were historical data derived from our previous study of male pigtail macaques. This gender difference between control and study animals may introduce variability and should be considered in future research. Nonetheless, our data provide novel and important discoveries contributing to the growing collection of SARS-CoV-2 resources. Further investigations into SARS-CoV-2 reinfection of SIV+ nonhuman primates could serve as a promising follow-up to this study. Our coinfection model demonstrated that the innate immune response was likely

efficient in eliminating SARS-CoV-2 infection. A study that compares reinfection rates and viral clearance upon secondary exposure would be an exciting next avenue to pursue.

Supplemental



Supplemental Figure 1. Temperature (A), weight (B), and saturation of peripheral oxygen (SpO₂) (C) levels were measured prior to and for 6 weeks following SARS-CoV-2 inoculation of SIV+ pigtail macaques. Day 0 indicates time of SARS-CoV-2 infection, 48 weeks post SIVmac239 exposure.

NV18**NV19**

Supplemental Figure 2. Radiographs of SIV-infected pigtail macaques (PTM) challenged with SARS-CoV-2. Radiographs were obtained prior to SARS-CoV-2 infection and at weeks 1-, 2-, and 5-weeks post infection (wpi). Baseline was established at 2 weeks prior to SARS-CoV-2 inoculation.

Supplemental Table 1.			
Fluorochrome	Antigen Target	Clone	Vendor
BV510	Live/Dead	Fixable Aqua Dead Cell Stain Kit	Invitrogen
BV650	CD8	SK1	BD Horizon
BV711	CD95	DX2	BD Horizon
BV750	PD-1 (CD279)	EH12.2H7	Biolegend
BUV395	CD45	D058-1283	BD Horizon
BUV496	CD4	L200	BD Optibuild
PE-Cy5	CD45RA	5H9	BD Pharmingen
APC	CD28	CD28.2	Biolegend
APC-C7	CD3	SPE4-2	BD Pharmingen
BV570	HLA-DR	L243	Biolegend
PCP-Cy5.5	CD95	DX2	BD Horizon
PacBlue	CD20	2H7	Biolegend
BV605	CD8	SK1	BD Horizon
BV650	CCR7	3D12	BD Horizon
BV711	CD11c	3.9	BD Horizon
BV786	CD103	Ber-ACT8	Biolegend
BUV737	CD14	M5E2	BD Horizon
PE	CD169	7-239	Biolegend
PE-CF594	CD69	FN50	BD Horizon
PE-Cy7	CD163	GHI/61	Biolegend
AL700	CD16	3G8	Biolegend
BV605	CD45	D058-1283	BD Horizon
BV650	CD4	L200	Biolegend
AL700	CD8	RPA-T8	BD Pharmingen
PE-Cy7	IFN- γ	B27	BD Pharmingen
AL700	TNF- α	MAb11	BD Pharmingen

Supplementary Table 2.1. Flow cytometry antibodies.

Supplemental Table 2	
XpressBio Simian ELISA Reagents	
Description	Cat #
SARS-CoV-2 Spike Protein (S1,S2) Wuhan Hu-1 ELISA Plate	SP864C
SARS-CoV-2 S1/S2 Positive Control	SPC864
SARS-CoV-2 Negative Control	595-200
SARS-CoV-2 Nucleoprotein (Wuhan Hu-1) ELISA Plate	SP865C
SARS-CoV-2 Nucleoprotein Positive Control	SPC865
SARS-CoV-2 RBD+M (Wuhan Hu-1) ELISA Plate	SP866C
SARS-CoV-2 RBD+M Positive Control	SPC866
ELISA Wash Buffer (20x)	827102
ELISA Serum Diluent	595-413
ELISA Anti-Simian IgG Peroxidase Conjugate	595-626
ELISA ABTS Peroxidase Substrate	595-419
ELISA Stop Solution	595-417

Supplementary Table 2.2. XpressBio Simian ELISA Reagents.

Chapter 3

Molecular Transcriptomic Signatures of Pulmonary T Cells in Non-Human Primates: Redefining Lung Vasculature T Cells Beyond Blood Contaminants Through Single-Cell RNA Sequencing

Alexandra Melton^{1,2}, Toni Penney¹, Clara Krzykwa¹, Lori A Rowe¹, Hunter Melton³, Nicholas J Maness^{1,4*}

¹Tulane National Primate Research Center, Covington, Louisiana

²Biomedical Science Training Program, Tulane University School of Medicine, New Orleans, Louisiana

³Florida State University, Department of Statistics, Tallahassee, Florida

⁴Department of Microbiology and Immunology, Tulane University School of Medicine, New Orleans, Louisiana

*Whom to address correspondence

Abstract

Intravascular staining (ivs) provides an innovative method for distinguishing tissue-resident cells from those within the vasculature, a distinction that is particularly important in highly vascularized organs such as the lung. Cells that stain positive for the infusion antibody (ivs+) have generally been considered “blood contaminants.” However, recent studies are beginning to call this into question. Our study aimed to elucidate defining characteristics and functions of ivs+ T cells in the pulmonary vasculature. Utilizing ivs, we analyzed T cells from the lung and respiratory mucosa of Rhesus Macaques (RhM) via flow cytometry and single-cell RNA sequencing (scRNAseq). Contrary to being dismissed as “blood contaminants,” we found that pulmonary ivs+ T cells represent a unique population. Notably, CD8+ T cells were enriched within this group and predominantly exhibited an effector phenotype, highlighted by increased Granzyme B (GZMB) expression. Moreover, these pulmonary vascular “resident-like” T cells demonstrated a gene profile enriched in cell adhesion and extravasation markers. In Simian Immunodeficiency Virus (SIV) infected RhMs, pulmonary ivs+ CD8+ T cells displayed heightened GZMB, IFN- γ , and TNF- α responses compared to tissue-resident memory (T_{RM}) cells. Our findings redefine the role of ivs+ cells in the lung, emphasizing their distinct immunological functions and potential impact on respiratory health.

Introduction

T cells play a pivotal role in defense against invading pathogens. Naïve T cells continuously circulate through the bloodstream and secondary lymphoid organs (SLO), poised to encounter their cognate antigen [1–3]. Upon antigen recognition, they undergo rapid proliferation, differentiating into effector T cells (T_{EFF}) that eradicate the infection [4]. As the infection resolves, the T_{EFF} population contracts, leaving a small pool of antigen-experienced memory T cells (T_{MEM}) ready to protect the host from future exposures [5,6].

T_{MEM} cells stand at the forefront of host defense, enabling rapid and efficient responses to previously encountered pathogens. T_{MEM} cells consist of a diverse repertoire characterized by distinct transcriptional profiles and protein expression, underpinning their varied functionalities, frequency, and localizations [7]. T_{MEM} are typically categorized into three primary subsets: central memory (T_{CM}), effector memory (T_{EM}), and tissue-resident memory T cells (T_{RM}) [8–10]. However, the growing recognition of their heterogeneous nature implies that creating strict, well-defined subsets may not be the most accurate approach. T_{RM} cells reside in nearly all tissues and are characterized by their non-circulating nature and specialized ability to coordinate rapid immune responses as well as maintain homeostasis within the local environment [11–14].

The lung, constantly exposed to various environmental factors, serves as a critical immunological effector site [15–18]. Its dual blood supply creates unique avenues for the migration and residency of immune cells [19]. The lungs' unique dual vascular system, which consists of bronchial and pulmonary arteries,

facilitates oxygen exchange and serves as a pathway for immune cell trafficking [20]. This vascular network's structure, from the tracheobronchial tree's microvasculature to the alveolar capillaries, plays a pivotal role in how leukocytes navigate and exert immune responses within the lung [21]. The less studied perivascular capillary bed found surrounding larger pulmonary arteries may provide a third route for leukocyte trafficking and allow for rapid immune responses [19].

A key challenge in studying tissue-resident T cells, especially within highly vascularized organs such as the lung, is distinguishing them from cells within the organs' vasculature. Intravascular staining, pioneered in mice and more recently utilized in non-human primates (NHPs), has emerged as a transformative tool to delineate tissue-resident cells from their vasculature-associated counterparts [22–26]. This technique involves infusing a fluorochrome-labeled antibody into the animal at subsaturation levels prior to necropsy. Cells present within the vasculature are tagged by the infused antibody (ivs+), whereas tissue-resident cells remain unlabeled (ivs-) [23]. Traditionally, cells staining positive for the infused antibody were perceived merely as “blood contaminants.” However, a recent study by Potter et al. challenges this notion [24].

Potter and colleagues used serial ivs with differentially labeled antibodies to assess lymphocyte trafficking patterns across time. In their study, they found distinct differences in peripheral blood mononuclear cells (PBMCs) and ivs+ (referred to as ivas+ in their study) cells across non-lymphoid tissues; in particular, they noted that the CD4:CD8 ratio and memory phenotypes of the ivs+

cells differed markedly from circulating cells. They also noted enhanced CD69 expression, a marker of tissue residence, which further set ivs+ cells apart from circulating cells. Serial ivs experiments revealed that the vast majority of ivs+ T cells in the lung were co-labeled with antibodies from the previous 6, 24, or 48-hour infusions, a pattern less frequently observed with T cells in the blood. They found that the majority of T cells in the blood were more likely to be unlabeled with previous infusion antibodies. Potter proposed the perivascular bed identified by Pabst and Tschernig as a potential residence for their ivs+ cells. Pabst and Tschernig described distinct leukocyte populations within the capillary beds surrounding pulmonary arteries, suggesting a unique niche allowing plasma access but restricting cell movement [19]. Designated “perivascular,” they proposed that these cells were distinct from those in the blood or lung parenchyma.

The lung anatomy of non-human primates closely resembles that of humans, making them the ideal animal model for pulmonary studies [27]. Here, we utilized Rhesus Macaques (RhM) to extensively investigate the phenotypic and functional capacities of ivs+ T cells in the lung using flow cytometry and single-cell RNA sequencing. To further understand the functional diversity of ivs+ T cells, we evaluated CD8+ T cell responses in simian immunodeficiency virus (SIV) infected RhMs, a model of HIV infection. Although not generally considered a respiratory disease, SIV/HIV has systemic implications, including a spectrum of respiratory complications, such as increased susceptibility to chronic lung disease, bacterial and pneumocystis pneumonia, lung cancer, and other

respiratory infections [28–34]. By characterizing the nuanced attributes of pulmonary ivs+ T cells through our study, particularly the enrichment of CD8+ T cells with enhanced functionality and upregulation of integrins associated with vascular endothelial cell interactions, we redefine them as a specialized population distinct from lingering blood lymphocytes. This distinction has unique implications for respiratory health and expands our understanding of tissue-specific immunity.

Materials and Methods

Intravascular Staining

Six Rhesus Macaques received a single injection of 30 µg/kg Anti-CD45 [ITS_rhCD45]-AF647 (CD45-ivs) antibody (Nonhuman Primate Reagent Resource (NHPRR), RRID: AB_2910539) diluted in five mL sterile phosphate-buffered saline (PBS) administered through a catheter placed in the saphenous vein 5 minutes prior to necropsy.

SIV Infection

Four RhM were inoculated intravenously with SIVmac239 and were placed on antiretroviral therapy (ART) two weeks post-inoculation. They were monitored for approximately one year, after which ART was discontinued. Four weeks post-ART-interruption, the animals were euthanized. Pre- and post-infection sampling included blood and bronchoalveolar lavage (BAL), which continued throughout the course of the study.

Viral RNA Isolation and Quantification

SIVmac239 viral RNA (vRNA) was isolated from EDTA plasma and BAL supernatant using the High Pure Viral RNA kit (Roche) following the manufacturer's protocol with the following modifications: the elution volume was increased from 50 to 100 μ L and supplemented with RNase Inhibitor (0.3 units/ μ L, Applied Biosystems). To further improve vRNA recovery, the eluted vRNA (100 μ L) samples were subjected to a second RNA extraction/elution using the RNA Clean and Concentrator kit – 25 (Zymo Research) as per the manufacturer's protocol. The final elution volume of 50 μ L was supplemented with RNase Inhibitor (0.8 units/ μ L, Applied Biosystems). Quantification of vRNA was performed as previously described [35].

Immune Cell Isolation

PBMCs were isolated from EDTA whole blood using SepMate-50 Isolation tubes (Stem Cell Technologies) following the manufacturer's recommended protocol. BAL samples were centrifuged at 1800 rpm for 5 minutes at room temperature. BAL supernatant was aspirated and stored at -80°C. Tissue samples were cut into small pieces (~0.5 cm) using scissors or surgical scalpels. Lung tissue was digested using type IV collagenase (Worthington) and deoxyribonuclease (DNase) I (Roche) at 37°C at 300 rpm for 45 minutes. Cold stop media (RPMI supplemented with 10% fetal bovine serum (FBS) and 1% anti-anti) was added to the digested lung tissue. Clumps were broken up using scissors, and the tissue was plunged ~10 times using a 50 mL serological

pipette. Samples were then filtered through a 100- μ m cell strainer and centrifuged at 400 g for 10 minutes at 4°C. Cells were resuspended in 30% Percoll and centrifuged for 12 minutes at 780 g at room temperature. Cells were then washed in PBS with 2% FBS. Red blood cells were lysed using 1x ACK lysis buffer for 5 minutes on ice, and samples were again washed in PBS with 2% FBS. Nasal mucosa was digested in Liberase TL (MilliporeSigma) and DNase I for 45 minutes at 37°C while shaking at 250 rpm. Cells were filtered over a 70- μ m filter, washed in RPMI supplemented with 20% FBS (R20) and centrifuged at 400 g for 10 minutes. If needed, red blood cells were lysed using 1x ACK buffer (Gibco), and samples were again washed in R20. Spleen and lymph nodes were mechanically disrupted and filtered using a 70- μ m cell strainer, washed in R10, and centrifuged at 1800 rpm for 5 minutes. Jejunum and colon tissues were digested first with Hanks Balanced Salt Solution (HBSS, Corning) supplemented with 1mM EDTA (Invitrogen) for 30 minutes at 37°C at 400 rpm. The supernatant was aspirated, and this process was repeated a second time. The tissue was then digested in Collagenase II (Sigma-Aldrich) for 30 minutes at 37°C at 400 rpm. Cells were filtered over a metal strainer, and the process was repeated for any remaining tissue. Cells were filtered over a metal strainer and washed in RPMI. Cells were either stained immediately for flow cytometry or cryopreserved in Bambanker cell freezing media (GC Lymphotec) at 1×10^7 cells/mL and stored at -80°C.

Flow Cytometry

Whole blood, freshly isolated mononuclear cells from blood, lung, nasal, gut, and lymph nodes, or thawed cryopreserved PBMCs, bronchial lymph node (BLN), and lung cells were washed in FACS buffer (PBS supplemented with 2% FBS). Cells were first stained with 5 μ L anti-CD69 antibody in 50 μ L Brilliant Stain Buffer (BD Biosciences) for 20 minutes at room temperature. Cells were washed and resuspended in 1 mL R10 with either DMSO (incubated for 6 hours) or SIV Gag peptides (incubated overnight) along with co-stimulatory antibodies (CD28 and CD49d at one μ L/mL) and Brefeldin-A (one μ L/mL, BioLegend) at 37°C, 5% CO₂. Cells were washed in FACS buffer and resuspended in live/dead stain cocktail (50 μ L PBS with 0.5 μ L live/dead stain) (Fixable Aqua Dead Cell Stain Kit, Invitrogen) in the dark for 20 minutes at room temperature. Cells were washed in FACS buffer, resuspended in a chemokine stain cocktail containing Brilliant Stain Buffer (BD Bioscience), and incubated at 37°C for 15 minutes. Surface staining cocktail was then added according to S1 Table with additional Brilliant Stain Buffer (for a total of 50 μ L Brilliant Stain Buffer), and samples were incubated in the dark for an additional 20 minutes at room temperature. Cells were washed in FACS buffer and incubated in Cytofix/Cytoperm Buffer (BD Biosciences) to fix the cells and allow for intracellular staining. Cells were washed in 1x BD Perm/Wash Buffer (BD Biosciences), resuspended in an intracellular stain cocktail, and incubated at room temperature for 30 minutes (S1 Table). In the relevant experiments, MHC Class-I tetramer (Mamu-A*01 SIV Gag 181-189, CM9, NIH Tetramer Core Facility) was added for 45 minutes at room

temperature immediately before the chemokine stain. Cells were washed and fixed in 1x BD Stabilizing Fixative (BD Biosciences). Samples were analyzed using the BD FACSymphony A5 Cell Analyzer (BD Bioscience) and FlowJo 10 for Mac OS (Tree Star).

For sorting experiments, thawed PBMC, lung, and bronchial lymph node (BLN) cells were stained in 15 mL conical tubes with live/dead and surface cocktails as described above but with 2x the typical antibody concentration. Cells were washed in FACS buffer and resuspended in RPMI-1640 without phenol red supplemented with 10% FBS. Cells were sorted using fluorescence-activated sorting (FACS) to isolate CD3⁺ T cells from blood and BLN as well as CD3⁺ ivs⁻ and CD3⁺ ivs⁺ cells from lung using the BD FACSAria (BD Bioscience) or MACSQuant Tyto (Miltenyi Biotec).

Single-Cell RNA Sequencing

CD3⁺ T cells from blood and BLN, as well as CD3⁺ ivs⁻ and CD3⁺ ivs⁺ cells from lung, were processed for single-cell RNA sequencing (scRNAseq) following the 10x Genomics® Single Cell Protocols – Cell Preparation Guide for the “preparation of limited samples.” The 10x Genomics Cell Ranger 3.1.0 pipeline was used to process raw data and generate separate barcodes, features, and matrix files for each sample, referencing GTF annotations for the Rhesus macaque genome (Macaca mulatta, GCA_003339765.3). Data analysis was performed using the Seurat package in R, as previously described in Chapter 2 [36]. Briefly, individual Seurat objects were generated for each sample,

and the raw count matrices were merged using the merge command. Cells with more than 5% mitochondrial genes or more than 2500 genes were excluded from further analysis. The standard Seurat workflow for downstream analyses comprised normalization, scaling, graph-based clustering using shared nearest-neighbor, differential gene expression (DEG), and data visualization. As described in Chapter 2, the Harmony algorithm was applied to account for batch effects and biological variability [37].

Differential Gene Expression (DEG) Analysis

DEG analysis was conducted by comparing T cells across tissues using Seurat's FindAllMarkers function. To illustrate these findings, volcano plots were created, highlighting genes with an average log₂ fold change (log₂fc) greater than 0.5 or less than -0.5 and an adjusted p-value less than 0.05 indicating statistical significance.

Gene Set Enrichment Analysis (GSEA)

GSEA was performed as described in Chapter 2 using Hallmark [38], KEGG (<http://www.pathway.jp>), and Reactome [39] gene collections from The Broad Institute Molecular Signature Database (MSigDB) [40,41]. The heatmap in Figure 10B illustrates the net enrichment scores (NES) of significantly enriched pathways in T cells from each tissue. A false discovery rate of 0.1 was used to determine significance.

CellChat

We conducted a thorough analysis of cell communication using the network analysis and pattern recognition methodologies offered by CellChat for R [42]. Following the standard workflow; we predicted the dominant signaling output and input pathways for T cells across tissues.

Results

Intravascular Staining (ivs) in Rhesus Macaques Reveals Differential Tissue

Distribution

Two uninfected Rhesus macaques (RhM) underwent intravascular staining (ivs) by receiving an anti-CD45-AL647 antibody via the saphenous vein, administered five minutes prior to necropsy. Following euthanasia, cells were isolated from tissues and stained for flow cytometry (Fig 1A). We observed varying frequencies of ivs+ cells across different tissues (Figs 1B and 1C). All CD45+ ex-vivo stained cells in the blood were identified as ivs+, confirming the successful administration of the ivs antibody. In the lung, approximately 75% of lymphocytes were ivs+, whereas the vast majority of lymphocytes in BAL, nasal mucosa, and gut were ivs-. Consistent with the findings of Potter et al., we detected CD69 expression, a canonical marker of tissue residence, on ivs- cells in tissues, which was mainly absent on cells in the blood (Fig 1D).

We also observed a distinct difference in the proportions of CD4+ and CD8+ T cells across blood and lung samples (Fig 1E). The CD4:CD8 ratio in

PBMCs was approximately 2, consistent with findings from other NHP studies [43,44]. In stark contrast, the CD4:CD8 ratio in pulmonary ivs+ cells was

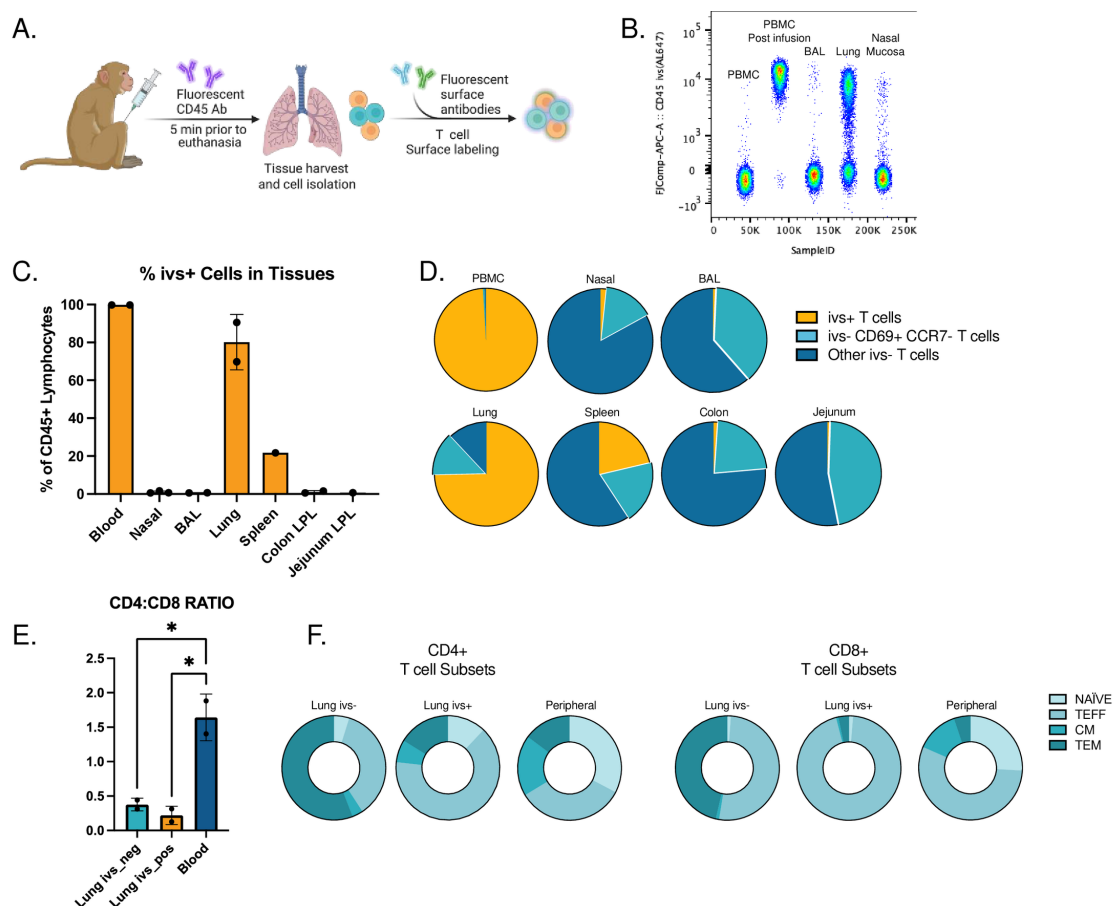


Figure 1. Intravascular staining (ivs) in Rhesus Macaques (RhM). **A.** 30 ug/kg anti-CD45-AL647 (CD45-ivs) was infused into the animals 5 minutes before necropsy. Cells were stained ex-vivo with anti-CD45-BUV395. Overlay plots of the infused antibody are shown for PBMCs (pre- and post-infusion) and tissues harvested at necropsy. **C.** Bar graph depicting ivs+ cells as a percentage of CD45+ Lymphocytes in examined tissues. **D.** Frequencies of ivs+ cells (orange), ivs- CD69+ CCR7- (light blue), and other ivs- (dark blue) T cells in harvested tissues. **E.** CD4 to CD8 T cell ratio in blood and ivs+ and ivs- lung cells. **F.** Proportion of naive (CD62L+ CD44-), effector (CD62L- CD44+), central memory (CM, CD62L+ CD44+), and effector memory (CD62L- CD95+ CD44+) subsets within the CD4 and CD8 T cell populations. n=2

significantly lower, revealing a dominance of CD8+ T cells — a pattern echoing the pulmonary ivs- population. This confirms the findings of Potter and colleagues and challenges the notion of ivs+ cells simply being “blood

contaminants,” for if they were, we would expect their CD4:CD8 ratio to closely resemble that of the blood [24]. Further underlying this divergence, we noted a pronounced shift in T cell subset distribution across the blood, lung ivs- and lung ivs+ populations (Fig 1F). Specifically, T_{EFF} predominated in the pulmonary ivs+ subset, far exceeding their proportions in both the blood and pulmonary ivs- compartments.

T cell Profiles in Blood, Lung, and Nasal Mucosa

To delve deeper into the characteristics distinguishing pulmonary ivs+ and ivs- cells, we conducted a tSNE analysis on T cells isolated from blood, lung, and nasal mucosa (Fig 2). This analysis revealed nine primary clusters of T cells, each characterized by a distinct presence across tissues (Fig 2A-F). Four of these clusters (Clusters 1, 6, 7, and 9) were identified within the vasculature (CD45-ivs+). Clusters 1 and 6 (comprised of CD4+ T cells) and Cluster 7 (CD8+ T cells) were enriched in the blood. Conversely, Cluster 9, characterized by CD8+ T cells, was found mainly in the lung vasculature. These pulmonary ivs+ CD8+ T cells exhibited enhanced cytotoxic potential, demonstrated by elevated GZMB expression (Figs 2B and S1), and constituted ~40% of the T cells isolated from the lung. These CD8+ T cells were predominantly CD45RA+ CD44+ CD62L-, with variable CD69 expression. Additionally, we identified four clusters (Clusters 2, 4, 5, and 8) of T cells exhibiting a resident memory phenotype (CD69+, ivs-) found in the lung, BAL, and nasal mucosa. Lastly, a separate

cluster of CD4+ T cells was found mainly within the nasal mucosa, primarily demonstrating a naïve phenotype (Cluster 3, CD4+ CD62L+ CD45RA+, ivs-).

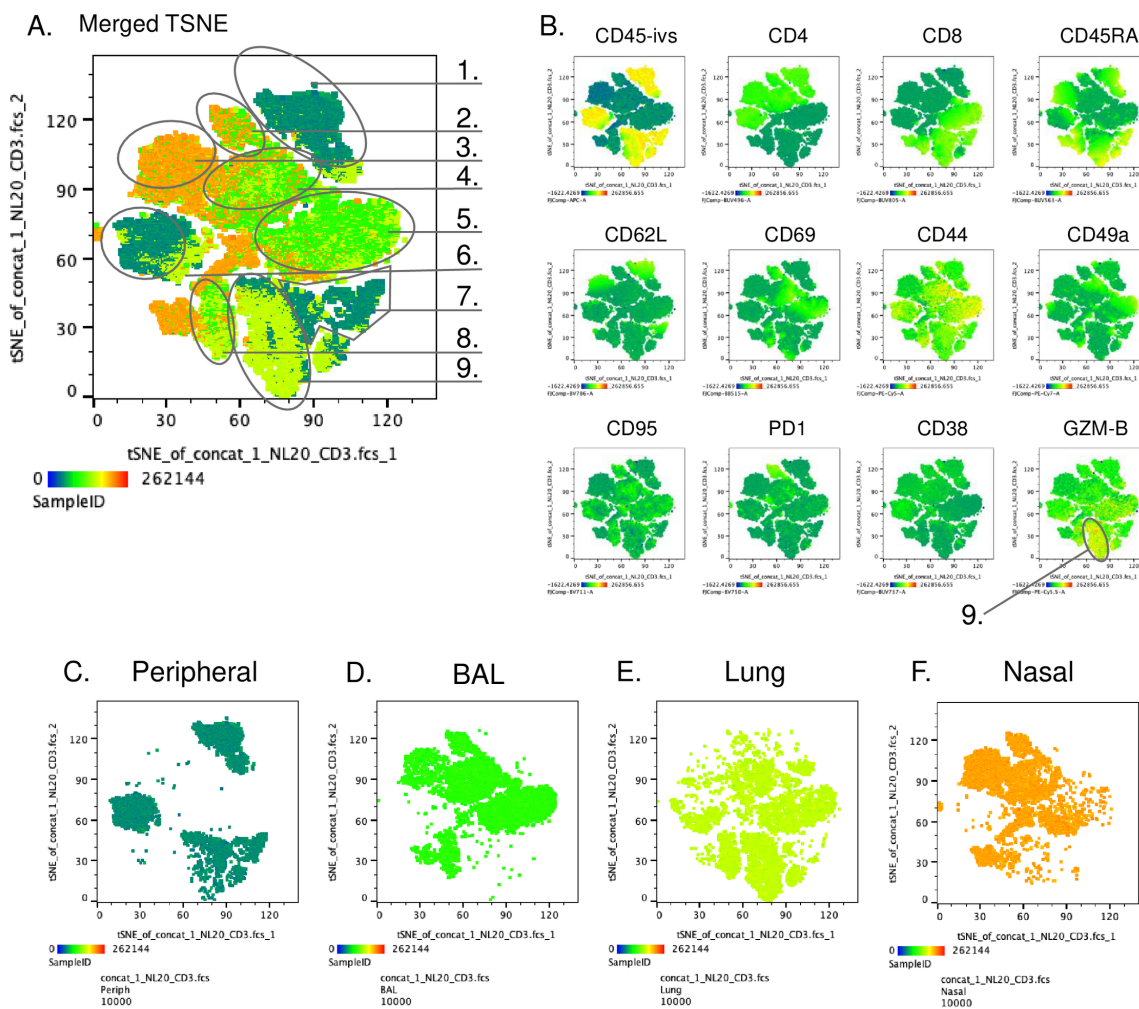


Figure 2. tSNE analysis of CD3+ T cells isolated from blood and respiratory tissue. A. Merged tSNE of CD3+ T cells isolated from Blood (C), BAL (D), lung (E), and nasal mucosa (F). Representative RM animal shown (NL20)

CD69 Expression Across Peripheral and Pulmonary T cells

CD69 serves a dual function in T cell phenotyping. Constitutive CD69 expression is a hallmark of T_{RM} , although this is not considered a perfect marker

as not all resident memory T cells express CD69. Confounding this, CD69 also acts as a marker of recent activation in effector T cells, which upregulate CD69 upon recognition of their cognate antigen, subsequently preventing their egress from tissues [15,45,46]. Here, we found that CD4⁺ and CD8⁺ T cells in the blood showed minimal to no expression of CD69 (Fig 3A). Conversely, in the lung, approximately 50% of the ivs⁻ CD4⁺ T cells and 70% of the ivs⁻ CD8⁺ T cells expressed CD69. While only a small fraction of pulmonary ivs⁺ CD4⁺ T cells expressed CD69, a considerable ~30% of the CD8⁺ T cells were CD69 positive. This expression pattern may reflect a recently activated status or hint towards a specialized vascular “resident-like” phenotype.

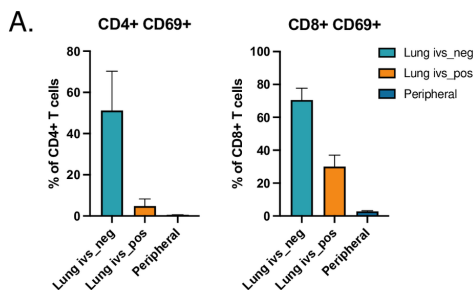


Figure 3. CD69 expression on T cells isolated from lung (ivs⁻ and ivs⁺) and blood. A. CD69 expression on CD4 and CD8 T cell populations isolated from lung (both ivs⁺ and ivs⁻) and peripheral blood. n=2

SIV Infection and T cell Dynamics in Rhesus Macaques

We then aimed to investigate the functional capabilities of pulmonary ivs⁺ and ivs⁻ CD8⁺ T cells in SIV-infected RhM. Four RhM were exposed to SIVmac239 and placed on antiretroviral treatment (ART) two weeks following

infection. ART treatment continued for approximately one year, after which the animals were euthanized four weeks following the cessation of ART (Fig 4A). Viral and T cell dynamics followed the typical pattern with peak viremia at approximately two weeks post-infection (Fig 4B). The animals experienced an initial decline in peripheral CD4⁺ T cells, which began to rebound two weeks after the initiation of ART treatment (Fig 4C and 4D). SIV was also detected in BAL at two- and four-weeks post-infection with CD4⁺ and CD8⁺ T cell kinetics similar to that in the blood (Figs 4E-4G). Sampling of BAL cells over the course of infection revealed SIV-specific T-cell responses during acute SIV infection and at low levels over the course of infection (Fig 4H and 4I).

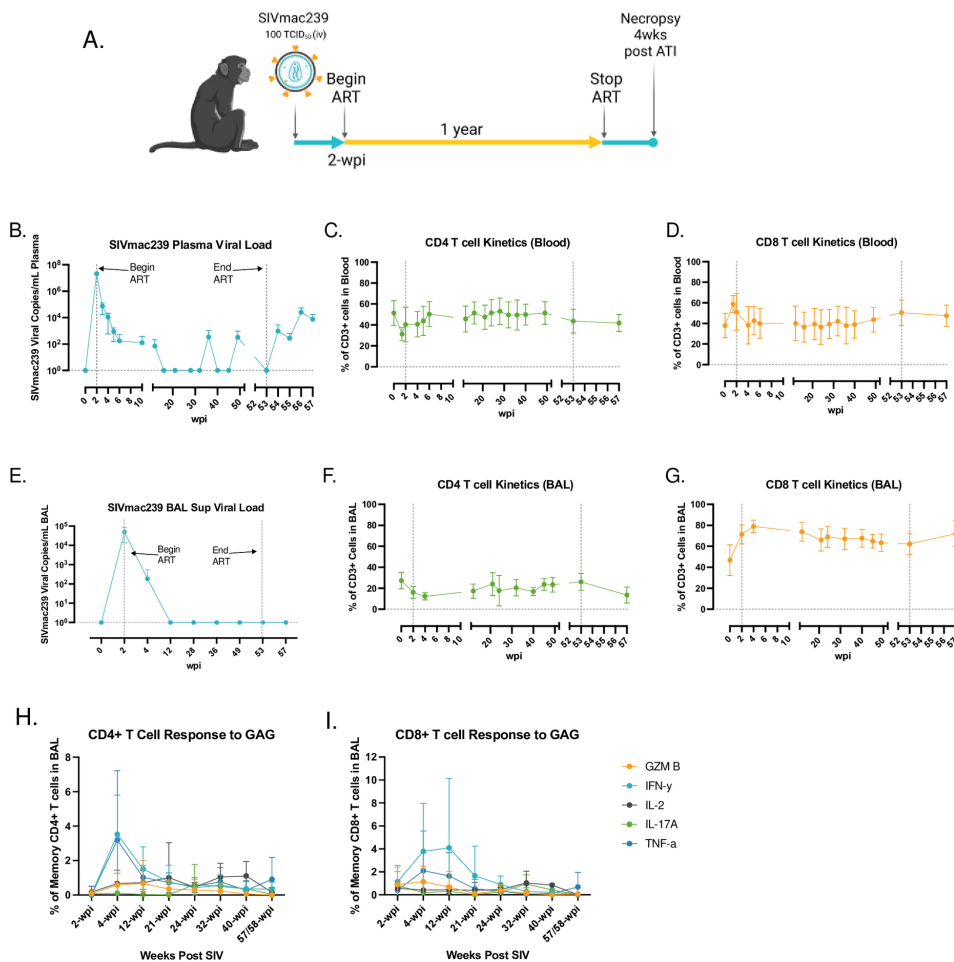


Figure 4. Viral and T cell Dynamics in SIVmac239 infected Rhesus Macaques (RhM). **A.** Overall study design. Four RhM were inoculated with SIVmac239 (100 TCID₅₀, iv). ART treatment was initiated 2 weeks after infection and continued for approximately one year. Animals were sacrificed 4 weeks post-ART interruption. **B&E.** Quantification of SIVmac239 RNA levels in plasma (**B**) and BAL (**E**) overtime (Quantitative RT-PCR). T cell kinetics in Blood (**C&D**) and bronchoalveolar lavage (BAL, **F&G**). **H&I.** Pulmonary SIV-specific T-cell responses were detected during acute SIV infection and at low levels over the course of infection. Longitudinal antigen-specific T cell responses plotted as mean +/- SD after background subtraction of unstimulated control.

Phenotypic Trends of *ivs*⁺ and *ivs*⁻ CD8⁺ T Cells Post-SIV Infection

Phenotypic analysis of pulmonary (*ivs*⁻ and *ivs*⁺) and peripheral T cells at necropsy revealed patterns similar to those of the naïve animals (Figs 1E, 1F, and 5). While SIV infection resulted in a decrease in CD4⁺ T cells and thus the CD4:CD8 ratio, the distribution of T cells was similar to that of the naïve animals

with far greater proportions of CD8+ T cells in both the lung tissue and lung vasculature as compared to the blood (Fig 5A). Again, we found that the ivs- cells had significantly higher expression of the memory marker CD95 compared to ivs+ cells, supporting the predominance of effector T cells in the pulmonary vasculature (Fig 5B). Similar to the naïve animals, pulmonary ivs- memory CD8+ T cells displayed significantly higher expression of CD69, with ivs+ cells exhibiting greater CD69 expression than those in the blood (Fig 5C and 6A).

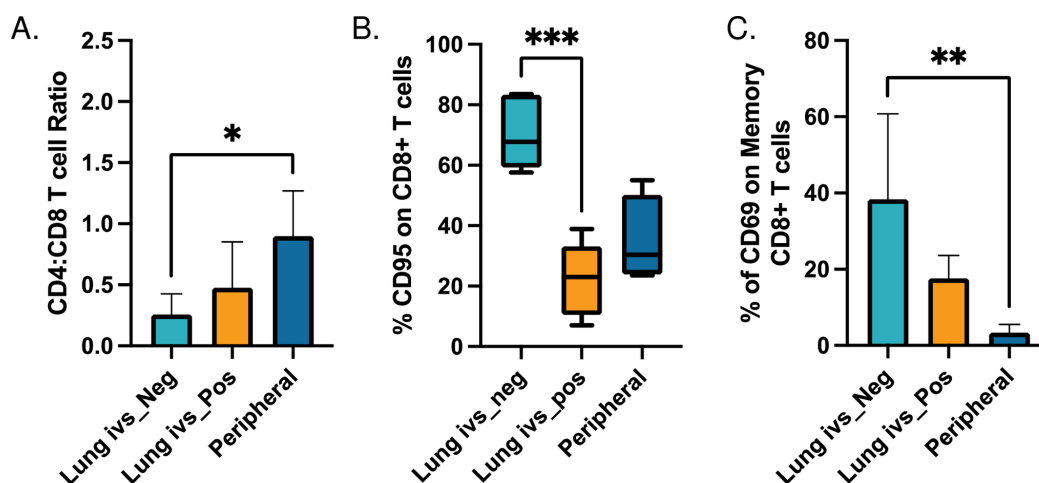


Figure 5. T cell phenotyping across blood and lung in SIV-infected Rhesus Macaques (RhM). **A.** CD4 to CD8 T cell ratio in blood and ivs+ and ivs- lung cells. **B.** CD8 T cell expression of memory marker CD95 across blood and lung (ivs+ and ivs-). **C.** CD69 expression frequency on memory CD8+ T cells in blood and lung. Plotted as mean \pm SD. The Kruskal-Wallis test for multiple comparisons was used to determine significance. *p < 0.05, **p < 0.01; ***p < 0.001

Functional Profiling of Memory CD8+ T Cells in the Lung

We then examined functional responses of memory CD8+ T cells present in the lung. Memory CD8+ T cells expressing GZMB, IFN- γ , and TNF- α were found in significantly higher proportions in the pulmonary ivs+ compartment,

whereas those producing IL-2 were predominantly located within the tissue (ivs-) (Fig 6A). We then assessed the frequency of cytokine-producing CD8+ T cells in peripheral and pulmonary ivs- and ivs+ compartments (S2 Fig). Because effector CD8+ T cells dominate in the pulmonary vasculature, we examined both the overall CD8+ T cell responses and the memory CD8+ T cell responses following overnight stimulation with SIV Gag peptides. We found that the pulmonary ivs+ cells had significantly higher levels of GZMB and TNF- α (overall CD8+ T cells, S2A Fig) with significantly lower levels of IL-2 (memory CD8+ T cells, S2B Fig).

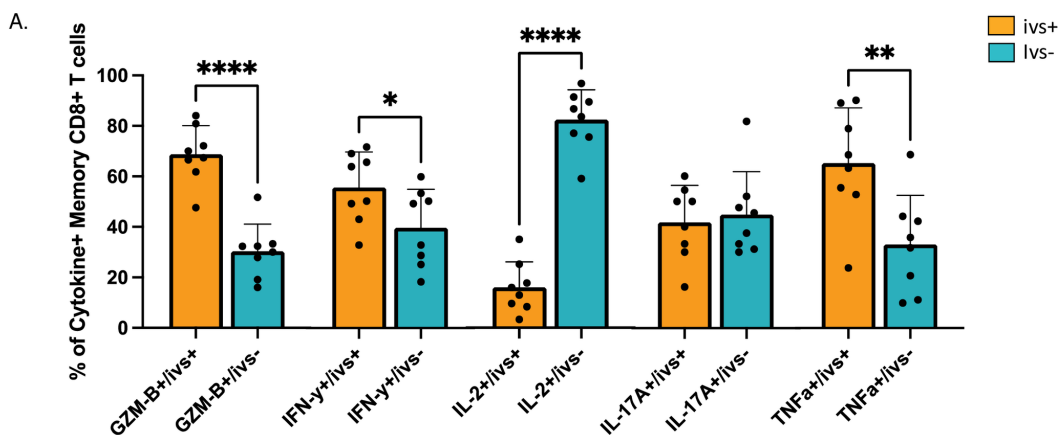


Figure 6. Pulmonary ivs+ CD8+ T cells have increased cytotoxic capacity. A. Frequency of cytokine-producing memory CD8+ T cells in ivs+ and ivs- cells isolated from lungs. Plotted as mean \pm SD (left and right lung). Unpaired t-test (and Shapiro-Walk test for normality) used to determine significance. * $p < 0.05$, ** $p < 0.01$; *** $p < 0.001$, **** $p < 0.0001$.

Gating strategy: Time>Live>Lymphocytes>Single cells>CD45_ex-vivo>CD3>CD8>CD95>Cytokine>ivs+/ivs-

Characterization of SIV-Specific CD8+ T cells Through MHC Class-I Tetramer

Staining

We then aimed to characterize SIV-specific CD8+ T cells through MHC Class-I tetramer staining (A01-CM9+) (Fig 7A – 7D) in one of the SIV-infected animals. Flow cytometry plots in Figure 7B illustrate Tetramer+ memory CD8 T cells present at 53 and 58 weeks post-SIV infection. Four weeks post-ART interruption (week 58), we observed a marked expansion of SIV-specific memory CD8+ T cells in both blood (rising from 1.58% to 7.61%) and BAL (rising from 1.00% to 5.56%). When comparing pulmonary tissue-resident and vasculature-associated cells, we found SIV-specific CD8+ T cells to be more abundant in the pulmonary tissues (ranging from 4-8%) than in the pulmonary vasculature (ranging between 2-3%), varying by lung lobe (Fig 7C). In this animal, we observed an unusually high proportion of ivs+ cells in BAL at ~ 10%. Typically, our findings show that only 1-2% of BAL cells stain positive for the infusion antibody. Given this, we suspect that the BAL sample from this particular animal likely contained significant blood contamination. As a result, we omitted the BAL ivs+ cells from further analysis.

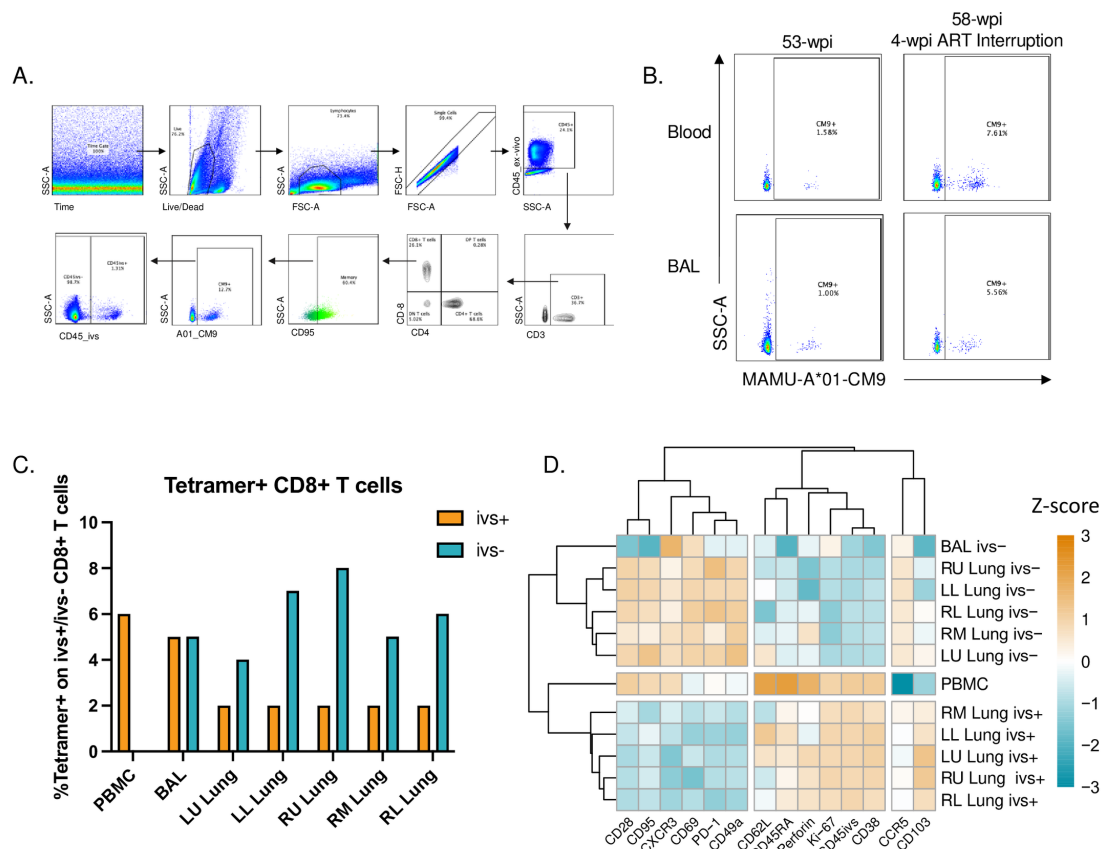


Figure 7. MHC Class-I tetramer staining of SIV-specific CD8+ T cells pre and 4 weeks post-ART cessation. **A.** Representative flow plots illustrating gating strategy. **B.** Flow cytometry plots of Tetramer+ (A01-CM9+) memory CD8+ T cells in blood and BAL at 53- and 58-weeks post SIV infection. Four weeks following the cessation of ART, an expansion of SIV-specific memory CD8+ T cells was identified in both blood and BAL.

Characterization of the phenotypic differences between the ivs+, ivs-, and circulating SIV-specific CD8+ T cells showed that ivs- cells in the lower respiratory tract expressed markers indicative of T_{RM}. These cells show higher expression of retention markers (CD69, CD49a), lower expression of markers that promote tissue egress (CD62L), exhibit higher expression of chemokine receptors associated with tissue residence (CXCR3, CCR5), and show evidence of memory (CD95, CD45RA-). Lack of Ki-67 and CD38 expression, combined

with expression of PD-1, suggests that the CD69 expression on ivs- cells is not a consequence of recent activation but rather signifies tissue residency.

In contrast, the ivs+ virus-specific CD8+ T cells isolated from the lung show characteristics consistent with a recently activated effector phenotype, underscored by elevated Ki-67 and CD38 expression. Setting them apart from virus-specific T cells in the blood, the pulmonary ivs+ cells exhibited reduced expression of CD62L and elevated expression of CD103 (a cell adhesion marker). Reflecting the predominance of effector-like CD8+ T cells within the pulmonary vasculature discussed earlier, these cells displayed decreased CD95 expression compared to both T_{RM} and peripheral T cells.

Single-Cell RNA Sequencing

We then set out to examine the transcriptomic profiles of pulmonary tissue-resident (ivs-) and vasculature-associated (ivs+) T cells (Fig 8A). Using FACS, we isolated CD3+ T cells from blood and bronchial lymph node (BLN) as well as CD3+ ivs- and CD3+ ivs+ cells from the lungs of an SIV-infected RhM and performed scRNAseq on each subset. Uniform manifold approximation and projection (UMAP) analysis revealed 10 unique T cell clusters with varying distribution across the four compartments (Figs 8B and 8C). Six of these clusters expressed *CD8A* (Pops 0, 1, 2, 3, 5, and 9), two expressed *CD4* (Pops 4 and 8), and the remaining two clusters were undefined (Pops 6 and 7).

Pop 0 (orange) had molecular signatures consistent with T_{RM}. These CD8+ T cells were characterized by expression of *CD69*, *ITGAE* (CD103), *ITGA1*

(CD49a), and *CD44*. Pop 0 was the dominant population in the pulmonary ivs- compartment at 34%, it was also found in the BLN, accounting for 26% of T cells in the BLN. Pop 1 (bright blue) consisted of CD8 T_{EFF}/T_{EM} cells, notably distinguished by their elevated *GZMB* expression. Unique to this cluster was the expression of the fractalkine/CX3CL1 receptor *CX3CR1*. Studies in mice have shown that *CX3CR1*^{hi} CD8⁺ T cells are primarily localized within the vasculature [47]. Here, this population was highly enriched in the pulmonary vasculature, accounting for 31% of the ivs⁺ T cells in the lung, was largely undetectable in tissues, and constituted 12% of T cells in the blood. Pop 2 (green) represented another distinct population of CD8⁺ T_{EFF}/T_{EM} cells. Pop 2 cells were similar to Pop 1 but with decreased expression of *GZMB*, *TGFBR2/3*, integrins *ITGA1*, *ITGA4*, *ITGAE*, *ITGAL*, *ITGAV*, *ITGB1*, and *ITGB2*, as well as markers associated with cell adhesion (*CX3CR1*, *CD99*) (Figs 8D-8E, Tables S2 and S3). Pop 2 cells were found in similar proportions in both the pulmonary ivs- and ivs⁺ compartments, appeared at lower levels in the blood, and were rarely detected in the BLN. Pop 3 (dark blue) was found in all four tissues and consisted of CD8⁺ T cells with elevated *CCL5*, *IL2RB*, and *KLRB1* expression (blood = 18%, lung ivs⁺ = 15%, lung ivs- = 9%, and BLN = 5%). Pop 4 (gray) represents naïve or resting CD4⁺ T cells. This population was characterized by markers such as *CCR7*, *SELL*, *TCF7*, and *PECAM1*, with a notable predominance in the BLN, making up 39% of the T cell subset. Pop 5 (yellow) consisted of CD8⁺ CCR7⁺ T_{CM} cells distinguished by residency markers *ITGA1* and *CD69* and were primarily localized within the BLN and lung tissue (ivs-). Pop 6 (pink) represents an

undefined subset of T cells largely found in the blood. Pop 7 (light blue), a rare cluster, appeared both in lung ivs- and ivs+ and closely resembled Pop 6. Pop 8 (brown), an extremely rare population found in the BLN and blood, possibly representing follicular helper or recently activated CD4+ T cells with expression of *PECAM1*, *BCL6*, *CXCR5*, *CD38*, *CD44*, and *SELL*. Lastly, Pop 9 (blue) consisted of proliferating CD8+ T cells (*MKI67* and *HMGB2*).

Each tissue environment seemed to favor specific T cell populations, reflecting the unique functional demands of those tissues. CD4+ T cells were the dominant T cell population in the BLN, whereas CD8+ T cells were dominant in the lung (both ivs- and ivs+). The blood displayed a more heterogeneous landscape of T cells, with no single population that was overwhelmingly dominant, which suggests a broader repertoire of T cell states, catering to systemic requirements.

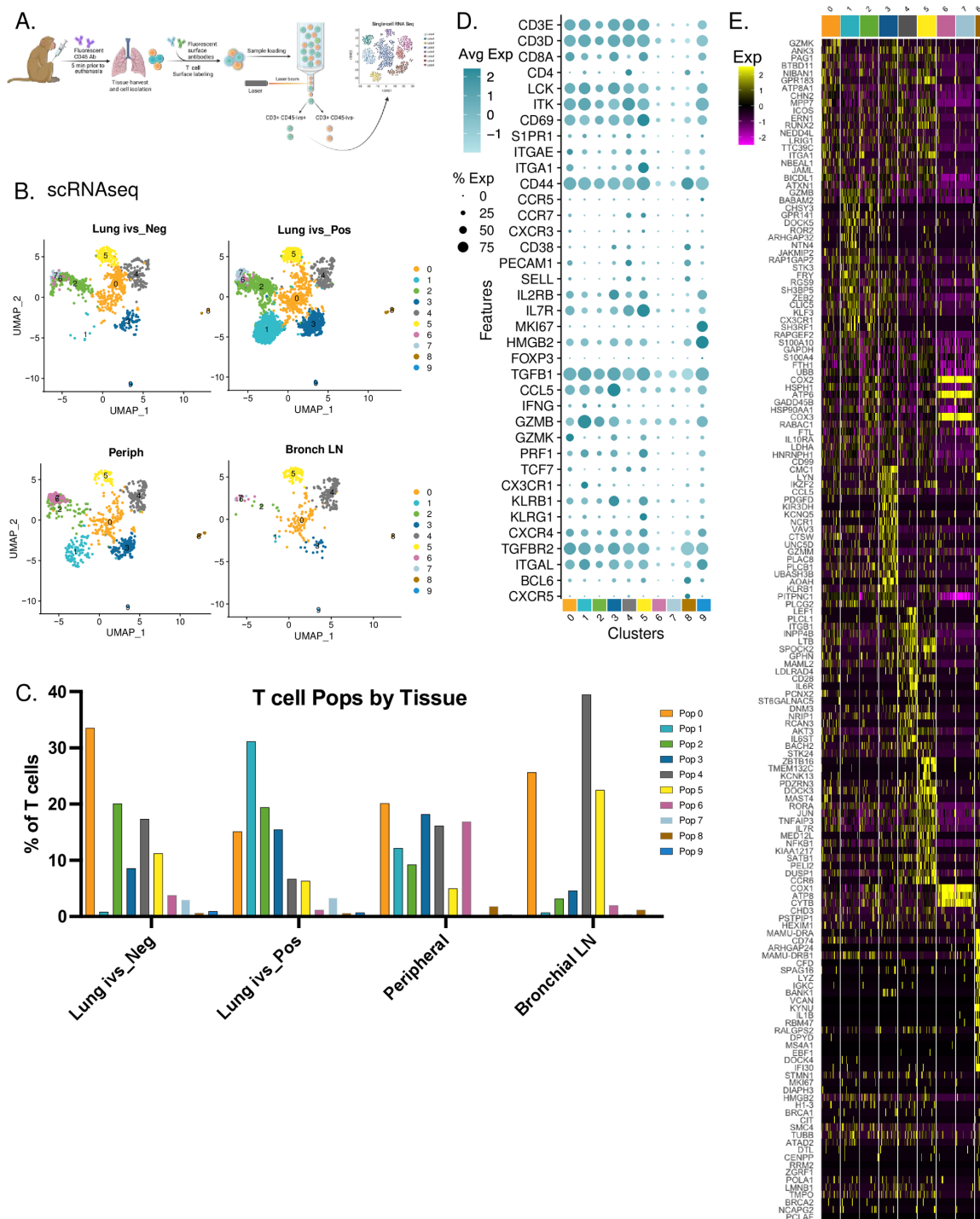


Figure 8. Single-cell sequencing analysis of CD3+ T cells isolated from lung (ivs+ and ivs-), bronchial lymph node (LN), and blood. **A.** Illustration of study design. 30 ug/kg anti-CD45-AL647 (CD45-ivs) was infused into a RhM 5 minutes prior to necropsy. Harvested cells from lung, bronchial lymph node, and blood were sorted using FACS to isolate CD3+ T cells. Additionally, we performed a two-way sort to isolate CD3+ ivs- and CD3+ ivs+ cells from lung. **B.** UMAP plots illustrating scRNAseq data of CD3+ T cells. Clustering analysis identified 10 unique T cell clusters. **C.** T cell subset distribution across lung ivs-, lung ivs+, blood, and bronchial LN populations. **D.** Markers used for cell type identification. The color of the dot indicates average gene expression (Avg. Expression), while the size of the dot signifies the percentage of cells expressing that particular gene (Percent Expressed). **E.** Top differentially expressed genes (DEGs) for each Seurat cluster.

Tissue-Specific Gene Expression Profiling of T Cells

We then set out to explore the phenotypic and functional transcriptomic profiles of T cells across tissues (Fig 9). Our analysis revealed distinct gene expression patterns related to tissue residency, lymph node homing, and T cell functionality. T cells from lung tissue (ivs-) consistently displayed the highest expression of transcripts associated with tissue residence (*CD69*, *ITGAE* (CD103), *ITGA1* (CD49a), *CD44*, and *RUNX3*) (Fig 9A). Notably, T cells in the lung vasculature (ivs+) displayed a marked increase in expression of residency markers *CD69* (compared to peripheral T cells) as well as *CD44* and *RUNX3* (compared to both peripheral and BLN T cells). As expected, T cells in the BLN demonstrated increased expression of lymph node homing receptors *CCR7* and *SELL* (CD62L).

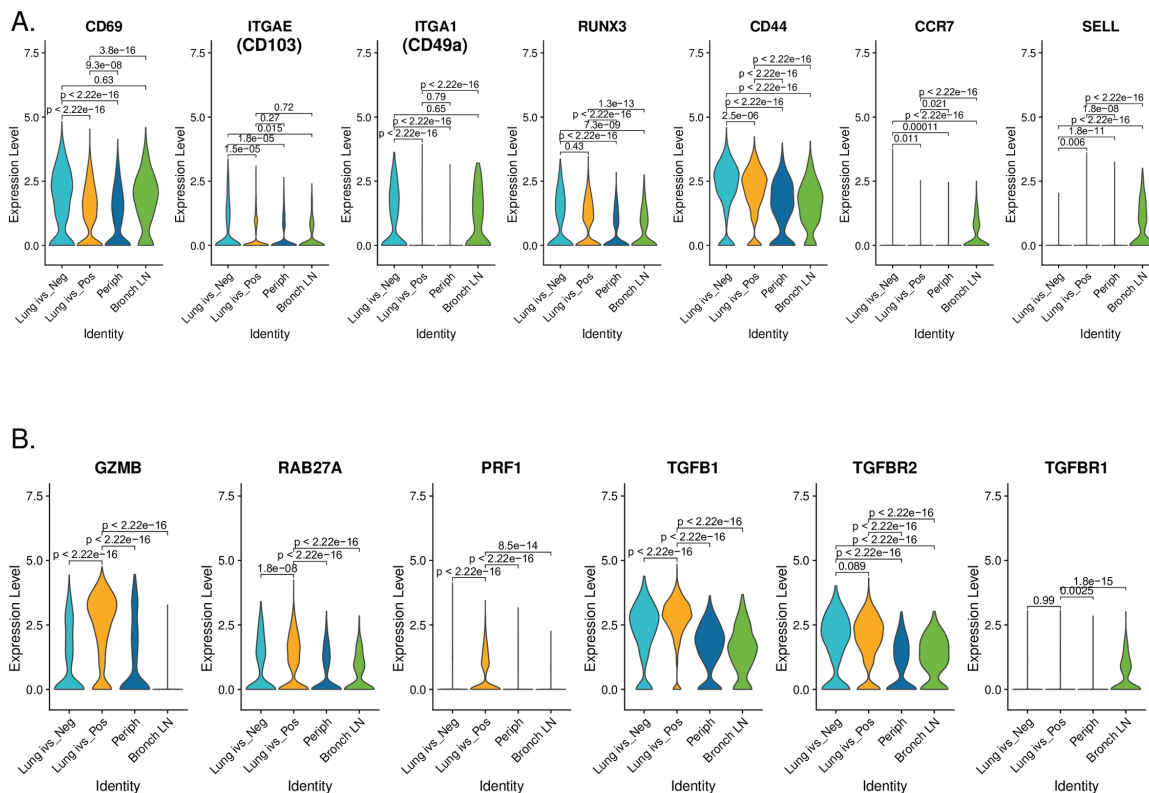


Figure 9. Single-cell analysis of T cells across tissues. A and B. Violin plots depicting gene expression of markers associated with tissue residence (*CD69*, *ITGAE*, *CD49a*, *CD44*, and *RUNX3*), lymph node homing (*CCR7* and *CD62L*) and T cell functions (*GZMB*, *RAB27A*, *PRF1*, *TGFB1*, *TGFB2*, and *TGFB1*). Kruskal-Wallis comparison of means used to determine significance. ggpubr/ggsignif package in R.

Functional profiling also showed distinct differences across tissues. The lung ivs+ cells were found to have high expression of transcripts associated with cytotoxic killer cells, with significantly higher levels of *GZMB*, *RAB27A*, and *PRFN1* compared to T cells from other sites. Both subsets of lung T cells – ivs- and ivs+ – featured considerably higher expression of *TGFB1* and *TGFB2*, while T cells in the BLN had the highest expression of *TGFB1* (Fig 9B).

Differential Transcriptomic Signatures

DEGs and GSEA revealed additional phenotypic and functional differences among the T cells (Figs 10 and S3). Lung ivs- T cells displayed enrichment in the TNF- α , IL-2, IL-4/IL-13, and IFN- γ inflammatory signaling pathways (Fig 10B). DEG analysis showed increased expression of genes associated with tissue residence, such as *ITGA1*(CD49a) and *ICOS* [48], further defining their tissue-bound nature (Figs 10A and S3).

GSEA of pulmonary vasculature (ivs+) T cells indicated unique immunological signaling pathways that differed from those in lung tissue. Specifically, the ivs+ cells displayed enrichment in immune signaling pathways linked to IL-10, IL-3/IL-5/GM-CSF, and Type I IFN (Fig 10B). *GZMB* ranked second among the top DEGs, emphasizing their cytotoxic capacity, which was further underscored by enrichment in genes associated with Natural Killer (NK) cell cytotoxicity (Figs 10A, 10B, and S3). Another notable feature of these cells was their upregulation of heat shock proteins (HSP), namely *HSP90A1*, *HSPH1*, and *HSPD1*. Recent studies have indicated that HSPs are upregulated upon CD3/CD28 stimulation [49]. We also noted the enrichment of several metabolism pathways, including glycosaminoglycan, heme, and lipids. Enrichment of the antigen processing and presentation and the platelet activation, signaling, and aggregation pathways was another interesting finding. Endothelial cells in the vasculature have the ability to act as semi-professional antigen-presenting cells [50]. The upregulation of the antigen processing and presentation pathway

suggests a possible engagement between the ivs+ cells and endothelial cells in the pulmonary vasculature.

T cells in the blood and BLN node were predominately characterized by pathways associated with protein synthesis and metabolism (Fig 10B). T cells localized to the BLN displayed genes linked to lymph node homing, including *SELL* and *PECAM1*, as well as elevated expression of *JUN*, *TCF7*, and *LEF1*, suggesting a predominance of cells with a more naïve or recently activated phenotype (Fig 10A). Interestingly, analysis of DEGs from T cells in the blood revealed marked downregulation of genes compared to the other tissues, highlighting these cells' less differentiated nature (Fig 10A).

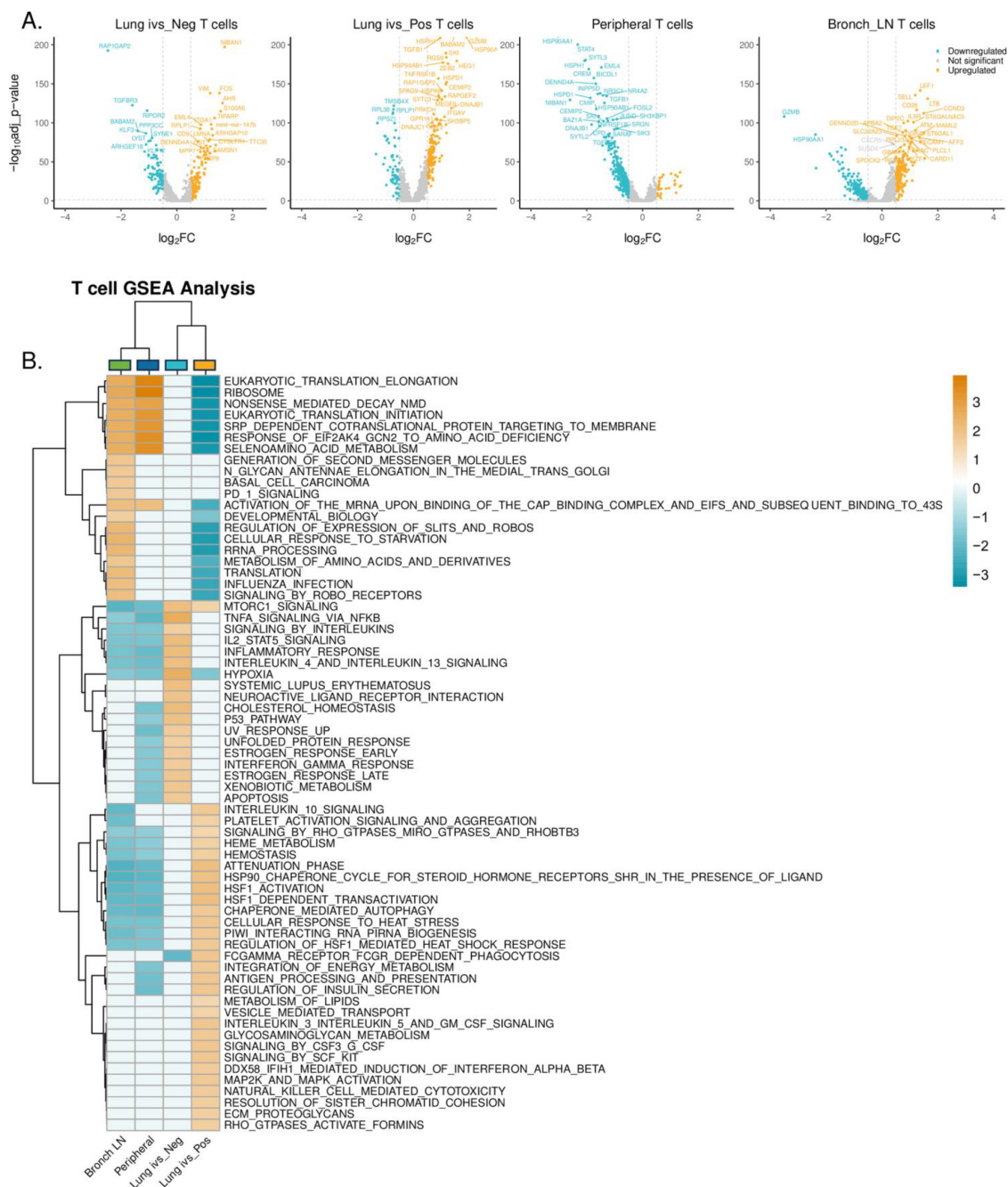


Figure 10. Differential gene expression (DEG) and gene set enrichment analysis (GSEA) of T cells across tissues. **A.** Volcano plots displaying significantly upregulated and downregulated DEGs in T cells isolated from lung (ivs+ and ivs-), blood (Periph), and bronchial LN (average log₂ fold change (log₂fc) greater than 0.5 or less than -0.5 and an adjusted p-value less than 0.05). **B.** GSEA results comparing DEGs in T cells isolated from lung (ivs+ and ivs-), blood (Periph), and bronchial LN. A false discovery rate (FDR) of 0.1 was used to determine significance.

Cellular Communication Analysis with CellChat

To elucidate communication patterns among T cells in the pulmonary tissue, pulmonary vasculature, blood, and BLN, we conducted CellChat analysis [42]. Signaling between soluble and membrane-bound factors significantly influences a range of cellular outcomes. While cell interactions predominately occur within limited spaces, the communication networks identified among T cells across various compartments extend beyond direct cell-to-cell contact. They can also offer a deeper understanding of the unique outgoing and incoming signaling characteristics specific to each location. Here, CellChat analysis identified 18 significant ligand-receptor pairs across our T cell subsets (Fig 11A). T cells within the pulmonary vasculature (ivs+) emerged as the dominant senders, displaying robust outgoing signaling patterns, while T cells in the BLN were the dominant receivers (Fig 11B). Although pulmonary ivs+ cells exhibited pathways related to soluble mediators such as TGF β and IL-2, a consistent theme was their enrichment in receptors/ligands linked to T cell migration, adhesion, and extravasation (Fig 11C). Key markers such as *CD99*, *ALCAM*, *ADGRE5*, *ITGB2*, *ITGAL*, and *SELPLG* were enriched in the pulmonary ivs+ T cells (Figs 11C and 11D) [51–55].

Analysis of cellular interactions within the pulmonary ivs- cells revealed pathways linked to the regulation of T cell effector responses, including cytotoxic capacity and cytokine secretion (CLEC2D-KLRB1) [56], as well as regulation of T cell activation and the suppression of inflammation (TRAIL) (Fig 11) [57–59]. The CLEC2D-KLRB1 pathway was also enriched in the ivs+ subset, although to a

lesser degree. Both the ivs- and ivs+ T cell subsets showed significant involvement in the TGF β pathway, aligning with the elevated expression of *TGFBR2* (Fig 9B). TGF β has been shown to promote differentiation and survival of T_{RM} [60,61]. The enhanced propensity for TGF β signaling in both ivs- and ivs+ cells supports a tissue-resident/tissue-resident-“like” phenotype. This, coupled with upregulation of CLEC2D-KLRB1 and TRAIL pathways in the ivs- subset, suggests a possible local adaptation within the lung environment, likely aimed at regulating immune responses to mitigate excessive inflammation and potential tissue damage.

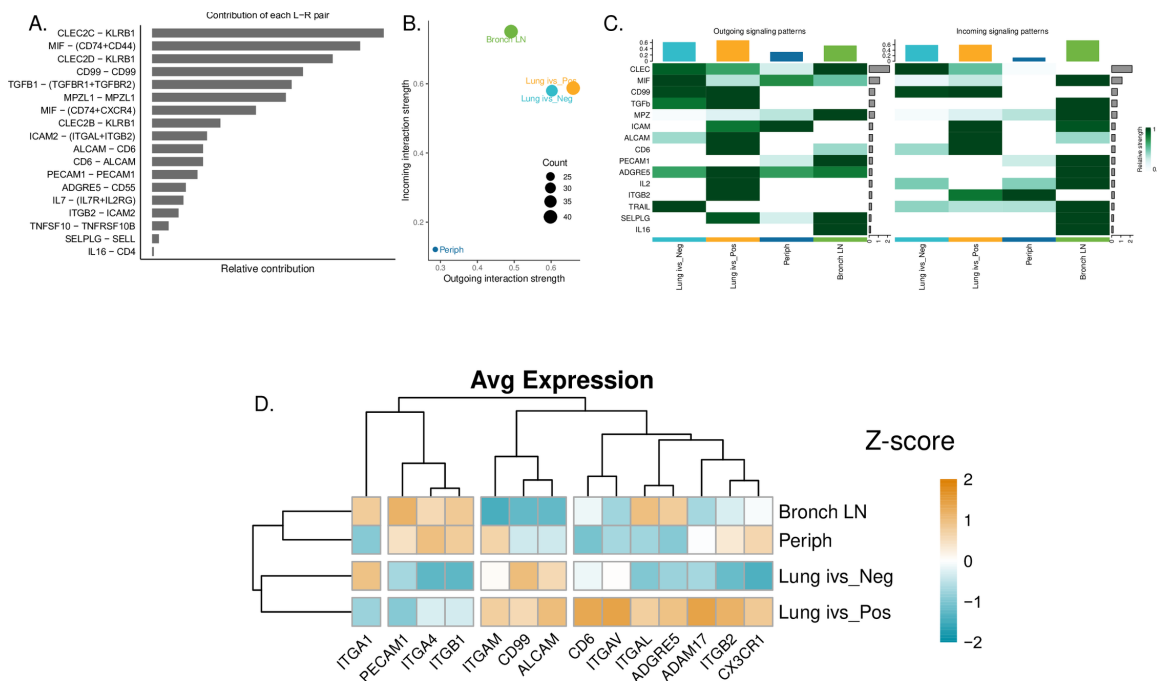


Figure 11. Cell-cell communication analysis reveals upregulation of transendothelial migration transcripts in pulmonary ivs+ T cells. **A.** Contribution analysis of individual ligand-receptor pairs to the overall signaling pathway. **B.** Scatter plot representing incoming and outgoing signaling strength of lung ivs-, lung ivs+, peripheral, and LN T cells. **C.** Patterns of outgoing and incoming signals. **D.** Heatmap illustrating expression of markers associated with cell adhesion and extravasation.

Adhesion and Extravasation Gene Analysis

We identified a heterogeneous expression profile upon examining adhesion and extravasation genes among the T cell subsets (Fig 11D). Lung ivs- and ivs+ cells displayed elevated expression of the genes *ALCAM* (cell adhesion) and *CD99* (extravasation). High expression of *CD99* suggests that the ivs+ cells are primed for or in the process of migrating into the lung tissue. For the ivs- T cells, the elevated expression of *CD99* could be a remnant of their extravasation process [62,63]. Transcripts for, *ITGAL* (CD11a), *ITGAM* (CD11b), and *ITGB2* (CD18) were also enriched in the ivs+ T cell population. *ITGAL* and *ITGB2* together form the integrin LFA-1, while *ITGAM* and *ITGB2* form Mac-1 [54,64–67]. These integrins are crucial for leukocyte adhesion. They establish high-affinity interactions with endothelial intercellular adhesion molecule 1 (ICAM-1) and ICAM-2, resulting in the cells' firm arrest and attachment to the vascular endothelium. In addition, the integrin alpha V subunit *ITGAV* and *CD6*, also involved in cell adhesion, were found mainly in ivs+ T cell subset [52].

The integrin alpha 1 subunit (*ITGA1*, CD49a), which is associated with tissue residence, was enriched in both lung ivs- and BLN T cells. T cells in the BLN also displayed markers similar to T cells in both the blood and lung ivs+ compartments. BLN and peripheral T cells exhibited elevated expression of *PECAM1*, *ITGA4*, and *ITGB1* transcripts. Together, *ITGA4* (CD49d) and *ITGB1* (CD29) form the integrin VLA-4, which binds to vascular cell adhesion molecule 1 (VCAM-1) on endothelial cells [68], suggesting T cells in the BLN and blood follow different adhesion and extravasation pathways than those in the lung.

Similar to T cells in the pulmonary vasculature, BLN T cells exhibited heightened expression of *ITGAL* and *ADGRE5*.

Pulmonary ivs+ CD8+ T cells have a transcriptomic profile distinct from peripheral CD8+ T cells

Because the pulmonary ivs+ subset was enriched in CD8+ T cells, we aimed to tease out the differences between the ivs+ CD8+ T cells and those in the periphery. We found that the ivs+ CD8+ T cells had significantly higher expression of markers promoting retention (*CD69*, *RUNX3*, and *CD44*) and decreased expression of markers linked to trafficking (*SELL/CD62L* and *KLF2*) (Fig 12) [69–72]. Pulmonary ivs+ CD8+ T cells also showed significant enrichment in genes coding for proteins involved in cytotoxicity (*GZMB*, *RAB27A*, *PRF1*, *KLRB1*, *IL21R*, *CCL3*, and *SEMA7A*) [73]. We then compared molecular signatures associated with cell surface interactions at the vasculature wall (Reactome pathway analysis, DOI 10.3180/REACT_12051.1). Our analysis revealed that CD8+ T cells within the lung vasculature displayed significantly higher expression of genes promoting cell surface-vascular wall interactions than their peripheral counterparts. Specifically, pulmonary ivs+ CD8+ T cells exhibited increased expression of key genes such as *LYN*, *TGFB1*, *PIK3R1*, *INPP5D*, *ITGAV*, *DOK2*, *ITGA5*, *CD44*, *SLC7A5*, *PLCG1*, *GRB2*, *SLC3A2*, *ITGB2*, *ATP1B3*, *ITGAL*, and *F11R* (Fig 13). This suggests a heightened ability for the pulmonary ivs+ T cells to interact with endothelial cells at the pulmonary vascular wall and lends additional evidence of a “resident-like” phenotype. Similar to the

overall peripheral T cell subset, peripheral CD8+ T cells had significantly higher *PECAM1*, *SELL*, and *ITGA4* expression.

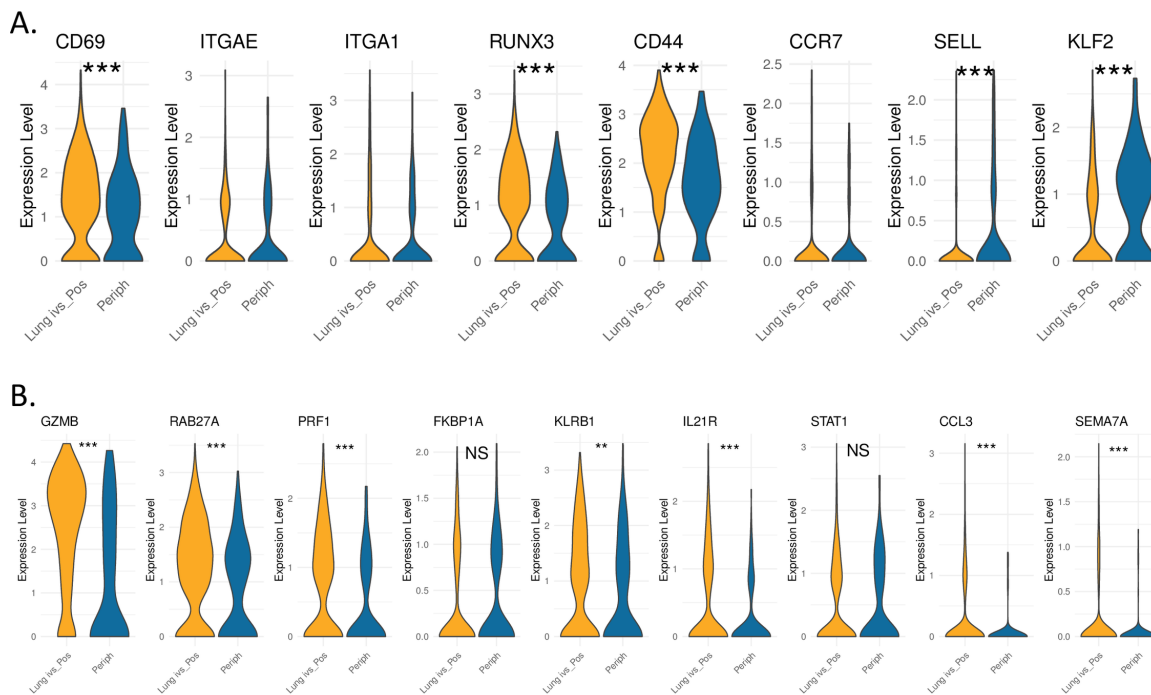


Figure 12. Transcriptomic expression of genes associated with tissue residency (A) and cytotoxicity (B) in pulmonary ivs+ and peripheral CD8 T cells. Wilcox rank sum test was used to determine significance. Only significant p-values are reported. p-value < 0.001 = ***, p-value < 0.01 = **, p-value < 0.05 = *. ggplot package in R.

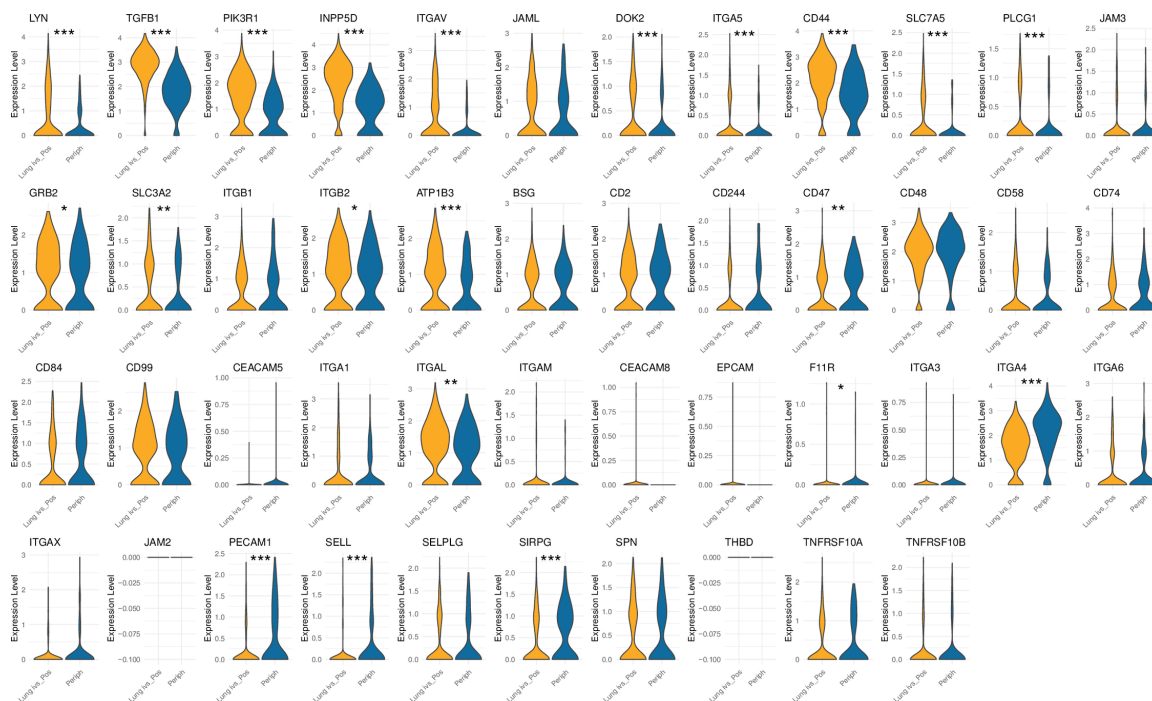


Figure 13. Transcriptomic expression of genes associated with vascular cell wall interactions in pulmonary ivs+ and peripheral CD8 T cells. Wilcox rank sum test was used to determine significance. Only significant p-values are reported. p-value < 0.001 = ***, p-value < 0.01 = **, p-value < 0.05 = *. ggplot package in R.

Discussion

Intravascular staining (ivs) offers a novel approach for distinguishing tissue-resident cells from vascular-associated counterparts, especially within highly vascularized organs such as the lung [22]. This technique involves infusing a fluorochrome-labeled anti-CD45 antibody, which labels leukocytes within the vasculature (ivs+) while tissue-resident cells remain unlabeled (ivs-). We utilized this method in Rhesus Macaques (RhM) to aid in the isolation of T cells from lung and respiratory mucosa for subsequent flow cytometric and single-cell RNA sequencing (scRNAseq) analysis.

Conventionally, pulmonary ivs+ cells are regarded as “blood contaminants” — cells residing in blood vessels of organs at the time of necropsy that inadvertently mix with tissue-resident cells during tissue processing [22,23]. However, our comprehensive analysis reveals that this population of T cells is phenotypically and functionally distinct from those in the blood. Notably, CD8+ T lymphocytes were shown to be enriched within the pulmonary vasculature, far exceeding their frequency in the blood. Delving deeper through flow cytometry and scRNAseq, we found that ivs+ CD8+ T cells predominantly exhibit an effector phenotype, highlighted by their elevated expression of cytolytic markers, indicating enhanced cytotoxic potential.

Echoing the findings from Potter et al., our results reiterate and expand upon the observations of distinct differences between PBMCs and ivs+ cells across non-lymphoid tissues [24]. We found increased expression of transcripts associated with a non-circulating phenotype, including *CD69*, *CD44*, and *RUNX3*, and low expression of genes that promote egress, such as *CCR7*, *SELL*, and *KLF2* [69–72]. Additionally, we detected elevated expression of *TGFB1*, a promoter of T_{RM} survival and differentiation similar to T cells in the lung parenchyma [60,61]. Potter and colleagues theorized the perivascular capillary bed as a potential residence for these ivs+ cells — a specialized niche, as characterized by Pabst and Tschernig, that allows plasma access but limits cell movement [19,20]. Such strategic positioning may allow for rapid immune responses and potentially foster alternative routes for cell migration [19].

By harnessing the granularity of single-cell RNA sequencing, we identified enrichment of cell adhesion and extravasation-associated genes in pulmonary ivs+ T cells. Studies in mice suggest that T cell migration to and retention in the pulmonary vasculature is mediated in part through interactions between vascular endothelial adhesion molecules, ICAM-1 and ICAM-2, and T cell expression of integrin LFA-1, a heterodimer of CD11a//*ITGAL* + CD18//*ITGB2* [74,75]. Here, our pulmonary ivs+ T cells had significantly higher expression of *ITGAL* and *ITGB2* transcripts. Comparison of peripheral and pulmonary ivs+ cells revealed that CD8+ T cells in the pulmonary vasculature had elevated expression of a number of genes associated with immune cell-endothelial cell interactions including *LYN*, *TGFB1*, *PIK3R1*, *INPP5D*, *ITGAV*, *DOK2*, *ITGA5*, *CD44*, *SLC7A5*, *PLCG1*, *GRB2*, *SLC3A2*, *ITGB2*, *ATP1B3*, *ITGAL*, and *F11R*. This further supports the concept of a specialized niche within the pulmonary vascular that selectively retains specific cell subsets.

Exploring the functional capabilities of pulmonary ivs+ T cells during SIV infection in RhMs revealed heightened activity upon SIV-Gag stimulation. CD8+ T cells expressing GZMB, IFN- γ , and TNF- α were found in significantly greater proportions in the pulmonary ivs+ compartment compared to the pulmonary tissue (ivs-). Utilizing SIV-tetramer staining, we identified virus-specific CD8+ T cells present in both blood and lung. Tetramer-specific CD8+ T cells in pulmonary tissue and airways (ivs-) exhibited a T_{RM} phenotype, whereas those in the pulmonary vasculature (ivs+) were characteristic of effector-oriented cells. As most models of CD8+ T cell-mediated protection against HIV/SIV focus almost

entirely on studies of peripheral blood, the identification of SIV-specific T cells within the pulmonary interstitium and pulmonary vasculature is a noteworthy finding that has implications for targeting pulmonary viral reservoirs and should be further explored.

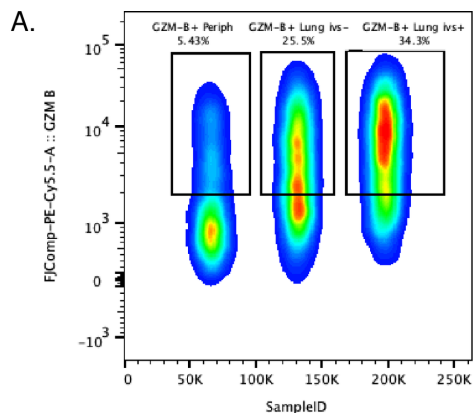
Consistent with our findings, Buggert et al. identified distinct subsets of cytotoxic CD8⁺ effector T cells in blood samples that were absent in thoracic duct lymph (TDL) collected from humans and NHP [76]. Buggert suggested that the retention of powerful cytotoxic T cells within the vasculature might serve a protective function, preventing immune-induced tissue damage. Our study further supports this idea, as we observed that the ivs⁺ CD8⁺ T cells in the pulmonary vasculature exhibited pronounced cytotoxicity, with increased molecular transcripts and protein expression of cytotoxic markers compared to CD8⁺ T cells in the lung parenchyma (ivs⁻). Our work identifies and defines a unique population of intravascular T cells which may serve as efficacious targets of diseases with known immunopathology. Targeting this highly activated subset before it can leave the vasculature and impact tissues may reduce disease severity in conditions proven to have immunopathology, such as COVID-19.

Collectively, our study reinforces the notion of a distinct vascular niche in non-lymphoid tissues, such as the lung, as illuminated by ivs. The unique features of pulmonary ivs⁺ T cells, particularly the enrichment of CD8⁺ T cells with enhanced functionality, redefine these cells as a specialized population, distinct from lingering blood lymphocytes, and highlight their intrinsic value in tissue immunity.

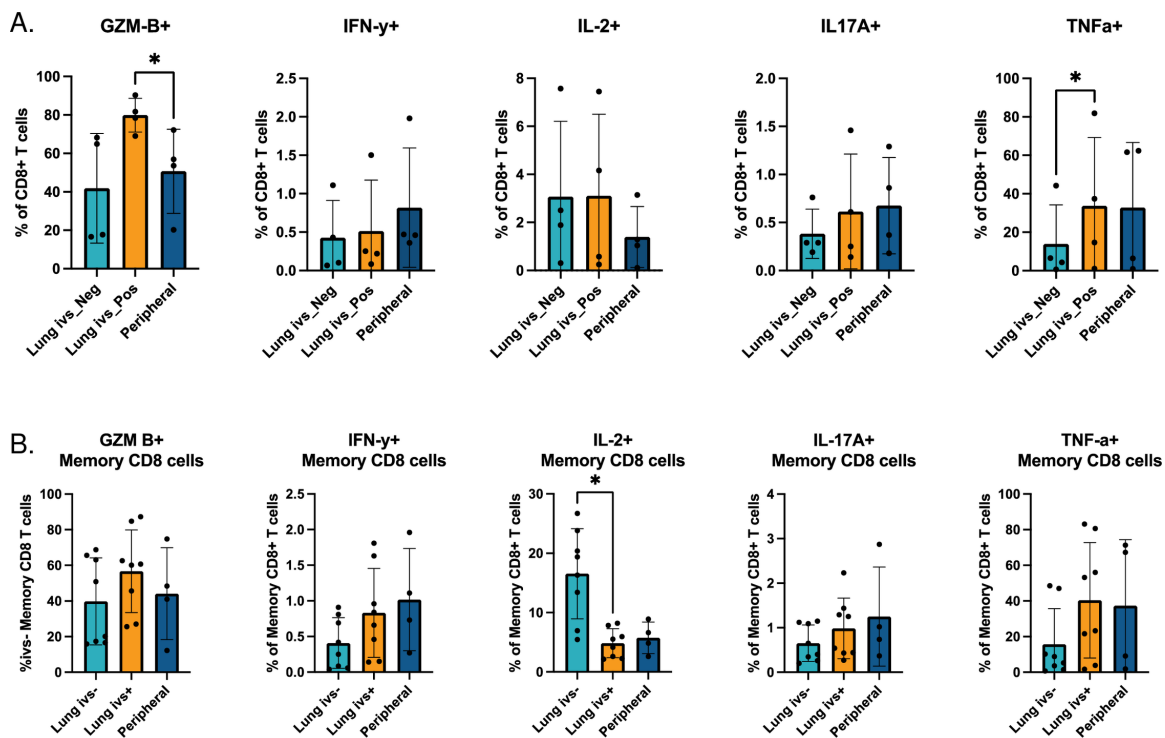
Conclusion

Our results challenge the conventional perspective of pulmonary ivs+ cells as “blood contaminants.” Instead, our findings bolster that of previous research suggesting that these cells are a unique cellular cohort, specific to the pulmonary vasculature, that plays a pivotal role in lung immunity. Understanding the nuanced differences between tissue-resident T cells, vascular “resident-like” T cells, and circulating blood T cells will help unlock deeper insights into lung immunology and its implications in diseases such as respiratory infections, asthma, COPD, and lung cancer.

Supplemental



Supplemental Figure 1. A. Granzyme B (GZM-B) expression on CD8 T cell populations isolated from lung (both ivs+ and ivs-) and peripheral blood. Pulmonary CD8 T cells have notably higher expression of the serine protease GZMB compared to peripheral CD8 T cells, Representative RM animal shown (NL20)



Supplemental Figure 2. Functional responses of pulmonary (ivs+ and ivs-) and peripheral CD8 T cells.

Frequency of cytokine-producing of total CD8+ (A) and memory CD8+ (B) T cells in ivs+ and ivs- cells isolated from lungs and blood.

Gating strategy panel A:

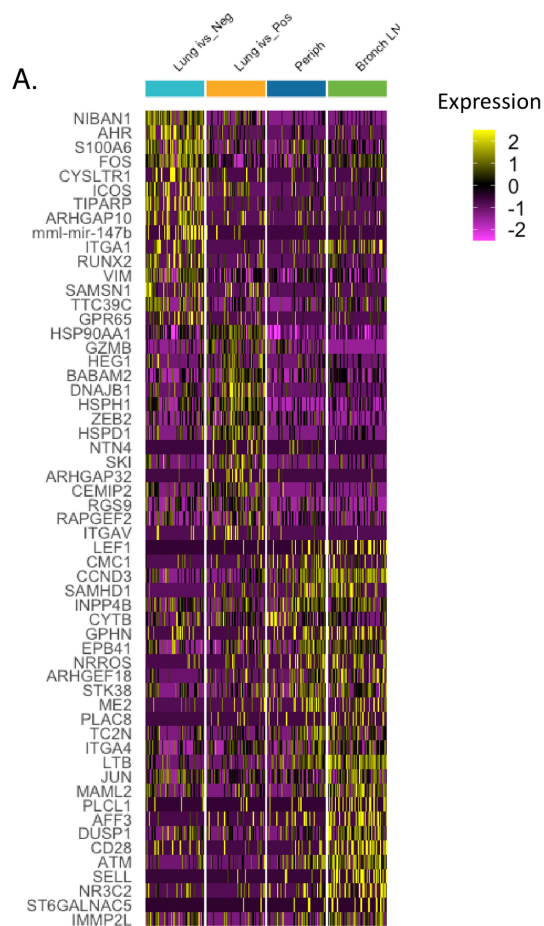
Time>Live>Lymphocytes>Single cells>CD45_ex-vivo>CD45_ivs+/ivs-> CD3>CD8>cytokine.

Gating strategy panel B:

Time>Live>Lymphocytes>Single cells>CD45_ex-vivo>CD45_ivs+/ivs-> CD3>CD8>CD95>cytokine.

Plotted as mean +/- SD. The Kruskal-Wallis test for multiple comparisons was used to determine significance.

*p < 0.05.



Supplemental Figure 3. Single-cell analysis of T cells across tissues. A. Heatmap of top 15 differentially expressed genes in T cells across tissue samples.

Supplemental Table 1				
Antibody	Fluorochrome	Clone	Vendor	Catalogue
CCR5	BUV805	3A9	BD Biosciences	748872
CCR7	BV650	3D12	BD Biosciences	563407
CD103	BV421	Ber-ACT8	Biologend	350214
CD134	BUV563	L106	BD Biosciences	749161
CD27	BUV615	O323	BD Biosciences	751685
CD28	APC	CD28.2	Biologend	302912
CD28	BUV496	CD28.2	BD Biosciences	741168
CD28	BUV737	CD28.2	BD Biosciences	612815
CD3	APC-C7	SPE4-2	BD Biosciences	557757
CD38	PE-CF594	OKT10	Caprico Bio	1008205
CD4	BUV737	L200	BD Biosciences	749213
CD4	BUV496	L200	BD Optibuild	750591
CD44	BV570	IM7	Biologend	103037
CD44	PE-Cy5	IM7	Biologend	103010
CD45	BUV395	D058-1283	BD Biosciences	564099
CD45RA	BUV563	5H9	BD Optibuild	741411
CD45RA	PE-Cy5	5H9	BD Biosciences	552888
CD49a	PE-Cy7	TS2/7	Biologend	328312
CD62L	BV786	SK11	BD Biosciences	565311
CD69	AL488	FN50	Biologend	310916
CD69	PCP-CY5.5	FN50	BD Biosciences	560738
CD69	PE-CF594	FN50	BD Biosciences	562617
CD8	BUV805	SK1	BD Biosciences	612889
CD8	BV605	SK1	BD Biosciences	564116
CD8	BV650	SK1	BD Biosciences	565289
CD95	BV711	DX2	BD Biosciences	563132
CXCR3 (CD183)	BUV661	1C6/CXCR3	BD Biosciences	741649
Granzyme B	PE	GB12	Invitrogen	MHGB04
Granzyme B	PE-Cy5.5	GB11	Invitrogen	GRB18
IFN- γ	BV570	4S.B3	Biologend	502534
IFN γ	PE-Cy7	B27	BD Biosciences	557643
IL-17A	BV605	BL168	Biologend	512326
IL-2	PCP-Cy5.5	MQ1-17H12	BD Biosciences	560708
IL-21	BV421	3A3-N2.1	BD Biosciences	564755
Ki-67	AL700	B56	BD Biosciences	561277
Ki-67	PE	B56	BD Biosciences	567719
PD-1 (CD279)	BV750	EH12.2H7	Biologend	329966
TNF- α	AL700	MAB11	BD Biosciences	557996
CD45-IVS	AL647	ITS	NHP Reagents	
Brefeldin-A	N/A	N/A	BioLegend	420601
Cell Stimulation Cocktail	N/A	N/A	BioLegend	423301
CD28 (one backup)	Unlabeled	CD28.2	BD Pharmingen	555725
CD49D (1 backup)	Unlabeled	9F10	BD Pharmingen	555501

Supplementary Table 1. Flow cytometry antibodies.

Supplemental Table 2						
Top differentially expressed genes (DEGs) for each seurat cluster						
cluster	gene	p_val	avg_log2FC	pct.1	pct.2	p_val_adj
0	GZMK	8.51E-129	1.403992915	0.511	0.168	1.41E-124
0	ANK3	8.42E-86	1.022380119	0.523	0.22	1.39E-81
0	PAG1	6.39E-108	0.943022072	0.838	0.5	1.06E-103
0	BTBD11	7.57E-81	0.878040908	0.785	0.454	1.25E-76
0	NIBAN1	7.47E-31	0.778818116	0.721	0.56	1.24E-26
0	GPR183	2.13E-63	0.71447396	0.519	0.25	3.53E-59
0	ATP8A1	1.61E-46	0.697296611	0.781	0.579	2.67E-42
0	CHN2	1.84E-45	0.684232364	0.848	0.663	3.04E-41
0	MPP7	1.73E-48	0.656291285	0.89	0.701	2.86E-44
0	ICOS	6.89E-35	0.641702625	0.563	0.354	1.14E-30
0	ERN1	9.40E-39	0.635764622	0.736	0.516	1.56E-34
0	RUNX2	2.21E-34	0.634798282	0.52	0.317	3.65E-30
0	NEDD4L	2.43E-51	0.627940088	0.644	0.396	4.02E-47
0	LRIG1	2.83E-37	0.621006398	0.629	0.434	4.69E-33
0	TTC39C	1.86E-41	0.62024571	0.798	0.607	3.09E-37
0	ITGA1	2.71E-38	0.612321742	0.455	0.243	4.49E-34
0	NBEAL1	6.07E-29	0.592802506	0.549	0.373	1.00E-24
0	JAML	2.27E-42	0.566630102	0.628	0.409	3.76E-38
0	BICDL1	4.24E-34	0.564501077	0.946	0.788	7.03E-30
0	ATXN1	1.17E-37	0.56251132	0.831	0.647	1.94E-33
0	ARHGAP10	4.28E-42	0.55902846	0.479	0.258	7.09E-38
0	IMMP2L	2.93E-26	0.550572725	0.641	0.46	4.86E-22
0	RHOH	3.80E-35	0.544850938	0.831	0.65	6.30E-31
0	SFMBT2	1.80E-32	0.53599458	0.41	0.229	2.97E-28
0	CPE	2.03E-39	0.524295841	0.255	0.098	3.37E-35
0	COTL1	7.41E-43	0.522616163	0.703	0.491	1.23E-38
0	NR3C2	8.36E-24	0.5212102	0.408	0.249	1.38E-19
0	PDZRN3	7.92E-12	0.517851571	0.277	0.18	1.31E-07
0	NBEA	1.57E-38	0.503313219	0.343	0.162	2.59E-34
1	GZMB	7.98E-266	1.578362559	0.983	0.548	1.32E-261
1	BABAM2	4.09E-263	1.519981045	0.986	0.692	6.78E-259
1	CHSY3	2.08E-124	1.399805444	0.275	0.037	3.44E-120
1	GPR141	4.32E-285	1.385577364	0.647	0.11	7.15E-281
1	DOCK5	2.26E-219	1.374950286	0.711	0.196	3.74E-215
1	ROR2	1.25E-170	1.365815938	0.491	0.107	2.08E-166
1	ARHGAP32	1.21E-138	1.333808376	0.451	0.11	2.00E-134
1	NTN4	1.58E-143	1.293371238	0.41	0.083	2.62E-139
1	JAKMIP2	1.60E-171	1.285447969	0.641	0.19	2.66E-167
1	RAP1GAP2	6.34E-199	1.244322381	0.929	0.408	1.05E-194
1	STK3	1.05E-93	1.088863654	0.419	0.138	1.73E-89
1	FRY	5.78E-173	1.087761223	0.603	0.164	9.57E-169
1	RGS9	5.28E-151	1.049877999	0.956	0.621	8.75E-147
1	SH3BP5	1.32E-133	1.035989524	0.584	0.2	2.18E-129
1	ZEB2	4.46E-114	0.972189247	0.941	0.606	7.39E-110
1	CLIC5	5.10E-114	0.935584	0.79	0.408	8.45E-110
1	KLF3	3.48E-133	0.929382897	0.779	0.378	5.77E-129
1	CX3CR1	9.16E-181	0.91887512	0.443	0.076	1.52E-176
1	SH3RF1	7.52E-74	0.909927037	0.338	0.104	1.25E-69
1	RAPGEF2	3.71E-94	0.909308384	0.911	0.659	6.14E-90
1	PTPRJ	7.69E-99	0.883231479	0.89	0.564	1.27E-94
1	DNAJC1	3.58E-118	0.852935203	0.971	0.718	5.94E-114
1	FAM102B	8.67E-77	0.845723711	0.616	0.304	1.44E-72
1	TTC3	7.12E-70	0.830676349	0.546	0.267	1.18E-65
1	SLCO3A1	7.84E-107	0.818004727	0.947	0.685	1.30E-102
1	NHSL2	5.31E-108	0.817299419	0.317	0.064	8.79E-104
1	TGFBR3	6.49E-77	0.795164516	0.846	0.505	1.07E-72
1	S100A10	1.21E-123	0.777653344	0.973	0.814	2.00E-119
1	SETBP1	3.75E-74	0.759802555	0.41	0.148	6.21E-70

Supplemental Table 2						
cluster	gene	p_val	avg_log2FC	pct.1	pct.2	p_val_adj
2	GZMB	6.86E-28	0.721440887	0.716	0.615	1.14E-23
2	S100A10	6.14E-16	0.50473822	0.771	0.859	1.02E-11
2	GAPDH	7.95E-07	0.479605066	0.703	0.834	0.013161
2	S100A4	5.88E-12	0.431994126	0.805	0.828	9.74E-08
2	FTH1	0.003614	0.426020558	0.752	0.884	1
2	UBB	7.22E-06	0.40683226	0.727	0.877	0.119559
2	COX2	1.83E-50	0.389776652	0.997	1	3.03E-46
2	HSPH1	0.007036	0.384218834	0.675	0.772	1
2	ATP6	3.47E-36	0.383744745	0.972	0.998	5.75E-32
2	GADD45B	0.004016	0.378380932	0.411	0.566	1
2	ND4L	0.000133	0.372032935	0.604	0.737	1
2	HSP90AA1	8.56E-11	0.366889782	0.857	0.926	1.42E-06
2	COX3	2.06E-31	0.364858178	0.995	1	3.40E-27
2	RABAC1	0.002161	0.364274625	0.312	0.451	1
2	FTL	0.000323	0.357903101	0.744	0.883	1
2	ND4	7.38E-18	0.333890909	0.925	0.994	1.22E-13
2	IL10RA	6.77E-06	0.33140136	0.279	0.432	0.112054
2	ND2	1.24E-14	0.317708526	0.894	0.988	2.05E-10
2	LDHA	0.002464	0.314660704	0.389	0.559	1
2	HNRNPH1	1.21E-06	0.314609478	0.485	0.735	0.020015
2	CD99	0.007567	0.309837726	0.431	0.616	1
3	CMC1	6.02E-196	1.756480243	0.711	0.207	9.96E-192
3	LYN	1.06E-183	1.670742321	0.672	0.173	1.76E-179
3	IKZF2	4.35E-214	1.646802002	0.814	0.231	7.21E-210
3	CCL5	1.58E-163	1.43400772	0.938	0.527	2.62E-159
3	PDGFD	2.36E-147	1.347289524	0.522	0.115	3.90E-143
3	KIR3DH	0	1.334132675	0.442	0.016	0
3	KCNQ5	6.07E-108	1.276331396	0.602	0.208	1.00E-103
3	BTBD11	4.10E-84	1.22396435	0.821	0.474	6.78E-80
3	NCR1	0	1.217602989	0.501	0.02	0
3	VAV3	3.24E-117	1.130636712	0.861	0.451	5.37E-113
3	CTSW	1.10E-133	1.119092706	0.661	0.217	1.81E-129
3	UNC5D	9.90E-89	1.103982169	0.393	0.101	1.64E-84
3	GZMM	2.13E-122	1.103073897	0.887	0.525	3.53E-118
3	PLAC8	8.39E-147	1.101329617	0.522	0.121	1.39E-142
3	PLCB1	5.37E-102	1.082155088	0.716	0.292	8.89E-98
3	UBASH3B	1.48E-89	1.069501364	0.711	0.334	2.45E-85
3	AOAH	1.15E-205	1.048460135	0.407	0.04	1.90E-201
3	KLRB1	3.15E-81	1.019813066	0.734	0.367	5.21E-77
3	PITPNC1	6.61E-136	0.986514227	0.998	0.905	1.09E-131
3	PLCG2	4.04E-108	0.964541416	0.651	0.235	6.68E-104
3	AFF3	1.36E-72	0.941986303	0.47	0.165	2.25E-68
3	ITGAX	1.87E-155	0.934828295	0.322	0.034	3.10E-151
3	SLC24A3	1.79E-83	0.93339208	0.3	0.062	2.96E-79
3	IL12RB2	2.93E-40	0.874452028	0.41	0.185	4.84E-36
3	TEC	1.45E-88	0.870926081	0.682	0.283	2.40E-84
3	PTPRM	8.53E-75	0.86840469	0.271	0.056	1.41E-70
4	LEF1	5.93E-278	2.250461267	0.472	0.037	9.82E-274
4	PLCL1	2.36E-157	1.549467314	0.359	0.044	3.91E-153
4	ITGB1	1.19E-75	1.477203402	0.68	0.393	1.97E-71
4	INPP4B	2.41E-97	1.348440068	0.861	0.561	3.99E-93
4	LTB	1.02E-108	1.317551954	0.795	0.423	1.70E-104
4	SPOCK2	1.76E-216	1.311301538	0.758	0.179	2.91E-212
4	GPHN	9.07E-55	1.258679738	0.425	0.174	1.50E-50
4	MAML2	4.05E-65	1.152521402	0.794	0.492	6.70E-61
4	LDLRAD4	1.11E-118	1.141698346	0.439	0.099	1.84E-114
4	CD28	2.67E-132	1.053409617	0.541	0.137	4.42E-128
4	IL6R	1.66E-255	1.029975478	0.38	0.019	2.76E-251

Supplemental Table 2						
cluster	gene	p_val	avg_log2FC	pct.1	pct.2	p_val_adj
4	PCNX2	1.33E-110	1.014627505	0.497	0.135	2.21E-106
4	ST6GALNA	1.36E-123	1.011964076	0.269	0.03	2.25E-119
4	DNM3	1.02E-62	1.006265173	0.406	0.149	1.69E-58
4	NRIP1	7.44E-43	0.993892944	0.464	0.222	1.23E-38
4	RCAN3	3.12E-152	0.954676967	0.409	0.064	5.17E-148
4	AKT3	1.09E-92	0.942031529	0.866	0.431	1.80E-88
4	IL6ST	5.36E-83	0.9411802	0.412	0.122	8.87E-79
4	BACH2	3.77E-46	0.917839009	0.541	0.276	6.25E-42
4	STK24	9.47E-63	0.91388723	0.652	0.338	1.57E-58
4	BCL2	4.13E-33	0.89991429	0.787	0.577	6.84E-29
4	PECAM1	9.31E-53	0.893232925	0.391	0.152	1.54E-48
4	DGKA	3.24E-86	0.864596144	0.588	0.235	5.37E-82
4	TLK1	3.33E-73	0.857511694	0.819	0.502	5.51E-69
4	MAML3	3.20E-39	0.857218843	0.266	0.093	5.29E-35
4	SUCLG2	9.92E-51	0.854397122	0.675	0.413	1.64E-46
4	SLC9A9	2.36E-32	0.842332393	0.77	0.581	3.91E-28
4	DIP2C	1.42E-140	0.837298021	0.367	0.054	2.35E-136
4	ITGA6	1.21E-58	0.821301756	0.475	0.197	2.01E-54
5	ZBTB16	0	2.230104767	0.727	0.024	0
5	TMEM132C	0	2.196655351	0.533	0.011	0
5	KCNK13	1.15E-116	2.170422966	0.361	0.051	1.91E-112
5	PDZRN3	1.17E-129	1.720588668	0.646	0.159	1.94E-125
5	DOCK3	1.90E-181	1.645931188	0.789	0.189	3.14E-177
5	MAST4	7.73E-187	1.573354432	0.56	0.078	1.28E-182
5	ITGA1	1.12E-113	1.53219377	0.747	0.244	1.86E-109
5	RORA	6.65E-106	1.522626348	0.953	0.631	1.10E-101
5	SPOCK2	8.48E-123	1.51081412	0.705	0.214	1.40E-118
5	JUN	4.40E-58	1.438726815	0.904	0.692	7.29E-54
5	TNFAIP3	3.66E-90	1.413116818	0.934	0.637	6.06E-86
5	IL7R	6.77E-105	1.413104468	0.919	0.491	1.12E-100
5	MED12L	3.93E-200	1.392123011	0.484	0.05	6.50E-196
5	NFKB1	1.01E-53	1.390476337	0.86	0.576	1.67E-49
5	KIAA1217	4.80E-200	1.362129423	0.514	0.057	7.95E-196
5	SATB1	9.13E-96	1.316410679	0.823	0.375	1.51E-91
5	PELI2	8.15E-153	1.310928453	0.491	0.073	1.35E-148
5	RUNX2	3.03E-93	1.309692167	0.794	0.318	5.02E-89
5	DUSP1	8.65E-65	1.296160499	0.835	0.514	1.43E-60
5	CCR6	4.82E-227	1.282234191	0.506	0.046	7.98E-223
5	SNX25	1.01E-72	1.275076221	0.757	0.372	1.67E-68
5	IRAK2	3.52E-57	1.195188922	0.69	0.363	5.83E-53
5	CD69	2.21E-40	1.190704036	0.872	0.683	3.66E-36
5	STAT4	4.85E-38	1.174783832	0.941	0.799	8.04E-34
5	PLXNC1	1.85E-84	1.169597872	0.622	0.204	3.07E-80
5	IL23R	8.83E-278	1.139847369	0.435	0.019	1.46E-273
5	RYR2	9.23E-120	1.10809254	0.273	0.024	1.53E-115
5	ADAM12	9.60E-123	1.108016917	0.518	0.102	1.59E-118
6	COX2	9.70E-112	2.960012517	1	1	1.61E-107
6	COX1	2.92E-106	2.92182672	0.995	0.993	4.83E-102
6	ND4L	2.05E-89	2.8828204	0.914	0.705	3.39E-85
6	ATP6	1.85E-109	2.804010058	1	0.993	3.07E-105
6	ND2	1.58E-105	2.740227596	0.986	0.972	2.61E-101
6	COX3	7.90E-102	2.715620493	1	0.999	1.31E-97
6	ATP8	5.58E-66	2.594854894	0.774	0.475	9.23E-62
6	ND4	3.83E-100	2.503730267	0.982	0.983	6.34E-96
6	ND3	8.83E-71	2.439889871	0.855	0.711	1.46E-66
6	ND6	3.83E-64	2.23528975	0.62	0.23	6.33E-60
6	CYTB	1.76E-58	2.169036033	0.778	0.531	2.92E-54
6	ND5	8.35E-43	1.787358633	0.597	0.294	1.38E-38

Supplemental Table 2						
cluster	gene	p_val	avg_log2FC	pct.1	pct.2	p_val_adj
6	CHD3	2.62E-06	0.390779742	0.176	0.388	0.043373
6	PSTPIP1	0.00135	0.307146472	0.145	0.27	1
7	ND4	1.97E-69	3.157078903	1	0.983	3.27E-65
7	COX3	2.09E-67	3.070272668	1	0.999	3.46E-63
7	ATP6	4.64E-68	3.011254511	1	0.994	7.69E-64
7	COX2	2.13E-67	3.007401534	1	1	3.52E-63
7	COX1	3.66E-67	2.944754398	1	0.993	6.06E-63
7	ND2	1.89E-65	2.787707981	1	0.972	3.12E-61
7	CYTB	1.28E-53	2.606733352	0.906	0.534	2.12E-49
7	ND4L	1.39E-53	2.494260548	0.966	0.709	2.30E-49
7	ND3	2.38E-57	2.232920371	0.974	0.711	3.95E-53
7	ATP8	5.64E-38	2.132178572	0.812	0.481	9.34E-34
7	ND5	1.82E-33	2.112356642	0.667	0.299	3.01E-29
7	ND6	2.55E-24	1.79482321	0.556	0.241	4.23E-20
7	HEXIM1	0.008632	0.297343251	0.12	0.252	1
8	MAMU-DRA	3.31E-98	4.93446038	0.837	0.063	5.49E-94
8	CD74	2.13E-33	4.695910899	0.93	0.32	3.53E-29
8	ARHGAP24	0	4.313994827	0.791	0.005	0
8	MAMU-DRE	2.65E-33	3.897661016	0.93	0.306	4.39E-29
8	CFD	6.84E-165	3.783609302	0.442	0.007	1.13E-160
8	SPAG16	8.01E-22	3.667506662	0.372	0.052	1.33E-17
8	LYZ	5.50E-255	3.659221419	0.605	0.008	9.11E-251
8	IGKC	1.46E-35	3.429401165	0.302	0.021	2.41E-31
8	BANK1	2.15E-56	3.415097783	0.605	0.053	3.56E-52
8	LYN	3.52E-38	3.306578602	0.953	0.235	5.83E-34
8	VCAN	4.19E-219	3.303642399	0.279	0.001	6.94E-215
8	KYNU	0	3.172643592	0.791	0.003	0
8	IL1B	5.84E-262	2.978438361	0.419	0.003	9.67E-258
8	RBM47	0	2.844013515	0.628	0.005	0
8	RALGPS2	1.42E-21	2.712107117	0.512	0.097	2.35E-17
8	DPYD	1.48E-142	2.679347772	0.535	0.014	2.44E-138
8	MS4A1	2.37E-270	2.673955836	0.395	0.002	3.93E-266
8	EBF1	5.65E-194	2.662643659	0.372	0.003	9.35E-190
8	DOCK4	3.48E-55	2.628173581	0.395	0.022	5.77E-51
8	IFI30	6.34E-165	2.591047424	0.744	0.025	1.05E-160
8	SOX5	1.80E-67	2.560910565	0.302	0.01	2.98E-63
8	SOD2	1.97E-17	2.553388602	0.558	0.143	3.26E-13
8	MAMU-DM	0	2.505497958	0.814	0.009	0
8	GOS2	4.07E-158	2.47411327	0.326	0.003	6.75E-154
8	PSAP	3.58E-14	2.446048791	0.674	0.246	5.92E-10
8	MEF2C	1.24E-172	2.438931705	0.744	0.023	2.06E-168
8	GAB2	1.20E-24	2.397588122	0.744	0.192	1.98E-20
8	IDO1	4.49E-176	2.381230419	0.349	0.003	7.43E-172
8	CST3	8.49E-213	2.344602805	0.442	0.005	1.41E-208
9	STMN1	2.08E-24	2.634555221	0.781	0.166	3.44E-20
9	MKI67	1.28E-74	2.597847719	0.781	0.053	2.13E-70
9	DIAPH3	7.37E-225	2.41407531	0.781	0.014	1.22E-220
9	HMGB2	3.77E-16	2.143179893	0.906	0.444	6.24E-12
9	H1-3	2.04E-24	2.098483009	0.594	0.088	3.37E-20
9	BRCA1	1.13E-50	1.867951151	0.719	0.065	1.88E-46
9	CIT	1.46E-121	1.862253794	0.688	0.022	2.42E-117
9	SMC4	3.14E-14	1.847860926	0.844	0.349	5.19E-10
9	TUBB	4.83E-13	1.735545218	0.812	0.327	8.00E-09
9	ATAD2	1.18E-21	1.680186899	0.719	0.155	1.95E-17
9	DTL	5.18E-65	1.662958826	0.562	0.029	8.57E-61
9	CENPP	9.26E-87	1.657267812	0.625	0.027	1.53E-82
9	RRM2	1.48E-166	1.649278133	0.469	0.006	2.45E-162
9	ZGRF1	1.55E-80	1.588887277	0.625	0.029	2.57E-76

Supplemental Table 2						
cluster	gene	p_val	avg_log2FC	pct.1	pct.2	p_val_adj
9	POLA1	8.32E-23	1.576522096	0.625	0.106	1.38E-18
9	LMNB1	2.67E-20	1.553268661	0.75	0.175	4.41E-16
9	TMPO	2.09E-14	1.54129672	0.688	0.223	3.46E-10
9	BRCA2	8.15E-139	1.534922252	0.625	0.015	1.35E-134
9	NCAPG2	6.44E-48	1.53284653	0.656	0.056	1.07E-43
9	PCLAF	0	1.503967385	0.5	0.002	0
9	ASPM	6.47E-296	1.489948627	0.625	0.005	1.07E-291
9	NSD2	1.66E-13	1.46953808	0.719	0.232	2.75E-09
9	TOP2A	5.49E-59	1.469517973	0.5	0.025	9.08E-55
9	SYNE2	5.04E-10	1.43609405	0.875	0.465	8.34E-06
9	UHRF1	4.53E-134	1.435374816	0.594	0.014	7.50E-130
9	TACC3	2.56E-17	1.388674843	0.656	0.145	4.24E-13
9	POLQ	1.17E-79	1.374273231	0.625	0.029	1.93E-75
9	POLE	7.36E-67	1.352562409	0.562	0.028	1.22E-62

Supplementary Table 2. Top differentially expressed genes (DEG) for each seurat cluster.

Supplementary Table 3					
Differential gene expression between seurat clusters 2 and 1					
gene_symbol	p_val	avg_log2FC	pct.1	pct.2	p_val_adj
CD99	2.06E-14	-0.0442761	0.431	0.761	3.41E-10
CX3CR1	4.04E-35	-0.5401608	0.143	0.443	6.68E-31
ITGA1	2.46E-05	0.7870831	0.122	0.068	0.40661186
ITGA4	4.15E-38	-0.582982	0.527	0.896	6.88E-34
ITGAE	6.58E-11	0.06436982	0.145	0.302	1.09E-06
ITGAL	5.80E-20	-0.2565312	0.454	0.773	9.60E-16
ITGAV	1.62E-26	-0.609355	0.166	0.42	2.69E-22
ITGB1	9.25E-26	-0.2973681	0.283	0.614	1.53E-21
ITGB2	5.52E-24	-0.2301722	0.41	0.774	9.14E-20
GZMB	5.35E-34	-0.5355009	0.716	0.983	8.86E-30
TGFBR2	1.35E-10	-0.1983989	0.608	0.883	2.24E-06
TGFBR3	1.32E-33	-0.6460895	0.492	0.846	2.19E-29

Supplementary Table 3. Top differentially expressed genes (DEG) for each seurat cluster.

Conclusion and Future Directions

We set out to establish a novel NHP model for COVID-19, assess the implications of immunosuppression during SARS-CoV-2 infection, and explore the roles and dynamics of T cells in the lungs.

1. **Animal Models and Immune Response Dynamics:** Through the exploration of the PTM as a novel model for COVID-19, our research reinforces the need for animal models that can fully recapitulate the full range of clinical manifestations seen in humans. While most NHPs fail to capture the severe spectrum of COVID-19, we show that PTMs provide an alternative animal model for understanding the intricate immune responses to SARS-CoV-2. Our findings provide insights into the cellular immune response, highlighting pulmonary infiltrates that were dominated by T cells, including a unique population of CD4⁺ T cells that upregulate CD8 and express cytotoxic molecules, as well as virus-specific T cells that were predominantly CD4⁺.
2. **Coinfections and Immunodeficiency:** Exploring the effects of immunosuppression on SARS-CoV-2 dynamics, our research underscores the implications of a compromised immune system during infection. Although our results in the PTM model indicated that SIV-induced immunodeficiency does not significantly alter the clinical course of COVID-19 or facilitate viral

persistence and evolution, the failure to generate adaptive immune responses, specifically neutralizing antibodies and virus-specific T cells, highlights the vulnerability of individuals with compromised immune systems to repeat infection.

3. **Pulmonary T cell Dynamics:** In building on our findings from the first two studies, we delved deeper into the dynamics of pulmonary T cells, with a specific focus on the lung's vascular system. This investigation sheds new light on the role of T cells in this vital organ. By leveraging intravascular staining (ivs), we challenge traditional views that dismiss ivs+ cells as mere "blood contaminants." Our research, alongside previous findings from Potter et al., posits that these cells represent a distinct subset selectively retained within the pulmonary vasculature. Their gene expression profile, enriched in cell adhesion and extravasation markers, including those typically associated with tissue residence indicates a specialized niche within the vascular system. Enrichment of CD8+ T cells with pronounced effector functions, evidenced by enhanced GZMB expression as well as heightened GZMB, IFN- γ , and TNF- α responses during SIV infection, highlight their significance in lung immunity.

In conclusion, our research contributes to the field of T cell biology within the realm of infectious disease and pulmonary immunology. Our findings provide valuable additions to the growing body of COVID-19 research and pave the way for future investigations. As we move forward, discerning the nuanced differences between tissue-resident T cells, vascular "resident-like" T cells, and circulating blood T cells will be pivotal. This knowledge will help unlock deeper

insights into lung immunology and its implications not only for designing novel therapeutic strategies targeting T cell responses but also for the development of more effective vaccine and treatment regimens.

Future Directions

Effector CD8 T cells are vital in defending against pathogens during acute infection [1–3]. As the infection resolves, the T_{EFF} population contracts, leaving a small population of antigen-experienced memory T cells poised to rapidly respond to future encounters [4,5]. Recent studies in mice suggest that not all remaining T_{EFF} cells differentiate into memory T cells. Some persist as “long-lived effector cells” (LLEC) with pronounced cytotoxicity, albeit with reduced proliferative capacity [6,7]. Cells with characteristics similar to LLECs have also been observed in humans [8]. CD8 T cells expressing CX3CR1, identified in both humans and mice, display an effector phenotype with high GZMB expression and a heightened ability to eliminate infected target cells [8]. This raises the question: Could the perivascular bed serve as a specialized niche for LLECs? The pulmonary ivs⁺ T cells in our third study showed elevated expression of GZMB, as well as genes associated with enhanced cytotoxicity, cell adhesion, extravasation, and tissue residence, with low expression of genes that promote egress, suggesting possibly so. Further studies could provide valuable insights into not only vascular-associated T cells (ivs⁺) but also LLECs and their possible retention within the pulmonary vasculature. Exploring the biology and potential applications of these cells could include:

- **Elucidating the Mechanisms of ivs+ T Cell Retention:** Investigating the precise mechanisms that retain the ivs+ T cells within the pulmonary vasculature remains an essential next step. Understanding how these cells avoid egress into the lung tissue while maintaining a vigilant state will provide insights into the immune surveillance strategies in the lung. Through scRNAseq, we found that the ivs+ cells had increased expression of genes associated with cell adhesion and interactions at the vasculature cell wall. Studies examining protein expression of integrins identified through our scRNAseq analysis, along with cell adhesion molecules expressed by lung endothelial cells in various vasculature compartments, will be needed to further support and expand upon our findings.
- **Comparative Analysis Across Non-Lymphoid Tissues:** Expanding our study of ivs+ T cells to other highly vascularized non-lymphoid tissues, such as the liver, spleen, or kidney, is essential to determine whether the observed vascular residency is unique to the lung or a common feature in other organs. Potter et al. found that the ivs+ cells (referred to as ivas+ in their study) in both the kidney and spleen were enriched in CD8 T cells, similar to what we observed in the lung. This suggests the potential presence of vasculature niches in other non-lymphoid tissues as well.
- **Harnessing Functional Potential of ivs+ T Cells:** An essential avenue for future research involves unraveling the intricate signals and cues that regulate ivs+ T cell activity within the pulmonary vasculature. Investigating strategies to modulate their function, whether by enhancing their

protective roles or mitigating potential harmful responses, holds promise for the development of innovative therapeutic interventions. Their unique location exposed to plasma — in contrast to tissue-resident T cells, which are shielded from the blood — offers opportunities for systemic administration of treatments targeting these distinct cell populations.

Targeting this highly activated subset before these cells migrate into the tissues has the potential to mitigate disease severity in conditions with known immunopathology, such as COVID-19.

- **Role in Respiratory Disease:** A logical progression of our studies would be to explore the role of pulmonary vasculature-associated T cells in respiratory diseases such as COVID-19. In our first study, we identified a unique population of pulmonary infiltrating CD4 T cells that expressed cytotoxic molecules and exhibited upregulation of CD8 upon stimulation. Interestingly, these cytotoxic CD4 T cells were present at all timepoints post-SARS-CoV-2 infection in the lung but notably absent in the blood. By leveraging intravascular staining, we can begin to identify the origin of these cells, potentially revealing their localization within the pulmonary vasculature. Understanding whether these cytotoxic CD4 T cells are recruited into the lung parenchyma and airways upon SARS-CoV-2 infection from a specialized vascular niche and delineating their potential roles in disease pathogenesis or host defense mechanisms could pave the way for novel therapeutic interventions.

- **Assessing LLECs in Various Disease States**: In our third study, we found that the pulmonary ivs+ CD8 T cells demonstrated enhanced functionality compared to their counterparts in the pulmonary tissue (ivs-) and blood within our cohort of SIV-infected animals. While further studies such as immunohistochemistry and spatial transcriptomics are needed to confirm the identity of LLECs within the ivs+ T cell compartment, their potential contribution to controlling viral reservoirs in chronic infections is an exciting prospect. Studies further investigating the ivs+ CD8 T cells, and in particular LLECs, in the context in which these cells are most prevalent and functionally significant will be important going forward. By adding additional cohorts of SIV-naive, untreated SIV-infected, and SIV-infected animals undergoing antiretroviral therapy (ART) we can begin to uncover additional insights into LLECs in the context of infectious disease. Examining how LLECs respond to infection and treatment, we can determine potential associations between their presence in the lung and distinct infection states. Further exploration of possible links between LLECs and viral reservoirs or viremia levels could provide valuable insights into the role of LLECs in controlling viral replication and persistence. Additionally, assessing the feasibility of targeting ivs+ T cells, including LLECs, as part of immunotherapies designed to combat infectious disease may hold promise for clinical applications.

Our findings lay the groundwork for increased exploration of ivs+ T cells in pulmonary immunology. The identified future directions not only promise to further unravel the mysteries of these cells but also offer potential clinical applications that can impact our understanding of respiratory health and the development of innovative therapies.

List of References

Introduction References

1. Organization WH. WHO COVID-19 Dashboard. World Health Organisation. 2023. Available: <https://covid19.who.int>
2. Sayampanathan AA, Heng CS, Pin PH, Pang J, Leong TY, Lee VJ. Infectivity of asymptomatic versus symptomatic COVID-19. *Lancet*. 2021;397: 93–94. doi:10.1016/S0140-6736(20)32651-9
3. Teo AKJ, Choudhury Y, Tan IB, Cher CY, Chew SH, Wan ZY, et al. Saliva is more sensitive than nasopharyngeal or nasal swabs for diagnosis of asymptomatic and mild COVID-19 infection. *Sci Rep*. 2021;11: 1–8. doi:10.1038/s41598-021-82787-z
4. Xie C, Li Q, Li L, Peng X, Ling Z, Xiao B, et al. Association of early inflammation with age and asymptomatic disease in covid-19. *J Inflamm Res*. 2021;14: 1207–1216. doi:10.2147/JIR.S304190
5. Zhu J, Ji P, Pang J, Zhong Z, Li H, He C, et al. Clinical characteristics of 3062 COVID-19 patients: A meta-analysis. *J Med Virol*. 2020;92: 1902–1914. doi:10.1002/jmv.25884
6. McElvaney OJ, McEvoy NL, McElvaney OF, Carroll TP, Murphy MP, Dunlea DM, et al. Characterization of the inflammatory response to severe COVID-19 illness. *Am J Respir Crit Care Med*. 2020;202: 812–821. doi:10.1164/rccm.202005-1583OC
7. Zhang R, Liu Y, Zhang B, Wu C, Zhou J, Zhang Y, et al. Coagulopathy is associated with multiple organ damage and prognosis of COVID-19. *EXCLI J*. 2021;20: 174–191. doi:10.17179/excli2020-2853
8. Zingaropoli MA, Nijhawan P, Carraro A, Pasculli P, Zuccalà P, Perri V, et al. Increased sCD163 and sCD14 Plasmatic Levels and Depletion of Peripheral Blood Pro-Inflammatory Monocytes, Myeloid and Plasmacytoid Dendritic Cells in Patients With Severe COVID-19 Pneumonia. *Front Immunol*. 2021;12: 1–12. doi:10.3389/fimmu.2021.627548

9. Zuo Y, Yalavarthi S, Shi H, Gockman K, Zuo M, Madison JA, et al. Neutrophil extracellular traps in COVID-19. *JCI Insight*. 2020;5. doi:10.1172/jci.insight.138999
10. Pandey K, Acharya A, Mohan M, Ng CL, Reid SP, Byrareddy SN. Animal models for SARS-CoV-2 research: A comprehensive literature review. *Transbound Emerg Dis*. 2020/12/20. 2021;68: 1868–1885. doi:10.1111/tbed.13907
11. Fahlberg MD, Blair R V., Doyle-Meyers LA, Midkiff CC, Zenere G, Russell-Lodrigue KE, et al. Cellular events of acute, resolving or progressive COVID-19 in SARS-CoV-2 infected non-human primates. *Nat Commun*. 2020;11: 1–14. doi:10.1038/s41467-020-19967-4
12. Blair R V, Vaccari M, Doyle-Meyers LA, Roy CJ, Russell-Lodrigue K, Fahlberg M, et al. Acute Respiratory Distress in Aged, SARS-CoV-2–Infected African Green Monkeys but Not Rhesus Macaques. *Am J Pathol*. 2021;191: 274–282. doi:10.1016/j.ajpath.2020.10.016
13. Hartman AL, Nambulli S, McMillen CM, White AG, Tilston-Lunel NL, Albe JR, et al. SARS-CoV-2 infection of African green monkeys results in mild respiratory disease discernible by PET/CT imaging and shedding of infectious virus from both respiratory and gastrointestinal tracts. *PLoS Pathog*. 2020;16: 1–24. doi:10.1371/journal.ppat.1008903
14. Munster VJ, Feldmann F, Williamson BN, van Doremalen N, Pérez-Pérez L, Schulz J, et al. Respiratory disease in rhesus macaques inoculated with SARS-CoV-2. *Nature*. 2020;585: 268–272. doi:10.1038/s41586-020-2324-7
15. Woolsey C, Borisevich V, Prasad AN, Agans KN, Deer DJ, Dobias NS, et al. Establishment of an African green monkey model for COVID-19 and protection against re-infection. *Nat Immunol*. 2020/11/24. 2021;22: 86–98. doi:10.1038/s41590-020-00835-8
16. McLean G, Kamil J, Lee B, Moore P, Schulz TF, Muik A, et al. The Impact of Evolving SARS-CoV-2 Mutations and Variants on COVID-19 Vaccines. *mBio*. American Society for Microbiology; 2022. doi:10.1128/mbio.02979-21
17. Lessells RJ. SARS-CoV-2 variants of concern: the knowns and unknowns. *Anaesthesia, Crit care pain Med*. 2021/04/22. 2021;40: 100868. doi:10.1016/j.accpm.2021.100868
18. Winger A, Caspari T. The Spike of Concern-The Novel Variants of SARS-CoV-2. *Viruses*. 2021;13: 1002. doi:10.3390/v13061002

19. Walensky RP, Walke HT, Fauci AS. SARS-CoV-2 Variants of Concern in the United States—Challenges and Opportunities. *JAMA*. 2021;325: 1037–1038. doi:10.1001/jama.2021.2294
20. Singh J, Rahman SA, Ehtesham NZ, Hira S, Hasnain SE. SARS-CoV-2 variants of concern are emerging in India. *Nat Med*. 2021;27: 1131–1133. doi:10.1038/s41591-021-01397-4
21. Olsen RJ, Christensen PA, Long SW, Subedi S, Hodjat P, Olson R, et al. Trajectory of Growth of SARS-CoV-2 Variants in Houston, Texas, January through May 2021 Based on 12,476 Genome Sequences. *Am J Pathol*. 2021; S0002-9440(21)00317–5. doi:10.1016/j.ajpath.2021.07.002
22. Shen X, Tang H, McDanal C, Wagh K, Fischer W, Theiler J, et al. SARS-CoV-2 variant B.1.1.7 is susceptible to neutralizing antibodies elicited by ancestral spike vaccines. *Cell Host Microbe*. 2021;29: 529-539.e3. doi:10.1016/j.chom.2021.03.002
23. Borges V, Isidro J, Cunha M, Cochicho D, Martins L, Banha L, et al. Long-Term Evolution of SARS-CoV-2 in an Immunocompromised Patient with Non-Hodgkin Lymphoma. *mSphere*. 2021;6: 1–8. doi:10.1128/msphere.00244-21
24. Baudou E, Lespine A, Durrieu G, André F, Gandia P, Durand C, et al. Persistence and Evolution of SARS-CoV-2 in an Immunocompromised Host. *new engl J Med*. 2020;February: 2008–2009.
25. Kemp SA, Collier DA, Datir RP, Ferreira IATM, Gayed S, Jahun A, et al. SARS-CoV-2 evolution during treatment of chronic infection. *Nature*. 2021;592: 277–282. doi:10.1038/s41586-021-03291-y
26. Avanzato VA, Matson MJ, Seifert SN, Pryce R, Williamson BN, Anzick SL, et al. Case Study: Prolonged Infectious SARS-CoV-2 Shedding from an Asymptomatic Immunocompromised Individual with Cancer. *Cell*. 2020;183: 1901-1912.e9. doi:10.1016/j.cell.2020.10.049
27. Stanevich O V., Alekseeva EI, Sergeeva M, Fadeev A V., Komissarova KS, Ivanova AA, et al. SARS-CoV-2 escape from cytotoxic T cells during long-term COVID-19. *Nat Commun*. 2023;14. doi:10.1038/s41467-022-34033-x
28. Schenkel JM, Masopust D. Tissue-resident memory T cells. *Immunity*. 2014/12/06. 2014;41: 886–897. doi:10.1016/j.immuni.2014.12.007
29. Pabst R. The periarterial space in the lung: its important role in lung edema, transplantation, and microbial or allergic inflammation. *Pathobiology*. 2004;71: 287–294. doi:10.1159/000081723

30. Lake Potter E, Gideon HP, Tkachev V, Fabozzi G, Chassiakos A, Petrovas C, et al. Measurement of leukocyte trafficking kinetics in macaques by serial intravascular staining. *Sci Transl Med*. 2021;13: 1–14. doi:10.1126/SCITRANSLMED.ABB4582
31. Eljalby M. CX3CR1: Re-defining exhausted CD8 + T cell populations. 2017.
32. Emerson H. Panum on Measles: Observations Made During the Epidemic of Measles on the Faroe Islands in the Year 1846 (A translation from the Danish). *American Journal of Public Health and the Nations Health*. 1940. pp. 1245–1246.
33. Altman JD, Moss PA, Goulder PJ, Barouch DH, McHeyzer-Williams MG, Bell JI, et al. Phenotypic analysis of antigen-specific T lymphocytes. *Science*. 1996;274: 94–96. doi:10.1126/science.274.5284.94
34. Murali-Krishna K, Altman JD, Suresh M, Sourdive DJ, Zajac AJ, Miller JD, et al. Counting antigen-specific CD8 T cells: a reevaluation of bystander activation during viral infection. *Immunity*. 1998;8: 177–187. doi:10.1016/s1074-7613(00)80470-7
35. Ahmed R, Gray D. Immunological memory and protective immunity: understanding their relation. *Science*. 1996;272: 54–60. doi:10.1126/science.272.5258.54
36. Hou S, Hyland L, Ryan KW, Portner A, Doherty PC. Virus-specific CD8+ T-cell memory determined by clonal burst size. *Nature*. 1994;369: 652–654. doi:10.1038/369652a0
37. Sprent J, Tough DF. T cell death and memory. *Science*. 2001;293: 245–248. doi:10.1126/science.1062416
38. Gunzer M, Schäfer A, Borgmann S, Grabbe S, Zänker KS, Bröcker EB, et al. Antigen presentation in extracellular matrix: interactions of T cells with dendritic cells are dynamic, short lived, and sequential. *Immunity*. 2000;13: 323–332. doi:10.1016/s1074-7613(00)00032-7
39. den Haan JM, Bevan MJ. Antigen presentation to CD8+ T cells: cross-priming in infectious diseases. *Curr Opin Immunol*. 2001;13: 437–441. doi:10.1016/s0952-7915(00)00238-7
40. Zhu J, Yamane H, Paul WE. Differentiation of effector CD4 T cell populations (*). *Annu Rev Immunol*. 2010;28: 445–489. doi:10.1146/annurev-immunol-030409-101212

41. De Smedt T, Pajak B, Muraille E, Lespagnard L, Heinen E, De Baetselier P, et al. Regulation of dendritic cell numbers and maturation by lipopolysaccharide in vivo. *J Exp Med*. 1996;184: 1413–1424. doi:10.1084/jem.184.4.1413
42. Azuma M, Cayabyab M, Buck D, Phillips JH, Lanier LL. CD28 interaction with B7 costimulates primary allogeneic proliferative responses and cytotoxicity mediated by small, resting T lymphocytes. *J Exp Med*. 1992;175: 353–360. doi:10.1084/jem.175.2.353
43. Lanier LL, O'Fallon S, Somoza C, Phillips JH, Linsley PS, Okumura K, et al. CD80 (B7) and CD86 (B70) provide similar costimulatory signals for T cell proliferation, cytokine production, and generation of CTL. *J Immunol*. 1995;154: 97–105.
44. Schultze J, Nadler LM, Gribben JG. B7-mediated costimulation and the immune response. *Blood Rev*. 1996;10: 111–127. doi:10.1016/s0268-960x(96)90040-5
45. Wong P, Pamer EG. Cutting edge: antigen-independent CD8 T cell proliferation. *J Immunol*. 2001;166: 5864–5868. doi:10.4049/jimmunol.166.10.5864
46. Kaech SM, Ahmed R. Memory CD8+ T cell differentiation: initial antigen encounter triggers a developmental program in naïve cells. *Nat Immunol*. 2001;2: 415–422. doi:10.1038/87720
47. Badovinac VP, Porter BB, Harty JT. Programmed contraction of CD8+ T cells after infection. *Nat Immunol*. 2002;3: 619–626. doi:10.1038/ni804
48. Homann D, Teyton L, Oldstone MB. Differential regulation of antiviral T-cell immunity results in stable CD8+ but declining CD4+ T-cell memory. *Nat Med*. 2001;7: 913–919. doi:10.1038/90950
49. Sallusto F, Geginat J, Lanzavecchia A. Central memory and effector memory T cell subsets: function, generation, and maintenance. *Annu Rev Immunol*. 2004;22: 745–763. doi:10.1146/annurev.immunol.22.012703.104702
50. Reinhardt RL, Khoruts A, Merica R, Zell T, Jenkins MK. Visualizing the generation of memory CD4 T cells in the whole body. *Nature*. 2001;410: 101–105. doi:10.1038/35065111
51. Masopust D, Vezys V, Marzo AL, Lefrançois L. Preferential localization of effector memory cells in nonlymphoid tissue. *Science*. 2001;291: 2413–2417. doi:10.1126/science.1058867
52. Sallusto F, Lenig D, Förster R, Lipp M, Lanzavecchia A. Two subsets of memory T lymphocytes with distinct homing potentials and effector functions. *Nature*. 1999;401: 708–712. doi:10.1038/44385

53. von Andrian UH, Mempel TR. Homing and cellular traffic in lymph nodes. *Nat Rev Immunol.* 2003;3: 867–878. doi:10.1038/nri1222
54. Weninger W, Crowley MA, Manjunath N, von Andrian UH. Migratory properties of naive, effector, and memory CD8(+) T cells. *J Exp Med.* 2001;194: 953–966. doi:10.1084/jem.194.7.953
55. Marzo AL, Klonowski KD, Le Bon A, Borrow P, Tough DF, Lefrançois L. Initial T cell frequency dictates memory CD8+ T cell lineage commitment. *Nat Immunol.* 2005;6: 793–799. doi:10.1038/ni1227
56. GOWANS JL, KNIGHT EJ. THE ROUTE OF RE-CIRCULATION OF LYMPHOCYTES IN THE RAT. *Proc R Soc London Ser B, Biol Sci.* 1964;159: 257–282. doi:10.1098/rspb.1964.0001
57. Masopust D, Lefrançois L. CD8 T-cell memory: the other half of the story. *Microbes Infect.* 2003;5: 221–226. doi:10.1016/s1286-4579(03)00014-5
58. Gebhardt T, Wakim LM, Eidsmo L, Reading PC, Heath WR, Carbone FR. Memory T cells in nonlymphoid tissue that provide enhanced local immunity during infection with herpes simplex virus. *Nat Immunol.* 2009;10: 524–530. doi:10.1038/ni.1718
59. Teijaro JR, Turner D, Pham Q, Wherry EJ, Lefrançois L, Farber DL. Cutting edge: Tissue-retentive lung memory CD4 T cells mediate optimal protection to respiratory virus infection. *J Immunol.* 2011;187: 5510–5514. doi:10.4049/jimmunol.1102243
60. Jiang X, Clark RA, Liu L, Wagers AJ, Fuhlbrigge RC, Kupper TS. Skin infection generates non-migratory memory CD8+ T(RM) cells providing global skin immunity. *Nature.* 2012;483: 227–231. doi:10.1038/nature10851
61. Carman C V, Martinelli R. T Lymphocyte-Endothelial Interactions: Emerging Understanding of Trafficking and Antigen-Specific Immunity. *Front Immunol.* 2015;6: 603. doi:10.3389/fimmu.2015.00603
62. Ley K, Laudanna C, Cybulsky MI, Nourshargh S. Getting to the site of inflammation: the leukocyte adhesion cascade updated. *Nat Rev Immunol.* 2007;7: 678–689. doi:10.1038/nri2156
63. Proudfoot AEI, Handel TM, Johnson Z, Lau EK, LiWang P, Clark-Lewis I, et al. Glycosaminoglycan binding and oligomerization are essential for the in vivo activity of certain chemokines. *Proc Natl Acad Sci U S A.* 2003;100: 1885–1890. doi:10.1073/pnas.0334864100

64. Goebeler M, Yoshimura T, Toksoy A, Ritter U, Bröcker EB, Gillitzer R. The chemokine repertoire of human dermal microvascular endothelial cells and its regulation by inflammatory cytokines. *J Invest Dermatol.* 1997;108: 445–451. doi:10.1111/1523-1747.ep12289711
65. Card CM, Yu SS, Swartz MA. Emerging roles of lymphatic endothelium in regulating adaptive immunity. *J Clin Invest.* 2014;124: 943–952. doi:10.1172/JCI73316
66. Middleton J, Neil S, Wintle J, Clark-Lewis I, Moore H, Lam C, et al. Transcytosis and surface presentation of IL-8 by venular endothelial cells. *Cell.* 1997;91: 385–395. doi:10.1016/s0092-8674(00)80422-5
67. Middleton J, Patterson AM, Gardner L, Schmutz C, Ashton BA. Leukocyte extravasation: Chemokine transport and presentation by the endothelium. *Blood.* 2002;100: 3853–3860. doi:10.1182/blood.V100.12.3853
68. Butcher EC, Williams M, Youngman K, Rott L, Briskin M. Lymphocyte trafficking and regional immunity. *Adv Immunol.* 1999;72: 209–253. doi:10.1016/s0065-2776(08)60022-x
69. Luo B-H, Carman C V, Springer TA. Structural basis of integrin regulation and signaling. *Annu Rev Immunol.* 2007;25: 619–647. doi:10.1146/annurev.immunol.25.022106.141618
70. Butcher EC. Leukocyte-endothelial cell recognition: three (or more) steps to specificity and diversity. *Cell.* 1991;67: 1033–1036. doi:10.1016/0092-8674(91)90279-8
71. Carveth HJ, Bohnsack JF, McIntyre TM, Baggiolini M, Prescott SM, Zimmerman GA. Neutrophil activating factor (NAF) induces polymorphonuclear leukocyte adherence to endothelial cells and to subendothelial matrix proteins. *Biochem Biophys Res Commun.* 1989;162: 387–393. doi:10.1016/0006-291x(89)92009-3
72. Detmers PA, Lo SK, Olsen-Egbert E, Walz A, Baggiolini M, Cohn ZA. Neutrophil-activating protein 1/interleukin 8 stimulates the binding activity of the leukocyte adhesion receptor CD11b/CD18 on human neutrophils. *J Exp Med.* 1990;171: 1155–1162. doi:10.1084/jem.171.4.1155
73. Luscinskas FW, Kansas GS, Ding H, Pizcueta P, Schleiffenbaum BE, Tedder TF, et al. Monocyte rolling, arrest and spreading on IL-4-activated vascular endothelium under flow is mediated via sequential action of L-selectin, beta 1-integrins, and beta 2-integrins. *J Cell Biol.* 1994;125: 1417–1427. doi:10.1083/jcb.125.6.1417

74. Schenkel AR, Mamdouh Z, Muller WA. Locomotion of monocytes on endothelium is a critical step during extravasation. *Nat Immunol.* 2004;5: 393–400. doi:10.1038/ni1051
75. Phillipson M, Heit B, Colarusso P, Liu L, Ballantyne CM, Kubes P. Intraluminal crawling of neutrophils to emigration sites: a molecularly distinct process from adhesion in the recruitment cascade. *J Exp Med.* 2006;203: 2569–2575. doi:10.1084/jem.20060925
76. Springer TA. Traffic signals for lymphocyte recirculation and leukocyte emigration: the multistep paradigm. *Cell.* 1994;76: 301–314. doi:10.1016/0092-8674(94)90337-9
77. Muller WA. Leukocyte-endothelial-cell interactions in leukocyte transmigration and the inflammatory response. *Trends Immunol.* 2003;24: 327–334. doi:10.1016/s1471-4906(03)00117-0
78. Aird WC. Phenotypic heterogeneity of the endothelium: I. Structure, function, and mechanisms. *Circ Res.* 2007;100: 158–173. doi:10.1161/01.RES.0000255691.76142.4a
79. Aird WC. Phenotypic heterogeneity of the endothelium: II. Representative vascular beds. *Circ Res.* 2007;100: 174–190. doi:10.1161/01.RES.0000255690.03436.ae
80. Bartholomäus I, Kawakami N, Odoardi F, Schläger C, Miljkovic D, Ellwart JW, et al. Effector T cell interactions with meningeal vascular structures in nascent autoimmune CNS lesions. *Nature.* 2009;462: 94–98. doi:10.1038/nature08478
81. Geissmann F, Cameron TO, Sidobre S, Manlongat N, Kronenberg M, Briskin MJ, et al. Intravascular immune surveillance by CXCR6+ NKT cells patrolling liver sinusoids. *PLoS Biol.* 2005;3: e113. doi:10.1371/journal.pbio.0030113
82. Alon R, Sportiello M, Kozlovski S, Kumar A, Reilly EC, Zarbock A, et al. Leukocyte trafficking to the lungs and beyond: lessons from influenza for COVID-19. *Nat Rev Immunol.* 2021;21: 49–64. doi:10.1038/s41577-020-00470-2
83. Pabst R, Tschernig T. Perivascular capillaries in the lung: An important but neglected vascular bed in immune reactions? *J Allergy Clin Immunol.* 2002;110: 209–214. doi:10.1067/mai.2002.126836
84. Galkina E, Thatte J, Dabak V, Williams MB, Ley K, Braciale TJ. Preferential migration of effector CD8+ T cells into the interstitium of the normal lung. *J Clin Invest.* 2005;115: 3473–3483. doi:10.1172/JCI24482

85. Stadler K, Masignani V, Eickmann M, Becker S, Abrignani S, Klenk H-D, et al. SARS--beginning to understand a new virus. *Nat Rev Microbiol.* 2003;1: 209–218. doi:10.1038/nrmicro775
86. Boni MF, Lemey P, Jiang X, Lam TT-Y, Perry BW, Castoe TA, et al. Evolutionary origins of the SARS-CoV-2 sarbecovirus lineage responsible for the COVID-19 pandemic. *Nat Microbiol.* 2020;5: 1408–1417. doi:10.1038/s41564-020-0771-4
87. Zhu N, Zhang D, Wang W, Li X, Yang B, Song J, et al. A Novel Coronavirus from Patients with Pneumonia in China, 2019. *N Engl J Med.* 2020;382: 727–733. doi:10.1056/NEJMoa2001017
88. Cui J, Li F, Shi Z-L. Origin and evolution of pathogenic coronaviruses. *Nat Rev Microbiol.* 2019;17: 181–192. doi:10.1038/s41579-018-0118-9
89. Peiris JSM, Lai ST, Poon LLM, Guan Y, Yam LYC, Lim W, et al. Coronavirus as a possible cause of severe acute respiratory syndrome. *Lancet (London, England).* 2003;361: 1319–1325. doi:10.1016/s0140-6736(03)13077-2
90. Yeung M-L, Yao Y, Jia L, Chan JFW, Chan K-H, Cheung K-F, et al. MERS coronavirus induces apoptosis in kidney and lung by upregulating Smad7 and FGF2. *Nat Microbiol.* 2016;1: 16004. doi:10.1038/nmicrobiol.2016.4
91. Gorse GJ, Patel GB, Vitale JN, O'Connor TZ. Prevalence of antibodies to four human coronaviruses is lower in nasal secretions than in serum. *Clin Vaccine Immunol.* 2010;17: 1875–1880. doi:10.1128/CVI.00278-10
92. V'kovski P, Kratzel A, Steiner S, Stalder H, Thiel V. Coronavirus biology and replication: implications for SARS-CoV-2. *Nat Rev Microbiol.* 2021;19: 155–170. doi:10.1038/s41579-020-00468-6
93. Chan JF-W, Kok K-H, Zhu Z, Chu H, To KK-W, Yuan S, et al. Genomic characterization of the 2019 novel human-pathogenic coronavirus isolated from a patient with atypical pneumonia after visiting Wuhan. *Emerg Microbes Infect.* 2020;9: 221–236. doi:10.1080/22221751.2020.1719902
94. Hermens JM, Kesmir C. Role of T cells in severe COVID-19 disease, protection, and long term immunity. *Immunogenetics.* 2023;75: 295–307. doi:10.1007/s00251-023-01294-9
95. Zhou P, Yang X-L, Wang X-G, Hu B, Zhang L, Zhang W, et al. A pneumonia outbreak associated with a new coronavirus of probable bat origin. *Nature.* 2020;579: 270–273. doi:10.1038/s41586-020-2012-7
96. Shang J, Ye G, Shi K, Wan Y, Luo C, Aihara H, et al. Structural basis of receptor recognition by SARS-CoV-2. *Nature.* 2020;581: 221–224. doi:10.1038/s41586-

- 020-2179-y
97. Anka AU, Tahir MI, Abubakar SD, Alsabbagh M, Zian Z, Hamedifar H, et al. Coronavirus disease 2019 (COVID-19): An overview of the immunopathology, serological diagnosis and management. *Scand J Immunol.* 2021;93: e12998. doi:10.1111/sji.12998
 98. Parasher A. COVID-19: Current understanding of its Pathophysiology, Clinical presentation and Treatment. *Postgrad Med J.* 2021;97: 312–320. doi:10.1136/postgradmedj-2020-138577
 99. Yoshida M, Worlock KB, Huang N, Lindeboom RGH, Butler CR, Kumasaka N, et al. Local and systemic responses to SARS-CoV-2 infection in children and adults. *Nature.* 2022;602: 321–327. doi:10.1038/s41586-021-04345-x
 100. Wiersinga WJ, Rhodes A, Cheng AC, Peacock SJ, Prescott HC. Pathophysiology, Transmission, Diagnosis, and Treatment of Coronavirus Disease 2019 (COVID-19): A Review. *JAMA.* 2020;324: 782–793. doi:10.1001/jama.2020.12839
 101. Moss P. The T cell immune response against SARS-CoV-2. *Nat Immunol.* 2022;23: 186–193. doi:10.1038/s41590-021-01122-w
 102. Pujadas E, Chaudhry F, McBride R, Richter F, Zhao S, Wajnberg A, et al. SARS-CoV-2 viral load predicts COVID-19 mortality. *The Lancet. Respiratory medicine.* England; 2020. p. e70. doi:10.1016/S2213-2600(20)30354-4
 103. Hadjadj J, Yatim N, Barnabei L, Corneau A, Boussier J, Smith N, et al. Impaired type I interferon activity and inflammatory responses in severe COVID-19 patients. *Science.* 2020;369: 718–724. doi:10.1126/science.abc6027
 104. Rydzynski Moderbacher C, Ramirez SI, Dan JM, Grifoni A, Hastie KM, Weiskopf D, et al. Antigen-Specific Adaptive Immunity to SARS-CoV-2 in Acute COVID-19 and Associations with Age and Disease Severity. *Cell.* 2020;183: 996-1012.e19. doi:10.1016/j.cell.2020.09.038
 105. Grau-Expósito J, Sánchez-Gaona N, Massana N, Suppi M, Astorga-Gamaza A, Perea D, et al. Peripheral and lung resident memory T cell responses against SARS-CoV-2. *Nat Commun.* 2021;12. doi:10.1038/s41467-021-23333-3
 106. Yu KK, Fischinger S, Smith MT, Atyeo C, Cizmeci D, Wolf CR, et al. Comorbid illnesses are associated with altered adaptive immune responses to SARS-CoV-2. *JCI insight.* 2021;6. doi:10.1172/jci.insight.146242
 107. Cohen KW, Linderman SL, Moodie Z, Czartoski J, Lai L, Mantus G, et al. Longitudinal analysis shows durable and broad immune memory after SARS-CoV-2 infection with persisting antibody responses and memory B and T cells. *Cell reports Med.* 2021;2: 100354. doi:10.1016/j.xcrm.2021.100354

108. Tarke A, Sidney J, Kidd CK, Dan JM, Ramirez SI, Yu ED, et al. Comprehensive analysis of T cell immunodominance and immunoprevalence of SARS-CoV-2 epitopes in COVID-19 cases. *Cell reports Med.* 2021;2: 100204. doi:10.1016/j.xcrm.2021.100204
109. Rha M-S, Jeong HW, Ko J-H, Choi SJ, Seo I-H, Lee JS, et al. PD-1-Expressing SARS-CoV-2-Specific CD8(+) T Cells Are Not Exhausted, but Functional in Patients with COVID-19. *Immunity.* 2021;54: 44-52.e3. doi:10.1016/j.immuni.2020.12.002
110. Bieberich F, Vazquez-Lombardi R, Yermanos A, Ehling RA, Mason DM, Wagner B, et al. A Single-Cell Atlas of Lymphocyte Adaptive Immune Repertoires and Transcriptomes Reveals Age-Related Differences in Convalescent COVID-19 Patients. *Front Immunol.* 2021;12: 701085. doi:10.3389/fimmu.2021.701085
111. Baird S, Ashley CL, Marsh-Wakefield F, Alca S, Ferguson AL, Lukeman H, et al. A unique cytotoxic CD4+ T cells signature defines critical COVID-19. 2023;12: 1–13. doi:10.1002/cti2.1463
112. Szabo PA, Dogra P, Gray JI, Wells SB, Connors TJ, Weisberg SP, et al. Longitudinal profiling of respiratory and systemic immune responses reveals myeloid cell-driven lung inflammation in severe COVID-19. *Immunity.* 2021;54: 797-814.e6. doi:10.1016/j.immuni.2021.03.005
113. Sahin U, Muik A, Vogler I, Derhovanessian E, Kranz LM, Vormehr M, et al. BNT162b2 vaccine induces neutralizing antibodies and poly-specific T cells in humans. *Nature.* 2021;595: 572–577. doi:10.1038/s41586-021-03653-6
114. Skelly DT, Harding AC, Gilbert-Jaramillo J, Knight ML, Longet S, Brown A, et al. Two doses of SARS-CoV-2 vaccination induce robust immune responses to emerging SARS-CoV-2 variants of concern. *Nat Commun.* 2021;12: 5061. doi:10.1038/s41467-021-25167-5
115. Deeks SG, Overbaugh J, Phillips A, Buchbinder S. HIV infection. *Nat Rev Dis Prim.* 2015;1: 15035. doi:10.1038/nrdp.2015.35
116. Faria NR, Rambaut A, Suchard MA, Baele G, Bedford T, Ward MJ, et al. HIV epidemiology. The early spread and epidemic ignition of HIV-1 in human populations. *Science.* 2014;346: 56–61. doi:10.1126/science.1256739
117. Keele BF, Van Heuverswyn F, Li Y, Bailes E, Takehisa J, Santiago ML, et al. Chimpanzee reservoirs of pandemic and nonpandemic HIV-1. *Science.* 2006;313: 523–526. doi:10.1126/science.1126531
118. HIV/AIDS research & treatment timeline 1998. Research initiative, treatment

- action : RITA. Jan 1999: 21–26.
119. Hayes R, Weiss H. *Epidemiology. Understanding HIV epidemic trends in Africa. Science.* 2006;311: 620–621. doi:10.1126/science.1124072
 120. Fanales-Belasio E, Raimondo M, Suligoi B, Buttò S. HIV virology and pathogenetic mechanisms of infection: a brief overview. *Ann Ist Super Sanita.* 2010;46: 5–14. doi:10.4415/ANN_10_01_02
 121. Luciw PA, Harada S. *AIDS 1998. Virology: overview. AIDS.* 1998;12 Suppl A: S1-3.
 122. Liu L. *Fields Virology, 6th Edition. Clin Infect Dis.* 2014;59: 613. doi:10.1093/cid/ciu346
 123. Popik W, Alce TM, Au W-C. Human immunodeficiency virus type 1 uses lipid raft-colocalized CD4 and chemokine receptors for productive entry into CD4(+) T cells. *J Virol.* 2002;76: 4709–4722. doi:10.1128/jvi.76.10.4709-4722.2002
 124. Berger EA, Murphy PM, Farber JM. Chemokine receptors as HIV-1 coreceptors: roles in viral entry, tropism, and disease. *Annu Rev Immunol.* 1999;17: 657–700. doi:10.1146/annurev.immunol.17.1.657
 125. Simon V, Ho DD, Abdool Karim Q. HIV/AIDS epidemiology, pathogenesis, prevention, and treatment. *Lancet. Elsevier B.V.;* 2006. pp. 489–504. doi:10.1016/S0140-6736(06)69157-5
 126. Shaw GM, Hunter E. HIV transmission. *Cold Spring Harb Perspect Med.* 2012;2. doi:10.1101/cshperspect.a006965
 127. Moir S, Chun T-W, Fauci AS. Pathogenic mechanisms of HIV disease. *Annu Rev Pathol.* 2011;6: 223–248. doi:10.1146/annurev-pathol-011110-130254
 128. Mattapallil JJ, Douek DC, Hill B, Nishimura Y, Martin M, Roederer M. Massive infection and loss of memory CD4+ T cells in multiple tissues during acute SIV infection. *Nature.* 2005;434: 1093–1097. doi:10.1038/nature03501
 129. Pedersen C, Lindhardt BO, Jensen BL, Lauritzen E, Gerstoft J, Dickmeiss E, et al. Clinical course of primary HIV infection: consequences for subsequent course of infection. *BMJ.* 1989;299: 154–157. doi:10.1136/bmj.299.6692.154
 130. Veazey RS, DeMaria M, Chalifoux L V, Shvets DE, Pauley DR, Knight HL, et al. Gastrointestinal tract as a major site of CD4+ T cell depletion and viral replication in SIV infection. *Science.* 1998;280: 427–431. doi:10.1126/science.280.5362.427

131. Addo MM, Yu XG, Rathod A, Cohen D, Eldridge RL, Strick D, et al. Comprehensive epitope analysis of human immunodeficiency virus type 1 (HIV-1)-specific T-cell responses directed against the entire expressed HIV-1 genome demonstrate broadly directed responses, but no correlation to viral load. *J Virol.* 2003;77: 2081–2092. doi:10.1128/jvi.77.3.2081-2092.2003
132. Ndhlovu ZM, Kanya P, Mewalal N, Kløverpris HN, Nkosi T, Pretorius K, et al. Magnitude and Kinetics of CD8+ T Cell Activation during Hyperacute HIV Infection Impact Viral Set Point. *Immunity.* 2015;43: 591–604. doi:10.1016/j.immuni.2015.08.012
133. Eller MA, Goonetilleke N, Tassaneetrithep B, Eller LA, Costanzo MC, Johnson S, et al. Expansion of Inefficient HIV-Specific CD8 T Cells during Acute Infection. *J Virol.* 2016;90: 4005–4016. doi:10.1128/JVI.02785-15
134. Matter MS, Claus C, Ochsenbein AF. CD4+ T cell help improves CD8+ T cell memory by retained CD27 expression. *Eur J Immunol.* 2008;38: 1847–1856. doi:10.1002/eji.200737824
135. Allen TM, Altfeld M, Geer SC, Kalife ET, Moore C, O'sullivan KM, et al. Selective escape from CD8+ T-cell responses represents a major driving force of human immunodeficiency virus type 1 (HIV-1) sequence diversity and reveals constraints on HIV-1 evolution. *J Virol.* 2005;79: 13239–13249. doi:10.1128/JVI.79.21.13239-13249.2005
136. Herbein G, Mahlkecht U, Batliwalla F, Gregersen P, Pappas T, Butler J, et al. Apoptosis of CD8+ T cells is mediated by macrophages through interaction of HIV gp120 with chemokine receptor CXCR4. *Nature.* 1998;395: 189–194. doi:10.1038/26026
137. Matano T, Shibata R, Siemon C, Connors M, Lane HC, Martin MA. Administration of an anti-CD8 monoclonal antibody interferes with the clearance of chimeric simian/human immunodeficiency virus during primary infections of rhesus macaques. *J Virol.* 1998;72: 164–169. doi:10.1128/JVI.72.1.164-169.1998
138. Jin X, Bauer DE, Tuttleton SE, Lewin S, Gettie A, Blanchard J, et al. Dramatic rise in plasma viremia after CD8(+) T cell depletion in simian immunodeficiency virus-infected macaques. *J Exp Med.* 1999;189: 991–998. doi:10.1084/jem.189.6.991

Chapter 1 References

1. Stadler K, Massignani V, Eickmann M, Becker S, Abrignani S, Klenk H-D, et al. SARS--beginning to understand a new virus. *Nat Rev Microbiol.* 2003;1: 209–218. doi:10.1038/nrmicro775
2. Boni MF, Lemey P, Jiang X, Lam TT-Y, Perry BW, Castoe TA, et al. Evolutionary origins of the SARS-CoV-2 sarbecovirus lineage responsible for the COVID-19 pandemic. *Nat Microbiol.* 2020;5: 1408–1417. doi:10.1038/s41564-020-0771-4
3. Gorbalenya AE, Baker SC, Baric RS, de Groot RJ, Drosten C, Gulyaeva AA, et al. The species Severe acute respiratory syndrome-related coronavirus: classifying 2019-nCoV and naming it SARS-CoV-2. *Nat Microbiol.* 2020;5: 536–544. doi:10.1038/s41564-020-0695-z
4. Sayampanathan AA, Heng CS, Pin PH, Pang J, Leong TY, Lee VJ. Infectivity of asymptomatic versus symptomatic COVID-19. *Lancet.* 2021;397: 93–94. doi:10.1016/S0140-6736(20)32651-9
5. Teo AKJ, Choudhury Y, Tan IB, Cher CY, Chew SH, Wan ZY, et al. Saliva is more sensitive than nasopharyngeal or nasal swabs for diagnosis of asymptomatic and mild COVID-19 infection. *Sci Rep.* 2021;11: 1–8. doi:10.1038/s41598-021-82787-z
6. Xie C, Li Q, Li L, Peng X, Ling Z, Xiao B, et al. Association of early inflammation with age and asymptomatic disease in covid-19. *J Inflamm Res.* 2021;14: 1207–1216. doi:10.2147/JIR.S304190
7. Zhu J, Ji P, Pang J, Zhong Z, Li H, He C, et al. Clinical characteristics of 3062 COVID-19 patients: A meta-analysis. *J Med Virol.* 2020;92: 1902–1914. doi:10.1002/jmv.25884
8. McElvaney OJ, McEvoy NL, McElvaney OF, Carroll TP, Murphy MP, Dunlea DM, et al. Characterization of the inflammatory response to severe COVID-19 illness. *Am J Respir Crit Care Med.* 2020;202: 812–821. doi:10.1164/rccm.202005-1583OC
9. Zhang R, Liu Y, Zhang B, Wu C, Zhou J, Zhang Y, et al. Coagulopathy is associated with multiple organ damage and prognosis of COVID-19. *EXCLI J.* 2021;20: 174–191. doi:10.17179/excli2020-2853
10. Zingaropoli MA, Nijhawan P, Carraro A, Pasculli P, Zuccalà P, Perri V, et al. Increased sCD163 and sCD14 Plasmatic Levels and Depletion of Peripheral Blood Pro-Inflammatory Monocytes, Myeloid and Plasmacytoid Dendritic Cells in Patients With Severe COVID-19 Pneumonia. *Front Immunol.* 2021;12: 1–12. doi:10.3389/fimmu.2021.627548

11. Zuo Y, Yalavarthi S, Shi H, Gockman K, Zuo M, Madison JA, et al. Neutrophil extracellular traps in COVID-19. *JCI Insight*. 2020;5. doi:10.1172/jci.insight.138999
12. Pandey K, Acharya A, Mohan M, Ng CL, Reid SP, Byrareddy SN. Animal models for SARS-CoV-2 research: A comprehensive literature review. *Transbound Emerg Dis*. 2020/12/20. 2021;68: 1868–1885. doi:10.1111/tbed.13907
13. Cleary SJ, Pitchford SC, Amison RT, Carrington R, Robaina Cabrera CL, Magnen M, et al. Animal models of mechanisms of SARS-CoV-2 infection and COVID-19 pathology. *Br J Pharmacol*. 2020;177: 4851–4865. doi:10.1111/bph.15143
14. Fahlberg MD, Blair R V., Doyle-Meyers LA, Midkiff CC, Zenere G, Russell-Lodrigue KE, et al. Cellular events of acute, resolving or progressive COVID-19 in SARS-CoV-2 infected non-human primates. *Nat Commun*. 2020;11: 1–14. doi:10.1038/s41467-020-19967-4
15. Blair R V, Vaccari M, Doyle-Meyers LA, Roy CJ, Russell-Lodrigue K, Fahlberg M, et al. Acute Respiratory Distress in Aged, SARS-CoV-2–Infected African Green Monkeys but Not Rhesus Macaques. *Am J Pathol*. 2021;191: 274–282. doi:10.1016/j.ajpath.2020.10.016
16. Munster VJ, Feldmann F, Williamson BN, van Doremalen N, Pérez-Pérez L, Schulz J, et al. Respiratory disease in rhesus macaques inoculated with SARS-CoV-2. *Nature*. 2020;585: 268–272. doi:10.1038/s41586-020-2324-7
17. Hartman AL, Nambulli S, McMillen CM, White AG, Tilston-Lunel NL, Albe JR, et al. SARS-CoV-2 infection of African green monkeys results in mild respiratory disease discernible by PET/CT imaging and shedding of infectious virus from both respiratory and gastrointestinal tracts. *PLoS Pathog*. 2020;16: 1–24. doi:10.1371/journal.ppat.1008903
18. Woolsey C, Borisevich V, Prasad AN, Agans KN, Deer DJ, Dobias NS, et al. Establishment of an African green monkey model for COVID-19 and protection against re-infection. *Nat Immunol*. 2020/11/24. 2021;22: 86–98. doi:10.1038/s41590-020-00835-8
19. Moothedath M, Muhamood M, Bhosale YS, Bhatia A, Gupta P, Reddy MRH, et al. COVID and Animal Trials: A Systematic Review. *J Pharm Bioallied Sci*. 2021/06/05. 2021;13: S31–S35. doi:10.4103/jpbs.JPBS_749_20
20. Liang B, Li H, Li L, Orange RW, Hai Y, Luo M. Current advances in HIV vaccine preclinical studies using Macaque models. *Vaccine*. Amsterdam : Elsevier Science; 2019. pp. 3388–3399. doi:10.1016/j.vaccine.2019.04.094

21. Canary LA, Vinton CL, Morcock DR, Pierce JB, Estes JD, Brenchley JM, et al. Rate of AIDS progression is associated with gastrointestinal dysfunction in simian immunodeficiency virus-infected pigtail macaques. *J Immunol.* 2013/02/11. 2013;190: 2959–2965. doi:10.4049/jimmunol.1202319
22. Klatt NR, Canary LA, Vanderford TH, Vinton CL, Engram JC, Dunham RM, et al. Dynamics of simian immunodeficiency virus SIVmac239 infection in pigtail macaques. *J Virol.* 2011/11/16. 2012;86: 1203–1213. doi:10.1128/JVI.06033-11
23. Klatt NR, Harris LD, Vinton CL, Sung H, Briant JA, Tabb B, et al. Compromised gastrointestinal integrity in pigtail macaques is associated with increased microbial translocation, immune activation, and IL-17 production in the absence of SIV infection. *Mucosal Immunol.* 2010/03/31. 2010;3: 387–398. doi:10.1038/mi.2010.14
24. Metcalf Pate KA, Lyons CE, Dorsey JL, Shirk EN, Queen SE, Adams RJ, et al. Platelet Activation and Platelet-Monocyte Aggregate Formation Contribute to Decreased Platelet Count During Acute Simian Immunodeficiency Virus Infection in Pig-tailed Macaques. *J Infect Dis.* 2013;208: 874–883. doi:10.1093/infdis/jit278
25. Kaneko N, Boucau J, Kuo H-H, Perugino C, Mahajan VS, Farmer JR, et al. Expansion of Cytotoxic CD4+ T cells in the lungs in severe COVID-19. medRxiv : the preprint server for health sciences. 2021. Available from: <https://www.medrxiv.org/content/10.1101/2021.03.23.21253885v1> doi:10.1101/2021.03.23.21253885
26. Beddingfield BJ, Maness NJ, Fears AC, Rappaport J, Aye PP, Russell-Lodrigue K, et al. Effective Prophylaxis of COVID-19 in Rhesus Macaques Using a Combination of Two Parenterally-Administered SARS-CoV-2 Neutralizing Antibodies. *Front Cell Infect Microbiol.* 2021;11: 753444. doi:10.3389/fcimb.2021.753444
27. Amir EAD, Davis KL, Tadmor MD, Simonds EF, Levine JH, Bendall SC, et al. ViSNE enables visualization of high dimensional single-cell data and reveals phenotypic heterogeneity of leukemia. *Nat Biotechnol.* 2013;31: 545–552. doi:10.1038/nbt.2594
28. Wickham H. *ggplot2: Elegant Graphics for Data Analysis.* Springer-Verlag New York; 1988. Available: <https://ggplot2.tidyverse.org>
29. Bancroft J, Gamble M, editors. *Theory and Practice of Histological Techniques.* 6th ed. Churchill Livingstone; 2007.

30. Shen X, Tang H, McDanal C, Wagh K, Fischer W, Theiler J, et al. SARS-CoV-2 variant B.1.1.7 is susceptible to neutralizing antibodies elicited by ancestral spike vaccines. *Cell Host Microbe*. 2021;29: 529-539.e3. doi:10.1016/j.chom.2021.03.002
31. Weissman D, Alameh MG, de Silva T, Collini P, Hornsby H, Brown R, et al. D614G Spike Mutation Increases SARS CoV-2 Susceptibility to Neutralization. *Cell Host Microbe*. 2021;29: 23-31.e4. doi:10.1016/j.chom.2020.11.012
32. Rockx B, Kuiken T, Herfst S, Bestebroer T, Lamers MM, Oude Munnink BB, et al. Comparative pathogenesis of COVID-19, MERS, and SARS in a nonhuman primate model. *Science*. 2020/04/17. 2020;368: 1012–1015. doi:10.1126/science.abb7314
33. Zhou F, Yu T, Du R, Fan G, Liu Y, Liu Z, et al. Clinical course and risk factors for mortality of adult inpatients with COVID-19 in Wuhan, China: a retrospective cohort study. *Lancet (London, England)*. 2020;395: 1054–1062. doi:10.1016/S0140-6736(20)30566-3
34. Yu H-H, Qin C, Chen M, Wang W, Tian D-S. D-dimer level is associated with the severity of COVID-19. *Thromb Res*. 2020/07/27. 2020;195: 219–225. doi:10.1016/j.thromres.2020.07.047
35. Rebnord EW, Strand E, Midttun Ø, Svingen GFT, Christensen MHE, Ueland PM, et al. The kynurenine:tryptophan ratio as a predictor of incident type 2 diabetes mellitus in individuals with coronary artery disease. *Diabetologia*. 2017;60: 1712–1721. doi:10.1007/s00125-017-4329-9
36. Lionetto L, Olivieri M, Capi M, De Bernardini D, Fazio F, Petrucca A, et al. Increased kynurenine-to-tryptophan ratio in the serum of patients infected with SARS-CoV2: An observational cohort study. *Biochim Biophys Acta - Mol Basis Dis*. 2021;1867: 166042. doi:10.1016/j.bbadis.2020.166042
37. Zheng M, Gao Y, Wang G, Song G, Liu S, Sun D, et al. Functional exhaustion of antiviral lymphocytes in COVID-19 patients. *Cell Mol Immunol*. 2020;17: 533–535. doi:10.1038/s41423-020-0402-2
38. Song CY, Xu J, He JQ, Lu YQ. COVID-19 early warning score: A multi-parameter screening tool to identify highly suspected patients. *medRxiv*. 2020. doi:10.1101/2020.03.05.20031906
39. Zhang B, Zhou X, Zhu C, Song Y, Feng F, Qiu Y, et al. Immune Phenotyping Based on the Neutrophil-to-Lymphocyte Ratio and IgG Level Predicts Disease Severity and Outcome for Patients With COVID-19. *Front Mol Biosci*. 2020;7. doi:10.3389/fmolb.2020.00157

40. Liu J, Liu Y, Xiang P, Pu L, Xiong H, Li C, et al. Neutrophil-to-lymphocyte ratio predicts critical illness patients with 2019 coronavirus disease in the early stage. *J Transl Med.* 2020;18: 1–12. doi:10.1186/s12967-020-02374-0
41. Mauvais-Jarvis F, Klein SL, Levin ER. Estradiol, Progesterone, Immunomodulation, and COVID-19 Outcomes. *Endocrinol (United States).* 2020;161: 1–8. doi:10.1210/endo/bqaa127
42. Bösmüller H, Matter M, Fend F, Tzankov A. The pulmonary pathology of COVID-19. *Virchows Arch.* 2021/02/19. 2021;478: 137–150. doi:10.1007/s00428-021-03053-1
43. Schulte-Schrepping J, Reusch N, Paclik D, Baßler K, Schlickeiser S, Zhang B, et al. Severe COVID-19 Is Marked by a Dysregulated Myeloid Cell Compartment. *Cell.* 2020;182: 1419-1440.e23. doi:10.1016/j.cell.2020.08.001
44. Hadjadj J, Yatim N, Barnabei L, Corneau A, Boussier J. *E (2 , 6 , 7).* 2020;724: 718–724.
45. Diao B, Wang C, Tan Y, Chen X, Liu Y, Ning L, et al. Reduction and Functional Exhaustion of T Cells in Patients With Coronavirus Disease 2019 (COVID-19). *Front Immunol.* 2020;11: 1–7. doi:10.3389/fimmu.2020.00827
46. Bellesi S, Metafuni E, Hohaus S, Maiolo E, Marchionni F, D’Innocenzo S, et al. Increased CD95 (Fas) and PD-1 expression in peripheral blood T lymphocytes in COVID-19 patients. *Br J Haematol.* 2020;191: 207–211. doi:10.1111/bjh.17034
47. Sattler A, Angermair S, Stockmann H, Heim KM, Khadzhynov D, Treskatsch S, et al. SARS–CoV-2–specific T cell responses and correlations with COVID-19 patient predisposition. *J Clin Invest.* 2020;130: 6477–6489. doi:10.1172/JCI140965
48. Diedrich CR, Gideon HP, Rutledge T, Baranowski TM, Maiello P, Myers AJ, et al. CD4CD8 Double Positive T cell responses during Mycobacterium tuberculosis infection in cynomolgus macaques. *J Med Primatol.* 2019;48: 82–89. doi:10.1111/jmp.12399
49. Meckiff BJ, Ramírez-Suástegui C, Fajardo V, Chee SJ, Kusnadi A, Simon H, et al. Imbalance of Regulatory and Cytotoxic SARS-CoV-2-Reactive CD4+ T Cells in COVID-19. *Cell.* 2020;183: 1340-1353.e16. doi:10.1016/j.cell.2020.10.001
50. Weiskopf D, Schmitz KS, Raadsen MP, Grifoni A, Okba NMA, Endeman H, et al. Phenotype and kinetics of SARS-CoV-2-specific T cells in COVID-19 patients with acute respiratory distress syndrome. *Sci Immunol.* 2020;5: 1–14. doi:10.1126/SCIIMMUNOL.ABD2071

51. Gandhi M, Yokoe DS, Havlir D V. Asymptomatic Transmission, the Achilles' Heel of Current Strategies to Control Covid-19. *N Engl J Med*. 2020/04/24. 2020;382: 2158–2160. doi:10.1056/NEJMe2009758
52. Gatto M, Bertuzzo E, Mari L, Miccoli S, Carraro L, Casagrandi R, et al. Spread and dynamics of the COVID-19 epidemic in Italy: Effects of emergency containment measures. *Proc Natl Acad Sci U S A*. 2020/04/23. 2020;117: 10484–10491. doi:10.1073/pnas.2004978117
53. Guan W-J, Ni Z-Y, Hu Y, Liang W-H, Ou C-Q, He J-X, et al. Clinical Characteristics of Coronavirus Disease 2019 in China. *N Engl J Med*. 2020/02/28. 2020;382: 1708–1720. doi:10.1056/NEJMoa2002032
54. Kujawski SA, Wong KK, Collins JP, Epstein L, Killerby ME, Midgley CM, et al. Clinical and virologic characteristics of the first 12 patients with coronavirus disease 2019 (COVID-19) in the United States. *Nat Med*. 2020;26: 861–868. doi:10.1038/s41591-020-0877-5
55. Wu JT, Leung K, Bushman M, Kishore N, Niehus R, de Salazar PM, et al. Estimating clinical severity of COVID-19 from the transmission dynamics in Wuhan, China. *Nat Med*. 2020/03/19. 2020;26: 506–510. doi:10.1038/s41591-020-0822-7
56. Fogarty H, Townsend L, Ni Cheallaigh C, Bergin C, Martin-Loeches I, Browne P, et al. COVID19 coagulopathy in Caucasian patients. *Br J Haematol*. 2020/05/17. 2020;189: 1044–1049. doi:10.1111/bjh.16749
57. Llitjos J-F, Leclerc M, Chochois C, Monsallier J-M, Ramakers M, Auvray M, et al. High incidence of venous thromboembolic events in anticoagulated severe COVID-19 patients. *J Thromb Haemost*. 2020/05/27. 2020;18: 1743–1746. doi:10.1111/jth.14869
58. Panigada M, Bottino N, Tagliabue P, Grasselli G, Novembrino C, Chantarangkul V, et al. Hypercoagulability of COVID-19 patients in intensive care unit: A report of thromboelastography findings and other parameters of hemostasis. *J Thromb Haemost*. 2020;18: 1738–1742. doi:https://doi.org/10.1111/jth.14850
59. Porfidia A, Pola R. Venous thromboembolism in COVID-19 patients. *J Thromb Haemost*. 2020;18: 1516–1517. doi:10.1111/jth.14842
60. Spiezia L, Boscolo A, Poletto F, Cerruti L, Tiberio I, Campello E, et al. COVID-19-Related Severe Hypercoagulability in Patients Admitted to Intensive Care Unit for Acute Respiratory Failure. *Thromb Haemost*. 2020/04/21. 2020;120: 998–1000. doi:10.1055/s-0040-1710018

61. Klok FA, Kruij MJHA, van der Meer NJM, Arbous MS, Gommers DAMPJ, Kant KM, et al. Incidence of thrombotic complications in critically ill ICU patients with COVID-19. *Thromb Res.* 2020/04/10. 2020;191: 145–147. doi:10.1016/j.thromres.2020.04.013
62. Varga Z, Flammer AJ, Steiger P, Haberecker M, Andermatt R, Zinkernagel AS, et al. Endothelial cell infection and endotheliitis in COVID-19. *Lancet (London, England).* 2020/04/21. 2020;395: 1417–1418. doi:10.1016/S0140-6736(20)30937-5
63. Bridwell R, Long B, Gottlieb M. Neurologic complications of COVID-19. *Am J Emerg Med.* 2020/05/16. 2020;38: 1549.e3-1549.e7. doi:10.1016/j.ajem.2020.05.024
64. Baden LR, El Sahly HM, Essink B, Kotloff K, Frey S, Novak R, et al. Efficacy and Safety of the mRNA-1273 SARS-CoV-2 Vaccine. *N Engl J Med.* 2020/12/30. 2021;384: 403–416. doi:10.1056/NEJMoa2035389
65. Polack FP, Thomas SJ, Kitchin N, Absalon J, Gurtman A, Lockhart S, et al. Safety and Efficacy of the BNT162b2 mRNA Covid-19 Vaccine. *N Engl J Med.* 2020/12/10. 2020;383: 2603–2615. doi:10.1056/NEJMoa2034577
66. Sadoff J, Le Gars M, Shukarev G, Heerwegh D, Truyers C, de Groot AM, et al. Interim Results of a Phase 1-2a Trial of Ad26.COV2.S Covid-19 Vaccine. *N Engl J Med.* 2021/01/13. 2021;384: 1824–1835. doi:10.1056/NEJMoa2034201
67. Winger A, Caspari T. The Spike of Concern-The Novel Variants of SARS-CoV-2. *Viruses.* 2021;13: 1002. doi:10.3390/v13061002
68. Singh J, Rahman SA, Ehtesham NZ, Hira S, Hasnain SE. SARS-CoV-2 variants of concern are emerging in India. *Nat Med.* 2021;27: 1131–1133. doi:10.1038/s41591-021-01397-4
69. Lessells RJ. SARS-CoV-2 variants of concern: the knowns and unknowns. *Anaesthesia, Crit care pain Med.* 2021/04/22. 2021;40: 100868. doi:10.1016/j.accpm.2021.100868
70. Walensky RP, Walke HT, Fauci AS. SARS-CoV-2 Variants of Concern in the United States—Challenges and Opportunities. *JAMA.* 2021;325: 1037–1038. doi:10.1001/jama.2021.2294
71. Olsen RJ, Christensen PA, Long SW, Subedi S, Hodjat P, Olson R, et al. Trajectory of Growth of SARS-CoV-2 Variants in Houston, Texas, January through May 2021 Based on 12,476 Genome Sequences. *Am J Pathol.* 2021; S0002-9440(21)00317–5. doi:10.1016/j.ajpath.2021.07.002

72. Abu-Raddad LJ, Chemaitelly H, Butt AA, Vaccination NSG for C-19. Effectiveness of the BNT162b2 Covid-19 Vaccine against the B.1.1.7 and B.1.351 Variants. *N Engl J Med.* 2021/05/05. 2021;385: 187–189. doi:10.1056/NEJMc2104974
73. Haas EJ, Angulo FJ, McLaughlin JM, Anis E, Singer SR, Khan F, et al. Impact and effectiveness of mRNA BNT162b2 vaccine against SARS-CoV-2 infections and COVID-19 cases, hospitalisations, and deaths following a nationwide vaccination campaign in Israel: an observational study using national surveillance data. *Lancet (London, England).* 2021/05/05. 2021;397: 1819–1829. doi:10.1016/S0140-6736(21)00947-8
74. Wu K, Werner AP, Koch M, Choi A, Narayanan E, Stewart-Jones GBE, et al. Serum Neutralizing Activity Elicited by mRNA-1273 Vaccine. *N Engl J Med.* 2021/03/17. 2021;384: 1468–1470. doi:10.1056/NEJMc2102179
75. Woolsey C, Borisevich V, Prasad AN, Agans KN, Deer DJ, Dobias NS, et al. Establishment of an African green monkey model for COVID-19 and protection against re-infection. *Nat Immunol.* 2020/11/24. 2021;22: 86–98. doi:10.1038/s41590-020-00835-8
76. Singh DK, Singh B, Ganatra SR, Gazi M, Cole J, Thippeshappa R, et al. Responses to acute infection with SARS-CoV-2 in the lungs of rhesus macaques, baboons and marmosets. *Nat Microbiol.* 2020/12/18. 2021;6: 73–86. doi:10.1038/s41564-020-00841-4
77. Pandrea I, Cornell E, Wilson C, Ribeiro RM, Ma D, Kristoff J, et al. Coagulation biomarkers predict disease progression in SIV-infected nonhuman primates. *Blood.* 2012/05/31. 2012;120: 1357–1366. doi:10.1182/blood-2012-03-414706
78. Schechter ME, Andrade BB, He T, Richter GH, Tosh KW, Policicchio BB, et al. Inflammatory monocytes expressing tissue factor drive SIV and HIV coagulopathy. *Sci Transl Med.* 2017;9: 1–14. doi:10.1126/scitranslmed.aam5441
79. Beck SE, Kelly KM, Queen SE, Adams RJ, Zink MC, Tarwater PM, et al. Macaque species susceptibility to simian immunodeficiency virus: increased incidence of SIV central nervous system disease in pigtailed macaques versus rhesus macaques. *J Neurovirol.* 2015;21: 148–158. doi:10.1007/s13365-015-0313-7
80. Jin X, Lian J-S, Hu J-H, Gao J, Zheng L, Zhang Y-M, et al. Epidemiological, clinical and virological characteristics of 74 cases of coronavirus-infected disease 2019 (COVID-19) with gastrointestinal symptoms. *Gut.* 2020;69: 1002 LP – 1009. doi:10.1136/gutjnl-2020-320926

81. Lee I-C, Huo T-I, Huang Y-H. Gastrointestinal and liver manifestations in patients with COVID-19. *J Chin Med Assoc.* 2020;83: 521–523. doi:10.1097/JCMA.0000000000000319
82. Hunt RH, East JE, Lanas A, Malfertheiner P, Satsangi J, Scarpignato C, et al. COVID-19 and Gastrointestinal Disease: Implications for the Gastroenterologist. *Dig Dis.* 2020/10/09. 2021;39: 119–139. doi:10.1159/000512152
83. Adams Waldorf KM, Stencel-Baerenwald JE, Kapur RP, Studholme C, Boldenow E, Vornhagen J, et al. Fetal brain lesions after subcutaneous inoculation of Zika virus in a pregnant nonhuman primate. *Nat Med.* 2016/09/12. 2016;22: 1256–1259. doi:10.1038/nm.4193
84. Fornek JL, Korth MJ, Katze MGBT-A in VR. Use of Functional Genomics to Understand Influenza–Host Interactions. Academic Press; 2007. pp. 81–100. doi:https://doi.org/10.1016/S0065-3527(07)70003-9
85. Song T-Z, Zheng H-Y, Han J-B, Feng X-L, Liu F-L, Yang X, et al. Northern pig-tailed macaques (*Macaca leonina*) infected with SARS-CoV-2 show rapid viral clearance and persistent immune response. *Zool Res.* 2021;42: 350–353. doi:10.24272/j.issn.2095-8137.2020.334
86. Costela-ruiz VJ, Illescas-montes R, Puerta-puerta JM, Ruiz C, Melguizo-rodríguez L. SARS-CoV-2 infection: The role of cytokines in COVID-19 disease. *Sci Direct.* 2020.
87. Miyazawa M. Immunopathogenesis of SARS-CoV-2-induced pneumonia: Lessons from influenza virus infection. *Inflamm Regen.* 2020;40: 1–13. doi:10.1186/s41232-020-00148-1
88. Zhou X, McElhaney JE. Age-related changes in memory and effector T cells responding to influenza A/H3N2 and pandemic A/H1N1 strains in humans. *Vaccine.* 2011;29: 2169–2177. doi:10.1016/j.vaccine.2010.12.029
89. Brown DM, Lee S, Garcia-Hernandez M de la L, Swain SL. Multifunctional CD4 cells expressing gamma interferon and perforin mediate protection against lethal influenza virus infection. *J Virol.* 2012/04/04. 2012;86: 6792–6803. doi:10.1128/JVI.07172-11
90. Hughes GJ, Cochrane A, Leen C, Morris S, Bell JE, Simmonds P. HIV-1-infected CD8+CD4+ T cells decay in vivo at a similar rate to infected CD4 T cells during HAART. *AIDS.* [Oxford] : Rapid Science Publishers; 2008. pp. 57–65. doi:10.1097/QAD.0b013e3282f151b9

91. Weiss L, Roux A, Garcia S, Demouchy C, Haeffner-Cavaillon N, Kazatchkine MD, et al. Persistent expansion, in a human immunodeficiency virus-infected person, of V beta-restricted CD4+CD8+ T lymphocytes that express cytotoxicity-associated molecules and are committed to produce interferon-gamma and tumor necrosis factor-alpha. *The journal of infectious diseases*. Chicago : Memorial Institute for Infectious Diseases,; 1998. pp. 1158–1162. doi:10.1086/515674
92. Miyake A, Ibuki K, Suzuki H, Horiuchi R, Saito N, Motohara M, et al. Early virological events in various tissues of newborn monkeys after intrarectal infection with pathogenic simian human immunodeficiency virus. *Journal of medical primatology*. [Copenhagen] : Blackwell Munksgaard; 2005. pp. 294–302. doi:10.1111/j.1600-0684.2005.00127.x

Chapter 2 References

1. Organization WH. WHO COVID-19 Dashboard. World Health Organisation. 2023. Available: <https://covid19.who.int>
2. Sayampanathan AA, Heng CS, Pin PH, Pang J, Leong TY, Lee VJ. Infectivity of asymptomatic versus symptomatic COVID-19. *Lancet*. 2021;397: 93–94. doi:10.1016/S0140-6736(20)32651-9
3. Teo AKJ, Choudhury Y, Tan IB, Cher CY, Chew SH, Wan ZY, et al. Saliva is more sensitive than nasopharyngeal or nasal swabs for diagnosis of asymptomatic and mild COVID-19 infection. *Sci Rep*. 2021;11: 1–8. doi:10.1038/s41598-021-82787-z
4. Xie C, Li Q, Li L, Peng X, Ling Z, Xiao B, et al. Association of early inflammation with age and asymptomatic disease in covid-19. *J Inflamm Res*. 2021;14: 1207–1216. doi:10.2147/JIR.S304190
5. Zhu J, Ji P, Pang J, Zhong Z, Li H, He C, et al. Clinical characteristics of 3062 COVID-19 patients: A meta-analysis. *J Med Virol*. 2020;92: 1902–1914. doi:10.1002/jmv.25884
6. McElvaney OJ, McEvoy NL, McElvaney OF, Carroll TP, Murphy MP, Dunlea DM, et al. Characterization of the inflammatory response to severe COVID-19 illness. *Am J Respir Crit Care Med*. 2020;202: 812–821. doi:10.1164/rccm.202005-1583OC
7. Zhang R, Liu Y, Zhang B, Wu C, Zhou J, Zhang Y, et al. Coagulopathy is associated with multiple organ damage and prognosis of COVID-19. *EXCLI J*. 2021;20: 174–191. doi:10.17179/excli2020-2853
8. Gao Y dong, Ding M, Dong X, Zhang J jin, Kursat Azkur A, Azkur D, et al. Risk factors for severe and critically ill COVID-19 patients: A review. *Allergy Eur J Allergy Clin Immunol*. 2021;76: 428–455. doi:10.1111/all.14657
9. Zhou Y, Chi J, Lv W, Wang Y. Obesity and diabetes as high-risk factors for severe coronavirus disease 2019 (Covid-19). *Diabetes Metab Res Rev*. 2021;37: e3377. doi:10.1002/dmrr.3377
10. Murray JF, Felton CP, Garay SM, Gottlieb MS, Hopewell PC, Stover DE, et al. Pulmonary complications of the acquired immunodeficiency syndrome. Report of a National Heart, Lung, and Blood Institute workshop. *N Engl J Med*. 1984;310: 1682–1688. doi:10.1056/NEJM198406213102529
11. Peters SG, Prakash UB. *Pneumocystis carinii* pneumonia. Review of 53 cases. *Am J Med*. 1987;82: 73–78. doi:10.1016/0002-9343(87)90380-9

12. Stringer JR, Walzer PD. Molecular biology and epidemiology of *Pneumocystis carinii* infection in AIDS. *AIDS* (London, England). England; 1996. pp. 561–571. doi:10.1097/00002030-199606000-00001
13. Altuntas Aydin O, Kumbasar Karaosmanoglu H, Kart Yasar K. HIV/SARS-CoV-2 coinfecting patients in Istanbul, Turkey. *Journal of Medical Virology*. John Wiley and Sons Inc; 2020. pp. 2288–2290. doi:10.1002/jmv.25955
14. Hattab S, Guiguet M, Carcelain G, Fourati S, Guihot A, Autran B, et al. Soluble biomarkers of immune activation and inflammation in HIV infection: Impact of 2 years of effective first-line combination antiretroviral therapy. *HIV Med*. 2015;16: 553–562. doi:10.1111/hiv.12257
15. Abbasi SAA, Noor T, Mylavarapu M, Sahotra M, Bashir HA, Bhat RR, et al. Double Trouble Co-Infections: Understanding the Correlation Between COVID-19 and HIV Viruses. *Cureus*. 2023. doi:10.7759/cureus.38678
16. Guo W, Ming F, Dong Y, Zhang Q, Liu L, Gao M, et al. Driving force of COVID-19 among people living with HIV in Wuhan, China. *AIDS Care*. 2022;34: 1364–1371. doi:10.1080/09540121.2022.2052259
17. Calza L, Bon I, Tadolini M, Borderi M, Colangeli V, Badia L, et al. COVID-19 in patients with HIV-1 infection: a single-centre experience in northern Italy. *Infection*. 2021;49: 333–337. doi:10.1007/s15010-020-01492-7
18. Lee KW, Yap SF, Ngeow YF, Lye MS. COVID-19 in People Living with HIV: A Systematic Review and Meta-Analysis. *International Journal of Environmental Research and Public Health*. 2021. doi:10.3390/ijerph18073554
19. Prabhu S, Poongulali S, Kumarasamy N. Impact of COVID-19 on people living with HIV: A review. *J Virus Erad*. 2020;6: 100019. doi:10.1016/j.jve.2020.100019
20. Geretti AM, Stockdale AJ, Kelly SH, Cevik M, Collins S, Waters L, et al. Outcomes of Coronavirus Disease 2019 (COVID-19) Related Hospitalization Among People With Human Immunodeficiency Virus (HIV) in the ISARIC World Health Organization (WHO) Clinical Characterization Protocol (UK): A Prospective Observational Study. *Clin Infect Dis*. 2021;73: e2095–e2106. doi:10.1093/cid/ciaa1605
21. Bhaskaran K, Rentsch CT, MacKenna B, Schultze A, Mehrkar A, Bates CJ, et al. HIV infection and COVID-19 death: a population-based cohort analysis of UK primary care data and linked national death registrations within the OpenSAFELY platform. *Lancet HIV*. 2021;8: e24–e32. doi:10.1016/S2352-3018(20)30305-2

22. Tesoriero JM, Swain CAE, Pierce JL, Zamboni L, Wu M, Holtgrave DR, et al. COVID-19 Outcomes among Persons Living with or without Diagnosed HIV Infection in New York State. *JAMA Netw Open*. 2021;4: 1–14. doi:10.1001/jamanetworkopen.2020.37069
23. Bertagnolio S, Thwin SS, Silva R, Nagarajan S, Jassat W, Fowler R, et al. Clinical features of, and risk factors for, severe or fatal COVID-19 among people living with HIV admitted to hospital: analysis of data from the WHO Global Clinical Platform of COVID-19. *Lancet HIV*. 2022;9: e486–e495. doi:10.1016/S2352-3018(22)00097-2
24. Nkosi T, Chasara C, Papadopoulos AO, Nguni TL, Karim F, Moosa MYS, et al. Unsuppressed HIV infection impairs T cell responses to SARS-CoV-2 infection and abrogates T cell cross-recognition. *Elife*. 2022;11. doi:10.7554/ELIFE.78374
25. Riou C, du Bruyn E, Stek C, Daroowala R, Goliath RT, Abrahams F, et al. Relationship of SARS-CoV-2–specific CD4 response to COVID-19 severity and impact of HIV-1 and tuberculosis coinfection. *J Clin Invest*. 2021;131: 1–15. doi:10.1172/JCI149125
26. Karim F, Moosa MYS, Gosnell BI, Cele S, Giandhari J, Pillay S, et al. Persistent SARS-CoV-2 infection and intra-host evolution in association with advanced HIV infection. *medRxiv*. 2021; 2021.06.03.21258228. doi:10.1101/2021.06.03.21258228
27. Melton A, Doyle-Meyers LA, Blair R V., Midkiff C, Melton HJ, Russell-Lodrigue K, et al. The pigtail macaque (*Macaca nemestrina*) model of COVID-19 reproduces diverse clinical outcomes and reveals new and complex signatures of disease. *PLOS Pathogens*. 2021. doi:10.1371/journal.ppat.1010162
28. Nichole Cline A, Bess JW, Piatak Jr M, Lifson JD. Highly sensitive SIV plasma viral load assay: practical considerations, realistic performance expectations, and application to reverse engineering of vaccines for AIDS. *J Med Primatol*. 2005;34: 303–312. doi:https://doi.org/10.1111/j.1600-0684.2005.00128.x
29. Beddingfield BJ, Maness NJ, Fears AC, Rappaport J, Aye PP, Russell-Lodrigue K, et al. Effective Prophylaxis of COVID-19 in Rhesus Macaques Using a Combination of Two Parenterally-Administered SARS-CoV-2 Neutralizing Antibodies. *Front Cell Infect Microbiol*. 2021;11: 753444. doi:10.3389/fcimb.2021.753444
30. Amanat F, White KM, Miorin L, Strohmeier S, McMahon M, Meade P, et al. An In Vitro Microneutralization Assay for SARS-CoV-2 Serology and Drug Screening. *Curr Protoc Microbiol*. 2020;58: 1–15. doi:10.1002/cpmc.108
31. Qin C, Zhou L, Hu Z, Zhang S, Yang S, Tao Y, et al. Dysregulation of Immune

- Response in Patients With Coronavirus 2019 (COVID-19) in Wuhan, China. *Clin Infect Dis an Off Publ Infect Dis Soc Am.* 2020;71: 762–768. doi:10.1093/cid/ciaa248
32. Wang D, Hu B, Hu C, Zhu F, Liu X, Zhang J, et al. Clinical Characteristics of 138 Hospitalized Patients With 2019 Novel Coronavirus-Infected Pneumonia in Wuhan, China. *JAMA.* 2020;323: 1061–1069. doi:10.1001/jama.2020.1585
 33. Gandhi M, Yokoe DS, Havlir D V. Asymptomatic Transmission, the Achilles' Heel of Current Strategies to Control Covid-19. *N Engl J Med.* 2020/04/24. 2020;382: 2158–2160. doi:10.1056/NEJMe2009758
 34. Gatto M, Bertuzzo E, Mari L, Miccoli S, Carraro L, Casagrandi R, et al. Spread and dynamics of the COVID-19 epidemic in Italy: Effects of emergency containment measures. *Proc Natl Acad Sci U S A.* 2020/04/23. 2020;117: 10484–10491. doi:10.1073/pnas.2004978117
 35. Guan W-J, Ni Z-Y, Hu Y, Liang W-H, Ou C-Q, He J-X, et al. Clinical Characteristics of Coronavirus Disease 2019 in China. *N Engl J Med.* 2020/02/28. 2020;382: 1708–1720. doi:10.1056/NEJMoa2002032
 36. Kujawski SA, Wong KK, Collins JP, Epstein L, Killerby ME, Midgley CM, et al. Clinical and virologic characteristics of the first 12 patients with coronavirus disease 2019 (COVID-19) in the United States. *Nat Med.* 2020;26: 861–868. doi:10.1038/s41591-020-0877-5
 37. Wu JT, Leung K, Bushman M, Kishore N, Niehus R, de Salazar PM, et al. Estimating clinical severity of COVID-19 from the transmission dynamics in Wuhan, China. *Nat Med.* 2020/03/19. 2020;26: 506–510. doi:10.1038/s41591-020-0822-7
 38. Canary LA, Vinton CL, Morcock DR, Pierce JB, Estes JD, Brenchley JM, et al. Rate of AIDS progression is associated with gastrointestinal dysfunction in simian immunodeficiency virus-infected pigtail macaques. *J Immunol.* 2013/02/11. 2013;190: 2959–2965. doi:10.4049/jimmunol.1202319
 39. Klatt NR, Canary LA, Vanderford TH, Vinton CL, Engram JC, Dunham RM, et al. Dynamics of simian immunodeficiency virus SIVmac239 infection in pigtail macaques. *J Virol.* 2011/11/16. 2012;86: 1203–1213. doi:10.1128/JVI.06033-11

40. Klatt NR, Harris LD, Vinton CL, Sung H, Briant JA, Tabb B, et al. Compromised gastrointestinal integrity in pigtail macaques is associated with increased microbial translocation, immune activation, and IL-17 production in the absence of SIV infection. *Mucosal Immunol.* 2010/03/31. 2010;3: 387–398. doi:10.1038/mi.2010.14
41. Metcalf Pate KA, Lyons CE, Dorsey JL, Shirk EN, Queen SE, Adams RJ, et al. Platelet Activation and Platelet-Monocyte Aggregate Formation Contribute to Decreased Platelet Count During Acute Simian Immunodeficiency Virus Infection in Pig-tailed Macaques. *J Infect Dis.* 2013;208: 874–883. doi:10.1093/infdis/jit278

Chapter 3 References

1. Ahmed R, Gray D. Immunological memory and protective immunity: understanding their relation. *Science*. 1996;272: 54–60. doi:10.1126/science.272.5258.54
2. Mackay CR, Marston WL, Dudler L. Naive and memory T cells show distinct pathways of lymphocyte recirculation. *J Exp Med*. 1990;171: 801–817. doi:10.1084/jem.171.3.801
3. Tomura M, Itoh K, Kanagawa O. Naive CD4+ T lymphocytes circulate through lymphoid organs to interact with endogenous antigens and upregulate their function. *J Immunol*. 2010;184: 4646–4653. doi:10.4049/jimmunol.0903946
4. Murali-Krishna K, Altman JD, Suresh M, Sourdive DJ, Zajac AJ, Miller JD, et al. Counting antigen-specific CD8 T cells: a reevaluation of bystander activation during viral infection. *Immunity*. 1998;8: 177–187. doi:10.1016/s1074-7613(00)80470-7
5. Busch DH, Pilip IM, Vijh S, Pamer EG. Coordinate regulation of complex T cell populations responding to bacterial infection. *Immunity*. 1998;8: 353–362. doi:10.1016/s1074-7613(00)80540-3
6. Badovinac VP, Porter BB, Harty JT. Programmed contraction of CD8+ T cells after infection. *Nat Immunol*. 2002;3: 619–626. doi:10.1038/ni804
7. Omilusik KD, Goldrath AW. Remembering to remember: T cell memory maintenance and plasticity. *Curr Opin Immunol*. 2019;58: 89–97. doi:10.1016/j.coi.2019.04.009
8. Mahnke YD, Brodie TM, Sallusto F, Roederer M, Lugli E. The who's who of T-cell differentiation: Human memory T-cell subsets. *Eur J Immunol*. 2013;43: 2797–2809. doi:10.1002/eji.201343751
9. Sallusto F, Lenig D, Förster R, Lipp M, Lanzavecchia A. Two subsets of memory T lymphocytes with distinct homing potentials and effector functions. *Nature*. 1999;401: 708–712. doi:10.1038/44385
10. Masopust D, Vezys V, Marzo AL, Lefrançois L. Preferential localization of effector memory cells in nonlymphoid tissue. *Science*. 2001;291: 2413–2417. doi:10.1126/science.1058867
11. Gebhardt T, Wakim LM, Eidsmo L, Reading PC, Heath WR, Carbone FR. Memory T cells in nonlymphoid tissue that provide enhanced local immunity during infection with herpes simplex virus. *Nat Immunol*. 2009;10: 524–530. doi:10.1038/ni.1718

12. Masopust D, Choo D, Vezys V, Wherry EJ, Duraiswamy J, Akondy R, et al. Dynamic T cell migration program provides resident memory within intestinal epithelium. *J Exp Med*. 2010;207: 553–564. doi:10.1084/jem.20090858
13. Jiang X, Clark RA, Liu L, Wagers AJ, Fuhlbrigge RC, Kupper TS. Skin infection generates non-migratory memory CD8⁺ T(RM) cells providing global skin immunity. *Nature*. 2012;483: 227–231. doi:10.1038/nature10851
14. Schenkel JM, Fraser KA, Vezys V, Masopust D. Sensing and alarm function of resident memory CD8⁺ T cells. *Nat Immunol*. 2013;14: 509–513. doi:10.1038/ni.2568
15. Rosato PC, Beura LK, Masopust D. Tissue resident memory T cells and viral immunity. *Curr Opin Virol*. 2017;22: 44–50. doi:10.1016/j.coviro.2016.11.011
16. Teijaro JR, Turner D, Pham Q, Wherry EJ, Lefrançois L, Farber DL. Tissue-retentive lung memory CD4 T cells mediate optimal protection to respiratory virus infection. *J Immunol*. 2011/11/04. 2011;187: 5510–5514. doi:10.4049/jimmunol.1102243
17. Wu T, Hu Y, Lee Y-T, Bouchard KR, Benechet A, Khanna K, et al. Lung-resident memory CD8 T cells (T RM) are indispensable for optimal cross-protection against pulmonary virus infection . *J Leukoc Biol*. 2014;95: 215–224. doi:10.1189/jlb.0313180
18. Zens KD, Chen JK, Farber DL. Vaccine-generated lung tissue–resident memory T cells provide heterosubtypic protection to influenza infection. *JCI Insight*. 2019;1. doi:10.1172/jci.insight.85832
19. Pabst R, Tschernig T. Perivascular capillaries in the lung: An important but neglected vascular bed in immune reactions? *J Allergy Clin Immunol*. 2002;110: 209–214. doi:10.1067/mai.2002.126836
20. Pabst R. The periarterial space in the lung: its important role in lung edema, transplantation, and microbial or allergic inflammation. *Pathobiology*. 2004;71: 287–294. doi:10.1159/000081723
21. McDonald DM. The ultrastructure and permeability of tracheobronchial blood vessels in health and disease. *Eur Respir J Suppl*. 1990;12: 572s-585s.
22. Anderson KG, Sung H, Skon CN, Lefrancois L, Deisinger A, Vezys V, et al. Cutting Edge: Intravascular Staining Redefines Lung CD8 T Cell Responses. *J Immunol*. 2012;189: 2702–2706. doi:10.4049/jimmunol.1201682

23. Anderson KG, Mayer-Barber K, Sung H, Beura L, James BR, Taylor JJ, et al. Intravascular staining for discrimination of vascular and tissue leukocytes. *Nat Protoc.* 2014;9: 209–222. doi:10.1038/nprot.2014.005
24. Lake Potter E, Gideon HP, Tkachev V, Fabozzi G, Chassiakos A, Petrovas C, et al. Measurement of leukocyte trafficking kinetics in macaques by serial intravascular staining. *Sci Transl Med.* 2021;13: 1–14. doi:10.1126/SCITRANSLMED.ABB4582
25. Mortlock RD, Wu C, Potter EL, Abraham DM, Allan DSJ, Hong SG, et al. Tissue Trafficking Kinetics of Rhesus Macaque Natural Killer Cells Measured by Serial Intravascular Staining. *Front Immunol.* 2022;12: 1–12. doi:10.3389/fimmu.2021.772332
26. Wu C, Espinoza DA, Koelle SJ, Potter EL, Lu R, Li B, et al. Geographic clonal tracking in macaques provides insights into HSPC migration and differentiation. *J Exp Med.* 2018;215: 217–232. doi:10.1084/jem.20171341
27. Estes JD, Wong SW, Brechley JM. Nonhuman primate models of human viral infections. *Nat Rev Immunol.* 2018;18: 390–404. doi:10.1038/s41577-018-0005-7
28. Barber SA, Gama L, Li M, Voelker T, Anderson JE, Zink MC, et al. Longitudinal Analysis of Simian Immunodeficiency Virus (SIV) Replication in the Lungs: Compartmentalized Regulation of SIV. *SIV Replication Lungs • JID.* 2006. Available: <https://academic.oup.com/jid/article/194/7/931/863281>
29. Hunegnaw R, Mushtaq Z, Enyindah-Asonye G, Hoang T, Robert-Guroff M. Alveolar macrophage dysfunction and increased PD-1 expression during chronic SIV infection of rhesus macaques. *Front Immunol.* 2019;10. doi:10.3389/fimmu.2019.01537
30. Stephenson SE, Wilson CL, Bond NG, Kaur A, Alvarez X, Midkiff CC, et al. Pericytes as novel targets for HIV/SIV infection in the lung. *Am J Physiol Cell Mol Physiol.* 2020;319: L848–L853. doi:10.1152/ajplung.00296.2020
31. Kunisaki KM. Will expanded ART use reduce the burden of HIV-associated chronic lung disease? *Curr Opin HIV AIDS.* 2014;9: 27–33. doi:10.1097/COH.0000000000000018
32. Nelson S, Happel KI, Zhang P, Myers L, Dufour JP, Bagby GJ. Effect of Bacterial Pneumonia on Lung Simian Immunodeficiency Virus (SIV) Replication in Alcohol Consuming SIV-Infected Rhesus Macaques. *Alcohol Clin Exp Res.* 2013;37: 969–977. doi:10.1111/acer.12070

33. Costiniuk CT, Salahuddin S, Farnos O, Olivenstein R, Pagliuzza A, Orlova M, et al. HIV persistence in mucosal CD4R T cells within the lungs of adults receiving long-Term suppressive antiretroviral therapy. *AIDS*. 2018;32: 2279–2289. doi:10.1097/QAD.0000000000001962
34. Twigg Iii HL, Weiden M, Valentine F, Schnizlein-Bick CT, Bassett R, Zheng L, et al. Effect of highly active antiretroviral therapy on viral burden in the lungs of HIV-infected subjects. *J Infect Dis*. 2008;197: 109–116. doi:10.1086/523766
35. Monjure CJ, Tatum CD, Panganiban AT, Arainga M, Traina-Dorge V, Marx PAJ, et al. Optimization of PCR for quantification of simian immunodeficiency virus genomic RNA in plasma of rhesus macaques (*Macaca mulatta*) using armored RNA. *J Med Primatol*. 2014;43: 31–43. doi:10.1111/jmp.12088
36. Butler A, Hoffman P, Smibert P, Papalexi E, Satija R. Integrating single-cell transcriptomic data across different conditions, technologies, and species. *Nat Biotechnol*. 2018;36: 411–420. doi:10.1038/nbt.4096
37. Korsunsky I, Millard N, Fan J, Slowikowski K, Zhang F, Wei K, et al. Fast, sensitive and accurate integration of single-cell data with Harmony. *Nat Methods*. 2019;16: 1289–1296. doi:10.1038/s41592-019-0619-0
38. Liberzon A, Birger C, Thorvaldsdóttir H, Ghandi M, Mesirov JP, Tamayo P. The Molecular Signatures Database Hallmark Gene Set Collection. *Cell Syst*. 2015;1: 417–425. doi:10.1016/j.cels.2015.12.004
39. Gillespie M, Jassal B, Stephan R, Milacic M, Rothfels K, Senff-Ribeiro A, et al. The reactome pathway knowledgebase 2022. *Nucleic Acids Res*. 2022;50: D687–D692. doi:10.1093/nar/gkab1028
40. Liberzon A, Subramanian A, Pinchback R, Thorvaldsdóttir H, Tamayo P, Mesirov JP. Molecular signatures database (MSigDB) 3.0. *Bioinformatics*. 2011;27: 1739–1740. doi:10.1093/bioinformatics/btr260
41. Subramanian A, Tamayo P, Mootha VK, Mukherjee S, Ebert BL, Gillette MA, et al. Gene set enrichment analysis: A knowledge-based approach for interpreting genome-wide expression profiles. *Proc Natl Acad Sci*. 2005;102: 15545–15550. doi:10.1073/pnas.0506580102
42. Jin S, Guerrero-Juarez CF, Zhang L, Chang I, Ramos R, Kuan C-H, et al. Inference and analysis of cell-cell communication using CellChat. *Nat Commun*. 2021;12: 1088. doi:10.1038/s41467-021-21246-9

43. Dykhuizen M, Ceman J, Mitchen J, Zayas M, MacDougall A, Helgeland J, et al. Importance of the CD3 marker for evaluating changes in rhesus macaque CD4/CD8 T-cell ratios. *Cytometry*. 2000;40: 69–75. doi:10.1002/(sici)1097-0320(20000501)40:1<69::aid-cyto9>3.0.co;2-7
44. Zheng H-Y, Zhang M-X, Zhang L-T, Zhang X-L, Pang W, Lyu L-B, et al. Flow cytometric characterizations of leukocyte subpopulations in the peripheral blood of northern pig-tailed macaques (*Macaca leonina*). *Dong wu xue yan jiu = Zool Res*. 2014;35: 465–473. doi:10.13918/j.issn.2095-8137.2014.6.465
45. Walsh DA, Borges da Silva H, Beura LK, Peng C, Hamilton SE, Masopust D, et al. The Functional Requirement for CD69 in Establishment of Resident Memory CD8 + T Cells Varies with Tissue Location . *J Immunol*. 2019;203: 946–955. doi:10.4049/jimmunol.1900052
46. Schenkel JM, Masopust D. Tissue-resident memory T cells. *Immunity*. 2014/12/06. 2014;41: 886–897. doi:10.1016/j.immuni.2014.12.007
47. Renkema KR, Huggins MA, Borges da Silva H, Knutson TP, Henzler CM, Hamilton SE. KLRG1(+) Memory CD8 T Cells Combine Properties of Short-Lived Effectors and Long-Lived Memory. *J Immunol*. 2020;205: 1059–1069. doi:10.4049/jimmunol.1901512
48. Peng C, Huggins MA, Wanhainen KM, Knutson TP, Lu H, Georgiev H, et al. Engagement of the costimulatory molecule ICOS in tissues promotes establishment of CD8+ tissue-resident memory T cells. *Immunity*. 2022;55: 98-114.e5. doi:10.1016/j.immuni.2021.11.017
49. Albakova Z, Mangasarova Y, Sapozhnikov A. Impaired Heat Shock Protein Expression in Activated T Cells in B-Cell Lymphoma. *Biomedicines*. 2022;10: 1–10. doi:10.3390/biomedicines10112747
50. Carman C V., Martinelli R. T lymphocyte-endothelial interactions: Emerging understanding of trafficking and antigen-specific immunity. *Front Immunol*. 2015;6. doi:10.3389/fimmu.2015.00603
51. Winger RC, Harp CT, Chiang M-Y, Sullivan DP, Watson RL, Weber EW, et al. Cutting Edge: CD99 Is a Novel Therapeutic Target for Control of T Cell-Mediated Central Nervous System Autoimmune Disease. *J Immunol*. 2016;196: 1443–1448. doi:10.4049/jimmunol.1501634
52. Ferragut F, Vachetta VS, Troncoso MF, Rabinovich GA, Elola MT. ALCAM/CD166: A pleiotropic mediator of cell adhesion, stemness and cancer progression. *Cytokine Growth Factor Rev*. 2021;61: 27–37. doi:https://doi.org/10.1016/j.cytogfr.2021.07.001

53. Nijmeijer S, Vischer HF, Leurs R. Adhesion GPCRs in immunology. *Biochem Pharmacol.* 2016;114: 88–102. doi:<https://doi.org/10.1016/j.bcp.2016.04.013>
54. Walling BL, Kim M. LFA-1 in T cell migration and differentiation. *Front Immunol.* 2018;9. doi:[10.3389/fimmu.2018.00952](https://doi.org/10.3389/fimmu.2018.00952)
55. Chen J, Hu S, Wang H, Zhao T, Song Y, Zhong X, et al. Integrated analysis reveals the pivotal interactions between immune cells in the melanoma tumor microenvironment. *Sci Rep.* 2022;12: 1–16. doi:[10.1038/s41598-022-14319-2](https://doi.org/10.1038/s41598-022-14319-2)
56. Braud VM, Meghraoui-Kheddar A, Elaldi R, Petti L, Germain C, Anjuère F. LLT1-CD161 Interaction in Cancer: Promises and Challenges. *Front Immunol.* 2022;13: 1–13. doi:[10.3389/fimmu.2022.847576](https://doi.org/10.3389/fimmu.2022.847576)
57. Chyuan IT, Hsu PN. TRAIL regulates T cell activation and suppresses inflammation in autoimmune diseases. *Cell Mol Immunol.* 2020;17: 1281–1283. doi:[10.1038/s41423-020-0410-2](https://doi.org/10.1038/s41423-020-0410-2)
58. Chyuan I-T, Chu C-L, Hsu C-L, Pan M-H, Liao H-J, Wu C-S, et al. T Cell–Specific Deletion of TRAIL Receptor Reveals Its Critical Role for Regulating Pathologic T Cell Activation and Disease Induction in Experimental Autoimmune Encephalomyelitis. *J Immunol.* 2022;208: 1534–1544. doi:[10.4049/jimmunol.2100788](https://doi.org/10.4049/jimmunol.2100788)
59. Chyuan IT, Tsai HF, Wu CS, Hsu PN. TRAIL suppresses gut inflammation and inhibits colitogenic T-cell activation in experimental colitis via an apoptosis-independent pathway. *Mucosal Immunol.* 2019;12: 980–989. doi:[10.1038/s41385-019-0168-y](https://doi.org/10.1038/s41385-019-0168-y)
60. Yenyuwadee S, Sanchez-Trincado Lopez JL, Shah R, Rosato PC, Boussiotis VA. The evolving role of tissue-resident memory T cells in infections and cancer. *Sci Adv.* 2022;8. doi:[10.1126/sciadv.abo5871](https://doi.org/10.1126/sciadv.abo5871)
61. Borges da Silva H, Peng C, Wang H, Wanhainen KM, Ma C, Lopez S, et al. Sensing of ATP via the Purinergic Receptor P2RX7 Promotes CD8(+) Trm Cell Generation by Enhancing Their Sensitivity to the Cytokine TGF- β . *Immunity.* 2020;53: 158-171.e6. doi:[10.1016/j.immuni.2020.06.010](https://doi.org/10.1016/j.immuni.2020.06.010)
62. Fonseca R, Beura LK, Quarnstrom CF, Ghoneim HE, Fan Y, Zebley CC, et al. Developmental plasticity allows outside-in immune responses by resident memory T cells. *Nat Immunol.* 2020;21: 412–421. doi:[10.1038/s41590-020-0607-7](https://doi.org/10.1038/s41590-020-0607-7)
63. Behr FM, Parga-Vidal L, Kragten NAM, van Dam TJP, Wesselink TH, Sheridan BS, et al. Tissue-resident memory CD8+ T cells shape local and systemic secondary T cell responses. *Nat Immunol.* 2020;21: 1070–1081. doi:[10.1038/s41590-020-0723-4](https://doi.org/10.1038/s41590-020-0723-4)

64. Hyun YM, Choe YH, Park SA, Kim M. LFA-1 (CD11a/CD18) and Mac-1 (CD11b/CD18) distinctly regulate neutrophil extravasation through hotspots I and II. *Exp Mol Med*. 2019;51: 1–13. doi:10.1038/s12276-019-0227-1
65. Dunne JL, Collins RG, Beaudet AL, Ballantyne CM, Ley K. Mac-1, but not LFA-1, uses intercellular adhesion molecule-1 to mediate slow leukocyte rolling in TNF- α -induced inflammation. *J Immunol*. 2003;171: 6105–6111. doi:10.4049/jimmunol.171.11.6105
66. Galkina E, Ley K. Vascular adhesion molecules in atherosclerosis. *Arterioscler Thromb Vasc Biol*. 2007;27: 2292–2301. doi:10.1161/ATVBAHA.107.149179
67. Fan Z, Ley K. Leukocyte arrest: Biomechanics and molecular mechanisms of β 2 integrin activation. *Biorheology*. 2015;52: 353–377. doi:10.3233/BIR-15085
68. Nandi A, Estess P, Siegelman M. Bimolecular complex between rolling and firm adhesion receptors required for cell arrest; CD44 association with VLA-4 in T cell extravasation. *Immunity*. 2004;20: 455–465. doi:10.1016/s1074-7613(04)00077-9
69. Milner JJ, Toma C, Yu B, Zhang K, Omilusik K, Phan AT, et al. Runx3 programs CD8(+) T cell residency in non-lymphoid tissues and tumours. *Nature*. 2017;552: 253–257. doi:10.1038/nature24993
70. Bankovich AJ, Shioh LR, Cyster JG. CD69 suppresses sphingosine 1-phosphate receptor-1 (S1P1) function through interaction with membrane helix 4. *J Biol Chem*. 2010;285: 22328–22337. doi:10.1074/jbc.M110.123299
71. Topham DJ, Reilly EC. Tissue-resident memory CD8+ T cells: From phenotype to function. *Front Immunol*. 2018;9. doi:10.3389/fimmu.2018.00515
72. David Masopust AGS. Tissue-Resident T Cells and Other Resident Leukocytes. *Annu Rev Immunol*. 2019.
73. Best JA, Blair DA, Knell J, Yang E, Mayya V, Doedens A, et al. Transcriptional insights into the CD8+ T cell response to infection and memory T cell formation. *Nat Immunol*. 2013;14: 404–412. doi:10.1038/ni.2536
74. Lehmann JCU, Jablonski-Westrich D, Haubold U, Gutierrez-Ramos J-C, Springer T, Hamann A. Overlapping and Selective Roles of Endothelial Intercellular Adhesion Molecule-1 (ICAM-1) and ICAM-2 in Lymphocyte Trafficking 1. *J Immunol*. 2003;171: 2588–2593. doi:10.4049/jimmunol.171.5.2588
75. Galkina E, Thatte J, Dabak V, Williams MB, Ley K, Braciale TJ. Preferential migration of effector CD8+ T cells into the interstitium of the normal lung. *J Clin Invest*. 2005;115: 3473–3483. doi:10.1172/JCI24482

76. Buggert M, Vella LA, Nguyen S, Wu V, Chen Z, Perez-potti A, et al. The identity of human tissue-emigrant CD8+ T cells. 2022;183: 1946–1961. doi:10.1016/j.cell.2020.11.019.The

Conclusion and Future Directions References

1. Ahmed R, Gray D. Immunological memory and protective immunity: understanding their relation. *Science*. 1996;272: 54–60. doi:10.1126/science.272.5258.54
2. Mackay CR, Marston WL, Dudler L. Naive and memory T cells show distinct pathways of lymphocyte recirculation. *J Exp Med*. 1990;171: 801–817. doi:10.1084/jem.171.3.801
3. Tomura M, Itoh K, Kanagawa O. Naive CD4⁺ T lymphocytes circulate through lymphoid organs to interact with endogenous antigens and upregulate their function. *J Immunol*. 2010;184: 4646–4653. doi:10.4049/jimmunol.0903946
4. Busch DH, Pilip IM, Vijn S, Pamer EG. Coordinate regulation of complex T cell populations responding to bacterial infection. *Immunity*. 1998;8: 353–362. doi:10.1016/s1074-7613(00)80540-3
5. Badovinac VP, Porter BB, Harty JT. Programmed contraction of CD8⁺ T cells after infection. *Nat Immunol*. 2002;3: 619–626. doi:10.1038/ni804
6. Renkema KR, Huggins MA, Borges da Silva H, Knutson TP, Henzler CM, Hamilton SE. KLRG1(+) Memory CD8 T Cells Combine Properties of Short-Lived Effectors and Long-Lived Memory. *J Immunol*. 2020;205: 1059–1069. doi:10.4049/jimmunol.1901512
7. Olson JA, McDonald-Hyman C, Jameson SC, Hamilton SE. Effector-like CD8⁺ T cells in the memory population mediate potent protective immunity. *Immunity*. 2013;38: 1250–1260. doi:10.1016/j.immuni.2013.05.009
8. Böttcher JP, Beyer M, Meissner F, Abdullah Z, Sander J, Höchst B, et al. Functional classification of memory CD8(+) T cells by CX3CR1 expression. *Nat Commun*. 2015;6: 8306. doi:10.1038/ncomms9306

Acknowledgments

I am deeply grateful to my advisor, Dr. Nick Maness, for the support and guidance over the past three and a half years. Your trust in granting me the freedom to explore countless avenues — following seemingly endless rabbit holes — has led to invaluable knowledge and skills. A heartfelt thank you to my committee members Drs. Miti Kaur, Robert Blair, Jen Manuzak, and JC Mudd. Your thoughtful feedback and patience have taught me the importance of selective pursuits, reminding me that perhaps not every rabbit hole warrants exploration.

Special thanks to the members of the Maness lab, both past and present: Dawn Szeltner, Toni Penney, and Clara Krzykwa. Your friendship and support have meant the world to me. To my student mentors, Drs. Matilda Mostrom, Giorgio Zenere, and Nathan Johnson, the tools and insights you shared were a daily resource for me. Your mentorship has truly shaped my time at Tulane.

My deepest appreciation goes to my family, who have been pillars of strength throughout my decades long academic career. To my parents, Dennis and Norma, thank you for your endless encouragement. Jack, my husband, your unwavering belief in me has been my driving force. And to my son Hunter, embarking on this PhD journey alongside you has been a truly special experience.

Biography

Alexandra was born in Athens, Georgia and spent most of her childhood in southeast Louisiana and northeast Texas. She attended the University of Texas at Arlington (UTA) where she earned a Bachelor of Business Administration degree with a concentration in Economics and subsequent Master's degree in Economics. It was at UTA that she met her future husband, Jack, during her first day of Freshman orientation. After a fulfilling period dedicated to raising her family, she chose to embark on a new journey in pursuit of a Doctoral degree in the Biomedical Sciences Program at Tulane University School of Medicine. Upon earning her Ph.D., Alexandra aspires to continue her research in the field of pulmonary immunology, with the hope of unraveling more about the nuanced attributes of T cells and their implications in human health and disease.